NEUTRON SCATTERING INVESTIGATION OF THE INTERPLAY BETWEEN LATTICE AND SPIN DEGREES OF FREEDOM IN GEOMETRICALLY FRUSTRATED MAGNETS

Inauguraldissertation
zur
Erlangung der Würde eines Doktors der Philosophie
vorgelegt der Philosophisch-Naturwissenschaftlichen Fakultät
der Universität Basel

von

Rafał Wawrzyńczak

von Polen

2020

Genehmigt von der Philosophisch-Naturwissenschaftlichen Fakultät
auf Antrag von

Prof. Dr. Michel Kenzelmann
Prof. Dr. Manfred Sigrist

Basel, 25.06.2019

Prof. Dr. Martin Spiess
The Dean of Faculty

Abstract

Geometrical frustration in magnetic systems brought on by the incompatibility of structural and magnetic interaction symmetries leads to the suppression of a long-range order via introduction of macroscopic degeneracy of the system ground-state. As a result magnetic moments in frustrated systems remain disordered but highly correlated and may fluctuate down to very low temperatures. It results in variety of exotic physical phenomena ranging from structural distortions relieving the frustration to appearance of fractional quasiparticle excitations.

This thesis presents results of studies on three examples of classical and quantum frustrated magnetic systems. The first is the family of chromate spinel breathing pyrochlore antiferromagnets $LiGa_{1-x}In_xCr_4O_8$. These accommodate an alternating distortion to the pyrochlore lattice of Cr^{3+} ions. This distortion with change of its magnitude drives the system between the singlet state of separated tetrahedron and the uniform pyrochlore lattice ground-state. Neutron and x-ray diffraction studies on $x = 0$ composition identified two magnetostructural transitions. The first at $T = 13.8$ K and the second at 12.5 K. They result in the mixture of two phases, one tetragonal described with C_A222_1 magnetic space group and the second following complex multi-$\boldsymbol{k}$ order whose exact nature could not be resolved with the available data. A small departure from the $x = 0$ stoichiometry to $x = 0.05$ have not suppressed the single anomaly present in specific heat. However, no long-range magnetic order or lattice distortion were detected in diffraction data. Reverse Monte Carlo treatment of the diffuse feature observed in the neutron scattering allowed to identify this transition as the onset of classical spin nematic phase concomitant with spin freezing. Nonetheless, spectroscopic studies have shown the presence of persistent fluctuations of magnetic moments down to the lowest temperatures.

The second example is $Tb_3Ga_5O_{12}$ (TGG). It hosts a hyperkagome magnetic sublattice of Tb^{3+} ions. TGG orders at a very low $T_N = 0.24$ K in an induced-moment type order. Neutron powder diffraction allowed to determine the value of the ordered magnetic moment $\mu = 3.6\ \mu_B$. The analysis of diffuse scattering have identified presence of correlated paramagnet phase above T_N. However, no dipolar order parameter for this phase was found in the refined spin structures. The inelastic neutron scattering on powder sample enabled the refinement of the set of CEF Hamiltonian parameters, using which the structure of CEF eigenstates was obtained. Following single-crystal experiment showed the presence of six dispersive magnetic excitons in place of the first excited CEF state. These are present in both the paramagnetic and ordered regimes, and reflect the collective character of usually single-ion crystal field effects acquired by magnetic interactions. A softening of one of these modes was observed at the magnetic propagation vector on cooling towards T_N. Nonetheless, no closing of the gap was detected. Measurements of phonon dispersion curves allowed to confirm the available results of density functional

theorem (DFT) calculations.

The third investigated system is $RbNiCl_3$ a $S = 1$ spin-1 antiferromagnetic Heisenberg chain. Polarization analysis of inelastic neutron scattering data in the quantum-disordered phase did not allow for unambiguous identification of the multi-particle states similar to these observed in quantum-disordered phase of closely related $CsNiCl_3$. However, signatures of continuum scattering at the antiferromagnetic point of the intrachain dispersion were found in the three-dimensional ordered phase. The strength of the continuum does not agree with predictions of field-theory for spin-1 chains. It supports assumptions of frustration between the chains being possible source of observed phenomena. Linear spin-wave theory (LSWT) fit to the magnetic excitaitons at $T < t_N$ have revealed a set of discrepancies the calculated and measured spectra. These suggest strong influence of quantum fluctuations on the physics of the ordered state and exclude the feasibility of LSWT in this system. Some of the discrepancies were positively identified as phonon modes using the available results of DFT calculations.

Contents

List of Figures

List of Tables

Chapter 1

Introduction

Since the times of the ancient Greek philosophers the exploration of magnetic properties of materials was an essential part of vast branch of a knowledge nowadays covered by the term solid state physics. Despite the centuries of interest, it was only in XIX century that James Clerk Maxwell has identified fundamental unity of electric and magnetic phenomena [1]. Following the development of special relativity by Albert Einstein [2] and the celebrated experiment conducted by Gerlach and Stern [3] it was realized that magnetism is a manifestation of both relativistic and quantum effects. It has eventually allowed to fully understand the simplest magnetic materials whose behaviour defied explanation within the framework of preceding theories.

These early works have cleared a path for the exploration of a wide range of exotic physics brought on by the presence of competing magnetic interaction mechanisms, lowered spatial dimensionality of the system, the coupling of spin and lattice degrees of freedom, or the relation between the geometries of magnetic interactions and the crystalline structure (i.e. geometrical frustration). These may vary from emergent electrodynamics in quantum spin ices [4] to Majorana fermions in Kitaev model [5]. Contemporary studies in the field focus on: examination of these effects in the materials known to the researchers for various other features, but overlooked previously due to lack of appropriate theoretical or experimental apparatus, and design of novel materials with internal parameters fine-tuned to produce the desired physics. Both approaches were made possible by persistent effort aiming at thorough understanding of the fundamental physical laws governing the world of magnetism.

Although all of the aspects presented in prior paragraphs were motivated by understanding the underlying theory of magnetism, these described progress have also led to extensively implemented technical applications of magnetic materials (e.g. data storage in electronic devices, active media in solid state lasers and other optoelectronic devices). Furthermore, one can easily formulate a long list of proposals, which may lead to further advances e.g. spintronics [6], magnetic refrigeration [7], spin caloritronics [8] or realizations of quantum computing employing the unusual properties of topological phases of matter [9, 10]. These perspectives provide continuous strong motivation fuelling progress in the field.

This work presents a study on three systems eligible for the geometrical frustration and associated interplay of magnetism and crystalline structure. These are chromate spinel $LiGa_{1-x}In_xCr_4O_8$ breathing pyrochlore antiferromagnets, a rare-earth garnet $Tb_3Ga_5O_{12}$

(terbium gallium garnet - TGG) and spin-1 antiferromagnetic Heisenberg chain. In Chapter 2 there is presented overview of the aspects of theory of magnetism referred to in the following parts of this manuscript. It includes the discussion of consequences of geometrical frustration and consequences and lowered dimensionality in the magnetic systems. Chapter 3 describes the experimental techniques implemented during the studies described in this work. It focuses mainly on neutron scattering techniques, which provided the data constituting the core of this thesis.

Chapter 4 describes results of the study on $x = 0$ and $x = 0.05$ of $LiGa_{1-x}In_xCr_4O_8$ family, starting with the determination of the character of transitions observed in $x = 0$ and associated with them low-temperature phases. It continues with the description of classical spin nematic phase of $x = 0.05$ and the character of spin dynamics above and below the transition point.

In Chapter 5 description of low-temperature ordered magnetic structure of TGG is provided. The results of exploration of correlated paramagnet phase present at $T > T_N$ are shown. Later the determination of details of the crystal electric field scheme in TGG is presented. Finally the observation of dispersive crystal field excitons is reported and their possible connection to the magnetic ordering process is discussed.

The results obtained on $RbNiCl_3$ are given in Chapter 6. It begins with the description of the observation of multi-particle scattering continuum. Afterwards the discussion of application of linear spin-wave theory to magnetic excitaitons present in the ordered phase is discussed.

A detailed summary of the results obtained for each of these systems and the perspectives for future developments of each study are presented at the end of respective chapter. Chapter 7 provide a brief general summary and closing remarks for the work presented in this manuscript.

Chapter 2

Theoretical framework

This chapter gives a brief overview of basic notions of the microscopic theory of magnetism and mainly aims at establishing conventions and definitions for more detailed discussion in following chapters. A further read on each topic, if not stated otherwise in respective section, can be found in Refs. [11, 12, 13, 14, 15, 16].

2.1 Single ion magnetism

2.1.1 Single electron magnetism

The fundamental building block of a magnetic system is a single electron which carries an intrinsic spin angular momentum $\boldsymbol{s}$, characterized by the quantum number $s = \frac{1}{2}$, and leads to the appearance of a spin magnetic moment of:

$$\boldsymbol{\mu}_s = -g\mu_{\mathrm{B}}\boldsymbol{s}, \tag{2.1}$$

with its magnitude:

$$\mu_s = g\sqrt{s(s+1)}\mu_{\mathrm{B}} = g\sqrt{s(s+1)}\frac{e\hbar}{2m_{\mathrm{e}}}, \tag{2.2}$$

and component along z axis:

$$\mu_{sz} = -gm_s\mu_{\mathrm{B}}, \tag{2.3}$$

where $\boldsymbol{s}$ is the electron's spin composed of s_x, s_y and s_z operators proportional to the Pauli spin matrices(σ_x, σ_y and σ_z). g is its g-factor ($g \sim 2$), μ_{B} is the Bohr magneton, $m_s = \pm\frac{1}{2}$ is one of the possible projections of spin angular momentum on a fixed axis, e is the elementary charge, $\hbar$ is the Dirac's constant and m_e is the electron mass. The Bohr magneton, $\mu_{\mathrm{B}} \approx 9.27 \times 10^{-24}$ J/T is a convenient unit for the microscopic description of magnetism as magnetic moments of atoms usually have the same order of magnitude.

Magnetic moments $\boldsymbol{\mu}_s$ interact with the magnetic field $\boldsymbol{B}$ via Zeeman coupling, which for a single electron is of the following form:

$$\mathcal{H}_{\mathrm{Zeeman}} = -\boldsymbol{\mu}_s \cdot \boldsymbol{B} = -g\mu_{\mathrm{B}}\boldsymbol{s} \cdot \boldsymbol{B}, \tag{2.4}$$

where $-g\mu_B B$ is the so-called Zeeman splitting describing the energy difference for anti-parallel moments in the same field.

2.1.2 Free ion magnetism

When residing in the spherical attractive Coulomb potential of the atomic nucleus and the single-electron wavefunction may be presented as the solution of Schrödinger equation in spherical coordinate system [11]:

$$\psi_{nlm}(r) = R_{nl}(r)Y_l^{m_l}(\theta,\phi), \tag{2.5}$$

giving the radial ($R_{nl}(r)$) and angular ()$Y_l^{m_l}(\theta,\phi)$) dependence of electrons wavefunction. The energy of single electron is defined by two quantum numbers n ($n = 1, 2, 3...$, l ($0 \leq l < n$) describing the occupied shell (radial component) and the orbital angular momentum respectively. The magnetic quantum number m_l ($-l \leq m_l \leq l$) describes the projection of the orbital angular momentum on a fixed axis. Therefore, apart from the spin angular momentum ($\boldsymbol{s}$) electron possesses also orbital angular momentum ($\boldsymbol{l}$) connected with an orbital motion around the center of the potential.

If the ion hosts more than one electron and their mutual interaction is considered as average potential acting on every single electron (Hartree approximation). The shells (groups of states with fixed n and l) are filled in the order of rising energy. The response of the magnetic material to the applied field (apart from, usually negligibly small, diamagnetic contribution - coupling of the field to the current loops of electron's orbital motion) comes from the unfilled shells. In case of filled shells the contribution from electrons having $\pm m_l$ and $\pm m_s$ cancels out ($\sum_i \boldsymbol{s}_i = 0$ and $\sum_i \boldsymbol{l}_i = 0$).

This leads to the shell occupied with i electrons and $2(2l+1)$ accessible orbitals (all possible m_l and m_s, giving $\binom{2(2l+1)}{i}$ possible filling patterns. For example Tb^{3+} ion with $4f^8$ configuration of the unfilled shell ($n = 4$, $l = 3$ marked by f in $0, 1, 2, 3... \rightarrow s, p, d, f...$ convention and $i = 8$) has $\binom{14}{8} = 3003$-fold degeneracy of the ground-state.

Departing from Hartree approximation, thus including the electron-electron electrostatic interactions:

$$\mathcal{H}_{\text{Coulomb}} = \sum_{i>j} \frac{e^2}{|\boldsymbol{r}_i - \boldsymbol{r}_j|}, \tag{2.6}$$

lifts partially this degeneracy [11]. $\boldsymbol{S} = \sum_i \boldsymbol{s}_i$, $\boldsymbol{L} = \sum_i \boldsymbol{l}_i$ the total spin and orbital angular momenta of the ion are sums of single electron momenta commute with the Hamiltonian Eq. 2.6 and are valid quantum numbers. The selection of the ground state, in most cases, follow the algorithm composed from the 1st and the 2nd Hund's rules according to which the ground-state must:

1. Maximize the value of the total spin angular momentum S.

2. Maximize the value of the total orbital angular momentum L.

The selected ground-state exhibits a $(2L+1)(2S+1)$ degeneracy. The selection of the Hund's ground-state for Tb^{3+} ion is schematically presented in Fig. 2.1 and gives $S = 3$

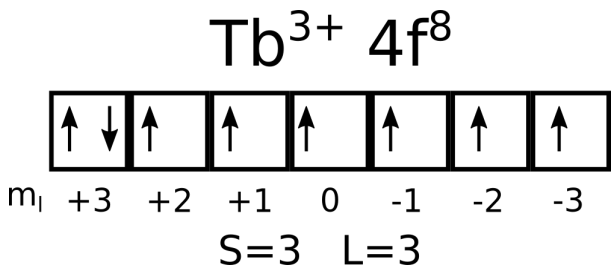

Figure 2.1: The ground-state of Tb^{3+} ion selected with 1st and the 2nd Hund's rules.

and $L = 3$. This limits the number of degenerate states with the lowest energy from 3003 to 49.

The electron's orbital motion around the nucleus in the reference frame of the electron is perceived as the charged nucleus orbiting around the electron. In this picture the magnetic field created by the moving charge can couple to the electron's spin magnetic moment. This spin-orbit coupling, can be accounted for with the following term in the Hamiltonian [11, 12]:

$$\mathcal{H}_{\mathrm{SO}} = \sum_i \lambda_i (\boldsymbol{l}_i \cdot \boldsymbol{s}_i), \tag{2.7}$$

with constant λ describing the strength of the spin-orbit coupling.

In the presence of the spin-orbit coupling the valid quantum number describing the magnetic moment of the electron is the total angular momentum $j = l + s$, which necessitates the replacement of the spin g-factor with the *Landé g-factor*:

$$g_j = \frac{3}{2} + \frac{s(s+1) - l(l+1)}{2j(j+1)}, \tag{2.8}$$

it results from the fact that only the components of angular momenta ($\boldsymbol{s}$ and $\boldsymbol{l}$) parallel to the $\boldsymbol{j}$ are now conserved quantities.

Constructing the Hamiltonian from those two terms:

$$\mathcal{H} = \mathcal{H}_{\mathrm{Coulomb}} + \mathcal{H}_{\mathrm{SO}} \tag{2.9}$$

we need to consider that the two limiting cases of this procedure are based on the relative strength $\mathcal{H}_{\mathrm{Coulomb}}$, defining the $\boldsymbol{l}_i$ and $\boldsymbol{s}_i$ of the single electron i, and $\mathcal{H}_{\mathrm{SO}}$. In case of $\mathcal{H}_{\mathrm{Coulomb}} \gg \mathcal{H}_{\mathrm{SO}}$, the spin-orbit term might be considered as a weak perturbation and expressed in much simpler form:

$$\mathcal{H}_{\mathrm{SO}} = \lambda(L,S)(\boldsymbol{L} \cdot \boldsymbol{S}), \tag{2.10}$$

where $\lambda > 0$ for less-than-half-filled shells and $\lambda < 0$ for more-than-half-filled shells [12]. This assumption allows to stay within a fixed (L,S) subspace of states. As both L and S are no longer conserved quantum numbers, but the $J = L+S$ is, the degenerate manifold of fixed (L,S) states is split into multiplets characterized by J, of $2J+1$-fold degeneracy, with J satisfying $|L - S| \leq J \leq L + S$. From those considerations there can be derived the 3rd Hund's rule requiring the ground state J-manifold to:

3. Minimize J ($J = |L-S|$) for less-than-half-filled shell and maximize it ($J = |L+S|$) for more-than-half-filled shells.

This approach is refereed to as *LS coupling*, or Russell-Saunders coupling. It gives a very good description of lighter elements due to their weak spin-orbit term and works reasonably well with rare earth elements, as the $4f$ orbitals occupy states close to atomic nuclei, increasing the strength of $\mathcal{H}_{\text{Coulomb}}$ [17].

The full set of Hund's rules enables us to determine the term symbol of the ground-state configuration: ${}^{2S+1}L_J$, where the subscript and superscript are numerals and the orbital part is given by a letter marking the right spectroscopic term (S, P, D, F... for 0, 1, 2, 3... respectively). As an example: ${}^7F_6$ is the ground-state term of Tb^{3+} ion with $S = 3$, $L = 3$ and $J = 3 + 3 = 6$. This step allowed for further reducing the degeneracy of terbium's single ion ground-state from 49 to $2J + 1 = 13$ For this ground-state term the expected effective moment should be $\mu_{\text{eff}} = g_J\mu_{\text{B}}\sqrt{J(J+1)} = 9.72\mu_{\text{B}}$.

The set of basis functions $\Psi = |S, L, J, m_J\rangle$ (with m_J varying in the range $\langle -J, J\rangle$) retrieved from this simple analysis might serve as a starting point for investigation of further, more subtle effects, treated as a perturbation to this model.

The opposite situation when $\mathcal{H}_{\text{SO}} \gg \mathcal{H}_{\text{Coulomb}}$ requires different treatment of the moments. The total angular momenta of single electrons $\boldsymbol{j}_i = \boldsymbol{l}_i + \boldsymbol{s}_i$ are evaluated and their sum $\boldsymbol{J} = \sum_i \boldsymbol{j}_i$ describes the magnetic state of the investigated atom. This case is often called as *jj coupling* and is applicable to heavier elements (i.e. $5d$ metals).

2.1.3 Single ion in crystalline environment

Although the crystal as a whole does not carry a net charge, this often does not hold to single ions forming its lattice. A magnetic ion when placed in a crystal environment is subjected to the anisotropic electrostatic field produced by neighbouring ions. Symmetry of this field, being the point symmetry of the ion's site, breaks the spherical symmetry of the free ion and thus lifts the degeneracy within single J manifold (formed by $2J + 1$ m_J states).

This can be accounted for with adding an additional crystal electric field (CEF) term to the Hamiltonian presented in Eq. 2.9:

$$\mathcal{H} = \mathcal{H}_{\text{Coulomb}} + \mathcal{H}_{\text{SO}} + \mathcal{H}_{\text{CEF}}. \tag{2.11}$$

Within this picture, two situations might be distinguished:

1. ($\mathcal{H}_{\text{Coulomb}} \gg$)$\mathcal{H}_{\text{CEF}} \gg \mathcal{H}_{\text{SO}}$ - (intermediate crystal field) observed in $3d$ metals where the $3d$ orbitals are spatially extended and weakly screened from surrounding ions. In this case the J is no longer a good quantum number, third Hund's rule cease to withhold and the manifold structure of the ground state is no longer observed. The system's eigenstates are composed of fixed L and S states [12].

2. ($\mathcal{H}_{\text{Coulomb}} \gg$)$\mathcal{H}_{\text{SO}} \gg \mathcal{H}_{\text{CEF}}$ - characteristic for rare earth elements, where $4f$ electrons are distributed closer to the nuclei (bigger effective charge of the nucleus - stronger spin-orbit [11]) and they are shielded form their local crystalline environment by other more spread orbitals. All Hund's rules apply and robust J manifold structure is observed.

The first case, ultimately, leads to the effect known as orbital quenching. In transition metals the unpaired d shells are the most spatially extended and there are not screened by other shells ($5s$ and $5p$ shells play this role in $4f$ elements). Due to that, they are strongly affected by the crystal electric fields, what in combination with rather weak spin-orbit effects in the atoms of light elements path a way to complete dominance of CEF effects. The real form of the electrostatic CEF potential (see below) requires its eigenfunctions to be real. As eigenfunctions of the $\hat{L}_z$ operator with eigenvalues m_l contain the azimuthal dependence in form of: $\mathrm{e}^{\mathrm{i}m_l\phi}$, in combination with real valued potential, it requires eigenstates of the complete Hamiltonian to adopt the form of linear combinations having equal contributions of both m_l and $-m_l$ eigenstates. It results with expectation values of all $\hat{\boldsymbol{L}}$ $i = x, y, z$ components being quenched: $\langle L_i \rangle = 0$. It can be observed that the experimentally determined values of effective moment, for numerous systems, are well described by the spin-only value: $\mu_{\mathrm{eff}} = 2\mu_{\mathrm{B}}\sqrt{S(S+1)}$ [13]. The observed deviations from this value appear due to small, but not always negligible, spin-orbit coupling admixing the non-zero L states, which changes the g-factor from 2 - the spin-only value.

The second scenario offers an opportunity to heavily reduce the complexity of the problem. The strong spin-orbit coupling allows for limiting the considerations to the ground-state multiplet determined by Hund's rules as the energy splitting to the higher multiplets is orders of magnitude larger than the intra-multiplet splittings. Within the framework of those limitations the Steven's equivalent operator method, described below, can be applied.

The CEF term in the Hamiltonian has the following form [18]:

$$\mathcal{H}_{\mathrm{CEF}} = -|e| \sum_i V_{\mathrm{c}}(\boldsymbol{r}_i), \tag{2.12}$$

where V_{c} is the electrostatic potential generated by neighbouring charges. It is reasonable to assume that the wave functions of the fairly localized $4f$ electrons do not overlap with those of the valence electrons of nearby ions. This assumption facilitate the use of Laplace equation: $\Delta V_{\mathrm{c}} = 0$, to calculate the electrostatic potential, giving the following solution:

$$V_{\mathrm{c}}(\boldsymbol{r}) = \frac{1}{4\pi\epsilon_0} \int \frac{\rho(\boldsymbol{R})}{|\boldsymbol{r} - \boldsymbol{R}|} \mathrm{d}^3\boldsymbol{R}, \tag{2.13}$$

where ϵ_0 is the electric permeability of vacuum and $\rho(\boldsymbol{R})$ describes the local charge distribution. This form of the potential might be expanded as a sum of tesseral harmonics Z_l^m, which are linear combinations of spherical harmonics producing purely real functions [18, 17], what is required by the real character of the electrostatic potential $V_{\mathrm{c}}(\boldsymbol{r})$. This expansion results in:

$$V_{\mathrm{c}}(\boldsymbol{r}) = \sum_{l=0}^{\infty} \sum_{m=-l}^{l} r^l Z_l^m(\Omega_r) \frac{1}{2l+1} \int \mathrm{d}^3 R \frac{\rho(\boldsymbol{R}) Z_l^m(\Omega_R)}{\epsilon_0 R^{l+1}}, \tag{2.14}$$

it can be understood as the interaction of $4f$ electron multipoles ($H_l^m = \sum_{i=1}^{N} r_i^l Z_l^m(\Omega_{r_i})$) with appropriate components of the electrostatic field generated by neighbouring ions ($\gamma_l^m = \frac{1}{2l+1} \int \mathrm{d}^3 R \frac{\rho(\boldsymbol{R}) Z_l^m(\Omega_R)}{\epsilon_0 R^{l+1}}$).

A major simplification appears due to the fact that the $4f$ electrons are only allowed to have $l < 7$ multipolar distributions. Additionally, the angular momentum addition rules, enclosed in the form of Clebsch-Gordan coefficients, applied while generating the $|S, L, J, m_J\rangle$ states in form of linear combinations of single particle $\Psi_{4f}^{mm_s}$ states exclude all terms with odd m. Those limit the first sum in Eq. 2.14 to $l = 2, 4, 6$ [18], which limits the number of Hamiltonian terms to 27.

Symmetry considerations further reduce the number of parameters needed to be accounted for by the ionic site symmetry being reflected in the symmetry of generated electric field and limiting the number of tesseral harmonics appearing in the expansion.

Separating out the coordinate-dependent terms from $Z_l^m(\Omega_r)$ and grouping the remainder, and the other prefactors from H_l^m together with γ_l^m, one can very conveniently apply the *Wigner-Eckart* theorem to the former part. It allows for use of equivalent operator method introduced by Stevens [19], where the matrix elements of coordinate-dependent potential operators are shown to be connected with the appropriate combinations of angular momentum operators by so called Wigner coefficients. This allows to express Eq. 2.12 in much more convenient form:

$$\mathcal{H}_{\mathrm{CEF}} = B_l^m O_l^m, \tag{2.15}$$

where B_l^m are the Steven's parameters and O_l^m are Steven's equivalent operators constructed with $\hat{J}_x$, $\hat{J}_y$, $\hat{J}_z$ and $\hat{\boldsymbol{J}}$ operators. The full list of the explicit form of the equivalent operators is presented in appendix A. of Ref. [18].

This method, considering only the ground-state J multiplet reduces complexity with respect to the intermediate crystal field case, where spin-orbit effects have to be fully accounted for and has been successfully applied to the vast set of rare-earth based magnetic compounds [20].

The B_l^m operators contain the information about the type of ion subjected to the field and the distribution of charges contributing to it. Their value can be calculated with a point-charge model, which describes the sources of the crystalline electric field ($\rho(\boldsymbol{R}) = \sum_i n_i e \delta(\boldsymbol{R} - \boldsymbol{R}_i)$) as point-charges placed at the ionic sites, although this approximation is often found to have scarce limitations.

CEF affects the magnetic anisotropy of the ions along the special symmetry directions of its local environment (e.g. its symmetry axis) necessitating the introduction of a g-tensor describing this anisotropy. Those effects for sites characterized by axially symmetric point groups can be represented by an effective anisotropy term in the spin Hamiltonian:

$$\mathcal{H}_{\mathrm{SIA}} = -DS_\alpha^2, \tag{2.16}$$

with $D > 0$ for the case of axial anisotropy, where S_α ($\alpha = x, y, z$) stands for the spin component along the axis of anisotropy and $D < 0$ in case of planar anisotropy fixing the magnetic moment to be in the plane perpendicular to the direction α.

2.2 Magnetic interactions within the crystal

The scope of this work covers exclusively the materials from the family of electronic insulators, where the electrons responsible for material's magnetism are localized at the

ionic sites, and no contributions from itinerant electrons are considered. Due to this fact the discussion of interactions leading to the collective magnetic behaviour will be limited to the ones present in aforementioned systems.

2.2.1 Dipolar interaction

When considering magnetic ions as hosting classical magnetic dipoles ($\boldsymbol{\mu}$) the energy of interaction between two of them, residing at $\boldsymbol{r_1}$ and $\boldsymbol{r_2}$, might be expressed as:

$$E_{\text{dip}} = \frac{\mu_0}{4\pi r^3}\left[\boldsymbol{\mu}_1 \cdot \boldsymbol{\mu}_2 - \frac{3(\boldsymbol{\mu}_1 \cdot \boldsymbol{r})(\boldsymbol{\mu}_2 \cdot \boldsymbol{r})}{r^2}\right], \tag{2.17}$$

where $\boldsymbol{r} = \boldsymbol{r}_2 - \boldsymbol{r}_1$ and μ_0 is the permeability of the vacuum. As it can be easily noticed this interaction shows strong anisotropy with respect to relative position and moment directions. The strength of this coupling can be easily evaluated and it is found usually to be of the order of 1 K or lower and starts playing significant roles in millikelvin temperature ranges. As it strongly depends on the size of the magnetic moment it is expected to be the strongest in rare-earth systems, whose numerous unpaired $4f$ electrons favour large moments.

2.2.2 Direct exchange

Vast majority of known materials, hosting long-range magnetic orders, exhibit the transitions to the ordered phase at tens or hundreds of Kelvins. This observation is strongly in contrast with the expected strength of dipole-dipole interactions lying within the classical framework.

The interaction responsible for this behaviour could be found only after taking into account some aspects of the quantum description of the multi-electron states. The many-body wavefunction of electrons, as fermions, is approximated by an antisymmetrized uncorrelated product function, that can be written as a single Slater determinant constituted by single-electron functions $\Psi_{ai} = \phi_a(\boldsymbol{r}_i)\chi_\alpha(\boldsymbol{s}_i)$ (where $\phi_a(\boldsymbol{r}_i)$ and $\chi_\alpha(\boldsymbol{s}_i)$ stand for orbital and spin part of the i^{th} electron's wavefunction). Introducing the antisymmetry of overall states, under the particel exchange, is done by carefully choosing the orbital and spin states of appropriate parity. Applying to those states the Hamiltonian describing Coulomb interactions between **electrons occupying partially overlapping orbitals**:

$$\mathcal{H}_{\text{Coulomb}} = \frac{\mathrm{e}^2}{|\boldsymbol{r}_i - \boldsymbol{r}_j|}, \tag{2.18}$$

one obtains two types of terms: the ordinary Coulomb repulsion term dependent on the relative charge distribution of the different electrons and the cross-terms resulting from antisymmetric spatial (orbital) parts of those composite wavefunctions.

The energy of the exchange term lifting the degeneracy of the repulsion term can be expressed using the spin-dependent part of the Hamiltonian. It can be enclosed in simple effective form of Heisenberg pair interactions:

$$\mathcal{H}_{\text{exchange}} = -\sum_{i,j} J_{i,j}\boldsymbol{S}_i \cdot \boldsymbol{S}_j, \tag{2.19}$$

where $J_{i,j}$ (exchange integral) contains the mentioned exchange terms of Hamiltonian in Eq. 2.19 and its sign determines the character of the described interaction either making it ferromagnetic ($J_{i,j} > 0$), or antiferromagnetic ($J_{i,j} < 0$).

2.2.3 Superexchange

The direct exchange between the magnetic ions requires the overlap of the magnetic ions' electronic orbitals which limits it to very short distances, and it is only relevant to consider $J_{i,j}$ only for very few nearest neighbours. It also rapidly decreases in strength with the distance, that in most systems looking only at nearest neighbours is enough. However this is not the only possible scenario. In case of so-called superexchange, the interactions are mediated by a non-metallic ion lying on the path between the magnetic ions (referred as M-N-M' path later on).

The energy gain here comes from relieving kinetical constraints imposed on the electrons occupying unpaired orbitals, by enlarging the space accessible for the unpaired electrons. It can be explained by analogy to the classical *particle in a box* where increasing the size of the box lowers the enclosed electron's kinetic energy. In detail, the specific (ferromagnetic or antiferromagnetic) relative orientation of the unpaired electrons on the magnetic ions enables the hopping processes otherwise limited by Pauli's exclusion principle.

This can be addressed by taking into account two possible hopping processes. The first one involves two electrons hopping of the intermediate ion N to the neighbouring cations M and M', and then coming back. This is described by the following effective coupling [12]:

$$J_{\text{eff}}^{(1)} \sim 2b^4(\epsilon_d - \epsilon_p), \tag{2.20}$$

where b is the orbital mixing amplitude obtained from perturbation theory, ϵ_d and ϵ_p are the energies of the electron on the d-orbital of M cation and p-orbital of N anion respectively.

The second process can be described by cross-exchange of electrons between M and M' via N and is accounted by [12]:

$$J_{\text{eff}}^{(2)} \sim \frac{(t_{MM'}^*)^2}{U}, \tag{2.21}$$

involving the hopping amplitude between M and M' $t_{MM'}^*$ and U represents the intraatomic Coulomb repulsion similar to Eq. 2.18. Giving all the above one can introduce the superexchange into the Hamiltonian with $J_{\text{eff}} = J_{\text{eff}}^{(1)} + J_{\text{eff}}^{(2)}$.

The sign of the superexchange depends on the overlap of the orbitals forming the bonds along the M-N-M' path. By this it can be determined by considering the symmetry of those orbitals, related to the local crystal field environment, and the angle formed by $M - N$ and $N - M'$ bonds [21]. This treatment, for common situations of octahedral or tetrahedral placement of surrounding anions, results with the general rule that with ions of the same chemical type occupying the M and M' sites (regardless if the d-orbitals of those ions are less or more than half-filled), one might expect the antiferromagnetic character of the superexchange interaction for the 180° angle (collinear alignment) of the

M-N-M' bonds, while the opposite character of interaction should be observed with the 90° angle (perpendicular alignment) of the M-N-M' bonds [21].

This sensitivity to the orbital overlap (distances and angles between the involved ions) often causes the vast variation of its strength in the families of isomorphous compounds, due to differences in ionic radii, which cause slight deviation of the M-N-M' bond angles.

2.2.4 Anisotropic exchange interactions

Perturbation by spin orbit coupling as stated in Eq. 2.10 on a system composed of interacting ions exhibiting the single-ion anisotropy with present exchange, might be expressed as the appearance of anisotropic exchange terms in the spin Hamiltonian [11]:

$$\mathcal{H}_{\text{aniso}} = -S^2 \sum_{\alpha,\beta}^{x,y,z} \sum_{i,j} [(\Gamma_{\alpha\beta}^{(i)} + \Gamma_{\alpha\beta}^{(j)}) - \delta_{\alpha\beta}(\Gamma_{xx}^{(i)} + \Gamma_{yy}^{(i)} + \Gamma_{zz}^{(i)})] S_{i\alpha} S_{j\beta}, \tag{2.22}$$

where $\Gamma_{\alpha\beta}^{(i)}$ is the effective anisotropic exchange calculated from perturbative treatment of the process, where the spin-orbit coupling excites one of the ions within the pair from the orbital ground-state. This excited state interacts with the second ion remaining in the ground-state. This interaction might be considered as the generalization of dipole-dipole interactions and due to that it is often referred as pseudo-dipolar interaction.

Going further and taking into account other possible processes, and by this the off-diagonal terms of L_α with respect to the exchange, results in additional antisymmetric interaction - the Dzyaloshinsky-Moriya interaction:

$$\mathcal{H}_{\text{DM}} = \boldsymbol{D} \cdot (\boldsymbol{S}_i \times \boldsymbol{S}_j). \tag{2.23}$$

where the $\boldsymbol{D}$ vector is the anisotropic exchange vector. It results from spin-orbit coupling mixing the eigenstates of the pure spin Hamiltonian. The direction of the $\boldsymbol{D}$ vector is constrained by the symmetry of the unit cell [22] and it vanishes if local crystal field environment has an inversion symmetry in the center of the section connecting the interacting sites.

2.3 Magnetically ordered phases

The interactions mentioned in the previous section might be found acting either alone or few at the time within all the systems hosting ions with unpaired electrons. Together with single ion effects, they might lead to the wide variety of ground states exhibiting long range magnetic orders. Ordering of the moments spontaneously break the rotational symmetry of the paramagnetic phase, where no preferred direction can found for the magnetic moments. As the Goldstone's theorem claims [14] in case of breaking the continuous symmetry (e.g. rotational for magnetic ordering, or translational for crystallization) and in absence of long-range interactions, one should expect appearance of gapless excitations following the statistics characteristic for non-interacting bosons (i.e. Goldstone bosons). Those are in case of the magnetic order acoustic magnons, precessive fluctuations of the ordered moments around their equilibrium direction.

The transition from the disordered (paramagnetic) state into the ordered phase, detected by appearance of the order parameter characterizing the latter, occurs at crossing the critical value of some external thermodynamical parameter (temperature, external field, pressure). The theory of second-order phase transitions was developed by Landau [23]. These are characterized by continuous changes in the value of the order parameter (in case of magnetic transitions magnitude of the ordered magnetic moment). In this treatment the free-energy-like function is represented as power expansion [14] (only terms even powers are present) with respect to the order parameter with coefficients being the analytical functions of the temperature. The second-order magnetic transitions are most commonly observed ones, although they are not the only possibility. The consequences in terms of the possible low-temperature ordered magnetic structure are described in Sec. 2.3.4.

2.3.1 Ferromagnetism

The simplest example of a magnetic order we can envision is ferromagnet, parallel arrangement of magnetic moments. It is imposed by positive exchange integral ($J_{i,j} > 0$). Ferromagnets have non-zero net magnetization ($\boldsymbol{M}$), which is present also in the absence of an external field (spontaneous magnetization). In the simplest case the spontaneous magnetization of a macroscopic sample would be directly proportional to the number of ions in the sample. In reality the magnetic structure of such a macroscopic samples is constituted by large number of domains whose magnetization directions are not necessarily parallel. It is due to delicate balance between the energy gain from the magnetostatic energy of the:

$$E_{\mathrm{mag}} = -\frac{\mu_0}{2}\int_V \boldsymbol{M}\cdot\boldsymbol{H}_{\mathrm{d}}\mathrm{d}\tau, \tag{2.24}$$

integrated over the volume of the sample, and energy cost of the magnetic moment misalignment at the domain walls (Eq. 2.19) [13]. The H_d in Eq. 2.24 represents the demagnetization field resulting from divergenceless character of magnetic the field requiring formation of the closed loops of field lines extending beyond the volume of the sample.

2.3.2 Antiferromagnetism

The negative sign of the exchange interaction ($J_{i,j} < 0$) by analogy to the case of ferromagnetism leads to antiparallel arrangement of the magnetic moments residing at neighbouring ions. In order to simplify mean-field treatment this model we can divide the system into two sublattices formed by sites hosting uniquely polarized moments and consider them as two separate ferromagnetic lattices. In contrast to ferromagnetic order the antiferromagnetic samples do not exhibit a net magnetization.

2.3.3 Helimagnetism

Presence of two or more competing interactions within the system often leads to more complex ordered states. In a layered structure with ferromagnetic interactions within the layer and inter-layer interactions between nearest-layer next-nearest-layer described

by J_1 and J_2 respectively. Depending on the specific ratio J_1/J_2 there are three possible ground-state configurations described by the angle between the moments residing at the neighbouring layers, namely collinear and anticollinear, which correspond to ferromagnetic and antiferromagnetic structures described in previous sections, and the helimagnetic structure, where moments residing at the neighbouring layers are rotated with respect to each other around a common axis by the angle θ determined by the exchange ratio ($\cos\theta = -J_1/4J_2$) [13]. This structure is observed in several of the rare-earth metals (i.e. Tb, Dy and Ho) [13].

Helimagnetism might be also caused by Dzyaloshinskii-Moriya interactions (Eq.2.23) [24] causing skewing of the magnetic moments directions between the neighbouring sites.

2.3.4 Magnetic structure determination - representation analysis

The ordered magnetic structure is inherently connected with the host's crystalline structure and its symmetry by the notion of propagation vector $\boldsymbol{k} = \langle k_h, k_k, k_l \rangle$, which describes the relation between the crystallographic and magnetic unit cell.

In the case of a simple ferromagnetic structure where moments residing at all magnetic ions are co-aligned and the $\boldsymbol{k} = \langle 0, 0, 0 \rangle$. What reflects the fact that the translational symmetry of the magnetic structure is the same as the one of crystal structure and the time reversal symmetry is breaking one of the rotational symmetries of crystalline space group with singling out the direction of ordered magnetic moments.

In general the magnetic magnetic moment of the j^{th} atom at the position $\boldsymbol{t} = x\boldsymbol{a} + y\boldsymbol{b} + z\boldsymbol{c}$, with $\boldsymbol{a}$, $\boldsymbol{b}$ and $\boldsymbol{c}$ - the unit vectors along the crystallographic axes, is described by[25]:

$$\boldsymbol{m_j} = \sum_{\boldsymbol{k}} \boldsymbol{\Psi}_j^{\boldsymbol{k}} \mathrm{e}^{-2\pi \mathrm{i} \boldsymbol{k}\cdot\boldsymbol{t}} = \sum_{\boldsymbol{k}} \mathrm{Re}(\boldsymbol{\Psi}_j^{\boldsymbol{k}}) \cos\left(-2\pi \mathrm{i} \boldsymbol{k}\cdot\boldsymbol{t}\right) + \mathrm{Im}(\boldsymbol{\Psi}_j^{\boldsymbol{k}}) \sin\left(-2\pi \mathrm{i} \boldsymbol{k}\cdot\boldsymbol{t}\right), \qquad (2.25)$$

with $\boldsymbol{\Psi}_j^{\boldsymbol{k}}$ representing, in general complex (non-zero imaginary part results in helical structures), $\boldsymbol{k}$-specific basis vector of the direction and magnitude equal to those of magnetic moment at site j. This expression describes unspecific multi-$\boldsymbol{k}$ structure. As it was mentioned, $\boldsymbol{\Psi}_j^{\boldsymbol{k}}$ is in general complex, in case of non-zero imaginary part of the basis vector relating it to the magnetic moment - a real value, one have to take into account the contribution to Eq. 2.25 from $-\boldsymbol{k}$ propagation vector, or define corresponding real basis finding proper linear combinations of the complex basis vectors. Both approaches eliminate the imaginary part of $\boldsymbol{\Psi}_j^{\boldsymbol{k}}$ and allow to relate it to $\boldsymbol{m}_j$ [25].

The propagation vector $\boldsymbol{k}$ can be determined by indexing the magnetic reflections (finding their k_h,k_k and k_l) appearing in neutron diffraction data collected in the ordered phase. With respect to the values of components of $\boldsymbol{k}$ there can be distinguished two types of magnetic structures: commensurate - it has a simple relation between crystallographic and magnetic unit cells (e.g. $\boldsymbol{k} = \langle \frac{1}{2}, 0, 0 \rangle$ - doubling of the unit cell along the a-direction) and incommensurate - the relation between those cells cannot be described by integer-like multiplicity (e.g. $\boldsymbol{k} = \langle 0.34567, 0, 0 \rangle$).

Only task left, necessary to determine the magnetic structure, is finding the basis vectors $\boldsymbol{\Psi}_j^{\boldsymbol{k}}$. It can be done with use of powerful tool of representational analysis. It

requires the knowledge of symmetry and structure of the unit cell and propagation vector of magnetic structure. Representational analysis uses the fact that the problem of finding irreducible representation of little group $G_{\boldsymbol{k}}$ is equivalent to finding the lowest-order term of power expansion of magnetic contribution to free energy in Landau's theory of phase transitions [23, 26]. According to Landau's theory all second order phase transitions must follow single irreducible representation [23], what allows to dramatically limit the number of considered possible magnetic structure.

Little group $G_{\boldsymbol{k}}$ is the subgroup of group G, consisting of all symmetry elements of space group describing the crystal structure of the system under the investigation, which is build exclusively from the elements leaving the propagation vector $\boldsymbol{k}$ unchanged. The representation Γ of $G_{\boldsymbol{k}}$ is a set of matrices describing the behaviour of magnetic moments under the action of symmetry elements from $G_{\boldsymbol{k}}$. Separating the representation into orthogonal irreducible representations Γ_ν of multiplicity n_ν (describing how many times it appears in the decomposition of Γ), allows to determine which of them are eligible for governing the phase transition and by that to find out set of basis vectors $\boldsymbol{\Psi}_j^{\boldsymbol{k}}$. The multiplicity of an irreducible representation in the decomposition of representation Γ might be calculated with [25]:

$$n_\nu = \frac{1}{n(G_k)} \sum_{h \in G_k} \chi_\Gamma(h) \chi^*_{\Gamma_\nu}(h), \tag{2.26}$$

with χ being the character of the representation given by the trace of its matrix form.

Magnetic basis vectors $\boldsymbol{\Psi}_j^{\boldsymbol{k}}$ are formed as linear combination of $\boldsymbol{\psi}_j^{i\lambda}$, which might be projected out of the matrix form $D_\nu^{\kappa\lambda}$ of irreducible representation Γ_ν with a series of trial functions $\boldsymbol{\phi}^\beta$ ($\boldsymbol{\phi}^1 = \langle 1,0,0\rangle$, $\boldsymbol{\phi}^2 = \langle 0,1,0\rangle$ and $\boldsymbol{\phi}^2 = \langle 0,0,1\rangle$) the following formula [25]:

$$\boldsymbol{\psi}_j^{i\lambda} = \sum_{g \in G_k} D_\nu^{*\lambda}(g) \delta_{i,gi} \mathrm{e}^{-2\pi \mathrm{i} \boldsymbol{k} \cdot (\boldsymbol{r}_{gi} - \boldsymbol{r}_i)} \det(h) R^h \boldsymbol{\phi}^\beta, \tag{2.27}$$

with rows of matrix representation κ being fixed and $\delta_{i,gi}$ (where gi is the position obtained by action of g on position i) checking checking if position i and gi are equivalent and $\lambda = 1, 2, ..., \mu$ for μ-dimensional irreducible representation. R^h and $det(h)$ are the rotation matrix of the symmetry element g and its determinant which is equal 1 or -1 for proper and improper rotations respectively.

Sets linear combinations of projected out basis vectors defines the set of possible symmetry allowed magnetic structures. Determination which of those structures describes the actual state requires performing an Rietveld refinement (see Sec. 3.1.1) on the neutron diffraction data. In case if the refinement procedure does not provide conclusive evidence to exclude all apart from one possible structures additional symmetry constraints, or data from other experimental techniques.

2.4 Magnetism in low-dimensions

Lowering the dimensionality of the magnetic system leads to striking results. The Mermin-Wagner theorem states that for the systems with anisotropic moments no long-range order breaking the continuous symmetry is expected in one and two dimensional systems at finite temperatures [27, 14]. It concerns both structural order (breaking the continuous

translation symmetry) and ordering of anisotropic moments (breaking the rotational symmetry of the system). This results might be described as a diverging density of states of low-energy (long-wavelength) thermal fluctuations of the order parameter (spin fluctuations or thermal displacements of ions forming the lattice) taking place in low-dimensional systems at finite temperature [14]. Huge population of Goldstone modes created at nearly zero-energy cost destabilizes the structure and results in melting of the long-range order.

As it was pointed, the Mermin-Wagner theorem applies only to breaking of continuous symmetries resulting in appearance of gapless excitaitons - Goldstone modes. It is not the case when the broken symmetry is of discrete character (e.g. strongly anisotropic easy-axis type moments). It does not mean that long-range order is always to be expected in presence of anisotropies. Ferromagnetically coupled easy-axis types of moments, residing on low-dimensional lattices, are considered in two canonical results by Ising [28] and Onsager [29], which provide the celebrated exact solutions. The former work by Ising show that in one-dimensional chain of easy-axis type of moments, one do not observe long-range order as the energy cost of the defects in form of flipped spins is exceeded by the free energy gain, due to entropy of the defect, as the length of the chain goes to infinity [28, 13]. The latter model describes a two-dimensional square lattice populated with the same types of moments, also coupled with nearest-neighbour ferromagnetic interactions. It concludes that, in contradiction to one-dimensional case, the long-range order should be expected for infinite size of the modelled lattice [29] due to the energy cost of the defect boundary length [13].

2.4.1 Antiferromagnetic Heisenberg spin chains

An excellent example of model exhibiting the significant consequences of lowered dimensionality are one-dimensional spin chains with antiferromagnetic nearest-neighbour Heisenberg exchange[30]:

$$\mathcal{H} = J \sum_i \boldsymbol{S}_i \cdot \boldsymbol{S}_{i+1}, \tag{2.28}$$

with $\boldsymbol{S}_i$ representing the spin operator acting on i-th site of the chain. In the classical limit ($S \to \infty$), one expects a Néel long-range order in form of alternating collinear moments aligned along common arbitrary direction in space. The excitation spectrum in that case consists of doublet Goldstone modes of spin waves representing slow rotations of the orientation of this arbitrary direction. On switching to the case of quantum spins, quantum fluctuations suppress the long-range order and regardless of the value of the S various spin-liquid phase ground-states are observed.

The suppression of long-range order in quantum spin-chains gives rise to variety of exotic low-energy excitations, which cannot be described with ordinary perturbative treatment of base Hamiltonian. Examination of those may be very convenient way of characterizing the spin-liquid phase, as their features are directly reflected in the dynamical structure factor of the system, accessible with neutron scattering techniques. Presence of a gap in the excitation spectrum, as it will be discussed further, might be an example of an easily traceable feature giving the information about the character of real-space spin-spin correlations within the chain and if spin-liquid phase is critical [30]. Moreover, observation of modes in form of sharp peaks or broad diffuse features in dynamical structure

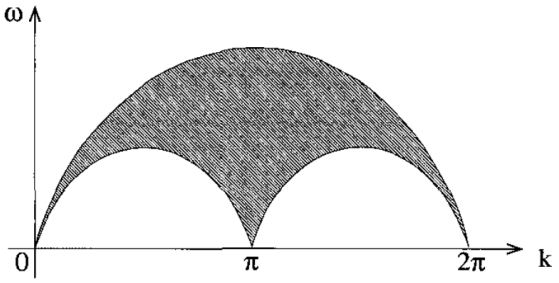

Figure 2.2: Two-spinon continuum in the spin-$\frac{1}{2}$ antiferromagnetic Heisenberg chain. Figure adapted from Ref. [30].

factor is revealing the spin quantum number characterizing the elementary excitations over the ground-state.

Half-integer spin chains (case of $S = \frac{1}{2}$)

A good example of such a system might be given by a chain of $\frac{1}{2}$ spins, which has an advantage of being fully solvable by means of Bethe ansatz approach [31], described already in 1931. Using this method a prediction of quasi-long-range order with power-law correlations and general gapless character of excitations [32]. Initial attempts of developments aiming at resolving the details of excitation spectrum in this model have produced inconsistent results of the character of lowest-lying excitaitons. Firstly, des Cloizeaux and Pearson [33] have found them to be triplet spin-1 spin waves with the $\epsilon_t(k) = \frac{1}{2}\pi|\sin(k)|$ dispersion relations, defining the arches of lower bounds of shaded region in Fig. 2.2. Following work by Ovchinnikov [34] has identified singlet states $\epsilon_s(k) = \pi|\sin(\frac{1}{2}k)|$, being the upper boundary of shaded region in Fig. 2.2.

A further work by Faddeev and Takhtajan [35] have arrived at striking conclusion of lowest excited level being of fourfold degeneracy and consisting of both triplet and singlet states. It has also postulated the presence of massless fractional ($S = \frac{1}{2}$) excitaitons called spinons with the following dispersion:

$$\epsilon_{\text{spinon}} = \frac{\pi}{2}\sin(k), \tag{2.29}$$

with k restricted to the half of the Brillouin zone ($0 < k < \pi$).

As spectroscopic probes (e.g. neutrons) operate with the base of a single spin flip ($\Delta S = 1$) the spectral signature of spinons will appear in form of broad continuum of two-particle scattering (Fig. 2.2) filled with all possible momentum-energy configurations (convolution) of two points at single spinon dispersion. It is in contrary to ordinary magnons characterized by $S = 1$ and marking their presence with sharp spectral lines of single-particle scattering. In this description spinons might be envisioned as domain walls between reverse antiferromagnetic domains counterpropagating, with no energy cost, along the chain.

Another striking feature of spinons is that, for some cases (i.e. Shastry-Haldane model [36, 37]), they no longer obey to neither bosonic or fermionic statistics, but are rather classified as semions, giving opportunity to probe the exotic concepts of fractional statistics [38].

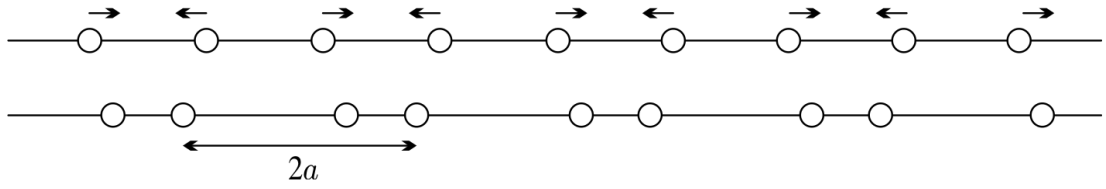

Figure 2.3: Peierls distortion of one-dimensional chain. Figure adapted from Ref. [15].

Experimental detection of those features clearly Even though real systems hosting the spin chains often suffer from interchain coupling, causing deviations from their one-dimensional character, several neutron spectroscopy studies has detected the multi-spinon continua and their gapless character. They were found in $KCuF_3$[39], $SrCuO_2$ [40] and $LiCuVO_4$ [41].

Spin-Peierls transition in $S = \frac{1}{2}$ chains. As it was mentioned, in reality it is extremely challenging to obtain purely one-dimensional system and most of the spin chain compounds undergo magnetic transition either ordering due to exchanges between chains [42], or to dimerized phase thanks to the coupling between spin and lattice degrees of freedom [43, 44], where the latter do not experience effects of dimensionality lowering affecting magnetic interactions. The second mechanism is dubbed spin-Peierls transition and results with pairing of the chain members associated with structural distortion bringing the paired ions closer together in the direction along the chain (Fig. 2.3) and altering the exchanges along elongated and shortened bonds. It is magnetic counterpart of electronic Peierls transition [45, 46] which takes place in metallic chains, where the electron-phonon coupling softens the $2k_F$-phonons leading to structural transition and opening the gap in the electronic band structure pushing the system from metallic into insulating state. In case of spin-Peirels [47] an opening of a gap between singlet ground-state and excited triplet is observed upon the transition [48].

Integer spin chains (case of $S = 1$)

There are no exactly solvable models for Heisenberg antiferromagnetic chains (following Eq. 2.28) with $S > \frac{1}{2}$ as Bethe ansatz is not applicable anymore. Therefore no analytical solution can be obtained for any example of integer-spin chain. Generally no fundamental difference between integer and half-integer case and conclusions of works by Haldane presented in Ref. [49] were rather large surprise. Haldane has noticed that, the problem of non-linear excitaitons in one-dimensional chain populated with semiclassical large-valued moments might be mapped onto non-linear $O(3)$ sigma model [50]. Exploiting of this non-intuitive connection produced striking results, namely predicted excitation spectrum was found to be gapless for half-integer spins and gapped in case of integer values of magnetic moments. Interestingly this gap does not result from magnetic anisotropy, but form the topological aspects of the model. Namely the different effect of time-reversal operator at the Kramers and non-Kramers type of systems. Expected ground-state for this model is a spin-liquid singlet, with exponentially decaying spin-spin correlations [30], and the observed excitaitons are singlet-to-triplet transition characterized in form of $S = 1$ particles.

The ground-state described by Haldane's theory might be pictured as diluted antiferromagnetic state, where the neighbouring sites of chain, hosting antiparallel magnetic moments might be separated by arbitrary number of sites carrying no magnetic moment (i.e. $\ldots \uparrow \circ \downarrow \uparrow \downarrow \uparrow \circ \circ \circ \downarrow \uparrow \downarrow \circ \uparrow \downarrow \ldots$, where $\circ$ marks the $S = 0$, $\uparrow$ $S = 1$ and $\downarrow$ $S = -1$ sites), where the length of non-diluted fragments resembles corresponds to the correlation length. In that case the observed $S = 1$ excitation is change of the site at the moment (ie. $\ldots \uparrow \circ \downarrow \uparrow \downarrow \uparrow \circ \circ \uparrow \downarrow \uparrow \downarrow \circ \circ \downarrow \ldots$).

The character of observed excitaitons should manifest in form of gapped sharp spectroscopic features strongly contrasting to gapless multiparticle continuum of scattering observed in case of $S = \frac{1}{2}$ chains. Following this report few experimental studies has confirmed existence of predicted gap in magnetic excitaitons of $S = 1$ systems in disordered phase [51, 52, 53]. Similarly to the previous case most of the experimentally investigated material (e.g. $A\mathrm{NiCl_3}$ family, where A =Cs,Rb...) display long-range order where additional terms (single ion anisotropy, interchain interactions) prevail over quantum fluctuations [53].

Apart from well-defined Haldane modes, signs of multiparticle states were also observed in $\mathrm{CsNiCl_3}$ [54, 55]. Haldane's theory predicts appearance of continuum dynamics [56], although it's predicted scattering weight is to small to explain the experimental observations [54]. As for now their nature stays unresolved and no theoretical models have produced predictions of these observation. One of the possible explanation points to the fact that in $A\mathrm{NiCl_3}$ family the chains of magnetic ions are arranged in triangular motif what in combination with antiferromagnetic coupling between them, as it will be explained in next section would suggest possibility of geometrical frustration playing role in the magnetic scheme. However, the interplay of quantum effects coming from lowered dimensionality and magnetic frustration is still unexplored area in terms of theoretical description.

2.5 Magnetic frustration

Important consequences of the frustration's presence in physical systems were noted for the first time by Pauling [57, 58], on the occasion of the study of finite residual low-temperature entropy of the hexagonal water ice. Its crystalline structure is presented in Fig. 2.4. Tetrahedrally coordinated oxygen ions form a rigid sublattice and every of them is connected with its nearest neighbours via hydrogen bonds. Two out of four surrounding H^+ ions are forming much shorter bonds with central O^{2-} ion. Relative directions of those two bonds are constrained by so-called "ice rules" [59], but no orientation with respect to global crystallographic directions is imposed. Energetic equivalence of all possible "two-in-two-out" configurations and low energy barriers separating them, allow for persistence of fluctuations between those states, even below the water freezing temperature. It gives rise to spurious violation of the second law of thermodynamics. The fundamental conclusion emerging from those considerations was the notion that the incompatibility of interaction geometry with the structural symmetry of the hosting system generates a vast degeneracy of ground-state minimizing the energy of those mentioned interactions.

Likewise, in terms of magnetic systems, frustration prevents simultaneous fulfillment of all interactions between magnetic moments. It has been considered for the first time in

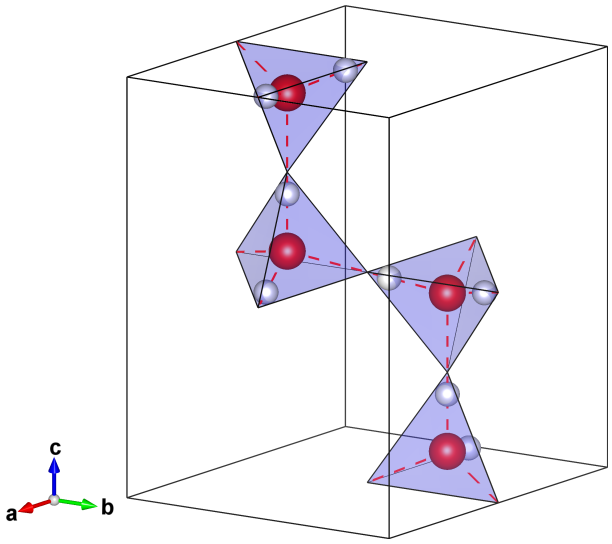

Figure 2.4: A unit cell of hexagonal ice crystal showing relevant oxygen (red spheres) and hydrogen (white spheres) ions, latter ones following one of possible configurations respecting "two-in-two-out" ice rule. Blue polyhedra show the tetrahedral coordination of oxygen positions. Figure created with `VESTA` software [60].

connection with spin-glasses and was identified by Anderson as crucial ingredient for their existence [61]. Generally, the most straight-forward consequences of magnetic frustration are suppression of the long range order far below the Curie-Weiss temperature (θ_{CW}) resulting in the cooperative paramagnet phase (spin-liquid) showing short-range spin-spin correlations within the system, but lacking the global order parameter. Frustration might be roughly quantified by frustration parameter $f = |\theta_{\mathrm{CW}}|/T_{\mathrm{N}}$ [62]. It describes the temperature range of expected spin-liquid phase, namely $T_{\mathrm{N}} < T < \theta_{\mathrm{CW}}$.

The simplest model system exhibiting magnetic frustration is the triangular lattice of antiferromagnetically coupled collinear classical moments shown in Fig. 2.5(a) [63]. It is easily seen that a single triangle can adopt six configurations minimizing the exchange couplings between nearest neighbours. This number is more than two resulting from Ising like symmetry of magnetic moments and it grows exponentially with number of nodes in the lattice. On lowering temperature moments in this system continue to fluctuate, although those fluctuations have correlated character due to constraints imposed by the ground-state configurations, forming a classical spin-liquid state. Few most common mechanisms of introducing magnetic frustration are shown in Fig. 2.5.

A very similar, but less constrained model of antiferromagnetically coupled isotropic quantum spins ($S = \frac{1}{2}$) was proposed by Anderson to host exotic ground-state in form of resonating valence bond (RVB) state [64]. In this terminology the "bonds" are formed by the singlet states formed between neighbouring sites. RVB state later on was proposed to contribute to the exotic superconducting states [65]. Upon cooling this system in contrary to the classical case continue to fluctuate down to temperatures where the energy of thermal excitations ($E \sim k_{\mathrm{B}}T$) becomes negligible and it should avoid ordering down to $T = 0$ K. It is the result of quantum fluctuations having relatively significant strength and lack of energy barriers between the ground-state configurations of the isotropic spins. This type of ground-state formed by the superposition of possible valence bond state

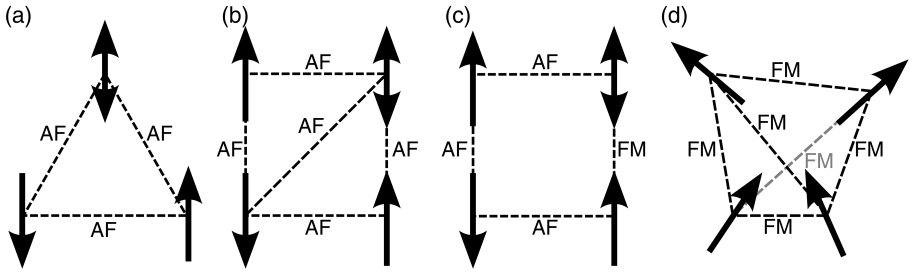

Figure 2.5: Exemplary sources of magnetic frustration in magnetic systems of different dimensionality. (a) triangular Ising antiferromagnet, (b) square lattice with further neighbour interactions, (c) square lattice with defect leading to alteration of coupling's character and (d) the non-collinear Ising pyrochlore ferromagnet. AF and FM mark respectively the antiferromagnetic and the ferromagnetic couplings along the bands.

configurations and belongs to the category of quantum spin-liquids [62].

A special case of classical frustrated systems are dubbed classical spin ices [66, 67, 68]. Those are pyrochlore ferromagnets (usually rare-earth pyrochlores) with strong axial anisotropy along the local $\langle 1,1,1\rangle$ direction (Fig. 2.5(d)) with effective nearest neighbour interactions. The label spin ice comes from the resemblance of the two-in-two-out constraint affecting the magnetic moments analogous to the ice rules governing the configuration of the protons in hexagonal water ice. The analogy goes even further and the spin entropy of the spin ice phase matches closely the residual entropy of the water ice [67]. It was followed by the proposal of spin ice materials hosting fractional excitations carrying an effective magnetic charge - long sought magnetic monopoles [69], in form of defects breaking the ice rules. First experimental detections of the monopole physics were to follow soon after [70, 71]. In the classical spin ice model magnetic monopoles behave akin to electrical charges following magnetostatics governed by Coulomb interactions [69]. The quantum counterpart of the classical spin ice where, at very low temperatures, the system is switching between the possible ground-state configurations by quantum fluctuations [72]. The quantum spin ice is a distinct type of quantum spin-liquid in which the excitaitons are governed by emergent gauge fields imitating the laws of electrodynamics with their own gapless photon-like excitaitons [73]. The ongoing experimental search fro those elusive phases is one of the recent focuses of the frustrated magnetism field [74, 75, 76].

Pyrochlore antiferromagnets

Pyrochlore lattice populated by isotropic moments (both classical and quantum), coupled to each other with nearest-neighbour Heisenberg-type exchange (Sec. 2.2.2) has been one of the most investigated frustrated systems in 3 dimensions. Lack of expected long-range order at zero temperature, due to the heavy ground-state degeneracy of pyrochlore lattice, even in case of much more constrained Ising type moments (axial anisotropy), was already pointed out by Anderson in his work form 1956 [77]. It was stated there that even very modest in strength long-range interactions would play a crucial role in formation of magnetic ground-state. Similar conclusion was made by Villian in 1979 [78] about the

isotropic moments on pyrochlore lattice avoiding ordering down to $T = 0$, where only short range correlations are present. It was confirmed with mean-field calculations [79].

The distinction between spin-glass and a non-magnetic phase present in pyrochlores, in the temperature regime where the correlations between magnetic moments play important was made for the first time by Villian and the latter one was named cooperative paramagnet or classical spin-liquid phase. Features of spin-liquid phase in Heisenberg pyrochlore antiferromagnet were investigated with use of classical Monte Carlo method [80] and its quantum counterpart was analyzed with perturbative expansions and exact diagonalization of finite-size samples [81, 82].

Thanks to the predictions of fractionalized excitaitons (e.g. deconfined spinons) and emergent quantum electrodynamics gauges [83, 84], the mentioned quantum spin-liquids are systems which have drawn substantial attention [62]. It results with ongoing experimental effort aimed at finding materials supporting this exotic phase [85, 86].

Relieving the frustration

In some cases the macroscopic degeneracy of the magnetic ground-state brought by frustration often leads to unusual phenomena which result with lifting of the degeneracy and thus enabling for the onset of a long-range order. This requires an additional interaction perturbing the nearest-neighbour Hamiltonian. The simplest mechanisms leading to such phenomena are single ion anisotropies and further neighbour interactions. These can make some of the ground-state configurations more energetically favourable over the other.

As lattice geometry in combination with specific interaction scheme is the source that leads to intuitive conclusion of possibility of coupling between lattice distortions and magnetism in those systems. It can be described with the biquadratic term in the effective magnetic Hamiltonian [87, 88] $b(\boldsymbol{S}_i^2 \cdot \boldsymbol{S}_j^2)$. The sign of biquadratic coupling constant determines if collinear or coplanar states are favoured. Extensive theoretical works presented in Refs. [87] and [88], made within this scheme have shown that when taken into account biquadratic coupling might lead to the counterpart of spin-Peierls transition in pyrochlore lattice. The more detailed discussion of those results and observed structural distortions with related magnetic ground-states is presented in Sec. 4.4.2.

Lifting of the ground-state degeneracy might be also provided by "order by disorder" type mechanisms [89], where the entropy part of free energy via thermal or quantum fluctuations governs the ground-state selection by lifting the degeneracy. Another way of selecting the ordered ground-state is direct coupling of magnetism to different degrees of freedom [90]. For example it can occur via coupling of spin and lattice degrees of freedom through the spin Jahn-Teller effect [91], lowering the crystalline symmetry of a system and by that removing the degeneracy, allowing the long-range order to appear.

2.5.1 Spin-glass

Spin-glasses are disordered systems which in contrary to paramagnets are non ergodic - their time average of magnetic moments is non-zero while the spatial average is (for paramagnet both of those quantities are equal zero) [92]. The paramagnet to spin-glass transition is distinct from ordinary second order transitions to the ordered states, as

should rather be perceived as a dynamical freezing analogous to the situation in molecular glasses [92]. The most explicit experimental signatures of spin-glasses are [16]:

- no signs of magnetic long-range order in neutron scattering data,
- cusp in zero-field susceptibility at the freezing temperature T_{f},
- no anomaly in heat capacity, only broad feature slightly above T_{f},
- bifurcation between zero-field-cooled (ZFC) and field-cooled (FC) magnetic susceptibility.

One can single out two sources of the magnetic glassy phases, randomness and frustration. The example of the former factor in action are dilute magnetic alloys with $3d$ magnetic ions being an impurity in a matrix of non-magnetic metallic crystal. those are called the canonical spin-glasses and the disordered frozen structure result from randomness of interactions between the magnetic impurities. The interactions in canonical spin-glasses are mediated by the conduction electrons not localized at the specific site but propagating in whole volume of the crystal (RKKY interactions [13]). This interaction changes its sign periodically depending on the distance between ions, leading to the randomness of interactions in canonical spin-glasses. In addition those material may also host anisotropic superexchange (DM interactions, see Sec. 2.2.4) [92]. The latter group consists of magnetic insulators hosting the geometrical frustration, either due to nearest neighbour interactions, or due to further neighbour interactions.

Chapter 3

Experimental techniques

3.1 Neutron scattering

Neutrons, the neutral subatomic particles carrying spin angular momentum of $s = \frac{1}{2}$, participate in formation of almost all known atomic species. They are stable only when confined within nuclei. However, their relatively long lifetime in an unbound state ($t_{1/2} \sim$ 10 min) enables their use in character of a probe in scattering techniques. Those use the wave-particle duality of neutrons and their application proved to be successful, especially in the field of condensed matter physics. First attempts of those experiments [93] took place very soon after the neutron discovery by Chadwick [94] in 1932.

Probing matter with neutrons is possible thanks to the fact that they primarily interact with atomic nuclei via the strong force and their spin magnetic moment can couple to the dipolar field originating from magnetic moments of unfilled electronic shells. The most important traits of neutrons in this aspect are [95, 96, 97]:

- de Broglie wavelengths of cold and thermal neutrons are of the order of interatomic distances found in condensed matter systems, favouring the diffraction condition, moreover their energies ($E < 100$ meV) are close to characteristic energies of many excitations in condensed matter systems (see Tab. 3.1), in combination giving access to both spatial and dynamical character of the investigated phenomena,

- lack of net electric charge makes neutrons insensitive to the electric charges of electrons and nuclei, enabling penetration of sample's volume and probing its bulk properties,

- limited interaction of neutron with the sample (small effective cross-section of the atomic nuclei and small magnitude of neutron's spin magnetic moment, both of the order of barns 1 b = 10^{-28} m^2) ensures the applicability of the first Born approximation (first-order perturbation treatment) and predominance of single scattering processes, both simplifying the data interpretation and enabling its full quantitative analysis,

Combination of those features made neutrons weapon of choice in numerous aspects of solid state physics and in particular magnetism.

Scattering techniques use the fact that wavelengths of thermal and cold neutrons are few orders of magnitude larger then radii of nuclei, what results in the s-wave type

Table 3.1: Convention for neutron energy ranges and their corresponding temperatures and wavelengths. Table adapted from Ref. [96].

Neutron range	Energy (meV)	Temperature (K)	Wavelength (Å)
cold	$0.1 - 10$	$1 - 120$	$30 - 3$
thermal	$5 - 100$	$60 - 1000$	$4 - 1$
hot	$100 - 500$	$1000 - 6000$	$1 - 0.4$

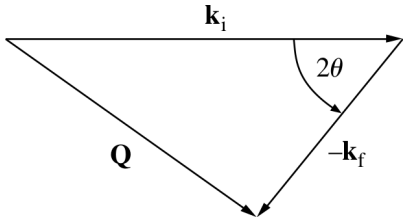

Figure 3.1: Schematic representation of scattering process in reciprocal space. Presented vectors correspond to quantities described in Eq. 3.1. Figure adapted from Ref. [97]

isotropic scattering. The neutron-sample interaction during scattering process, schematically presented in Fig. 3.1, is characterized by following quantities [96]:

- momentum transfer
$$\hbar \boldsymbol{Q} = \hbar(\boldsymbol{k}_\mathrm{i} - \boldsymbol{k}_\mathrm{f}), \tag{3.1}$$
- energy transfer
$$\hbar\omega = E_\mathrm{i} - E_\mathrm{f} = \frac{(\hbar k_\mathrm{i})^2}{2m_\mathrm{n}} - \frac{(\hbar k_\mathrm{f})^2}{2m_\mathrm{n}}, \tag{3.2}$$

where $\boldsymbol{k}$ and k are neutron wavevector and its magnitude, E is neutron energy, indices i and f stand for initial and final states of the scattering process, and m_n is the mass of neutron. Basic relations between quantities describing a neutron's state are as follows:

$$E = k_\mathrm{B}T = \frac{1}{2}m_\mathrm{n}v^2 = \frac{\hbar^2}{2m_\mathrm{n}\lambda^2} = \frac{\hbar k^2}{2m_\mathrm{n}}, \tag{3.3}$$

where k_B is the Boltzmann constant, T is the temperature, v and λ are neutron velocity and wavelength respectively.

Applying Fermi's golden rule to the scattering process, depicted schematically in Fig. 3.1, one can formulate an expression for the double differential cross-section [96], the quantity measured during the neutron scattering experiment, describing the number of neutrons scattered into the small solid angle $d\Omega$ covered by the detector, in unit of time, with final energy within small dE around E_f:

$$\left(\frac{\mathrm{d}^2\sigma}{\mathrm{d}\Omega \mathrm{d}E_\mathrm{f}}\right)_{\mathrm{i}\to\mathrm{f}} = \frac{k_\mathrm{f}}{k_\mathrm{i}}\left(\frac{m_\mathrm{n}}{2\pi\hbar^2}\right)^2 |\langle \boldsymbol{k}_\mathrm{f}, \boldsymbol{\sigma}_\mathrm{f}, \lambda_\mathrm{f}|V|\boldsymbol{k}_\mathrm{i}, \boldsymbol{\sigma}_\mathrm{i}, \lambda_\mathrm{i}\rangle|^2 \delta(E_{\lambda_\mathrm{i}} - E_{\lambda_\mathrm{f}} + E_\mathrm{i} - E_\mathrm{f}), \tag{3.4}$$

where $\boldsymbol{\sigma}$ is the neutron's spin state, λ and E_λ describe the state and the energy of the scattering system, and the scattering potential V, which might be separated into nuclear (V_nuc) and magnetic part (V_mag). σ is the total scattering cross-section of the system

representing the ratio of incoming and scattered fluxes ($\sigma = I_\mathrm{f}/I_0$) measured in barns (1 b=10^{-28} m^2).

Due to the fact that, radii of atomic nuclei are few orders of magnitude smaller than the wavelength of incoming neutron, such a point-like potential can be fairly well described by the effective Fermi pseudopotential:

$$V_\mathrm{nuc}(\boldsymbol{r}) = \frac{2\pi\hbar^2}{m_\mathrm{n}} b\delta(\boldsymbol{r}), \tag{3.5}$$

where $\delta(\boldsymbol{r})$ is the Dirac delta function and b is the scattering length of the nuclei, measured in fm (10^{-15} m). Fourier transform of Eq. 3.5 into the momentum space, in which the scattering process is described, leaves only the constant prefactor of the full potential with nucleus-dependent scattering length b.

The magnetic scattering of neutrons, takes place due to interaction of the neutron spin magnetic moment:

$$\boldsymbol{\mu}_\mathrm{n} = -g_\mathrm{n}\mu_\mathrm{n}\boldsymbol{\sigma}_\mathrm{n}, \tag{3.6}$$

where $g_\mathrm{n} = 1.913$ stands for the neutron's gyromagnetic ratio, $\mu_\mathrm{n} = \frac{e\hbar}{2m_\mathrm{p}}$ is the nuclear magneton and $\boldsymbol{\sigma}_\mathrm{n}$ is the Pauli spin operator. The scattering potential due to the dipolar field created by the spin magnetic moment ($\boldsymbol{\mu}$) and the kinematic momentum ($\boldsymbol{p}$) of the electron is of the following form [96]:

$$V_\mathrm{mag}(\boldsymbol{r}) = -\boldsymbol{\mu}_\mathrm{n}\frac{\mu_0}{4\pi}\left(\mathrm{curl}\left(\frac{\boldsymbol{\mu}\times\boldsymbol{r}}{r^2}\right) - \frac{2\mu_\mathrm{B}}{\hbar}\frac{\boldsymbol{p}\times\boldsymbol{r}}{r^2}\right). \tag{3.7}$$

Inserting this potential into Eq. 3.4 results with following magnetic contribution to the scattering cross-section:

$$\left(\frac{\mathrm{d}^2\sigma}{\mathrm{d}\Omega\mathrm{d}E_\mathrm{f}}\right)_\mathrm{mag} = \frac{(g_\mathrm{n}r_0)^2}{2\pi\hbar}\frac{k_\mathrm{f}}{k_\mathrm{i}}\left(\frac{g}{2}F(\boldsymbol{Q})\right)^2 \sum_{\alpha,\beta}^{(x,y,z)} (\delta_{\alpha\beta} - \hat{Q}_\alpha\hat{Q}_\beta) S^{\alpha\beta}(\boldsymbol{Q},\omega), \tag{3.8}$$

where $r_0 = \frac{\mu_0 \mathrm{e}^2}{4\pi m_e}$ is the classical radius of the electron and $S^{\alpha\beta}(\boldsymbol{Q},\omega)$ - the sample's magnetic scattering function describing static and dynamic correlations within the magnetic system:

$$S^{\alpha\beta}(\boldsymbol{Q},\omega) = \frac{N}{2\pi\hbar}\sum_{m,n}\int_{-\infty}^{\infty}\mathrm{d}t\mathrm{e}^{-\mathrm{i}\omega t}\langle \mathrm{e}^{\mathrm{i}\boldsymbol{Q}\cdot\boldsymbol{r}_m} J_m^\alpha(0)\mathrm{e}^{\mathrm{i}\boldsymbol{Q}\cdot\boldsymbol{r}_n} J_n^\beta(t)\rangle, \tag{3.9}$$

with $J_m^\alpha(t)$ representing the α-component ($\alpha = x, y, z$) of the total angular momentum carried by the m^th ion. $F(\boldsymbol{Q})$ in Eq. 3.8 is the magnetic form factor:

$$F(\boldsymbol{Q}) = \int \mathrm{e}^{\mathrm{i}\boldsymbol{Q}\cdot\boldsymbol{r}} J(\boldsymbol{r})\mathrm{d}r^3, \tag{3.10}$$

describing the spatial distribution of unpaired electrons contributing to the magnetization of a single ion in form of the Fourier transform of the magnetic moment density $J(\boldsymbol{r})$. The $F(\boldsymbol{Q})$ in contrast to analogous nuclear scattering length b shows a Q-dependence, it is normalized to unity at $\boldsymbol{Q} = 0$ and smoothly decays to zero as $\boldsymbol{Q}$ increases [98]. It is the consequence of the fact that sizes of electronic orbitals contributing to the ion's

magnetization are of similar order of magnitude as wavelengths of thermal neutrons. The $\delta_{\alpha\beta} - \hat{Q}_\alpha \hat{Q}_\beta$ factor in Eq. 3.8, appearing while Fourier transforming the potential in Eq. 3.7, shows that neutrons are only sensitive to the magnetization component being perpendicular to the scattering wavevector $\boldsymbol{Q}$, which is a direct consequence of anisotropic dipole-dipole interactions (see Sec. 2.2.1).

Nuclear scattering from a composite system might be also described in terms of correlation functions between the system's constituents. As b is isotope dependent it varies also within the single element population. It results in two components contributing to the nuclear double differential scattering cross-section, namely coherent and incoherent:

$$\begin{aligned}\left(\frac{\mathrm{d}^2\sigma}{\mathrm{d}\Omega \mathrm{d}E_\mathrm{f}}\right)_\mathrm{coh} &= \langle b \rangle^2 \frac{k_\mathrm{f}}{k_\mathrm{i}} N S_\mathrm{coh}(\boldsymbol{Q}, \omega) \\ &= \langle b \rangle^2 \frac{k_\mathrm{f}}{k_\mathrm{i}} N \frac{1}{2\pi\hbar} \iint G(\boldsymbol{r}, t) \mathrm{e}^{\mathrm{i}(\boldsymbol{Q}\cdot\boldsymbol{r} - \omega t)} \mathrm{d}\boldsymbol{r}\mathrm{d}t,\end{aligned} \tag{3.11}$$

$$\begin{aligned}\left(\frac{\mathrm{d}^2\sigma}{\mathrm{d}\Omega \mathrm{d}E_\mathrm{f}}\right)_\mathrm{inc} &= \left\{\langle b^2 \rangle - \langle b \rangle^2\right\} \frac{k_\mathrm{f}}{k_\mathrm{i}} N S_\mathrm{inc}(\boldsymbol{Q}, \omega) = \\ &= \left\{\langle b^2 \rangle - \langle b \rangle^2\right\} \frac{k_\mathrm{f}}{k_\mathrm{i}} N \frac{1}{2\pi\hbar} \iint G_\mathrm{s}(\boldsymbol{r}, t) \mathrm{e}^{\mathrm{i}(\boldsymbol{Q}\cdot\boldsymbol{r} - \omega t)} \mathrm{d}\boldsymbol{r}\mathrm{d}t,\end{aligned} \tag{3.12}$$

where the two scattering functions $S_\mathrm{coh}(\boldsymbol{Q}, \omega)$ and $S_\mathrm{inc}(\boldsymbol{Q}, \omega)$ are Fourier transforms of the time-dependent pair-correlation function $G(\boldsymbol{r}, t)$ and the time-dependent self-correlation function $G_\mathrm{s}(\boldsymbol{r}, t)$ respectively.

The first of those correlation functions describes, for classical systems, the probability of, while having an atom at position $\boldsymbol{r} = 0$ at $t = 0$, observing any other atom at $\boldsymbol{r}$ and $t > 0$. It gives the information about the crystalline structure and coherent lattice dynamics - phonons. The second one, again for classical systems, describes the probability of, while having an atom at position $\boldsymbol{r} = 0$ at $t = 0$, observing the same atom at $\boldsymbol{r}$ and $t > 0$. It provides the information about molecular dynamics (diffusion processes) within the system.

Some of the atomic nuclei posses a non zero spin magnetic momentum, which fluctuates and orders only in extremely low temperatures of micro and millikelvin ranges. In this case there are possible two channels of nuclear scattering for which the neutron's and nuclear spins are aligned parallel or antiparallel. This results in two values of scattering lengths for different nuclear spin populations and leads to the nuclear spin-incoherent scattering [96].

3.1.1 Neutron diffraction

During a neutron diffraction experiment one measures the differential scattering cross-section $\frac{\mathrm{d}\sigma}{\mathrm{d}\Omega}$, where the most details of sample's microscopic structure are contained in the elastic scattering, with $E_\mathrm{i} = E_\mathrm{f} \equiv E$ and $k_\mathrm{i} = k_\mathrm{f} \equiv k$, described by Bragg's law of the form [97]:

$$Q = 2k \sin\theta = \frac{(4\pi \sin\theta)}{\lambda}, \tag{3.13}$$

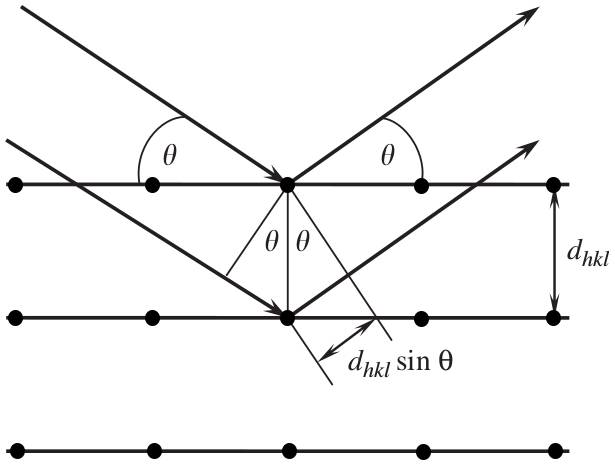

Figure 3.2: Diffraction from planes of the crystal lattice, separated by d_{hkl}, leads to the difference in optical path equal to $d_{hkl} \sin\theta$. Figure adapted from Ref. [99].

where θ is half of the angle between the transmitted and the scattered beam.

This shows that the diffraction condition might be fulfilled by adjusting either one of two parameters, scattering angle 2θ, or neutron wavelength (energy) λ. Those two approaches are represented in two different realizations of neutron diffraction: constant-wavelength diffraction and time-of-flight diffraction. The first one described in next two sub-sections (for single crystal and powder cases) and the last one in the third paragraph of this section.

If the scattering system is in the form of a crystalline solid (atoms are occupying a periodic lattice), scattering takes place from crystal planes indexed with Miller indices $[h, k, l]$ with interplane distances d_{hkl} as shown in Fig. 3.2. This introduces the constraint in form of constructive interference conditions, requiring the difference of optical paths of diffracted waves to be equal to the multiple of their wavelength. It is contained in the Bragg's law in direct space [99]:

$$n\lambda = 2d_{hkl} \sin\theta. \tag{3.14}$$

Neutron single crystal diffraction

In reciprocal space, the constraint of constructive interference conditions presented in Eq. 3.14, results in the requirement of the scattering vector $\boldsymbol{Q}$ to match one of the reciprocal lattice vectors $\boldsymbol{H} = h\boldsymbol{a}^* + k\boldsymbol{b}^* + l\boldsymbol{c}^*$ $(h, k, l \in \mathbb{N})$, being normal to the $[h, k, l]$ plane in direct space, where $\boldsymbol{a}^* = \frac{\boldsymbol{2\pi(b\times c)}}{\boldsymbol{a\cdot(b\times c)}}$, $\boldsymbol{b}^* = \frac{\boldsymbol{2\pi(c\times a)}}{\boldsymbol{a\cdot(b\times c)}}$ and $\boldsymbol{c}^* = \frac{\boldsymbol{2\pi(a\times b)}}{\boldsymbol{a\cdot(b\times c)}}$ are translation vectors of the reciprocal lattice related to vectors $\boldsymbol{a}$, $\boldsymbol{b}$ and $\boldsymbol{c}$ establishing the unit cell of the crystalline structure in the direct space [14].

The described scattering process is presented in Fig. 3.3, where the Ewald sphere is constructed with incoming wavevector $\boldsymbol{k}_\mathrm{i}$ around the origin of reciprocal space O. The interference condition is fulfilled for all reciprocal space points $P = (h, k, l)$ lying on the surface of the sphere with a scattering wavevector $\boldsymbol{Q} = \boldsymbol{H}_{hkl}$ defined as in Eq. 3.1. As an effect, the Bragg reflection might be detected in the direction defined by the center of

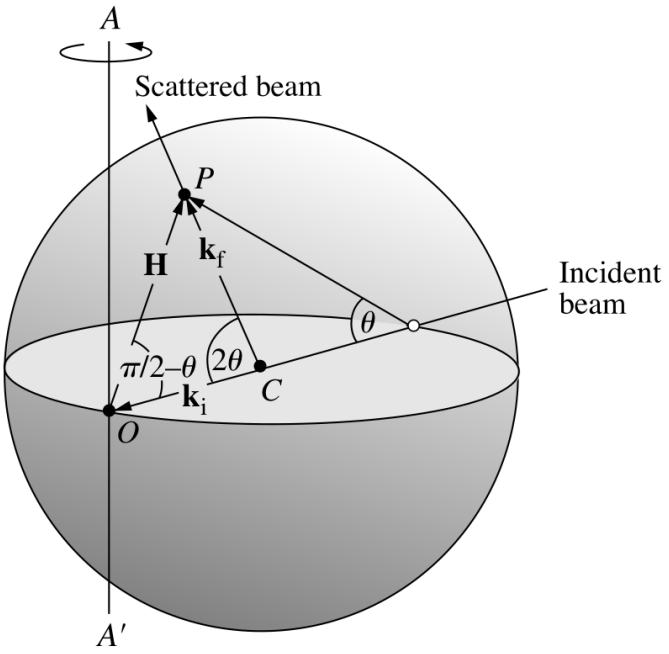

Figure 3.3: Ewald sphere construction representing the scattering process on the reciprocal space point P lying its surface. Figure adapted from Ref. [97].

a sphere (C) and every reciprocal space point (P) lying on the surface of the sphere.

In practice it can be realized with the use of single crystal diffractometers, the schematic view of two of those instruments are presented in Fig. 3.4. In the left panel of this figure there is presented the layout of D23 single-crystal neutron diffractometer. It uses the monochromatic beam, which is obtained by one of two single crystal monochromators. $(0, 0, 2)$ Bragg reflection of pyrolytic graphite and $(2, 0, 0)$ reflection of copper crystal allow to adjust the incoming neutron wavelength within the $1 - 3$ Å range [100]. The ω rotation of the sample corresponds to the rotation of the Ewald sphere around the axis marked by AA' in Fig. 3.3, containing the point O. The detector's horizontal plane rotation γ and detector's inclination angle ν allow to probe point's on the Ewald sphere lying out of the incident beam, within their range of rotation.

While using single-crystal neutron diffractometer one can directly measure the integrated intensity of a (h, k, l) Bragg reflection I_{hkl}, with $I_{hkl} \sim S_{coh}(\boldsymbol{Q}) \sim |F_{hkl}|^2$, where F_{hkl} is the nuclear structure factor defined as following [97]:

$$F_{hkl} = \sum_j b_j \mathrm{e}^{2\pi \mathrm{i}(hx_j + ky_j + lz_j)} \mathrm{e}^{-\frac{1}{2}Q^2 \bar{u_j^2}}, \tag{3.15}$$

summed over all of the atoms at (x_j, y_j, z_j) forming an unit cell with $U(Q) = \mathrm{e}^{-\frac{1}{2}Q^2 \bar{u_j^2}}$ standing for Debye-Waller factor decreasing the measured reflection's intensity, due to thermal vibrations described by mean-square atomic displacement $\bar{u_j^2}$.

Similarly with use of Eq. 3.8 one can deduce the contribution to the Bragg scattering from the ordered magnetic moments, which also contribute to the Bragg scattering at the right $\boldsymbol{Q} = (h, k, l)$ positions corresponding to the periodicity of magnetic structure. The

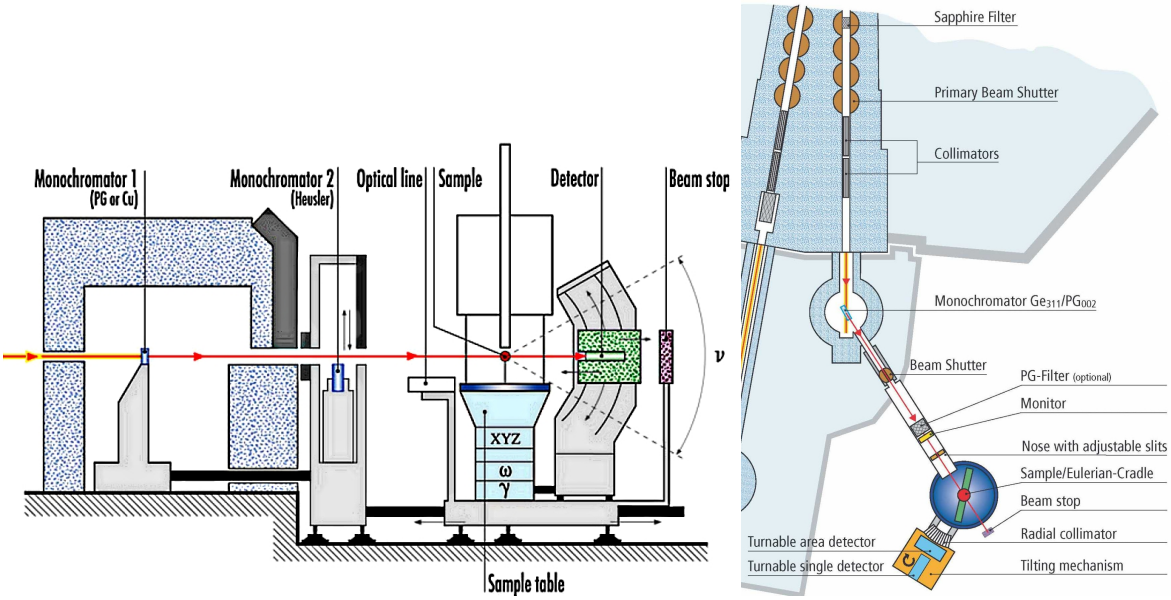

Figure 3.4: (*left*) Schematic representation (side view) of the D23 single crystal neutron diffractometer operating at ILL. Figure adapted from Ref. [100]. (*right*) Schematic representation (top view) of the ZEBRA single crystal neutron diffractometer operating at SINQ. Figure adapted from Ref. [101].

main difference between those two contribution is their $\boldsymbol{Q}$-dependence, where in case of magnetic scattering it is dictated by the ion-type specific magnetic form factor given in Eq. 3.10.

Neutron powder diffraction

It is often the case that single crystals of sizes appropriate for neutron diffraction cannot be obtained, or the material develops a multi-domain structure, as a result of phase transitions occurring with the temperature change.

This situation can be resolved with use of powder diffraction method, whose principle of operation is presented in Fig. 3.5. In this method the polycrystalline sample consists of large number of randomly oriented grains. The monochromatized incoming beam scatters at the angles $2\theta_{hkl}$ from the population of grains having common direction of the $|CO|$ section of the Ewald sphere (Fig. 3.3), but being rotated around this axis by a random angle. It results in appearance of Debye-Scherrer cones, formed by point-like Bragg reflections, detected by stripe-like position-sensitive detector (PSD). In most instruments (like D20 and HRPT, whose layouts are presented in Fig. 3.6 the PSD is placed in the horizontal plane and covers angular range of a bit less than 180°.

The described experimental setup produces the angle dependent diffraction pattern similar to the one presented at the bottom of of Fig. 3.5. At the angles 2θ corresponding to proper $|\boldsymbol{Q}|$ of $Q = (h, k, l)$ - the position on the surface of the Ewald sphere constructed with the incoming wavelength λ (Fig. 3.3), the peak of intensity is detected as the Debye-Scherrer cone is crossing the surface of the detector. It is contained by the relation Eq. 3.14. The main difference with respect to single-crystal measurements is the powder-

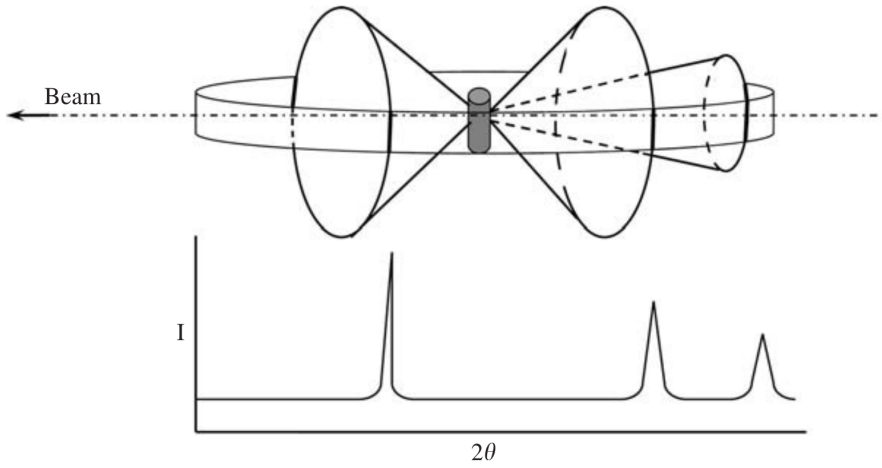

Figure 3.5: Principle of of operation of the Debye-Scherrer powder diffraction method. Figure adapted from Ref. [99].

averaging which result in significant loss of information about the reciprocal space picture of the investigated material. In special cases when at least two dimensions of the direct (a, b, c) and by this reciprocal (a^*, b^*, c^*) unit cell are identical leads to the reflection degeneracy, e.g. for the cubic structure where $a = b = c$ the following takes place: $|\boldsymbol{Q}_{100}| = |\boldsymbol{Q}_{010} = |\boldsymbol{Q}_{001}|$ giving $2\theta_{100} = 2\theta_{010} = 2\theta_{001}$. It can also happen for multiple reflections accidentally sharing the same $|\boldsymbol{Q}|$.

Top views of two neutron powder diffractometers, namely D20 and HRPT, are presented in Fig. 3.6. Monochromatization of the incoming neutron beam is achieved in the same way as in the single-crystal diffractometers. The main difference between those two types of instruments is the wide-angle PSD detector being in stark contrast to single-pixel detectors required in the basic single-crystal diffraction technique.

Generally the resolution of the constant-wavelength diffractometers depends strongly on the collimation of incoming and scattered beams which discriminates the neutrons propagating at angles deviating from the deserved values. In powder diffractometers the additional factor contributing to the resolution effects is produced by the projection of the Debye-Scherrer on the detector strip having finite size in out of plane direction. This effect is angle-dependent as in-plane coverage of the cone's projection on the detector is changing with opening angle. It is pictured in Fig. 3.5 as the width of detected peaks.

Another important factor contributing to the final resolution of the instrument taken into account at the stage of design is the scattering angle from monochromator. Using Eq. 3.14 one can find the relative uncertainty of the final wavelength in Bragg scattering process [102]:

$$\frac{\Delta\lambda}{\lambda} = \cot\theta_{\mathrm{B}}\Delta\theta_{\mathrm{B}} + \frac{\Delta d}{d}, \tag{3.16}$$

where the first term describes the angle dependence of this uncertainty and the second one covers the structural imperfections of monochromatizing crystal. It can be easily shown that the first term reaches its minimum for $\theta_{\mathrm{B}} = 90°$ (i.e. in backscattering geometry). This allows to realize the high-resolution operating modes of the instruments by

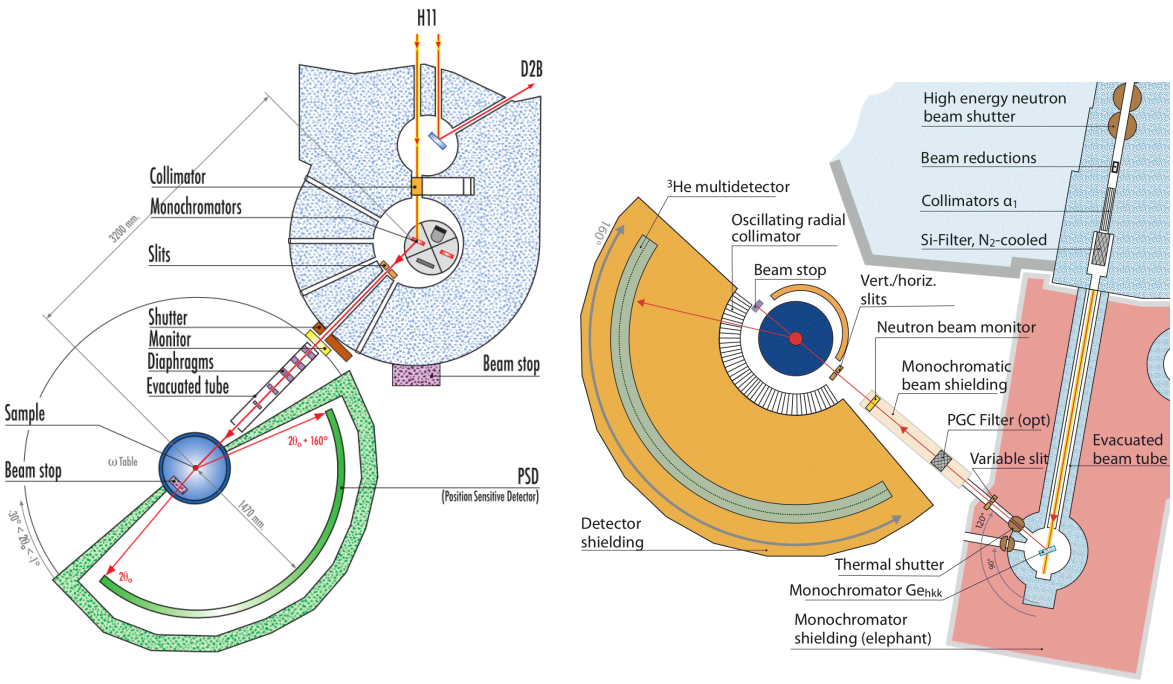

Figure 3.6: (*left*) Schematic representation (top view) of the D20 powder neutron diffractometer operating at ILL. Figure adapted from Ref. [100]. (*right*) Schematic representation (top view) of the HRPT powder neutron diffractometer operating at SINQ. Figure adapted from Ref. [101].

using the appropriate Bragg reflections at the angles as close to this optimal value as possible. Although one have to keep in mind that narrowing bandwidth $\Delta\lambda$ results in lower number of usable neutrons as monchromatization of neutron beam is a discriminatory process.

Time-of-flight neutron powder diffraction

The previous two sections described the family of constant-wavelength neutron powder diffraction techniques, those are optimal when using a continuous neutron source producing the steady flux over whole operation time. In pulsed neutron sources, where the beam is produced in short-timed pulses of very high intensity, a much more reasonable approach is time-of-flight diffraction as it takes advantage of the pulsed character of the produced beam. It uses the whole spectrum of incoming neutron energies compensating for lower time-averaged flux provided by the pulsed sources. Another design feature employed to increase the use of neutrons is providing the time-of-flight diffractometers with multiple detector banks covering small 2θ range each, covering the large solid angle [99].

The time-of-flight diffraction uses the linear relationship between neutron's wavelength λ and the time t required by the neutron to travel the distance L [97]:

$$\frac{h}{\lambda} = m_{\mathrm{n}} v = m_{\mathrm{n}} \left(\frac{L}{t} \right), \tag{3.17}$$

where v is the neutron's wavelength. Using this relation the direct space form of Bragg's law (Eq. 3.14) might be rewritten as [99]:

$$d_{hkl} = \frac{ht}{2mL \sin\theta}. \tag{3.18}$$

In this operational mode a single diffraction pattern is recorded at each bank with fixed 2θ, by acquiring the time of neutron's detection events. Given the information one can retrieve d_{hkl} of the planes from which the detected particle has scattered.

Most pulsed sources use the spallation technique for neutron creation - the heavy-element rich target is bombarded with high energy charged particles (i.e. proton beams produced in accelerators). Produced neutrons are brought down to the thermal energy range by moderation. The moderation process takes place when a neutron beam is passing through the volume of low absorption cross-section and high scattering cross-section material (i.e. liquid hydrogen, solid methane) kept at the desired stable temperature. The moderated neutron beam acquires a Maxwellian energy distribution defined by the moderator's temperature.

Using Eq. 3.18 one can easily derive the resolution of time-of-flight diffractometer [102]:

$$\frac{\Delta d}{d} = \sqrt{\left(\frac{\Delta t}{t}\right)^2 + \left(\frac{\Delta L}{L}\right)^2 + \Delta\theta^2 \cot\theta^2}, \tag{3.19}$$

where the uncertainty of event detection time, depending on employed electronic components, is usually neglected as being very small. The angle dependent term is fully defined by position and design of the detector banks. The second term being a function of total neutron path of flight might be minimized by increasing the moderator-sample distance at the stage of instrument design process allowing for optimizing the resolution with respect to the purpose of designed instrument.

Time-of-flight diffraction has the advantage of recording the whole diffraction pattern at the fixed angle providing the constant resolution across whole of it. On the others hand the data acquisition involves huge number of events to be recorded, what makes the data reduction process significantly more complex than in case of constant-wavelength diffraction.

The major disadvantage of time-of-flight powder diffraction in comparison to constant-wavelength mode of this technique is relatively more complex peak profile of the recorded reflection. For the latter method the peak profile is usually well described with Voigt profile [99], which is convolution Gauss and Lorentz functions. In time-of-flight diffractometers the shape of incoming pulse and finite length of the moderator along the path of the neutron results with strongly asymmetric peak profile, which can be described as two exponential curves placed back-to-back convoluted with both Gauss and Lorentz functions [103]. The description of this profile requires much more parameters and might complicate quantitative description of some aspects of applied model, which manifest themselves in changes of peak profile.

Diffraction data analysis

Most commonly applied methods of structural information retrieval from powder diffraction data are Rietveld refinement [104] and Le Bail profile fitting [105]. The former one compares the model-based calculated pattern ($y_{\mathrm{calc}}(\boldsymbol{Q_i})$, where i goes over the discrete measurement points), parametrized by system-related quantities (e.g. scale, unit cell dimensions, atomic positions within the unit cell, Debye-Waller factors) with the measured diffraction pattern ($y_{\mathrm{obs}}(\boldsymbol{Q_i})$). The $y_{\mathrm{calc}}(\boldsymbol{Q_i})$ is obtained by calculating the peak position using the unit cell parameters and placing at those positions peaks of intensity $|F_{hkl}|^2$ convoluted with peak profile determined by instrumental (resolution) and sample features (e.g. microscopic structural strain). The weighted sum of squares differences:

$$\bar{S} = \sum_i w_i (y_{\mathrm{obs}}(\boldsymbol{Q_i}) - y_{\mathrm{calc}}(\boldsymbol{Q_i}))^2, \tag{3.20}$$

with the weight w_i based on experimental uncertainty, is minimized by means of least-squares method.

The latter method uses a model-free approach (apart from reflection positions), it allows the intensity of a single peak to vary freely refining the peak position (lattice constants) and the instrumental resolution-related parameters defining the overall peak shape profile. It is often used as a preliminary step to the Rietveld analysis allowing to separate the refinement of sample and instrumental contribution.

In order to retrieve the structural information from single-crystal diffraction data one has to retrieve the integrated intensities (areas under the measured peaks of Bragg reflections) I_{hkl}, which after correcting for the sample's absorption and Lorentz factor [99] is proportional to the structure factor defined in Eq. 3.15. The similar least-squared minimization is performed on corresponding weighted sum of squares differences between calculated and observed integrated intensities I_{hkl}.

All diffraction data analysis with both Rietveld refinement and Le Bail profile fitting presented in this work were performed with `FULLPROF` software suite [106].

3.1.2 Neutron spectroscopy

Full $S(\boldsymbol{Q}, \omega)$ from coherent double differential cross-section (Eq. 3.11), measured with neutron spectroscopy, provides valuable information about the dynamics of the system (lattice excitations - phonons), magnetic excitations e.g. spin waves). The measurement strategy is to fix either $\boldsymbol{k}_{\mathrm{i}}$, or $\boldsymbol{k}_{\mathrm{f}}$, and record the changes in the other. Combining the expressions for momentum and energy transfers (Eqs. 3.1 and 3.2) one can obtain the expression describing constraints of the dynamical range of the neutron spectrometer, the set of accessible (Q, ω) points, (Fig. 3.7) at given fixed $\boldsymbol{k}_{\mathrm{i}}$, or $\boldsymbol{k}_{\mathrm{f}}$ [107]:

$$Q^2 = k_{\mathrm{i}}^2 + k_{\mathrm{f}}^2 - 2k_{\mathrm{i}}k_{\mathrm{f}}\cos(2\theta). \tag{3.21}$$

Thanks to the fluctuation-dissipation theorem [17], connecting the spontaneous fluctuations within the system with the response it gives to the external perturbation, one can connect the dynamic structure factor $S(\boldsymbol{Q}, \omega)$ with the complex generalized dynamic susceptibility $\chi(\boldsymbol{Q}, \omega)$ by the following relation:

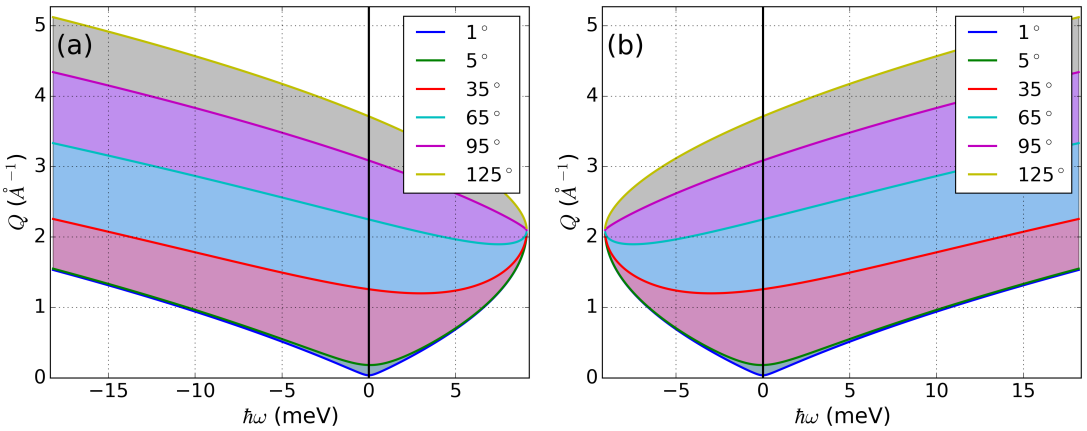

Figure 3.7: (*a*) Dynamical range of neutron spectrometer in fixed $\boldsymbol{k}_\mathrm{i} \approx 2.1$ Å^{-1} ($\lambda_\mathrm{i} = 3$ Å) configuration. (*b*) Dynamical range of neutron spectrometer in fixed $\boldsymbol{k}_\mathrm{f} \approx 2.1$ Å^{-1} ($\lambda_\mathrm{i} = 3$ Å) configuration. Positive energies $\hbar\omega$ represent the neutron energy loss side of the elastic line. The solid lines mark the trajectories in Q and $\hbar\omega$ corresponding to the appropriate 2θ angles.

$$S(\boldsymbol{Q},\omega) = \frac{1}{\pi}\frac{1}{1-\mathrm{e}^{-\hbar\omega/k_\mathrm{B}T}}\chi''(\boldsymbol{Q},\omega), \tag{3.22}$$

where $\chi''(\boldsymbol{Q},\omega)$ is the imaginary part of $\chi(\boldsymbol{Q},\omega)$ and the second term results from differences in thermal population of the states of different energy. Knowledge of $\chi''(\boldsymbol{Q},\omega)$ is the crucial step to describe the physics of the system in question.

The following sections describe two of the set of neutron spectroscopy techniques, namely three-axis neutron spectroscopy and time-of-flight neutron spectroscopy, constituting the core of the neutron toolkit for studying magnetism and condensed matter physics.

Three-axis neutron spectroscopy

Layouts of two three-axis (TAS) neutron spectrometers, ThALES (ILL) and EIGER (SINQ, PSI), are shown in Fig. 3.8. They exhibit a strong resemblance to single-crystal diffractometers, with the crystal monochromator, selecting the k_i, and another monochromator playing the role of the analyzer, responsible for k_f selection, placed in between the sample and the detector. In contrast to the single-crystal diffractometers TAS spectroscopy measures only scattering processes contained in the fixed horizontal scattering plane.

In the basic setup employing a single-pixel detector the TAS spectrometer measures a single point of the four-dimensional $S(\boldsymbol{Q},\omega)$ function. It is achieved by selecting both k_i and k_f to correspond to proper Q in the sample's reciprocal lattice and at the same time provide the desired energy transfer (3.2). One can do that by carefully adjusting 5 angles, 3 of them being truly independent [107]):

- $A_1 = \theta_\mathrm{m}$ - the angle between the incoming white beam and the monochromator's surface, defining the k_i

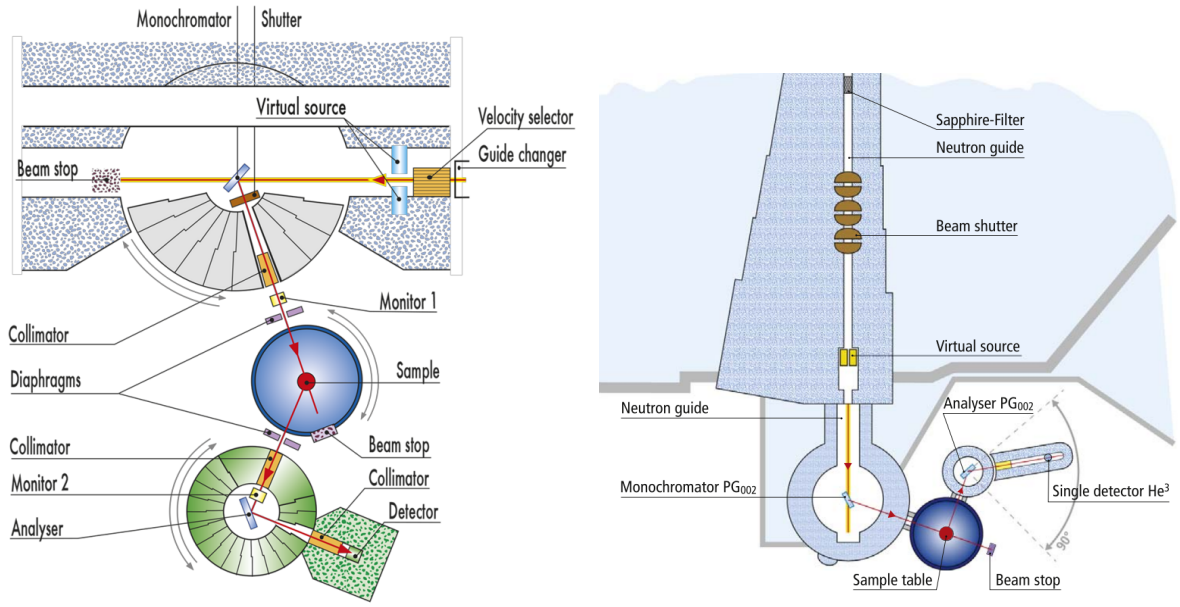

Figure 3.8: (*left*) Schematic representation (top view) of the ThALES three-axis neutron spectrometer operating at ILL. Figure adapted from Ref. [100]. (*right*) Schematic representation (top view) of the EIGER three-axis neutron spectrometer operating at SINQ. Figure adapted from Ref. [101].

- $A_2 = 2\theta_\mathrm{m} = 2A_1$ - the angle between the incoming white beam and the reflected monochromatic beam
- $A_3 = \omega$ - the orientation of the sample, with rotation of the scattering plane with respect to $\boldsymbol{k}_\mathrm{i}$ in conjunction with A_4, it fixes the desired $\boldsymbol{Q} = \boldsymbol{H}_{hkl} + \boldsymbol{q}$, where $\boldsymbol{q}$ is the vector within the Brillouin zone
- A_4 - the angle between the incoming beam and the beam scattered by the sample
- $A_5 = \theta_\mathrm{a}$ - the Bragg angle between the beam scattered by the sample and the analyzed monochromatic beam, defining the k_f

In general the TAS neutron experiment for practical reasons consists of series of step-by-step scans with either $\boldsymbol{Q}$ or $\hbar\omega$ being fixed and the second parameter varying. It allows to determine the position of the dispersion curve (e.g. phonon or magnon) with respect to the varied parameter.

The simplest way of performing a single scan is to vary one of the k_i, k_f parameters keeping the other one fixed. As the number of neutrons reflected from monochromator (analyzer) crystals depends on the $2\theta_\mathrm{m}$ ($2theta_\mathrm{a}$) angle and may change abruptly with change of this angle, the fixed-k_f (fixed $2theta_\mathrm{a}$) method is generally preferred. It results from the opportunity of normalizing a single-point scan time to the counts of the monitor placed between the monochromator and the sample, correcting for the changes in monochromator's reflectivity and intensity fluctuations of the neutron source.

TAS spectroscopy is definitely most optimal when the detailed picture of limited sections of $S(\boldsymbol{Q}, \omega)$ is of interest, i.e. following the well-defined dispersion relation. The

open construction of the instrument makes it versatile in terms of employing wide range of sample environments not compatible with other kinds of neutron spectrometers (e.g. high pressure cells, polarization analysis, various types of cryo-magnets). In addition the instrumental resolution of TAS instruments, contributing to the linewidths of observed excitations, has been successfully described in both analytical [108, 109] and numerical approaches [110], this gives the TAS instruments the advantage when detailed effects of instrumental resolution has to be taken into account.

Time-of-flight neutron spectroscopy

Similarly to single-crystal diffractometers, TAS spectrometers are optimal solution for continuous neutron sources. In case of pulsed neutron sources the commonly met type of neutron spectrometers are time-of-flight neutron spectrometers (TOF), although they are also installed at the continuous sources.

In TOF spectrometer short pulses of neutron beam hit the sample. The dispersion of neutrons propagating with different velocities, results in the differences in their time of arrival at the detector. This is used to deduce the energy transfer between detected neutrons and the sample. As pictured in Fig. 3.7 this might be achieved in two ways and it is done so in direct geometry TOF spectrometers (fixed E_i) and indirect geometry TOF spectrometers (fixed E_f) [107].

In the first scenario short pulses are either provided by the neutron source itself, or created with a set of pulse-shaping choppers (first set of choppers in Fig. 3.9(a)), neutrons within the pulse gain dispersion along the guide and the chosen energy is selected with monochromatizing choppers. Additional set of choppers might be added in between the pulse-shaping and monochromatizing choppers, those so-called frame-overlap choppers (middle set of choppers in Fig. 3.9(a)) are preventing the overlapping of the scattered neutrons from the neighbouring pulses [111]. The large solid angle covered by the array of PSD detectors allows TOF instrument to cover all (Q, ω) phase space marked in Fig. 3.7(a) at the same time. Thanks to that, TOF neutron scattering is suitable technique when the large coverage of $S(\boldsymbol{Q}, \omega)$ is necessary. In contrast to TAS, TOF is also convenient technique for experiments on polycrystalline samples, providing the picture of whole accessible $S(Q, \omega)$ at a single measurement.

Indirect geometry TOF spectrometers use pulses of the white beam. Final energy E_f of scattered neutrons is selected by Bragg reflection of the crystal analyzers (Fig. 3.9(b)). Proper design of such instrument can utilize the minimization of negative analyzer's resolution effects in the backscattering geometry ($\theta_\mathrm{a} = 90°$) [107]. It allows achieving excellent energy resolution of the order of few μeV. The reflected, in terms of energy, dynamical range of indirect geometry spectrometers (Fig. 3.7(b)) enables accessing high energy transfers at the neutron energy loss side, which is favoured in terms of detailed balance (Eq. 3.22) by the thermal population of the states in the investigated system, making it more convenient for measuring high energy excitations.

3.1.3 Polarization analysis in neutron scattering

As mentioned in Sec. 3.1 neutrons posses spin angular momentum and via that a magnetic moment, which enable their interaction with magnetic moments (both nuclear and

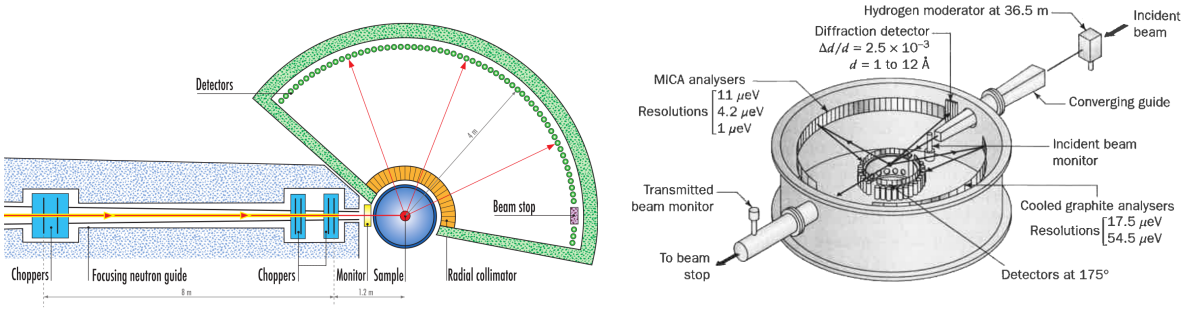

Figure 3.9: (*left*) Schematic representation (top view) of the IN5 direct geometry time-of-flight neutron spectrometer operating at ILL. Figure adapted from Ref. [100]. (*right*) Schematic representation (top view) of the IRIS indirect geometry time-of-flight neutron spectrometer operating at ISIS Neutron and Muon Source. Figure adapted from Ref. [107].

electronic). In external magnetic field the component of the spin angular momentum parallel to the direction of the field can take only one of two values: $s_z = \pm\frac{\hbar}{2}$. The polarization of a neutron beam is described by the following relation [97]:

$$P = \frac{n_+ - n_-}{n_+ + n_-}, \tag{3.23}$$

where $n_\pm$ is the fraction of the neutrons in states characterized by $s_z = \pm\frac{\hbar}{2}$. The $P = \pm 1$ and $P = 0$ describe the fully polarized and completely unpolarized beams respectively.

The polarized beam in the experimental setups is usually prepared by one of those methods: Bragg scattering from magnetized ferromagnetic crystal, the total reflection from magnetized mirror, or supermirror [97].

The first method has the advantage of simultaneous polarization and monochromatization of the beam, what makes it particularly suitable for TAS spectrometers and constant-wavelength diffractometers. The differential cross-section for the neutrons of opposite polarizations with respect to the magnetic moments at the sites of crystal lattice and magnetic field at the same time(parallel - "+" and antiparallel - "-") follows [97]:

$$\frac{\mathrm{d}\sigma}{\mathrm{d}\Omega}^{\pm} = |F_{hkl}(Q) \pm F_{\mathrm{m}hkl}(Q)|^2, \tag{3.24}$$

with $F_{hkl}(Q)$ and $F_{\mathrm{m}hkl}(Q)$ standing for nuclear and magnetic structure factor (Eq. 3.15) of the hkl reflection. The optimal situation $F_{hkl}(Q) = F_{\mathrm{m}hkl}(Q)$ produces in principle a fully polarized beam. This has been found for the $(1, 1, 1)$ reflection of the Heusler alloy - Cu_2MnAl.

Magnetic mirrors and supermirros use the difference in the neutron refractive index and by that critical total reflection angle from magnetized materials for neutrons of different polarization [97]:

$$\theta_{\mathrm{c}}^{\pm} = \lambda \left[\left(\frac{N}{\pi} \right) (\bar{b} \pm p) \right]^2, \tag{3.25}$$

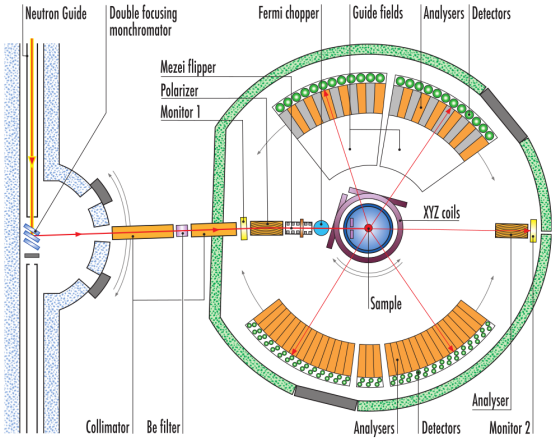

Figure 3.10: Schematic representation (top view) of the D7 diffuse scattering neutron spectrometer operating at ILL. D7 enables the XYZ-difference polarization analysis. Figure adapted from Ref. [100].

with p representing the magnetic scattering length. To increase the efficiency of mirror polarizers the multistructure devices with magnetic/non-magnetic bilayers are employed. Carefully choosing the thickness profile of the stacked bilayers (e.g. Fe/Si) the neutron polarizing supermirror is created, which is characterized by broad energy band of neutrons being reflected and thus polarized. The same devices might be also employed as the polarization analyzers, filtering out the scattered neutrons of specific spin state from being detected.

In order to maintain the beam polarization, a small (tens of mT) continuous field along the polarization direction has to be provided at the whole length of neutrons' path. In addition to perform a polarization analysis experiment, separating the scattering contribution from processes involving the change of neutron's magnetic state (spin-flip processes) and the ones leaving it unchanged (non-spin-flip processes), use of the flipping devices, reorienting the neutrons magnetic moments - spin flippers is necessary. They utilize one of two kinds of processes, namely the adiabatic and non-adiabatic rotations. The adiabatic process involves the rotation of magnetic field generated by the flipper along the neutrons path at the rate much slower than the frequency of neutron magnetic moment's Larmor precession due to the guide field. In that case the component of the magnetic moment along the field maintains the direction of the field and the transverse one precesses around it. The second case causes the whole magnetic precessing around the new direction of the external field [97].

The XYZ-difference method of polarization analysis [112, 113] uses the fact that nuclear, magnetic and nuclear spin incoherent scattering contribute differently to the spin-flip and non-spin-flip channels for 3 perpendicular directions of polarization (X, Y and

Z) [114, 115, 113]:

$$\left(\frac{\mathrm{d}\sigma}{\mathrm{d}\Omega}\right)_x^{\mathrm{NSF}} = \frac{1}{2}\sin^2\alpha\left(\frac{\mathrm{d}\sigma}{\mathrm{d}\Omega}\right)_{\mathrm{mag}} + \frac{1}{3}\left(\frac{\mathrm{d}\sigma}{\mathrm{d}\Omega}\right)_{\mathrm{si}} + \left(\frac{\mathrm{d}\sigma}{\mathrm{d}\Omega}\right)_{\mathrm{nuc}}, \tag{3.26a}$$

$$\left(\frac{\mathrm{d}\sigma}{\mathrm{d}\Omega}\right)_x^{\mathrm{SF}} = \frac{1}{2}(\cos^2\alpha + 1)\left(\frac{\mathrm{d}\sigma}{\mathrm{d}\Omega}\right)_{\mathrm{mag}} + \frac{2}{3}\left(\frac{\mathrm{d}\sigma}{\mathrm{d}\Omega}\right)_{\mathrm{si}}, \tag{3.26b}$$

$$\left(\frac{\mathrm{d}\sigma}{\mathrm{d}\Omega}\right)_y^{\mathrm{NSF}} = \frac{1}{2}\cos^2\alpha\left(\frac{\mathrm{d}\sigma}{\mathrm{d}\Omega}\right)_{\mathrm{mag}} + \frac{1}{3}\left(\frac{\mathrm{d}\sigma}{\mathrm{d}\Omega}\right)_{\mathrm{si}} + \left(\frac{\mathrm{d}\sigma}{\mathrm{d}\Omega}\right)_{\mathrm{nuc}}, \tag{3.26c}$$

$$\left(\frac{\mathrm{d}\sigma}{\mathrm{d}\Omega}\right)_y^{\mathrm{SF}} = \frac{1}{2}(\sin^2\alpha + 1)\left(\frac{\mathrm{d}\sigma}{\mathrm{d}\Omega}\right)_{\mathrm{mag}} + \frac{2}{3}\left(\frac{\mathrm{d}\sigma}{\mathrm{d}\Omega}\right)_{\mathrm{si}}, \tag{3.26d}$$

$$\left(\frac{\mathrm{d}\sigma}{\mathrm{d}\Omega}\right)_z^{\mathrm{NSF}} = \frac{1}{2}\left(\frac{\mathrm{d}\sigma}{\mathrm{d}\Omega}\right)_{\mathrm{mag}} + \frac{1}{3}\left(\frac{\mathrm{d}\sigma}{\mathrm{d}\Omega}\right)_{\mathrm{si}} + \left(\frac{\mathrm{d}\sigma}{\mathrm{d}\Omega}\right)_{\mathrm{nuc}}, \tag{3.26e}$$

$$\left(\frac{\mathrm{d}\sigma}{\mathrm{d}\Omega}\right)_z^{\mathrm{SF}} = \frac{1}{2}\left(\frac{\mathrm{d}\sigma}{\mathrm{d}\Omega}\right)_{\mathrm{mag}} + \frac{2}{3}\left(\frac{\mathrm{d}\sigma}{\mathrm{d}\Omega}\right)_{\mathrm{si}}, \tag{3.26f}$$

where the x and y are perpendicular directions contained within the scattering plane. In case of single detector instruments x is usually chosen to be parallel to the scattering vector $\boldsymbol{Q}$ and z is perpendicular to the scattering plane. This choice ($\alpha = 0$) allows to remove nuclear contribution from x spin-flip channel and leaves only the nuclear-spin incoherent contribution in y spin-flip channel. Subtraction of those to channels with appropriate multipliers allows to separate purely magnetic contribution to the total scattering.

When applying this formalism to multidetector instruments (Fig. 3.10) different angles between every detector and beam polarization must be accounted. It is solved by considering the trigonometrical factors connected with the Schärpf angle α, being the angle between the scattering vector recorded at the single detector within the array and the analyzed beam polarization direction [112, 116].

Eqs. 3.26 show that with use of simple arithmetic operations one can extract the nuclear $\left(\frac{\mathrm{d}\sigma}{\mathrm{d}\Omega}\right)_{\mathrm{nuc}}$, magnetic $\left(\frac{\mathrm{d}\sigma}{\mathrm{d}\Omega}\right)_{\mathrm{mag}}$ and nuclear spin-incoherent $\left(\frac{\mathrm{d}\sigma}{\mathrm{d}\Omega}\right)_{\mathrm{si}}$ contributions to the total differential scattering cross-section $\left(\frac{\mathrm{d}^2\sigma}{\mathrm{d}\Omega}\right)_{\mathrm{tot}}$.

The XYZ-difference method is restricted to samples which does not exhibit net magnetization (e.g. antiferromagnets, paramagnets and correlated paramagnets, where $M_x = M_y = Mz$), as the demagnetization field would cause precession of the neutron moments changing the beam's polarization from the desired state (beam depolarization).

3.2 Magnetization and magnetic susceptibility

The response of the medium to the magnetic field described by vector $\boldsymbol{H}$ is given by the magnetic field induction [13]:

$$\boldsymbol{B} = \mu_0(\boldsymbol{H} + \boldsymbol{M}), \tag{3.27}$$

with $\boldsymbol{M}$ magnetization - the change of system's free energy in presence of external field [14]. The dependence of magnetization on the applied field is usually described by the magnetic susceptibility [14]

$$\chi = \left.\frac{\partial M}{\partial H}\right|_{H=0}, \tag{3.28}$$

evaluated at low field usually assumed to be linear for the static fields ($\chi \approx M/H$).

Magnetic susceptibility may be accessed by magnetometry measurements. Further chapters of this work present the results of DC magnetization measurements where the response of the sample to steady field is measured. The standard devices commonly used for that purpose are MPMS (Magnetic Properties Measurement System) produced by Quantum Design [117], equipped with superconducting quantum interference device (SQUID), based on the Josephson junction [118], providing unique sensitivity of the magnetization detection.

The measurement procedure involves moving the sample through the detection coil made out of superconducting wire. The sample and the coil are placed inside the other superconducting solenoid producing strong magnetic fields up to several Tesla. The magnetization of the moving sample couples to the detection coil by inducing current in superconducting wire, which is forming another coil at its other end incorporated in RF SQUID device [119] placed in the protective compartment (superconducting shielding protects against the fluctuations of the background field) [120]. The squid device using the Josephson effect [119] works effectively as a proportional current to voltage converter.

Specific details of experimental procedures, the data resulting from which, are presented in appendix A.

Chapter 4

$LiGa_{1-x}In_xCr_4O_8$ - breathing pyrochlores

4.1 Chromate spinels ACr_2O_4

The spinel structure of transition metal oxides AB_2O_4, with space group $Fd\bar{3}m$, makes them very appealing systems for studying the effects of interplay of lattice with spin (e.g. ACr_2O_4), charge (e.g. AV_2O_4) [90] and orbital (ASc_2S_4) degrees of freedom [121]. The frustration arises from the octahedrally coordinated transition metal cations at the B-site form three-dimensional array of corner-sharing tetrahedra, i.e. the pyrochlore lattice (Fig. 4.1).

The chromate spinels ACr_2O_4, are Mott insulators with antiferromagnetically coupled Cr^{3+} ions carrying $S = \frac{3}{2}$ spin moment and with the A-site populated by a nonmagnetic cation (e.g. Cd^{2+}, Hg^{2+}, Mg^{2+} or Zn^{2+}), and are highly valued for the wide range of magnetic ground-states they exhibit (Tab. 4.1). The nearly octahedral coordination of B-site results in the e_g orbitals lying above the t_{2g} ground-state in the crystal field Hamiltonian [12]. The dominating magnetic interaction in chromate spinels is the nearest neighbour magnetic exchange. It results from direct overlap of the Cr^{3+} t_{2g} orbitals. This causes a vast variation of the interaction strength with respect to the Cr-Cr distances [122, 123]. Those distances can be adjusted by the choice of A^{2+} cation and thus by selecting proper A-site ion system might be tuned to exhibit specific ratio between strength of primary and further interacitons.

The nearest neighbour exchange of antiferromagnetic character classically imposes a zero spin sum rule on each tetrahedron i.e. $\sum_{\text{tetr}} \boldsymbol{S}_i = 0$ [80]. Simulations accounting exclusively for this interactions lead to the conclusion of their ground-state being spin-liquid lacking the long-range magnetic order [80, 82, 124]. In contrast to these results, most members of the chromate spinel family exhibit the magnetic long-range order, whose onset might be observed at temperatures much lower than the Weiss constant (θ_{W}), reflecting the strength of the magnetic interactions (Tab. 4.1). On one hand $T_{\text{N}} \ll \theta_{\text{W}}$ shows the highly-frustrated character of those systems and possibility of existence of correlated paramagnet phase in the $\theta_{\text{W}} > T > T_{\text{N}}$ temperature range. However, the departure from a spin-liquid ground-state requires a perturbation that lifts the degeneracy of the degenerate low-energy configurations inherent to the nearest-neighbour pyrochlore antiferromagnets. As the usually observed phase transitions in chromate spinels are of

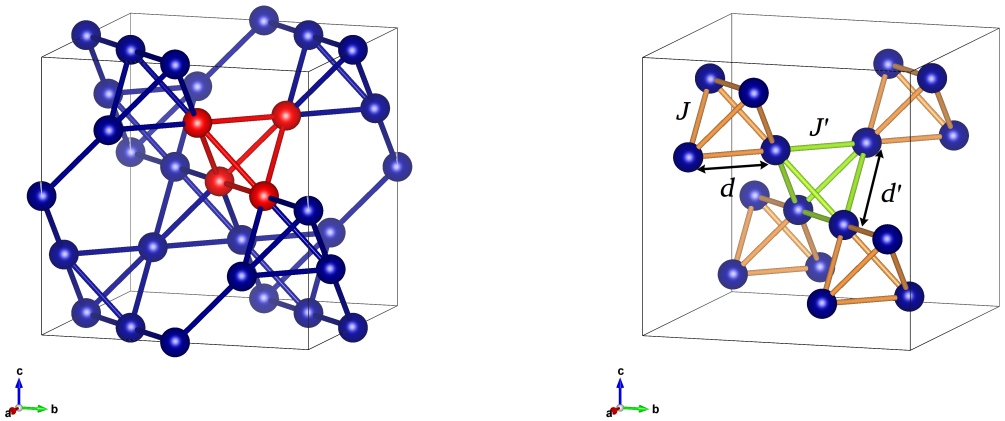

Figure 4.1: (*left*) Pyrochlore lattice formed by the B-site of AB_2O_4 spinel oxides. A single tetrahedron is outlined by the red colour. (*right*) Breathing pyrochlore lattice of $LiGa_{1-x}In_xCr_4O_8$ spinels. The small and large tetrahedra are outlined by green and orange bonds respectively. J, J' and d, d' mark varying exchanges and Cr-Cr distances in small and large tetrahedra. Figure created with `VESTA` software [60].

magnetostructural character this clearly points to the magnetoelastic coupling as playing important role in symmetry breaking process. Its action is most simply accounted for by adding a biquadratic term to the spin Hamiltonian, producing the bilinear-biquadratic model (BBM) [87, 125, 126]:

$$\mathcal{H} = J \sum_{i,j} \boldsymbol{S}_i \cdot \boldsymbol{S}_j + b \sum_{i,j} (\boldsymbol{S}_i \cdot \boldsymbol{S}_j)^2, \tag{4.1}$$

where b describes the strength of biquadratic term. The sign of the biquadratic coupling imposes the anisotropy of magnetic moments in the way: $b > 0$ favours coplanar moments, while $b < 0$ favours collinear arrangement of the moments. Results obtained with this model show how the spin-lattice coupling leads to the symmetry lowering and partial lifting of the degeneracy of the magnetic ground-state, enabling additional perturbations (e.g. further neighbour coupling) for the onset of long-range order [87, 88, 127, 128, 126], in a process referred to as spin Jahn-Teller effect. It is the magnetic counterpart of orbital Jahn-Teller effect, where the orbital degeneracy is lifted by a lattice distortion and consequent splitting of crystal electric field levels [12].

Monte Carlo studies using the BBM Hamiltonian has given correct description of temperature-magnetic field ($T - H$) phase diagram, which hosts a half-magnetization plateau, for a few of the chromate spinel pyrochlores [125, 129, 90]. Another factor playing a role in the physics of antiferromagnetic pyrochlores are couplings between further neighbours, mediated by superexchange interactions. These where identified as influencing the appearance of Néel state [130, 126] as well, and might be used as an extension of BBM model. Additionally, the influence of bond disorder in connection with further neighbour interactions on the suppression of ordered phase was investigated in simula-

Table 4.1: Magnetic and structural properties of several ACr_2O_4 chromate spinels.

A^{2+}	Zn^{2+} [131, 90, 132]	Mg^{2+} [139, 132, 133]	Cd^{2+} [42]	Hg^{2+} [140]
θ_W (K)	-288	-368	-70	-32
T_N (K)	12.3	12.9	7.8	5.8
J (K)	$33-45$	21	9	4
Cr-Cr (Å)	2.944	2.9461	3.041	3.062
Low-T crystal structure	$I\bar{4}m2$	$I4_1/amd(+Fddd)$	$I4_1/amd$	$Fddd$
Magnetic order type	coplanar	coplanar	spiral	coplanar

tions presented in Ref. [126], which concluded the possibility of existence of spin-nematic state, characterized by a multipolar order parameter.

As mentioned previously, most chromate spinel pyrochlores undergo magnetostructural phase transitions. The known details of the low temperature crystalline structures for A =Zn,Mg,Cd and Hg are shown in Tab. 4.1. Although good quality single-crystal samples were studied for almost all of these compositions (with the exception of A =Hg) the symmetry (and even number) of low-temperature phases still is not certainly determined [131, 90, 132, 133]. Moreover, apart from case of A =Cd, where a single incommensurate magnetic wave vector ($\boldsymbol{k} = (0, \delta, 1)$, with $\delta \sim 0.09$) was identified [134], the rest of the family members seem to host multi-$\boldsymbol{k}$ type (or multi-domain) magnetic structures with $\boldsymbol{k} = (1, 0, 1/2)$, $(1, 0, 0)$ for A =Hg [42], $\boldsymbol{k} = (1/2, 1/2, 0)$, $(1, 0, 1/2)$, $(1, 0, 0)$ and $(1/2, 1/2, 1/2)$ for A =Zn [131], and $\boldsymbol{k} = (1/2, 1/2, 0)$, $(1, 0, 1/2)$, $(1, 0, 0)$ for A =Mg [133]. Also, suppression of the ordered magnetic moment from the free ion value is suggested in many compounds by the neutron diffraction experiments [131, 133]. With only an incomplete knowledge of the structural symmetry breaking involved into the observed transitions and striking signs of complexity characterizing the accompanying magnetic orders the question of the low-temperature properties of those materials still awaits an unambiguous resolution.

Apart from complex long-range order, another intriguing aspect of the chromate spinels are weak low-energy excitations detected in some of the family members [135, 134] at $T > T_N$ and local spin resonances [136] observed below the phase transition [137, 138]. The former manifests the character of spin-liquid phase above the transition and the latter suggesting the spin Jahn-Teller effect changing the length of part of the bonds, and thereby singling out small molecular clusters (tetramers, hexamers, or heptamers).

4.2 $LiGa_{1-x}In_xCr_4O_8$ family

$LiGa_{1-x}In_xCr_4O_8$ family are examples of A-site ordered spinels ($AA'Cr_4O_8$), where the A site is occupied by two types of ions. These crystallize in a structure described by the $F\bar{4}3m$ space group [141] a subgroup of $Fd\bar{3}m$. In $LiGa_{1-x}In_xCr_4O_8$ the A-site is populated by two ions of different valency, one of those being monovalent and the other trivalent. Minimization of the electrostatic interactions between these cations (favouring larger spatial separation between highly charged ions) forces them to order in the alternating manner [142, 143]. The difference between the ionic radii leads to a spatially varying chemical pressure exerted on the neighbouring ions which influences the sizes of

Figure 4.2: Powder samples of (left) $LiGaCr_4O_8$ and (right) $LiInCr_4O_8$.

surrounding tetrahedra constituting the pyrochlore lattice. It results in their sizes varying in periodic manner. This alternation is called the "breathing" distortion and its extent can be adjusted by choosing A and A' with different ratios of ionic radii.

As mentioned, the strength of magnetic interactions in chromate spinels depends greatly on the distance between the magnetic ions, thus the exchange between ions within small (J') and large tetrahedra (J) vary as well (Fig. 4.1). The degree of frustration of a breathing pyrochlore system can be quantified by the breathing factor $B_f = J'/J$ [142], with the limiting cases of 0 and 1 corresponding to separated small tetrahedra and a uniform pyrochlore lattice respectively. The expected ground-state for those, assuming only nearest-neighbour interactions, are tetramer singlet and a classical spin-liquid respectively.

Breathing pyrochlore chromate spinels similarly to undistorted pyrochlores of this family host disordered correlated paramagnet regime, possibly characterized by variety of spin-liquid ground states, which are of the interest on their own. They also provide an opportunity to explore the interplay of geometrical frustration with bond alteration, whose extent might be smoothly adjusted according to the needs by choosing the appropriate stoichiometry. This presumably leads to appearance exotic phases of matter, giving insight into new physics and allowing for observation of unique fractionalized excitations.

Samples

Polycrystalline samples of the end-member compositions usedin this work were prepared by Okamoto et al. using the solid state reaction method described in Ref. [142]. $LiGaCr_4O_8$ powdered samples are of brownish green colour, while $LiInCr_4O_8$ can be described as rich dark green (Fig. 4.2). The intermediate compositions were obtained by sintering a stoichiometricallly balanced mixture of $x = 0$ and $x = 1$ powder samples, as described in Ref. [143]. ^{7}Li isotopicaly enriched samples were prepared for neutron scattering experiments as ^{6}Li (7.5% natural abundance) is characterized by high value of neutron absorption cross section ($\sigma_{\text{abs}} = 940.(4)$ barns for neutrons with $E = 25.3$ meV [144]).

4.2.1 $LiGaCr_4O_8$ ($x = 0$) and $LiInCr_4O_8$ ($x = 1$)

Further details of experimental procedures whose results are presented in following parts of this chapter are given in Table A.1 in Appendix A.

Both end-member compounds were characterized by means of bulk measurement techniques in Refs. [142, 145, 146]. X-ray and neutron diffraction studies suggest no occurrence of site mixing between Li-sites and Ga(In)-sites, proving a true A-site ordered structure. The magnetic susceptibility measurements show large negative θ_W for both materials (see Tab. 4.2) confirming the antiferromagnetic character of averaged magnetic interactions. Moreover, it suggests the development of antiferromagnetic short-range correlations at $T \sim 45$ K for $x = 0$ similar to the one observed in uniform pyrochlore lattice of $ZnCr_2O_4$. In contrast an apparent spin-gap behaviour (with a gap of $\Delta = 56.8$ K) fairly well described by an isolated tetrahedron model [142] is exhibited by $x = 1$. This observation falls well in agreement with the evaluated values of breathing distortion based on the Cr-Cr bond length (Tab. 4.2). Results of heat capacity measurements divided by temperature (C_p/T) show peak-shaped anomalies at $T = 13.8$ K and $T = 15.9$ K for $x = 0$ and $x = 1$ respectively. The peak measured in the $x = 0$ composition shows departures from the shape expected for a conventional second-order magnetic transition (see Fig. 4 in Ref. [142]) in form of broad shoulder at temperatures $13.8 < T < 20$ K.

^{7}Li nuclear magnetic resonance spectra on $x = 0$ have shown a coexistence of a paramagnetic and an antiferromagnetic phases for the temperature range $T = 16 - 13.5$ K [145], suggesting the first-order and distributed nature of the transition. On the other hand, the paramagnetic component of the nuclear spin-lattice relaxation rate ($1/T_1$) shows a critical divergence while approaching 13 K (characteristic for second-order type transitions), where the paramagnetic phase seems to completely vanish as it takes place in a first-order transition. This combination of behaviours points to the vicinity of the $x = 0$ system to a tricritical point [145], where the character of the transition (second or first order) might be changed by a fine adjustment of some of the system parameters, e.g. breathing distortion. For $x = 1$ NMR spectra show a gradual broadening characteristic of a second-order transition. In this case, the spin-lattice relaxation rate shows a thermal activation behaviour for $T > 18$ K with a gap $\Delta = 31$ K, almost half of the value extracted from $\chi(T)$, and a peak marking the transition to an antiferromagnetic phase at $T = 13$ K. This value is lower than $T = 15.9$ K, where a C_p/T anomaly is observed, which suggests that the observed transition is two-stage, with the upper transition being predominantly structural. This is confirmed by a neutron diffraction study [146], first a structural distortion, that lowers the system's symmetry (from cubic $F\bar{4}3m$ to tetragonal $I\bar{4}m2$), takes place at $T_u = 15.9$ K (subscript u stands for upper). This structural distortion does not take place in the whole volume of the sample resulting in a phase separation, with a ratio of the phase fractions $p_t/p_c \approx 2$ (t and c mark tetragonal and cubic phases respectively). This is clearly seen in C_p/T, but less pronounced in $1/T_1$, as NMR performed on polycrystalline samples is less sensitive to structural changes. The second stage involves the onset of complex two-up-two-down magnetic long-range order (2U2D - referring to the directions of magnetic moments on a single tetrahedron) in the tetragonal phase [146], with no onset of long-range order detected in the remaining volume of the cubic phase. Inelastic neutron scattering has shown that the gap observed in susceptibility and NMR measurements is filled with magnetic states, e.g. resulting

Table 4.2: Comparison between features of end-member compounds of $LiGa_{1-x}In_xCr_4O_8$ family [142, 143, 146]. T_u and T_l mark the upper and lower transition temperatures of two-stage processe observed in $x = 0$ and $x = 1$.

$AA'Cr_4O_8$	$LiGaCr_4O_8$	$LiInCr_4O_8$
θ_W (K)	-659	-332
T_u (K)	20	15.9
T_l (K)	13.8	12.9
$J'/J = B_f$ (K)	$30/50 = 0.6$	$6/60 = 0.1$
d'/d (Å)	2.867/2.970	2.903/3.052
Δd (%)	3.5	4.9
Low-T crystal structure	$I\bar{4}m2$+?	$I\bar{4}m2$

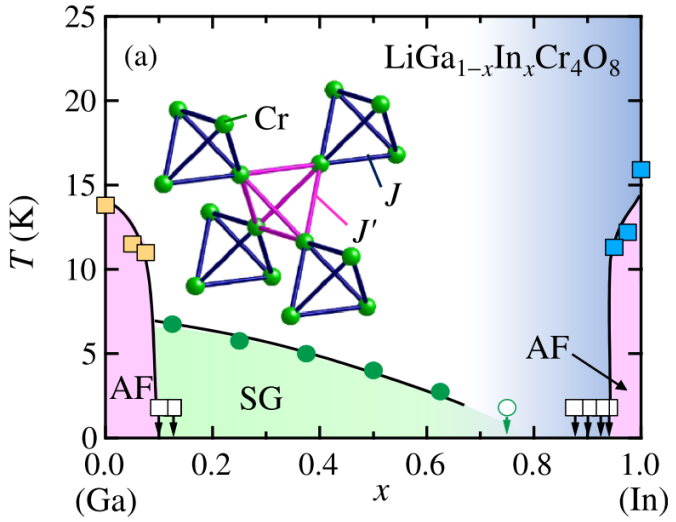

Figure 4.3: Magnetic phase diagram of family of solid solutions $LiGa_{1-x}In_xCr_4O_8$. Figure adapted from Ref. [143].

from defects or disorder, forming a pseudo-gap. Moreover, the pseudo-gap behaviour might be reinforced due to inter-tetrahedral coupling.

Intermediate members of $LiGa_{1-x}In_xCr_4O_8$ family provide an opportunity to investigate the joint effect of geometrical frustration and bond alteration. Their phase diagram was studied with magnetic susceptibility and heat capacity measurements in Ref. [143]. The results of which are presented in Fig. 4.3. It shows the rapid suppression of the Néel state on the departure of stoichiometry from the end-member compositions ($0.1 \leq x \leq 0.94$), and the development of spin glass-like freezing ($0.1 \leq x \leq 0.625$). Spin-gap behaviour is also observed in the magnetic susceptibility for stoichiometries $x \leq 0.625$, suggesting possible spin-liquid regime.

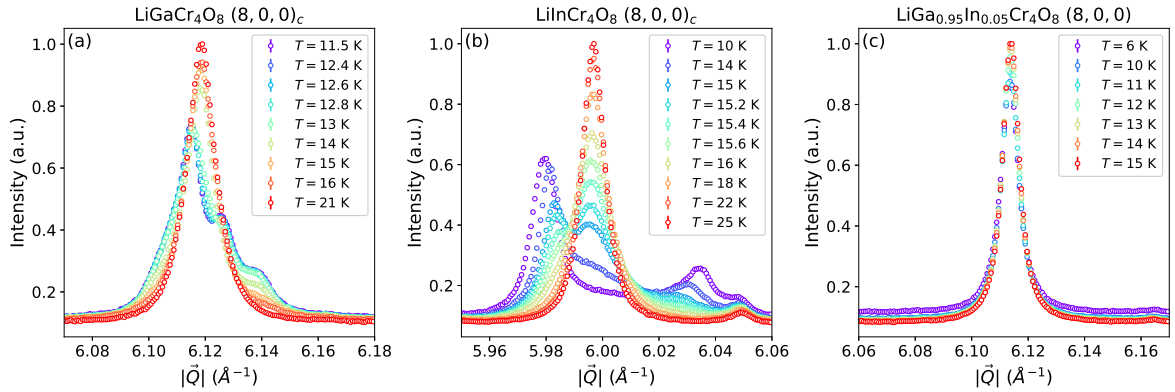

Figure 4.4: Temperature dependence of $(8,0,0)_c$ peak (c stands for high temperature $F\bar{4}3m$ cubic phase) in high resolution x-ray powder diffraction data of the end-member compounds (a) and (b) and $LiGa_{0.95}In_{0.05}Cr_4O_8$ (c). Data measured at MS - X04SA beamline of SLS facility at PSI, with x-ray wavelength $\lambda = 0.565$ Å.

4.3 Low-temperature structure of $LiGaCr_4O_8$ ($x = 0$)

4.3.1 Structural distortions in $LiGaCr_4O_8$

In the work by Saha et al. [147] it was concluded after an analysis of specific heat, magnetization and dielectric constant data from powder samples, that the magnetostructural transition in $x = 0$ resembles the one in $x = 1$ [146], resulting in the mixture of the same structural phases at low temperature, namely cubic $F\bar{4}3m$ and tetragonal $I\bar{4}m2$. The magnetic order in the cubic phase was assigned to follow the $\boldsymbol{k}_c = (0,0,1)$ magnetic propagation vector, while the magnetic structure of tetragonal phase corresponds to $\boldsymbol{k}_t = (1/2,1/2,1/2)$ (with c and t denoting cubic and tetragonal basis respectively). The reported magnetostructural structural distortion occurs at $T = 14.5$ K. Specific heat data presented in this work hints at two stages of the observed transition separated by 0.4 K, but this possibility has not been further explored.

On the other hand, Lee et al. [148] have reported results of multiple resonance techniques, giving strong evidence for the two-stage nature of the observed symmetry breaking, with a cubic-to-tetragonal transition accompanied by second order antiferromagnetic ordering observed in the range $T = 15.2 - 15.8$ K with use of different techniques. The second stage of the process was recognized as the onset of antiferromagnetic order with different magnetic propagation vectors at $T = 12.1 - 12.9$ K.

In order to get deeper insight in the structural distortion, in this work neutron and x-ray diffraction experiments have been performed. In this particular case lowering the unit cell symmetry form cubic to tetragonal, or orthorhombic is most easily noticeable by inspecting the high-$\boldsymbol{Q}$ $(h,0,0)$ reflections of the high-T cubic phase. In chromate spinel breathing pyrochlores, an especially useful for diagnostic reflection purposes is $(8,0,0)$ whose temperature dependence measured with synchrotron x-ray diffraction (SXRPD) for $x = 0$, $x = 1$ and $x = 0.05$ compositions is depicted in Fig. 4.4 (a-c)).

Figure 4.4(a) reflects the development of structural distortions in $x = 0$ upon cooling down. In contrast to data measured on $x = 1$ (Fig. 4.4(b)) the magnitude of the $(8,0,0)$

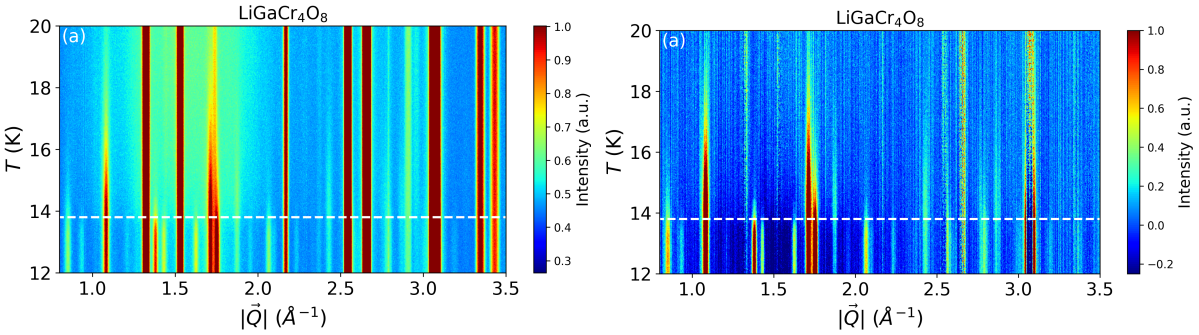

Figure 4.5: (a) Thermodiffractogram of $LiGaCr_4O_8$ measured in the range of temperatures between $T = 20$ and $T = 12$ K at D20 diffractometer with $\lambda = 2.41$ Å. (b) The same data set subtracting the diffraction pattern measured at $T = 22$ K. The white dashed line marks the temperatures of the lower phase transition $T_l = 13.8$ K, where the second tetragonal phase appears. Upper and lower cutoff values were imposed on intensity to demonstrate changes in weak magnetic intensity.

reflection splitting due to the distortion is clearly smaller, and makes it harder to resolve contributions from all of the present phases. It is visible though, that the observed transition consists of two stages. The $(8, 0, 0)$ cubic reflection appearing at $|\boldsymbol{Q}| \approx 6.12$ Å^{-1} is labelled in further discussion as peak A. The first stage takes place over the $T = 16 - 13$ K range featuring a gradual building up of intensities at $|\boldsymbol{Q}| \approx 6.10$ and $|\boldsymbol{Q}| \approx 6.14$ Å^{-1}, labelled later on as peaks B and C respectively. Meanwhile, the main reflection coming from the paramagnetic cubic phase seems to be unchanged, apart from modest change in its intensity. A more abrupt change in the diffractogram takes place in between 13 and 14 K, where the $(8, 0, 0)_c$ reflection (subscript c marks the cubic phase as the source of intensity) vanishes being split into two relatively strong peaks (of much higher intensity that the ones emerging in $T = 16 - 13$ K range) at $|\boldsymbol{Q}| \approx 6.11$ and $|\boldsymbol{Q}| \approx 6.13$ Å^{-1}, labelled later on as peaks D and E. Due to even less distinguishable changes in the remaining parts of the diffraction pattern neither Rietveld nor Le Bail refinement could provide a consistent temperature evolution of phase fractions within the sample.

In order to check this qualitative picture, least-squares fitting was performed around the $(8, 0, 0)_c$ reflection of 53 SXRPD diffractograms measured at different temperatures. The expected sets of reflections were fitted with a Voigt profile. One can distinguish in the data four temperature regimes characterized by presence of different sets of structural phases. The phases presented in those regimes are as follows: only cubic for the first one, cubic and tetragonal-I for the second one, cubic, tetragonal-I and tetragonal-II for the third one, tetragonal-I and tetragonal-II for the last one. Results of fits in these regimes are presented in Fig. 4.6. The position and peak shape parameters of the cubic $(8, 0, 0)_c$ reflection (dashed line in the Fig. 4.6) were retrieved from a single peak fit to the high-T data ($T = 25$ K) and subsequently fixed for the other datasets. The other peak shape parameters were constrained to be the same for reflections coming from the same phase in all datasets. Also, the intensity of the peak E of the tetragonal-II phase (green dashed-dotted line in Fig.. 4.6), visually identified to be present only for $T < 13.8$ K, was fixed

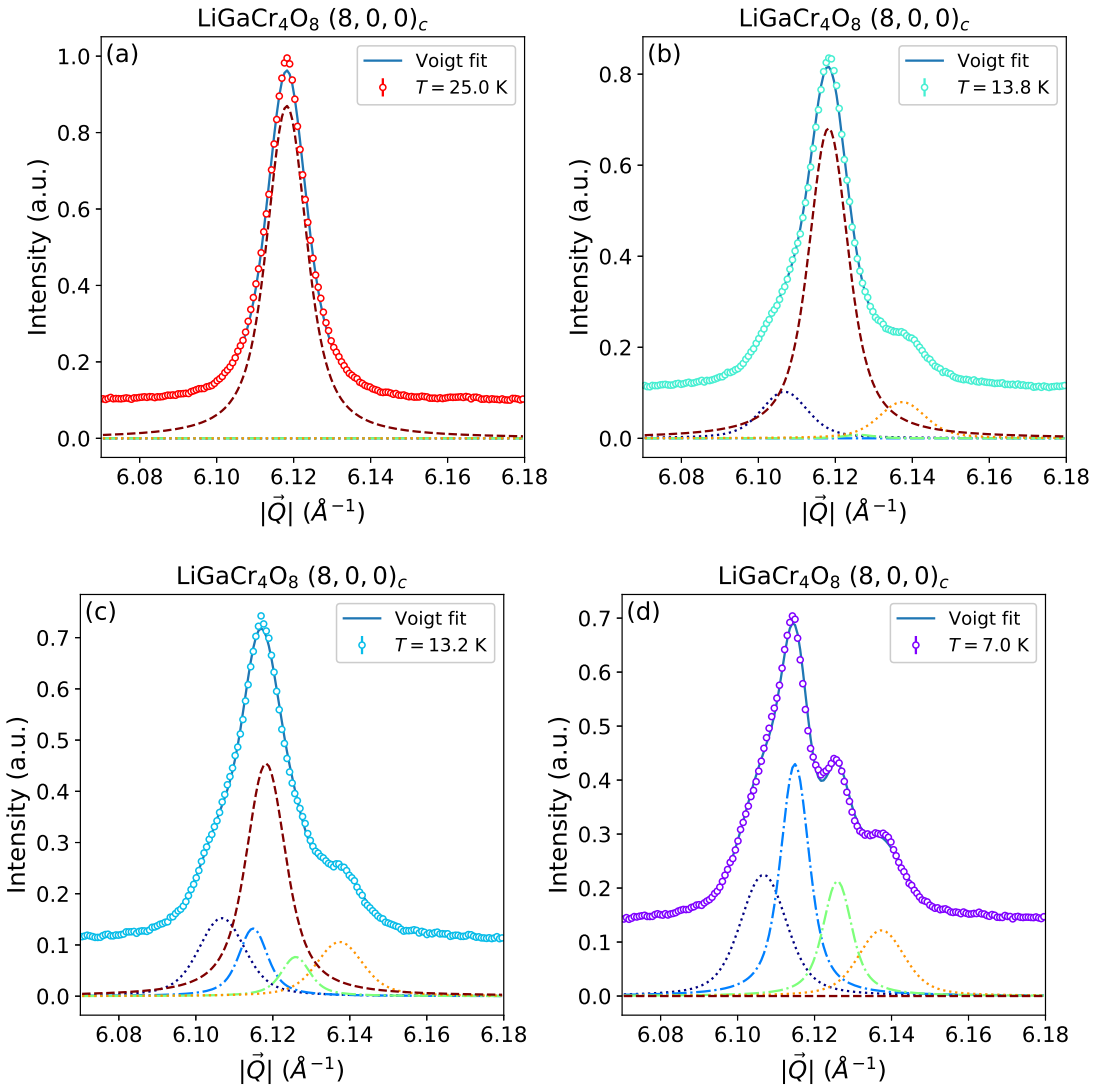

Figure 4.6: Fitted components in split $(8, 0, 0)$ cubic reflection of synchrotron x-ray powder diffraction measured in $LiGaCr_4O_8$. Solid line is the sum of peak components resulting from three different phases namely: high-T cubic, first tetragonal phases I and II plotted below the curve with dashed and dashed-dotted lines respectively. Colors of component curves are consistent between panels. The red dashed curve mark the single peak of high-temperature cubic $F\bar{4}3m$ phase at $|\boldsymbol{Q}| \approx 6.12$ Å^{-1} referred elsewhere as peak A. The purple and the yellow dotted curves mark the two reflections of the tetragonal-I phase at $|\boldsymbol{Q}| \approx 6.10$ and $|\boldsymbol{Q}| \approx 6.14$ Å^{-1}, referred elsewhere as peaks B and C respectively. The green and the blue dashed-dotted curves mark the two reflections of the tetragonal-II phase at $|\boldsymbol{Q}| \approx 6.11$ and $|\boldsymbol{Q}| \approx 6.13$ Å^{-1}, referred elsewhere as peaks D and E.

Table 4.3: Cell parameter estimates of low temperature structural phases in $LiGaCr_4O_8$.Δa_c represents the compression of the structure along a direction of cubic unit cell.

Phase	$a = b$ (Å)	c (Å)	Δa_c (%)
$F\bar{4}3m$ (cubic high-T)	8.216	8.216	-
Tetragonal-I	5.792	8.231	0.30
Tetragonal-II ($T_s = 13.8$ K)	5.802	8.220	0.13

to zero for $T > 14$ K as some finite but very small presence of this peak appeared in fits, in the range $25 < T < 16$ K, as falsely contributing to the, single peak of the cubic phase. The rest of the parameters were allowed to vary freely within the range of physically sensible values (non-negative intensities and peak width parameters). The fitting procedure is very stable and has shown very steep convergence. The temperature dependence of integrated intensities of each component is plotted in Fig. 4.10(a). It matches very well with initial visual observations confirming the two-stage structural distortion. Interestingly the fitted intensities show complete suppression of the cubic phase below $T = 11$ K which is in contrast with observations made previously on $x = 1$ using neutron diffraction [146]. No signs of thermal hysteresis were observed in the results.

Based on the observation of 2 peaks per phase contributing to the low-temperature pattern around $(8, 0, 0)_c$ it is reasonable to assume that both lower symmetry phases are of tetragonal symmetry. Comparison with the $x = 1$ compound and some other chromate spinels ($CdCr_2O_4$, $ZnCr_2O_4$) can provide estimates on variaitons along the c-direction and related (preserving tetragonal symmetry) compression/expansion along a and b, giving the lattice parameters in the low-T phases. The values obtained by analyzing the fitted positions of the low-T components are presented in Tab. 4.3, an assumption of exactly the same transformation between the cubic and tetragonal cell as found in one of the models proposed for $CdCr_2O_4$ [149, 131] was assumed ($c_t \parallel c_c$ and $a_t \parallel [110]_c$, where subscripts c and t refer to cubic and tetragonal phases). The first tetragonal phase is characterized by a 0.2% expansion along the cubic c which is close to the value observed in $CdCr_2O_4$ (0.3%), but much smaller than the on in $x = 1$ (0.6% contraction).

This scenario of structural distortion in the low-temperature crystal structures shows strong similarities to results of x-ray diffraction studies on $MgCr_2O_4$ and $ZnCr_2O_4$ presented in Ref. [132]. In this picture, the high-temperature cubic $Fd\bar{3}m$ phase is replaced by a mixture of $I4_1/amd$ tetragonal and $Fddd$ orthorhombic phases. In contrast to the observations described in the previous paragraph, in Ref. [132], it is proposed that the structural distortion does not show a distribution over finite temperature range, and results in complete disappearance of the high-temperature phase. The former can be excluded based on data presented in this work, but the latter aspect is unclear from observations made on high-resolution SXRPD studies of $x = 0$ compound (Fig. 4.4(a)).

It should at this point be mentioned that the results based on measurements on powder samples from Ref. [132], are not confirmed by other studies on single-crystal samples [131, 133], which proves that providing an unambiguous description of the low-temperature structure in these compounds might be very challenging even with the availability of single-crystal samples and employing state of the art instruments. The discrepancies between powder and single-crystal results are attributed to nonstoichiometries,

inhomogenities, defects and disorder varying between different samples [150, 133].

Similarly to the mentioned cases, the complexity of structural distortions in the $x = 0$ sample does not allow unambiguous identification of the structures involved. Namely the Rietveld analysis on powder diffraction data does not allow to single out any of few qualitatively and quantitatively differing models, it is due to the subtle differences between results calculated with their use. These difficulties are enhanced by microstructural properties like anisotropic strain present in the cubic phase upon cooling down towards the transition temperature. The broadening makes the overlap between reflections coming from different phases and placed very close to each even bigger. Single crystal studies might provide enough information to solve this otherwise under-constrained problem.

4.3.2 Magnetic ordering in $LiGaCr_4O_8$

Observations of the structural aspect involved in both of the stages of symmetry breaking in $x = 0$ are consistent with the evolution of magnetic scattering in neutron powder diffraction patterns on cooling down (Fig 4.5(a) and Fig. 4.5(b)). This data can be easily divided into two regimes below and above $T = 13.8$ K by investigating two groups of magnetic Bragg reflections showing different temperature dependence. The first signs of magnetic reflections appear already at $T = 17 - 18$ K as shown in Fig. 4.7, which shows the differences between NPD patterns measured below $T = 18$ K and $T = 22$ K. Five such reflections were identified and they continuously develop their intensity down to $T = 14$ K, so they are not yet saturated upon the appearance of the second group of reflections marking the entering into the second regime. The positions of these reflections are marked in Figs. 4.7 and 4.8 with black dotted lines and with red stars in Fig. 4.9.

Figure 4.9 shows the positions of satellite peaks produced by the magnetic propagation wavevectors most frequently identified in other chromate spinels. It is easily recognizable that reflections associated with the first magnetic phase can be assigned to $\mathbf{k} = (0, 0, 1)$, also found to play a role in $x = 1$ [146].

The second group of reflections appear at $T = 14$ K and their intensity is already fully saturated at $T \approx 13$ K. This is reminiscent of the intensity of D and E components of the split $(8, 0, 0)_c$ reflection (Fig. 4.6), marking the appearance of the tetragonal-II phase. It is connected with the disappearance of a substantial amount of spectral weight from the diffuse scattering distributed between $|\boldsymbol{Q}| = 1.2{-}2$ Å^{-1} (Fig. 4.5), suggesting the ordering of a much larger population of magnetic moments, than in the first transition, which is consistent with the large entropy release observed in specific heat measurements [142, 147]. Seven reflections following the same temperature dependence can be recognized. There reflections do not match a single propagation vector, nor a combination of known propagation vectors for the chromate spinels. This strongly suggests a new type of multi-$\boldsymbol{k}$ phase of the second low-T magnetic structure. The existence of multi-$\boldsymbol{k}$ structures and magnetostructural orders is consistent with the presence of strong frustration within the system and resulting near-degeneracy of those phases. After analyzing the positions of reflections associated with the second low-T magnetic phase one can find that they correspond to positions generated by $\boldsymbol{k}_1 = (1/2, 1/2, 0)$ and $\boldsymbol{k}_2 = (1, 0, 1/2)$ in cubic basis (blue markers in Fig. 4.9). Although those two propagation vectors cannot account for all of the observed magnetic reflections, the remaining positions do not match any of the magnetic propagation vectors found in other chromate spinels and cannot be indexed

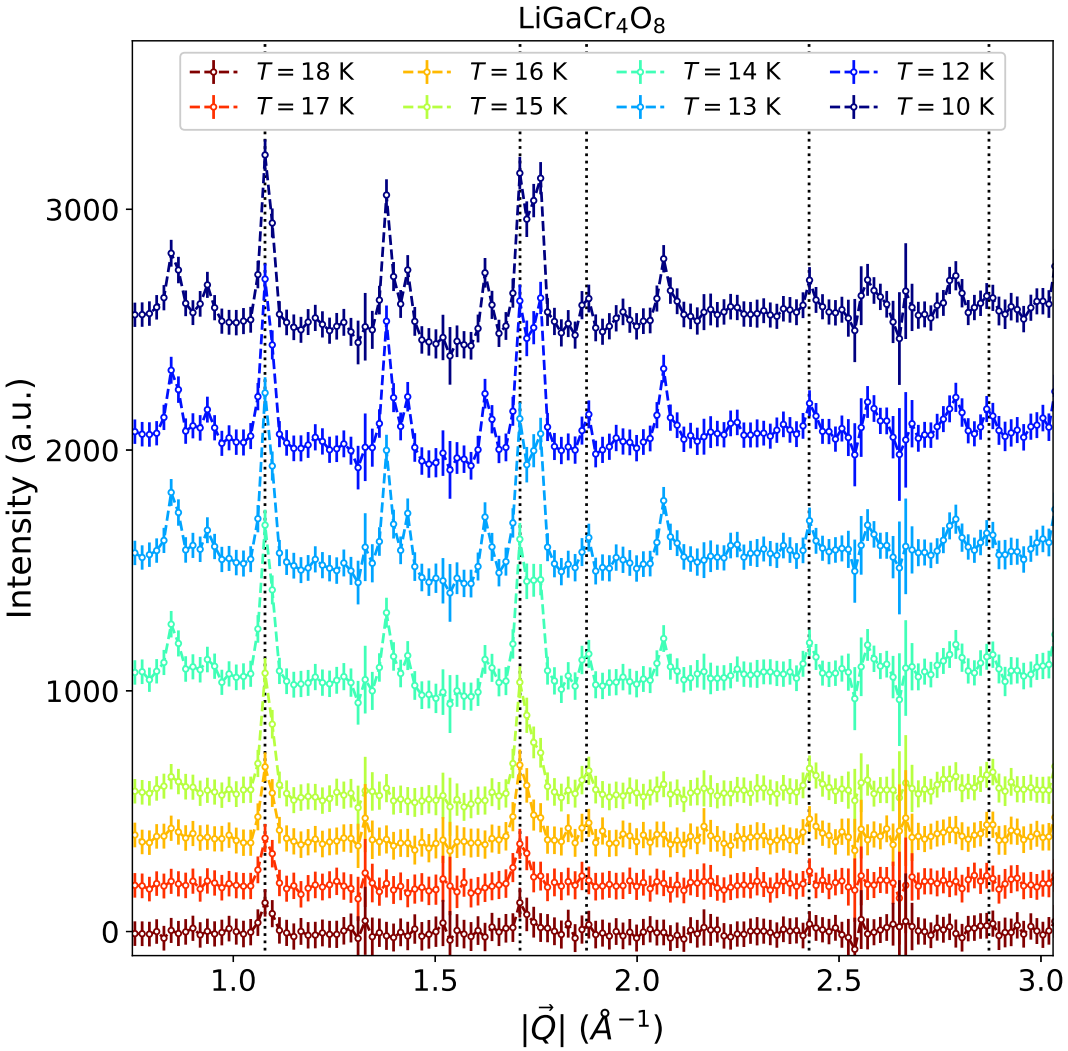

Figure 4.7: The difference between diffraction patterns measured in LiGaCr$_4$O$_8$ at several temperatures between $T = 18 - 10$ K and the pattern measured at $T = 22$ K. The black dotted lines mark the magnetic peaks associated with first stage of the magnetostructural transition. An offset was added to every data set to increase readability. The data measured at the D20 diffractometer with $\lambda = 2.41$ Å.

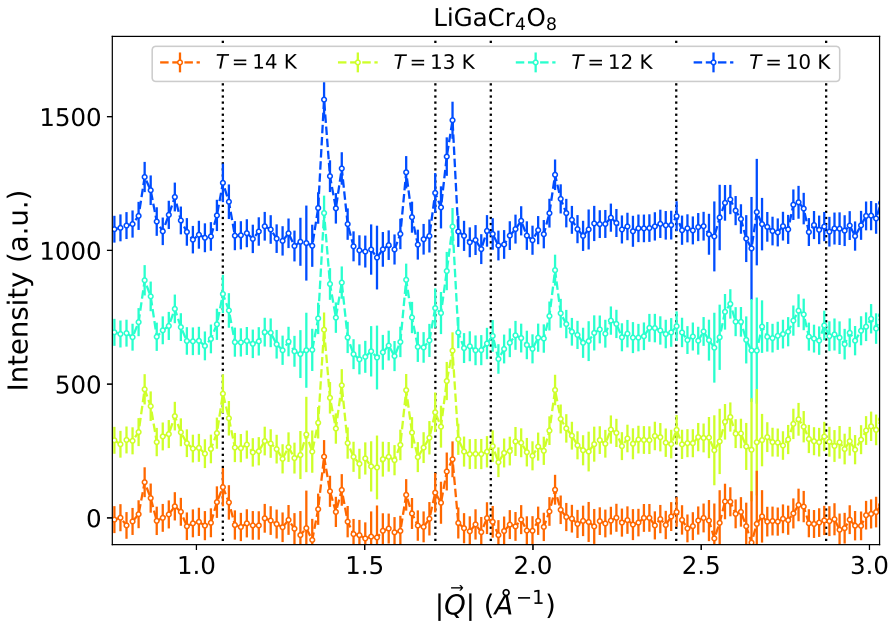

Figure 4.8: The difference between diffraction patterns measured in $LiGaCr_4O_8$ at few temperatures from range $T = 14-10$ K and the pattern measured at $T = 15$ K. The black dotted lines mark the magnetic peaks associated with first stage of the magnetostructural transition. An offset was added to every data set to increase readability. Data measured at the D20 diffractometer with $\lambda = 2.41$ Å.

consistently with any commensurate propagation vector in cubic basis.

In order to investigate the temperature dependence of the magnetically-ordered phases in $LiGaCr_4O_8$, a small fragment of the diffractograms covering a few chosen reflections (Fig. 4.9) were extracted, and intensities of those reflections retrieved. Due to their small relative strength and noisy peak profile a numerical integration on flat background-subtracted data was performed instead of peak fitting as was done for structural peaks in the x-ray data (Fig. 4.10(a)). The integrated intensities plotted in Fig. 4.10(b) and 4.10(c) clearly show that magnetic peaks associated with different stages of symmetry breaking follow distinct temperature dependences. The first one takes place over the temperature range $18 - 12.5$ K The second one behaves as an antiferromagnetic transition with $T_N \sim 13.8$ K, producing a sharp anomaly in specific heat data. These characteristics show excellent agreement with the similar evolution of the components B and C after splitting of the structural $(8, 0, 0)_c$ reflection. This provides a strong argument in favour of both stages of transition being of magnetostructural character, but having rather different thermodynamical character, showing signs of thermal crossover and first-order transition respectively. It should be also noted here that both magnetic and structural reflections following either of the temperature dependences reaches the full saturation at common $T \approx 12.5$ K.

In order to find the ordered magnetic structure of the higher-T tetragonal phase, an assumption of the same structure in this phase as the one as in $x = 1$ [146] and for $x = 0$ in Ref. [147], namely tetragonal $I\bar{4}m2$ was made. Representational analysis was used to determine the structure (Sec. 2.3.4). The $\boldsymbol{k} = (0, 0, 1)$ is the same vector in both

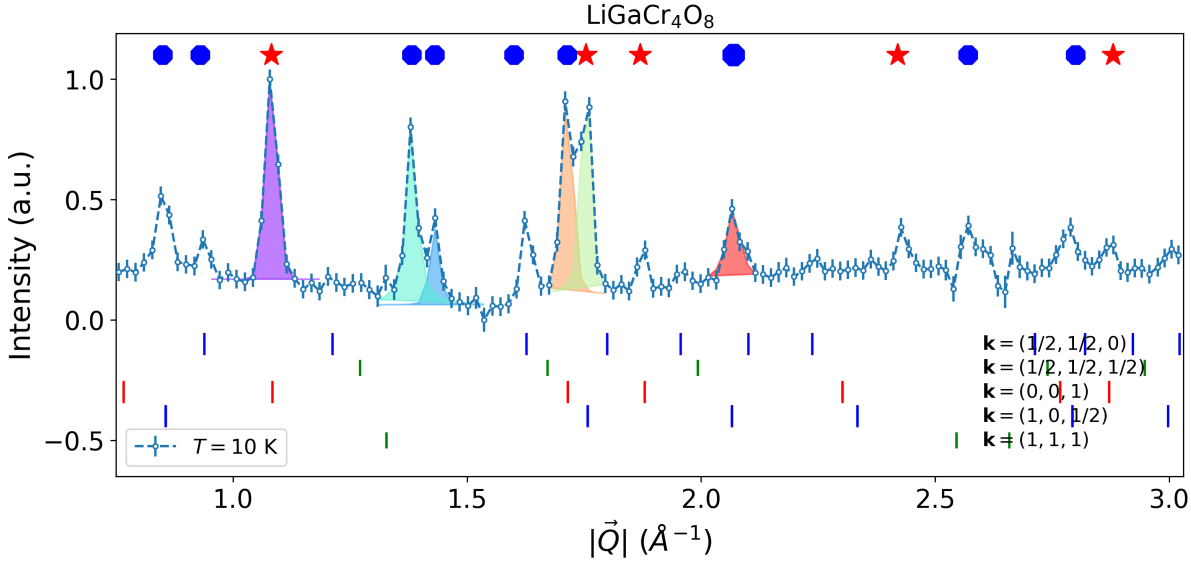

Figure 4.9: Magnetic peaks in the difference between diffraction patterns measured in $LiGaCr_4O_8$ at $T = 10$ and $T = 22$ K. Reflections connected with different magnetic phases are marked by red stars (higher temperature phase) and blue octagons (lower temperature phase. Shaded areas below the peaks mark the features whose integrated intensity is presented in Fig. 4.10(a) and 4.10(b) (colours of shading and data plots correspond each other). Red green and blue bars are showing calculated positions for magnetic propagation vectors found in other chromate spinels.

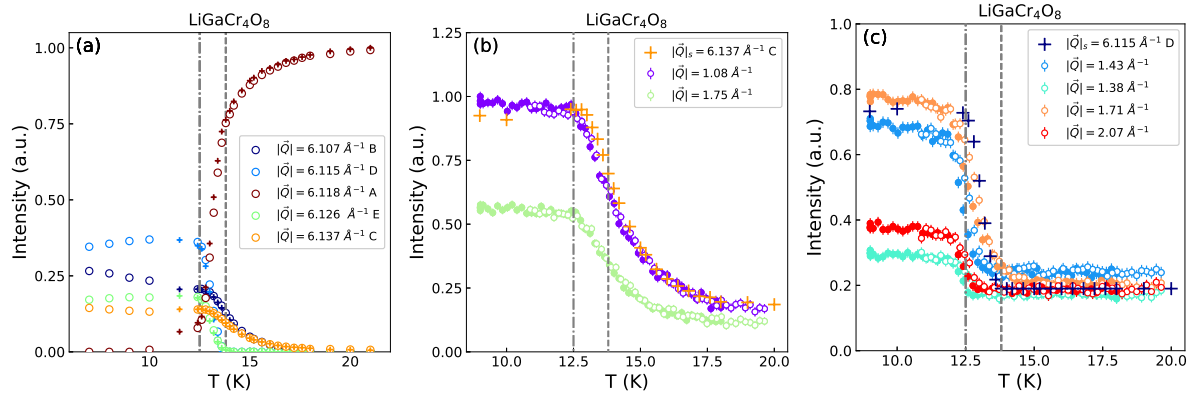

Figure 4.10: Integrated intensities of (a) components derived from the $(8, 0, 0)_c$ structural reflection (Fig. 4.6) by the fitting procedure described in the text, and selected magnetic reflections in measured in $LiGaCr_4O_8$. Panels (b) and (c) show the temperature dependences of the two families of magnetic reflections. The empty and filled symbols represent heating and cooling processes respectively. The crosses in (b) and (c) are selected curves from a (colors correspond between these panels) scaled and with added offset in order to show similarities in temperature dependence. The grey dashed line marks the peak of sharp anomaly observed in specific heat at $T = 13.8$ K [142]. The grey dashed-dotted line marks the common temperature of full saturation observed for all reflections $T = 12.5$.

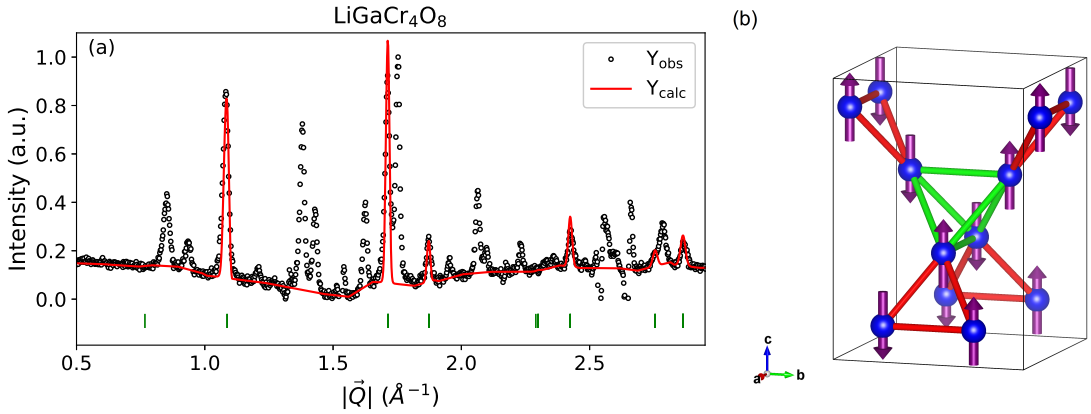

Figure 4.11: (a) Rietveld refinement of magnetic diffraction data separated by subtraction of $T = 25$ K data set from $T = 2$ K data. The refined model used basis vectors of mM_5 irreducible representation (Miller-Love notation [151])) of the $I\bar{4}m2$ space group. (b) refined higher-T ordered structure in $LiGaCr_4O_8$ described by C_A222_1 magnetic space group.

cubic and tetragonal basis. This $\boldsymbol{k}$-vector is is equivalent to special vector $\boldsymbol{M} = (1, 1, 1)$ resulting with five mM_i $i = 1-5$ (Miller-Love notation [151]) irreducible representations, which were tested. The basis vectors for all of these were generated with `BASIREPS` software, part of the `FULLPROF` suite [106]. mM_i, $i = 1-4$ are one dimensional and mM_5 is two-dimensional. An excellent agreement between Rietveld refinement and data (Sec. 3.1.1) was found for mM_5 (Fig. 4.11(a)). The resulting magnetic structure is a linear combination of 6 basis vectors generated in mM_5. Four of these contribute to components along the tetragonal a and b directions (in cubic coordinates $\langle 110 \rangle$-type directions) had their scales fixed to 0 as they otherwise led to appearance of $(0, 0, 1)$ magnetic reflection ($|\boldsymbol{Q}| = 0.76$ Å^{-1}) completely absent in the diffraction data. The two remaining vectors which contribute exclusively to the c-component were refined separately (with the other set to 0, as their strong co-dependence led to divergence of the refinement) acquiring the same value of the scaling parameter. Those two results correspond to the same structure with magnetic moments following the behaviour of axial vectors reflected by a (100) plane. The structure of the final solution is described by the C_A222_1 space group. It is worth noting that the direction of ferromagnetic bonds, expected to elongate due to spin Jahn-Teller effect producing the structural distortion, is consistent with the expansion of the cubic unit cell along the c-axis, as all of them are lying along $[101]_c$ or $[011]_c$ cubic directions, doubling the contribution to the distortion along the c-direction in comparison with a and b.

4.4 Ground-state of $LiGa_{0.95}In_{0.05}Cr_4O_8$ ($x = 0.05$)

Substantial part of results presented in the following section was published in Ref. [152].

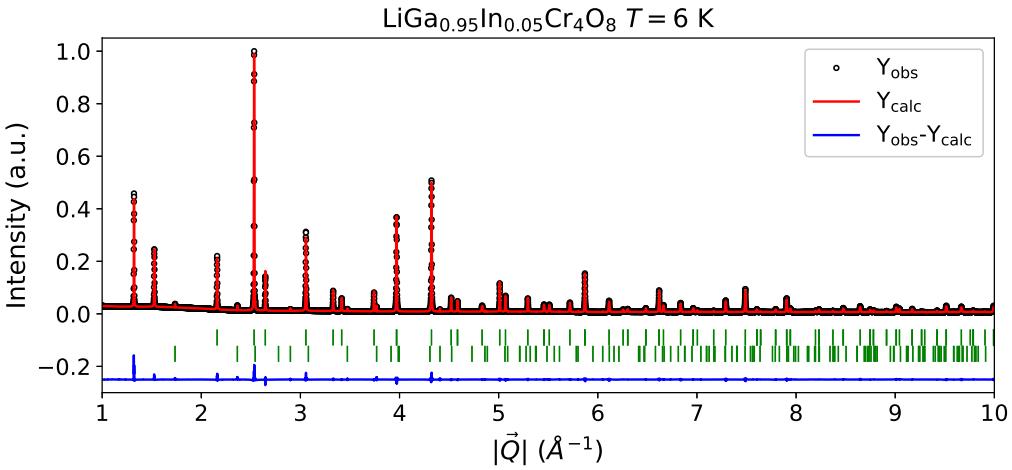

Figure 4.12: Rietveld refinement of x-ray powder diffraction pattern of $LiGa_{0.95}In_{0.05}Cr_4O_8$ measured at $T = 6$ K. Green markers show the expected positions of Bragg reflections. The second row of markers accounts for a small amount of Cr_2O_3 impurity. Data measured at the MS - X04SA beamline of SLS - PSI facility with x-ray wavelength $\lambda = 0.565$ Å.

4.4.1 Structural distortions in $LiGa_{0.95}In_{0.05}Cr_4O_8$

The phase diagram of the $LiGa_{1-x}In_xCr_4O_8$ family presented in Ref. [143] (Fig. 4.3) suggests that the presence of even a small amount of bond disorder should suppress the structural phase transition and the onset of the Néel state. From experiments [143] it is expected to take place, at the Ga-rich side of the phase diagram, for x below 0.075, with decreasing ordering temperature on departure from $x = 0$. Fig. 4.4(c) depicts the $(8, 0, 0)_c$ reflection of $x = 0.05$ in high resolution SXRPD data. It is striking that without any doubts, no signs of structural distortion might be observed upon cooling down to 6 K, while the heat capacity shows a λ-like anomaly centered at $T = 11.2$ K, suggesting the existence of a phase transition. The linewidth of ^{7}Li NMR spectra measured on $x = 0.05$ gradually broadens upon cooling, strongly resembling the behaviour observed for $x = 1$ rather than $x = 0$, despite the stoichiometric proximity. The nuclear spin-lattice relaxation rate exhibit a sharp peak at $T = 11.1$ K, which is in agreement with the apparent observation of a second-order phase transition in heat capacity.

In order to resolve the nature of the observed transition, showing signs of purely magnetic nature in thermodynamical and NMR measurements, a detailed analysis of the temperature dependence of x-ray diffraction data and time-of-flight neutron powder diffraction (NPD) experiments were performed. Fig. 4.12 shows the Rietveld refinement of SXRPD data measured at $T = 6$ K. The whole pattern can be very well accounted for with a refinement based on the exclusive presence of the high-T cubic phase ($F\bar{4}3m$). The same observation was made on NPD data. The low-$\boldsymbol{Q}$ region of the diffractogram measured in the low-angle detector bank of the WISH time-of-flight diffractometer is presented in Fig. 4.13. Apart from the already mentioned lack of any structural symmetry lowering it does not show any signs of the onset of magnetic long-range order down to $T = 1.5$ K, in contrary to the expectations from the previously established phase diagram (Ref. [143] and Fig. 4.3). The structural parameters obtained from the simultaneous refinement of

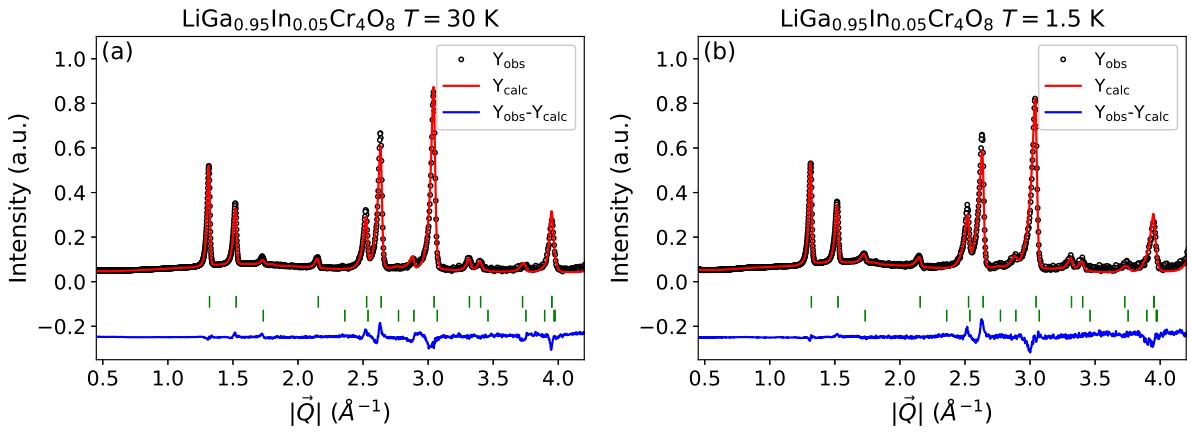

Figure 4.13: Rietveld refinement of the low-$\boldsymbol{Q}$ range of neutron powder diffraction data measured in $LiGa_{0.95}In_{0.05}Cr_4O_8$ at (a) $T = 30$ K and (b) $T = 1.5$ K. Green markers show the expected positions of nuclear Bragg reflections. The second row of markers accounts for a small amount of Cr_2O_3 impurity. Data measured at low-angle detector banks ($2\theta = 27°$) of the WISH time-of-flight diffractometer at the ISIS neutron source.

Table 4.4: Structural parameters obtained by corefinement of synchrotron x-ray powder diffraction data measured in $LiGa_{0.95}In_{0.05}Cr_4O_8$ at $T = 6$ K ($\chi^2_{\text{global}} = 103$,). Values of isotropic thermal displacements (B_{iso}) are provided by analysis of neutron powder diffraction data (Fig. 4.13).

Atom	Wyckoff position	x	y	z	Occupancy	B_{iso} (Å^2)
Li1	4*a*	0	0	0	0.994(2)	2.2(2)
Ga1	4*d*	0.75	0.75	0.75	0.932(6)	0.41(6)
Ga2	4*a*	0	0	0	0.006(4)	0.41(6)
Li2	4*d*	0.75	0.75	0.75	0.002(4)	2.2(2)
In	4*d*	0.75	0.75	0.75	0.066(6)	0.41(6)
Cr	16*e*	0.37185(4)	0.37185(4)	0.37185(4)	4	0.38(4)
O1	16*e*	0.1370(1)	0.1370(1)	0.1370(1)	4	0.51(2)
O2	16*e*	0.6180(2)	0.6180(2)	0.6180(2)	4	0.51(2)

neutron and x-ray data at $T = 6$ K are presented in Tab. 4.4. The refinement of the site occupancy suggests a stoichiometry $x = 0.066(6)$ in the investigated sample.

The only two effects detected in the diffraction data upon cooling through the temperature at which the heat capacity and spin-lattice relaxation time anomalies were observed are a saturation or a step-like change in some structural parameters of the Rietveld refinements (Fig. 4.14) and a subtle change in the form of the magnetic structure factor of the diffuse magnetic scattering in neutron diffraction data (Fig. 4.15). As the peak profile of the WISH diffractometer requires complex multi-parameter function [103] and the high-$\boldsymbol{Q}$ region of data suffers strongly from peak overlap, strain parameters (S_{hkl}) influencing the width of recorded peaks were extracted from the SXRPD data, given the better angular resolution of x-ray measurements. B_{iso} and the fractional x coordinate of chromium were derived from NPD data providing much more stable refinement, as expected.

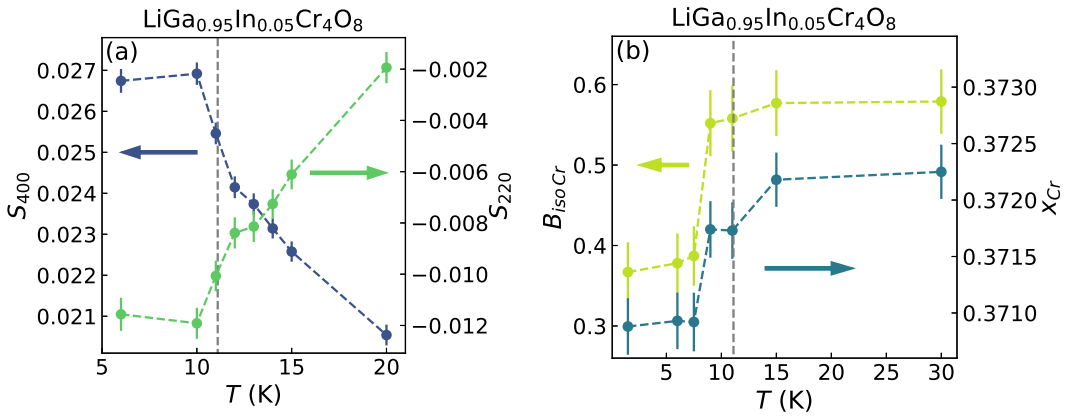

Figure 4.14: Temperature dependence of (a) strain parameters in $LiGa_{0.95}In_{0.05}Cr_4O_8$ retrieved from Rietveld refinements of high resolution x-ray diffraction data and (b) isotropic thermal displacement parameter and the fractional coordinates of chromium ions in the unit cell, retrieved from Rietveld refinements of time-of-flight neutron powder diffraction data. Coloured dashed lines are guides for the eye. The grey dashed line marks the transition temperature.

The FULLPROF software allows for refinement of line broadening due to anisotropic microstrain (the broadening is not a smooth function of d-spacing), by means of a model presented in Ref. [153]. It uses S_{HKL} parameters ($H + K + L = 4$) which are related to the variance of the inter-planar distances d_{hkl}:

$$\sigma^2(1/d^2) = \sum_{HKL} S_{HKL} h^H k^K l^L. \tag{4.2}$$

Generally one has to consider 15 S_{HKL} parameters, but symmetry reduces this number to 2 in the case of cubic structures, only S_{400} and S_{220} are required, which describe the variance for $[h, 0, 0]$ and $[h, k, 0]$ types of planes respectively. A continuous increase in the absolute values of these parameters (Fig. 4.14(a)) in the diffraction data measured upon cooling towards the transition temperature shows the building-up of local tetragonal distortions, consistent with the anticipated effect of biquadratic coupling and hence the magnetoelastic phenomomena in a pyrochlore antiferromagnet (Eq. 4.1) [87]. In addition, the step-like changes of the isotropic thermal displacement (B_{iso}) of the magnetic chromium ions and their position in the unit cell, might be a signal of the magnetic character of the observed transition, with a significant role played by the spin-lattice coupling in $LiGa_{0.95}In_{0.05}Cr_4O_8$, as expected.

The second change upon cooling down is the change in the structure factor of the low-$\boldsymbol{Q}$ diffuse scattering measured in NPD (Fig. 4.15). At high temperature this is concentrated in broad feature centered around $|\boldsymbol{Q}| = 1.55$ Å^{-1}, as expected for the undistorted pyrochlore lattice with Coulomb-like power-law decay of correlations between magnetic moments [154]. The two most striking details in the evolution of the diffuse intensity are the sharp anomaly at $|\boldsymbol{Q}| \sim 1.1$ Å^{-1}, fully developed at $T = 15$ K (Fig. 4.16(a)) and a broad bump around $|\boldsymbol{Q}| = 0.85$ Å^{-1} most pronounced at $T \leq 11$ K. The former can be identified as a magnetic reflection coming from an impurity of the $x = 0$ precursor phase, which can be identified in thermodiffractograms presented in Fig. 4.5(a) and Fig. 4.5(b).

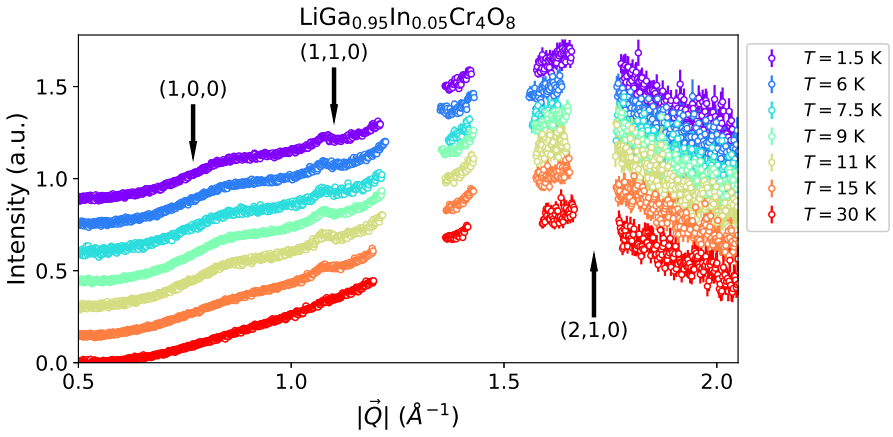

Figure 4.15: Temperature dependence of the low-$\boldsymbol{Q}$ magnetic diffuse scattering from $LiGa_{0.95}In_{0.05}Cr_4O_8$ measured by neutron powder diffraction on the WISH time-of-flight neutron powder diffractometer at the ISIS neutron source. Three narrow $\boldsymbol{Q}$-ranges covering the area with nuclear Bragg reflections, were removed. An offset was added to every data set for better viewing. Arrows mark the positions corresponding to the scattering wavevectors given in the labels. The intensity was normalized to $I(0.5) = 0$, as previous polarized neutron experiments on other members of the family have shown consistently that the magnetic scattering vanishes at this wavevector(See Fig. 3 in Ref. [143]).

The presence of this impurity might be expected taking into account the minute In doping ($x = 0.05$), which could lead to inhomogeneities in the sample's local composition. The latter feature, as its appearance coincides with the observation of a phase transition in C_p/T and NMR deserves a closer look.

4.4.2 Reverse Monte Carlo analysis of diffuse paramagnetic scattering in neutron diffraction data of $LiGa_{0.95}In_{0.05}Cr_4O_8$ ($x = 0.05$)

The lack of magnetic Bragg reflections in the neutron diffraction data excludes the possibility of dipolar long-range order being the ground-state of $LiGa_{0.95}In_{0.05}Cr_4O_8$. On the other hand detected anomalies in heat capacity and spin-lattice relaxation time, and the changes in the diffuse magnetic neutron scattering strongly suggest a change in magnetic correlations within the system on crossing the transition. To determine the nature of the change the reverse Monte Carlo (RMC) refinement technique [155] might be employed. Using the Metropolis algorithm [156], it refines the orientations of magnetic moments, localized at the crystallographic positions of magnetic ions, within the simulation box. The starting point of every separate box is a unique random configuration. The main difference between conventional Monte Carlo simulations and RMC is the minimized function. In the first case, the algorithm minimizes the energy calculated with the provided magnetic interactions present within the system. In RMC, one minimizes the sum of squared residuals [155]:

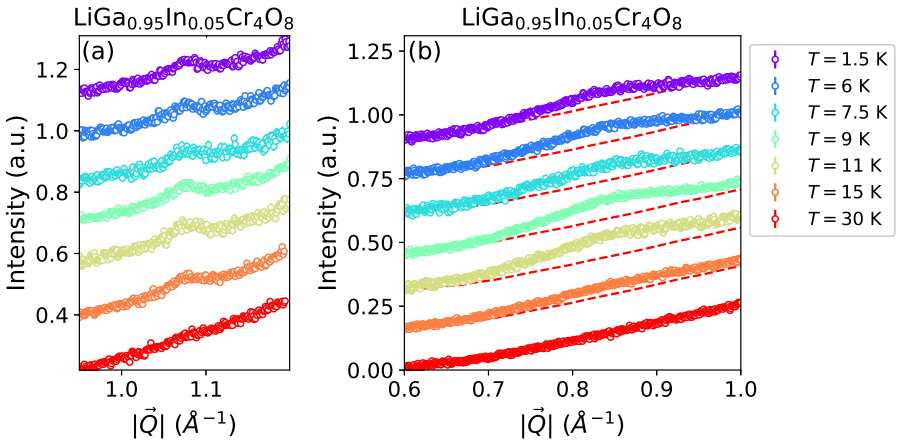

Figure 4.16: Detailed view of features in diffuse scattering presented in Fig. 4.15. Red dashed lines are $T = 30$ K data set put at the appropriate offset in order to depict the difference.

$$\chi^2 = W \sum_Q \left[\frac{I_{\text{calc}}(Q) - I_{\text{exp}}(Q)}{\sigma(Q)} \right]^2, \tag{4.3}$$

between paramagnetic diffuse neutron scattering intensities calculated for the simulation box ($I_{\text{calc}}(Q)$) and the measured data ($I_{\text{exp}}(Q)$). The goodness of fit is weighted with the experimental uncertainty ($\sigma(Q)$). W is an empirical weight parameter corresponding to the inverse of the temperature in conventional Monte Carlo simulations, and allows for acceptance of "bad" moves, thus increasing the χ^2 in order to avoid false minima.

Therefore RMC allows for the determination of the correlations between the magnetic moments in the correlated paramagnet phase, rather than giving an insight into the magnetic interactions between the ions. In contrast to Rietveld refinement of magnetic structures, it also allows for the characterization of so-called "hidden orders" characterized by order parameters beyond dipolar order, which are not directly detectable in the neutron scattering experiment (magnetic neutron scattering takes place via dipole-dipole interaction, see Eq. 3.8). However, these orders might indirectly manifest themselves in the analysis of simulation boxes [157].

All of the refinements whose results are presented in the following part of this section were performed with the `SPINVERT` software [155]. Unless stated otherwise, the simulation box consisted of $6 \times 6 \times 6$ unit cells of the breathing pyrochlore lattice, containing 3456 magnetic ions, with the RMC refinement involving 900 moves per moment inside the simulation box. Refinements were performed on 10 simulation boxes at the same time giving 10 final spin configurations. `SPINVERT` enables the refinement of the moments with three types of anisotropy: spherically isotropic, moments with planar anisotropy (confined within arbitrary plane) and moments with axial anisotropy. The direction of the anisotropy (if present) has to be defined for every site within the unit cell. With $W = 1$ ($W = 0.6$) for isotropic (axially anisotropic) moments, the best reproduction of observed scattering intensity was achieved.

Figure 4.17 shows the results of RMC refinements of diffuse scattering shown in Fig. 4.15. In this procedure isotropic magnetic moments were assumed. Fairly good

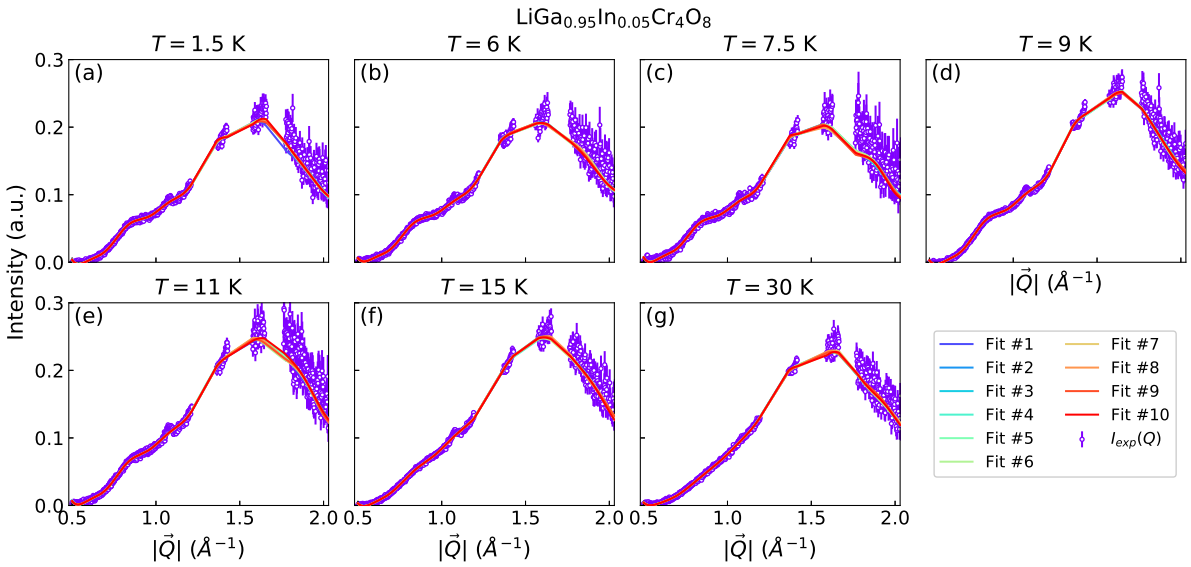

Figure 4.17: Reverse Monte Carlo refinements of diffuse neutron scattering from $LiGa_{0.95}In_{0.05}Cr_4O_8$ (Fig. 4.15). Refinements use the magnetic structure consisting of isotropic magnetic moments. The different fits correspond to the different simulation boxes refined separately.

agreement was achieved between results from all the simulation boxes and the experimental data. The refinements starting from different random configurations arrive at virtually identical final result. For all of the refinements, convergence was reached after around 100 out of 900 reorientations of the moments inside the box. The dependence of the final χ^2 on the temperature at which the data set was recorded is presented in Fig. 4.19(a). The goodness of fit smoothly becomes slightly worse upon cooling down towards the transition. Just below its temperature it looses this trend and again shows better agreement for the lowest recorded temperatures.

The temperature dependence of the radial spin correlations averaged over all simulation boxes is presented in Fig. 4.19(b). No significant change between any of the temperatures are observed, most importantly no discrepancy is observed between the correlations retrieved from data measured above and below the temperature of the thermodynamical anomaly. This observation stands in contradiction with the clearly visible rearrangement of diffuse intensity upon cooling down and might imply that either the assumption of isotropic magnetic makes the refinement under-constrained, or the relative change in the structure factor is too subtle.

Based on the observations of collinear ordered magnetic structures in the end-member compounds [146, 147], a refinement of magnetic moments with axial anisotropy was attempted. The main crystallographic directions: [001], [011] and [111] were tested as the easy axis. Refinements at the base temperature $T = 1.5$ K data show a very similar final goodness of fit for all of the directions of anisotropy axis, with slightly better value obtained with $\langle 011 \rangle$-type moments (see Tab. 4.5). In order to check if the similar χ^2 results from the equal relevance of the refined magnetic configurations a simple energetical argument was applied. A pyrochlore lattice populated with antiferromagnetically cou-

Table 4.5: Goodness of fit χ^2 and the population of different tetrahedra configuration in spin structures obtained with RMC refinements of $T = 1.5$ K data for different directions of axial anisotropy of magnetic moments. 3U1D and 4U0D configurations include the opposite cases (i.e. 1U3D and 0U4D).

Direction of anisotropy axis	[001]	[011]	[111]
χ^2	1316	1216	1361
2U2D	15095	9908	13653
3U1D	2178	7284	3608
4U0D	7	88	19

pled moments possessing the collinear axial anisotropy has well-defined local constraints, namely the two-up-two-down (2U2D) configurations (ice rules) [61] as they minimize the nearest neighbour exchanges.

The populations of different tetrahedral configurations in the spin structures of 10 refined simulation boxes for all three easy axis directions are given in Tab. 4.5. The comparison shows a much greater number of defect tetrahedra (not obeying the ice rules) in the case of [011] and [111] anisotropy axes, drastically increasing the energy, based on assumption of nearest neighbour exchange only, associated with refined magnetic configurations. The remaining $\langle 001 \rangle$-type anisotropy would furthermore be consistent with observations made on $x = 0$ and $x = 1$ [146, 147], where the same direction was found for one of magnetically ordered phases.

RMC refinements of the same datasets as presented in Fig. 4.18, but now using axially anisotropic magnetic moments, parallel to the [001] direction, are presented in Fig. 4.18. Low-temperature refinements reproduced the data similarly well (Fig. 4.18(a) and Fig. 4.18(b)) as in case of isotropic magnetic moments, which is reflected in χ^2 (Fig. 4.19(a)). The situation changes as temperatures get closer to the transition and passes above it (Figures 4.18(c)-4.18(g)) where the high-$\boldsymbol{Q}$ part of the diffuse scattering cannot be refined properly assuming anisotropic magnetic moments. It is reflected in final χ^2 of the refinements for different temperatures (Fig. 4.19(a). For datasets measured at $T < 9$ K, refining both isotropic and anisotropic magnetic moments gives very similar values. At $T > 7.5$ K, applying the rather strong constraint of axial anisotropy results in much worse agreement between data and the refinement. An abrupt improvement of the goodness of fit parameter is observed already at $T = 9$ K, just below the transition. Although the refinement quality worsen drastically for $T = 7.5$ K dataset and improves significantly below this point. Similar changes are observed in refinements of isotropic moments, but their abrupt character in the anisotropic case might point to appearance of some kind of artifact of the RMC method. However, this does not affect datasets measured at $T < 7.5$ K whose refinements consistently show a very good agreement.

The radial spin correlations, similarly to the refinements of the isotropic moments, do not show any significant changes upon cooling down (Fig. 4.19(c)), emphasizing the lack of a dipolar order parameter in the resulting spin structures.

The comparison between goodness of fit parameters for the two types of moments shows the following: (i) the simulation boxes consisting of isotropic moments reproduce the diffuse data at all temperatures, (ii) applying strong constraint of axial anisotropy substantially reduce the quality of fit for high-T data sets, but barely influences the

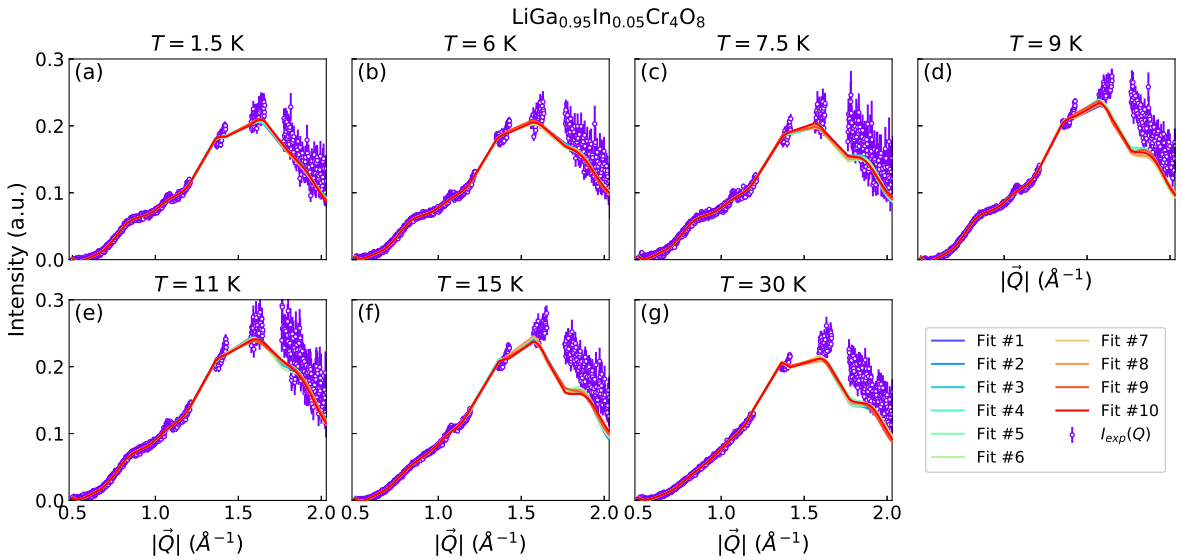

Figure 4.18: Reverse Monte Carlo refinements of diffuse neutron scattering from $LiGa_{0.95}In_{0.05}Cr_4O_8$ (Fig. 4.15). Refinements use the magnetic structure consisting of anisotropic magnetic moments. The different fits correspond to the different simulation boxes refined simultaneously.

quality of refinements for the data sets recorded at the lowest temperatures below the transition.

Classical spin-nematic transition in $LiGa_{0.95}In_{0.05}Cr_4O_8$

Combining all of the above observations it might be concluded that above the transition magnetic moments are of rather isotropic character and their radial spin correlations might be roughly described with a power-law decay. Another conclusion which might be drawn is that upon cooling below the transition temperature, there occurs an increase in collinearity of magnetic moments, connected with local lattice distortions and critical slowing down [152], but no global symmetry breaking, or magnetic long-range order is observed.

In order to understand the high-temperature behaviour, we refer to Ref. [4], where the spin-spin correlations are calculated, as functions of exchanges and temperature, in breathing pyrochlore system in Self Consistent Gaussian Approximation (SCGA). For both J and J' antiferromagnetic the expected ground state is a so-called Coulomb spin-liquid governed by algebraic long-range correlations. Fig. 4.20 presents a comparison between single-crystal diffuse scattering reconstructed with the `SPINDIFF` software [155] from 10 simulation boxes refined on $T = 30$ K data and results of calculations with the SCGA method for the breathing pyrochlore lattice with breathing factor $B_f \approx 0.67$. The calculations were done for $T = \bar{J}/2$, where $\bar{J}$ describes the overall energy scale of nearest neighbour interactions. The ratio of the exchanges on the differently sized tetrahedra described by parameter θ: $J = \cos(\theta)\bar{J}$ and $J' = \sin(\theta)\bar{J}$, for $\theta = \frac{3\pi}{16}$ [4], being quite close to the $x = 0$ case. Both patterns exhibit a characteristic bow-tie shaped scattering signalling the onset of algebraic correlations. The qualitative agreement with

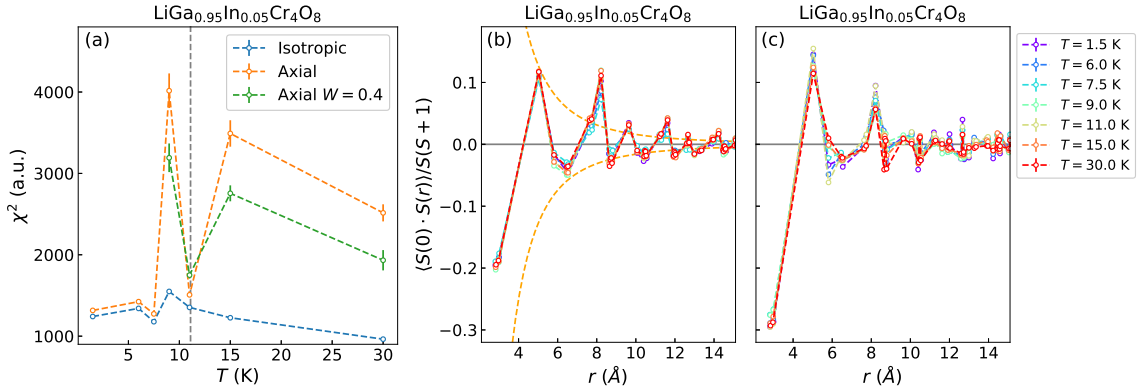

Figure 4.19: (a) χ^2 goodness of fit parameter and (b), (c) radial spin correlations of RMC refinements of diffuse neutron scattering on $LiGa_{0.95}In_{0.05}Cr_4O_8$ performed with (b) isotropic magnetic moments and (c) in presence of axial anisotropy along [001] direction. The envelope in (b) plotted with orange dashed line shows the $f(r) \sim r^{-3}$ dependence, the expected form of radial correlations for Coulombic spin-liquid phase [4].

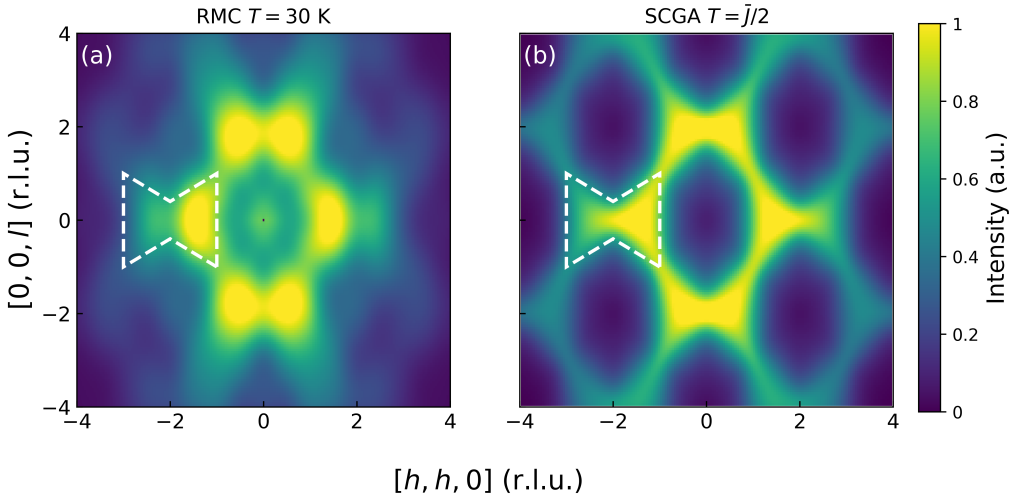

Figure 4.20: Single crystal diffuse neutron scattering (a) reconstructed from RMC fit with `SPINDIFF` software [155] from 10 simulation boxes refined on $T = 30$ K data and (b) calculated with SCGA method for breathing pyrochlore lattice ($B_f \approx 0.67$ and $T = \bar{J}/2$). Data in (b) shared by O. Benton et al. from Fig. 8(f) in Ref. [4]. The white dashed polygon highlights the characteristic bow-tie shaped scattering.

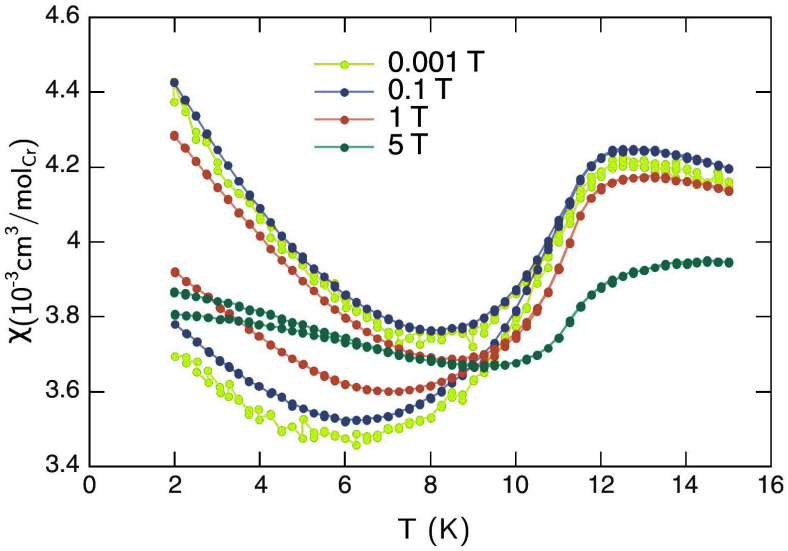

Figure 4.21: Field-dependence of bifurcation between zero-field-cooled and field-cooled magnetic susceptibility $\chi(T)$ of $LiGa_{0.95}In_{0.05}Cr_4O_8$. Courtesy of Y. Okamoto.

RMC reconstruction points to the presence of the Coulombic spin-liquid phase present in $x = 0.05$ at temperatures above the transition ($T > 11.1$ K).

In case of the second of the suggestion of classical spin-nematic phase, due to the lack of appropriate theoretical works describing breathing pyrochlore lattice, a comparison with the closely related undistorted case was made. Classical Monte Carlo simulations employing the bilinear-biquadratic model (Eq. 4.1) on a Heisenberg (isotropic moments) pyrochlore antiferromagnet with the presence of Gaussian bond disorder suggest the onset of a spin-nematic collinear state (for a biquadratic coupling term $b < 0$), with the spin glass freezing (concomitant at T comparable with bond disorder Δ). The schematic phase diagram based on those calculations is presented in Fig. 4.22. The nematic phase described in Ref. [126] is not characterized by a dipolar order, but it possesses a quadrupolar and a spin glass-like order parameter [126]. This would be consistent with the observations made using scattering techniques, NMR and thermodynamical measurements, described in the above paragraphs. However, the MC simulations suggest the existence of a weak first-order type transition for small Δ and the second-order type one for larger Δ in the region where spin freezing is simultaneous with the onset of nematic phase. However, to resolve this discrepancy a simulation taking into account the presence of a breathing distortion would be required.

On the other hand, the predicted nematic phase is expected to be much more robust against an external magnetic field than the canonical spin glasses [126]. The field-dependence of the bifurcation between zero-field-cooled (ZFC) and field-cooled (FC) magnetic susceptibility as a function of temperature is presented in Fig. 4.21. It persists up to the field strength of 5 T, which is a rather large value and should not be expected from a conventional spin glass [92].

As the low temperature state of $x = 0.05$ does not manifest a dipolar order parameter, an attempt was made to detect possible bond ordering in the nematic phase. For this discussion we draw on the theory of spin-Peierls phases in antiferromagnet pyrochlores

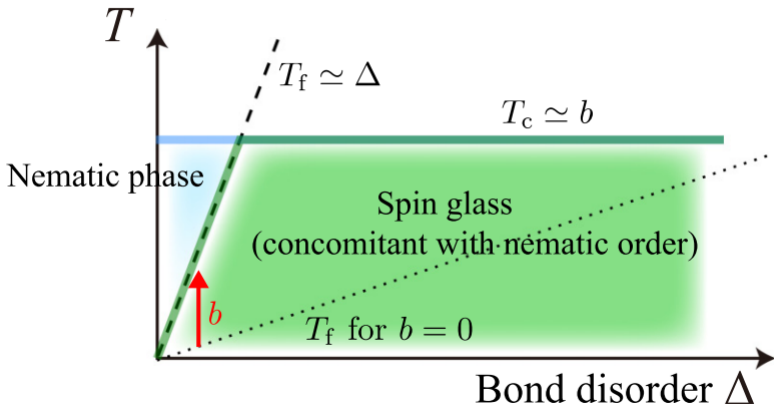

Figure 4.22: Schematic phase diagram (temperature vs bond disorder) based on results of classical Monte-Carlo simulations for bilinear-biquadratic model in pyrochlore antiferromagnet in presence of Gaussian bond disorder (Δ). Figure adapted from Ref. [126].

presented in Refs. [87, 88]. Following the classification of local distortion by the direction of stronger/weaker (shorter/longer, or antiferromagnetic/ferromagnetic) bonds, one can label possible collinear $S_{\text{tot}} = 0$ (following the ice rules) configurations with three colors: red, green and blue. Fig. 4.23 shows this classification with respect to the bond disparity $\boldsymbol{f} = (f_1, f_2)$ [87] characterizing the bond dimerization within a single tetrahedron and playing the role of an order parameter:

$$\begin{aligned} f_1 &= [(\boldsymbol{S}_1 + \boldsymbol{S}_2) \cdot (\boldsymbol{S}_3 + \boldsymbol{S}_4) - 2\boldsymbol{S}_1 \cdot \boldsymbol{S}_2 - 2\boldsymbol{S}_3 \cdot \boldsymbol{S}_4]/\sqrt{12} \\ f_2 &= (\boldsymbol{S}_1 \cdot \boldsymbol{S}_3 + \boldsymbol{S}_2 \cdot \boldsymbol{S}_4 - \boldsymbol{S}_2 \cdot \boldsymbol{S}_3 - \boldsymbol{S}_1 \cdot \boldsymbol{S}_4)/2, \end{aligned} \tag{4.4}$$

where $\boldsymbol{S}_n$ represents the magnetic moments at the corners of the tetrahedra. In the theory of Ref. [87] the tetragonal distortion is a result of coupling between long-wavevector phonons (i.e. $\boldsymbol{q} \simeq 0$) to the spin degrees of freedom. The conclusion might be drawn, that the breaking of the cubic symmetry should be associated with the onset of magnetic order. The corners of this phase diagram present the collinear states being of interest in the light of our observations. They correspond to the long, ferromagnetic (connecting the moments pointing at the same direction, represented by dashed lines in Fig. 4.23) bond along the [011] - red (R), [1011] - green (G) and [110] - blue (B).

Color population of tetrahedra within RMC simulation boxes is presented in Tab. 4.6. The blue tetrahedra significantly outnumber the other two colors, appearing in a very similar quantity. An imbalance is also observed in the number of bonds between tetrahedra of different kinds, presented in Tab. 4.7. The relative numbers suggest that in refined structures there is tendency for neighbouring tetrahedra to be of different colours. Using this convention the proposed ordered states in $x = 0$ and $x = 1$ could be described as RG (Fig. 4.11) and BG orders respectively, with layers of single-colored tetrahedra occupying the sites of a diamond dual lattice of the pyrochlore lattice, stacked along the [001] direction (it is shared for both cubic and tetragonal structure), which is identical to the anisotropy axis of magnetic moments.

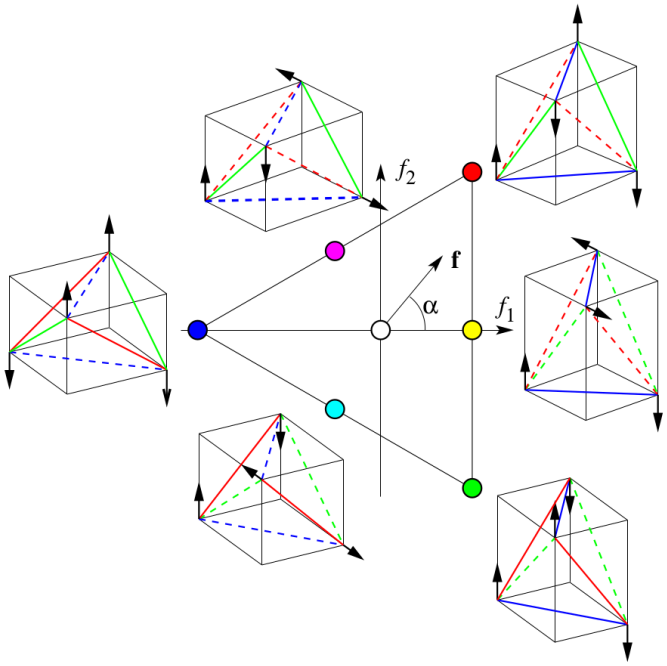

Figure 4.23: Phase diagram of possible tetrahedra distortions for different values of the bond disparity vector $\boldsymbol{f}$ (Eq. 4.4). The dashed lines represent elongated bonds connecting sites hosting with parallel magnetic moments. Figure adapted from Ref. [87].

Table 4.6: Populations of tetrahedral configurations averaged over 10 RMC simulation boxes refined with diffuse scattering measured at $T = 1.5$ K.

Tetrahedron configuration	Red	Green	Blue
	431.5	442.7	635.3

Table 4.7: Populations of bond configurations averaged over 10 RMC simulation boxes refined with diffuse scattering measured at $T = 1.5$ K.

Bondconfiguration	Red-Red	Green-Green	Blue-Blue	Red-Green	Red-Blue	Green-Blue
	211.5	226	289.4	344.9	825.8	842.6

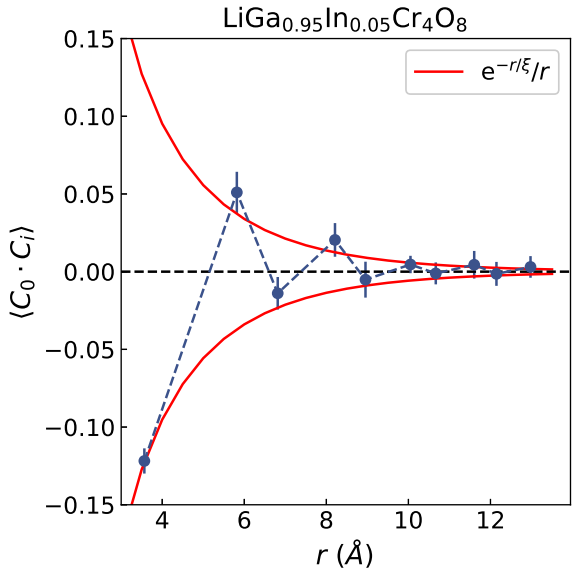

Figure 4.24: Radial color correlations in $LiGa_{0.95}In_{0.05}Cr_4O_8$.

The broad feature in the diffuse scattering appearing upon the transition is positioned at $\boldsymbol{Q} = (0, 0, 1)$ (Fig. 4.15), a forbidden reflection for the diamond lattice, and it should vanish for any type of perfect color order. This suggests that it may result from a deviation of the phase factor of the scattering structure factor, which is produced by small domains hosting some kind of partially broken color order. The color populations of single tetrahedra and the bond configurations would point to the possibility of the existence of RB/GB type of domains, with the minority colors (R and G) filling in between the layers of majority color (B) in alternating manner.

In order to quantify the content of such domains the radial color correlation was defined as $\langle C_0 C_i \rangle$ which takes values 1 and -1 for the i^{th} tetrahedron being of the same and different color as the 0^{th} one, respectively, summed in the further neighbour shells and weighted by their population. The r-dependence of this function is shown in Fig. 4(b) of Ref. [152]. The obtained function might be characterized with exponential decay ($f(r) = \mathrm{e}^{-r/\xi}/r$ [158]) with a correlation length $\xi = 3.2$ Å and $\langle C_0 C_1 \rangle = 0.14$ showing the preference for "anticolor" arrangements. The retrieved correlation length is rather small, but some of much larger domains might be singled out during visual inspection of refined structures (Fig. 4(a) in Ref. [152]).

4.5 Spin dynamics in $LiGa_{0.95}In_{0.05}Cr_4O_8$ ($x = 0.05$)

Substantial part of results presented in the following section was published in Ref. [159].

4.5.1 Temperature evolution of inelastic scattering in $LiGa_{0.95}In_{0.05}Cr_4O_8$

In order to probe changes in the spin dynamics of $LiGa_{0.95}In_{0.05}Cr_4O_8$ across the transition to a nematic spin-liquid, time-of-flight inelastic neutron scattering was conducted on the same powder sample as the one used for the diffraction experiment. The temperature

dependence of the dynamical structure factor $S(|\boldsymbol{Q}|, E)$ is presented in Fig. 4.25. At $T = 152$ K one can observe a quasielastic rod of scattering at $|\boldsymbol{Q}| \sim 1.6$ Å^{-1}. This wavevector roughly corresponds to the average Cr-Cr distance within the tetrahedron. The scattering intensity might be observed up to energy transfers of $E = 15$ meV. On cooling down the spectral weight moves toward the elastic line and below the transition a gapped, broad inelastic feature appears at $E \sim 5.8$ meV. Fig. 4.26) shows the relative change of scattering intensities around the elastic line and at the energies between elastic line and the resonant feature appearing at $T < 11.2$ K, showing that indeed the spectral weight at low energies is increasing and separates into the inelastic and elastic part below the transition.

While the high temperature ($T > 18$ K) dynamic structure factor (Fig. 4.25(a)) resembles the one observed in both end-member compounds [146, 160], on cooling down, its evolution shows similarities to the behaviour of $x = 0$. This is in contrast to $x = 1$, where an inelastic peak appears around $T = 50$ K and softens on cooling below $T = 20$ K. Furthermore, at lowest temperatures, spin wave-like modes are clearly noted (Fig. 4.27(b)). On the other hand, $x = 0$ shows a similar shift of scattering weight towards the elastic line and at the lowest temperatures a dominant resonant mode is accompanied by a weaker spin- wave scattering (Fig. 4.27(a)).

Apart from the shift of spectral weight in energy on cooling down, an increase in the modulation in $|\boldsymbol{Q}|$ is also observed (Fig. 4.28(a)). This is a sign of the development of longer-ranged correlations between the magnetic moments. To determine their character and length, $S(|\boldsymbol{Q}|)$ integrated in the $2 - 7$ meV range was fitted to a shell model (Fig. 4.28(b)) corresponding to the Fourier transform of pairwise spin correlations on moving forward from a central atom:

$$S(|\boldsymbol{Q}|) = f(|\boldsymbol{Q}|)^2 \sum_i \langle S(0) \cdot S(r_i) \rangle N_i \frac{\sin(|\boldsymbol{Q}| r_i)}{|\boldsymbol{Q}| r_i}, \tag{4.5}$$

with the magnetic form factor of the Cr^{3+} ion $f(Q)$, and r_i standing for the radius of the shell occupied by N_i ions. As the difference between r_i seen from the ionic position placed at large and small tetrahedra is relatively insignificant, an average of those distances was employed in the calculations for simplicity. $\langle S(0) \cdot S(r_i) \rangle$ are the values of radial correlations fitted within the model.

In the course of fitting it was observed that including shells further than third nearest neighbours did not improve the quality of the fit at at any T. The resulting correlations are of an alternating character, namely antiferromagnetic for the nearest neighbours, ferromagnetic in the case of the second-nearest neighbours and antiferromagnetic again for the third shell. The extracted wight of the correlations at $T = 152$ K match exactly the results of RMC refinements employing isotropic magnetic moments (Fig. 4.28(b)). These values are developing smoothly until reaching $T = 24$ K, where the separation of quasielastic intensity begins (Fig. 4.26). From that point, they do not exhibit large changes down to lowest temperature of the measurement - $T = 5.2$ K and correspond very well to the values calculated for hexamer cluster of Cr ions.

By means the of fluctuation-dissipation theorem [17], one can retrieve the imaginary part of the magnetic dynamic susceptibility from the dynamic structure factor:

$$\chi''(|\boldsymbol{Q}|, E) = \pi(1 - \mathrm{e}^{-\frac{E}{k_B T}}) S(|\boldsymbol{Q}|, E). \tag{4.6}$$

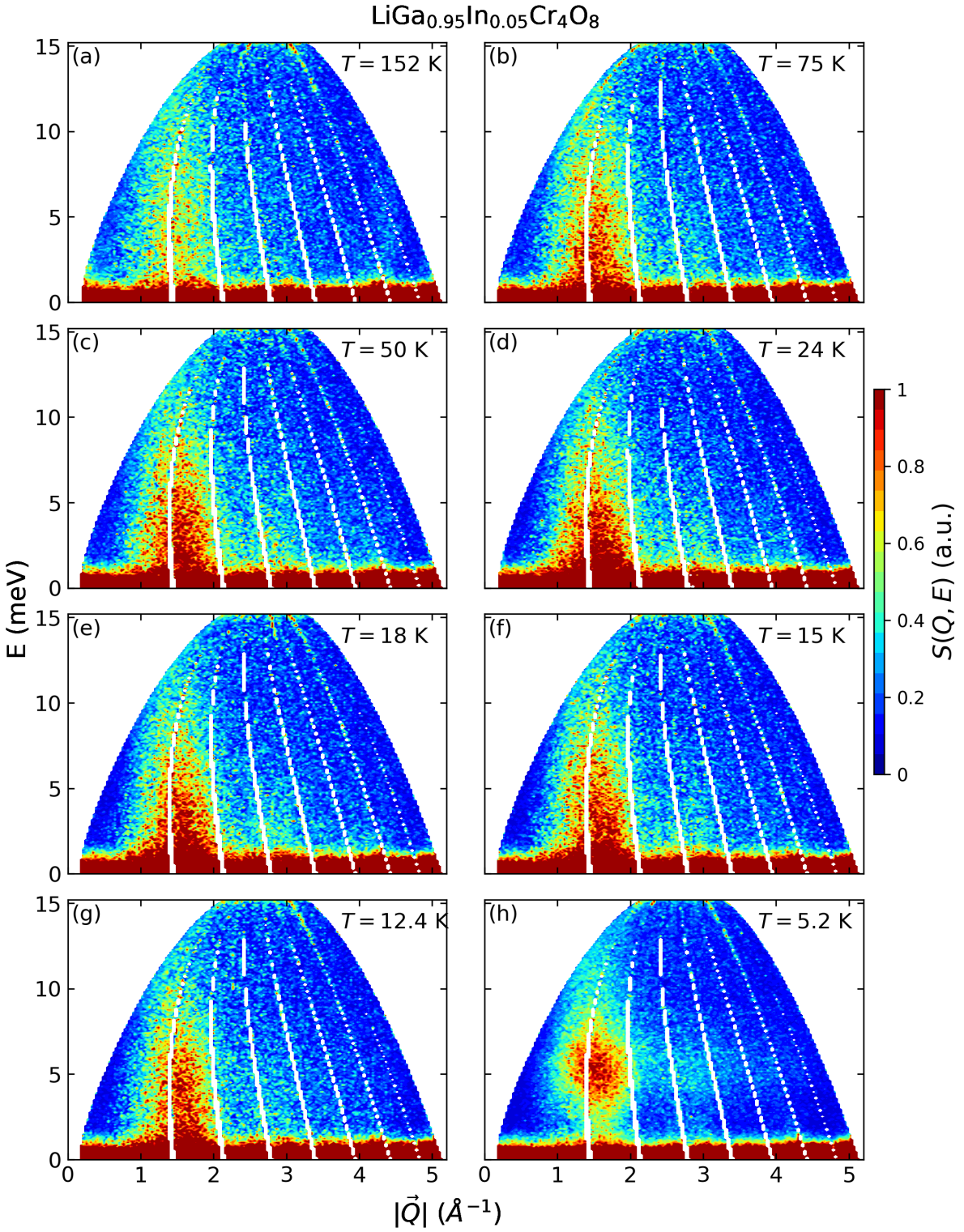

Figure 4.25: Temperature dependence of dynamic structure factor measured $S(|\boldsymbol{Q}|, E)$ in $LiGa_{0.95}In_{0.05}Cr_4O_8$. Data measured with incoming neutron energy $E_i = 16$ meV on the MARI time-of-flight spectrometer at the ISIS neutron source.

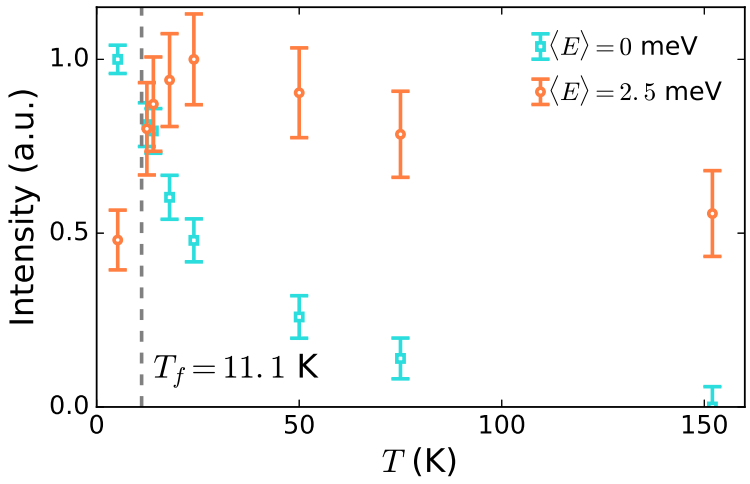

Figure 4.26: Temperature dependence of elastic and quasielastic neutron scattering intensity. $S(|\boldsymbol{Q}|, \omega)$ was integrated in range $E = -1.1 - 1.1$ meV for elastic and $E = 1.5 - 3.5$ meV for inelastic signal, and $|\boldsymbol{Q}| = 1 - 2$ Å^{-1} in both cases. Both data sets are normalized to 1 and the cutoff of elastic signal is set to show the changes with respect to $T = 152$ K dataset.

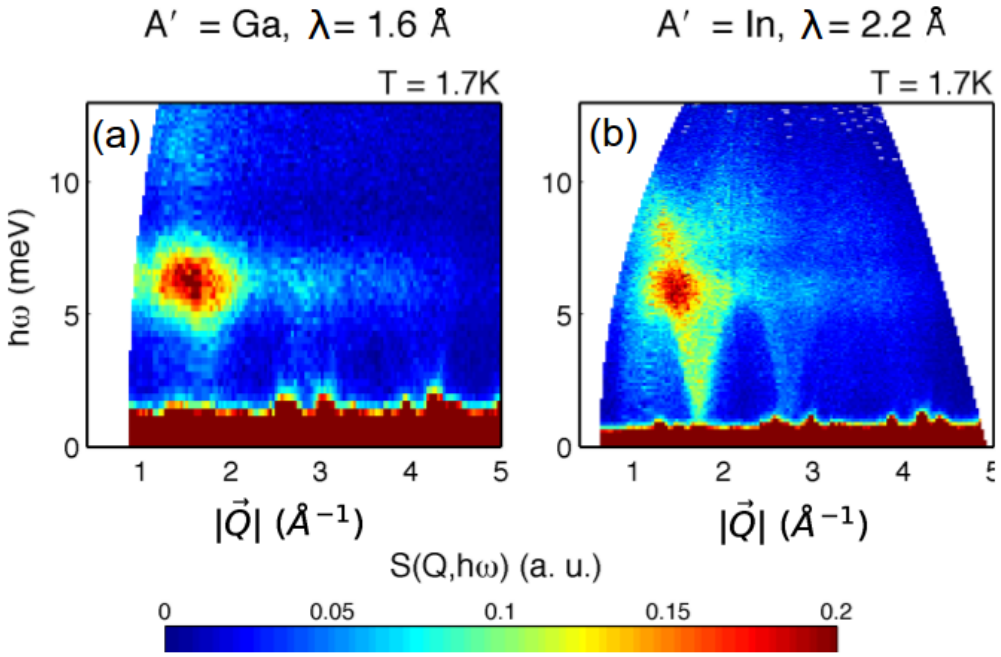

Figure 4.27: Low-temperature dynamic structure factor $S(|\boldsymbol{Q}|, \hbar\omega)$ measured in $LiGaCr_4O_8$ and $LiInCr_4O_8$. Figure adapted from Ref. [160]

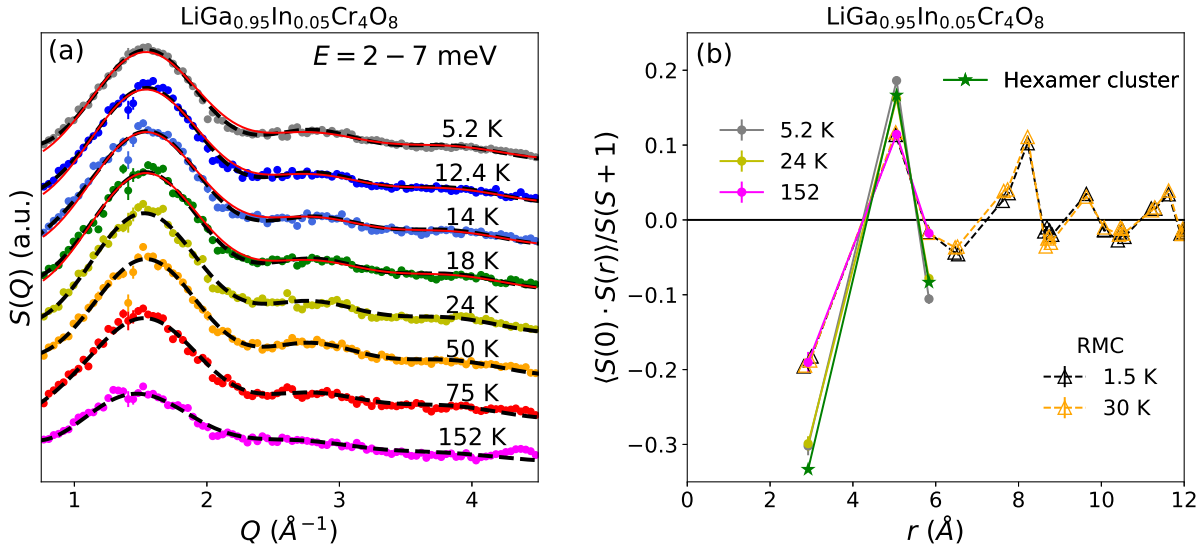

Figure 4.28: (a) $|\boldsymbol{Q}|$-dependence of inelastic neutron scattering from $LiGa_{0.95}In_{0.05}Cr_4O_8$ for different temperatures. Black dashed lines are results of fitting with the shell model (Eq. 4.5). Solid red lines are scaled results of structure factor calculations for antiferromagnetically coupled hexagonal Cr ring. (b) radial spin-spin-correlations fitted to the shell model. Green stars mark the results of calculations for the mentioned hexagonal loop. Empty triangles are results of RMC simulations presented in Sec. 4.4.2, in Fig. 4.19(b).

At high temperatures, the energy-dependence $\chi''(E)$ of quasielastic feature can be very well described with a quasielastic Lorentzian function (Fig. 3(a) in Ref. [159]):

$$\chi''(E) = \chi'\Gamma/(E^2 + \Gamma^2), \tag{4.7}$$

with χ' representing the static susceptibility. This expression is the Fourier transform of the exponential decay $f(t) = \mathrm{e}^{\frac{-t}{\tau}}$. It leads to the conclusion that the spin dynamics in this regime might be described by a relaxation process with a single relaxation time τ. According to theoretical predictions [161, 80, 162] $\Gamma \propto T$ for isotropic spins on pyrochlore lattice. In the case of $x = 0.05$ it was found that $\Gamma(T)$ rather follows a power law $\Gamma(T) = T^{0.64}$ (Fig. 3(b) in Ref. [159]). A similar discrepancy is observed in $ZnCr_2O_4$, where $\Gamma(T) = T^{0.81}$, but its source remains unknown.

The situation changes while cooling down below $T = 18$ K where the χ'' can no longer be described by a single relaxation process. A possible explanation to that is onset of critical fluctuations above T_f. This occurs simultaneously with the appearance of a stretch exponent $\beta < 1$ in spin-lattice relaxation times T_1 witnessed in ^{7}Li NMR [163].

4.5.2 Low-energy dynamics in $LiGa_{0.95}In_{0.05}Cr_4O_8$

Alongside with the resonant feature quasielastic intensity extending out to ~ 2 meV is observed at low temperature. To investigate these slower dynamics in more detail at longer times (lower E) neutron spin echo (NSE) experiment was performed. NSE

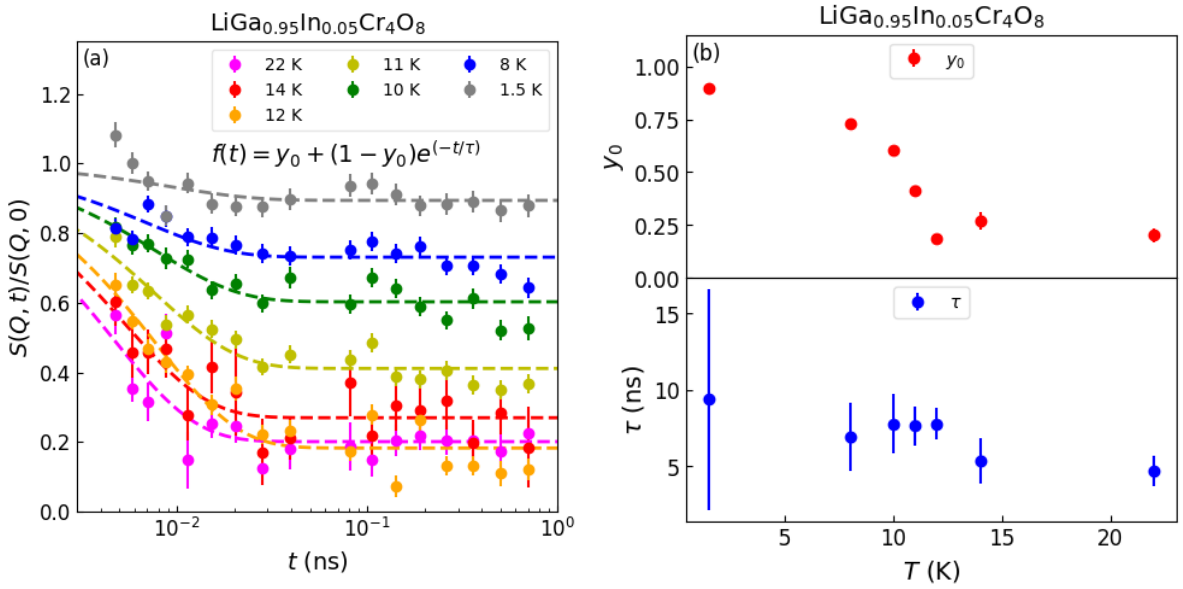

Figure 4.29: (a) normalized spin echo intermediate scattering function measured with neutron spin-echo spectroscopy in $LiGa_{0.95}In_{0.05}Cr_4O_8$ at few temperatures from range $22 - 1.5$ K with $\lambda = 5.5$ Å^{-1}. Dashed curves are fits to the Arrhenius law. Data measured on the IN11 spectrometer at the ILL neutron facility. $S(|\boldsymbol{Q}|, t)$ was normalized with a standard sample $(Ho,Y)_2Ti_2O_7$ at $T = 2$ K. (b) parameters of fits to the Arrhenius law, where y_0 is the scaling factor reflecting the fraction of the magnetic moments being dynamically frozen within the spetrometers time window.

allows to retrieve the intermediate scattering function $S(|\boldsymbol{Q}|, t)$ - the time Fourier transform of the dynamic structure factor $S(|\boldsymbol{Q}|, E)$, which carries the information about the time-dependent correlation function for fluctuations with the wave vector $|\boldsymbol{Q}|$ [102]. Normalized intermediate scattering functions measured at a few temperatures and parameters resulting from fits to the Arrhenius law ($1/\tau = A \exp(-\Delta/k_B T)$), are presented in Fig. 4.29. A small step-like increase in the spin relaxation is observed on cooling down to the transition temperature and gradual freezing of spin dynamics is observed below the transition point. A lack of saturation of $S(|\boldsymbol{Q}|, t)/S(|\boldsymbol{Q}|, 0)$ at $T = 1.5$ K suggests that the Cr^{3+} ion moments are not completely frozen at this point. One of the explanations for the remaining spin dynamics could be collective flips of magnetic moments within small scale molecular clusters (possibly hexagons), expected to produce quasielastic signal, with its width showing a temperature dependence. These excitations transfer the system between configurations realizing the 2U2D constraint in the nematic state analogously to the hexagon flips proposed for isotropic spins in kagomé antiferromagnet [164, 165].

4.5.3 Resonant scattering in $LiGa_{0.95}In_{0.05}Cr_4O_8$

The broad inelastic feature, centered at $E = 5.8$ meV in $S(|\boldsymbol{Q}|, E)$ below the transition (Fig. 4.25(h)) shows a similar $|\boldsymbol{Q}|$-dependence as the inelastic scattering below $T = 24$ K (Fig. 4.28(a)), which is very well reproduced by shell model calculations for hexagonal

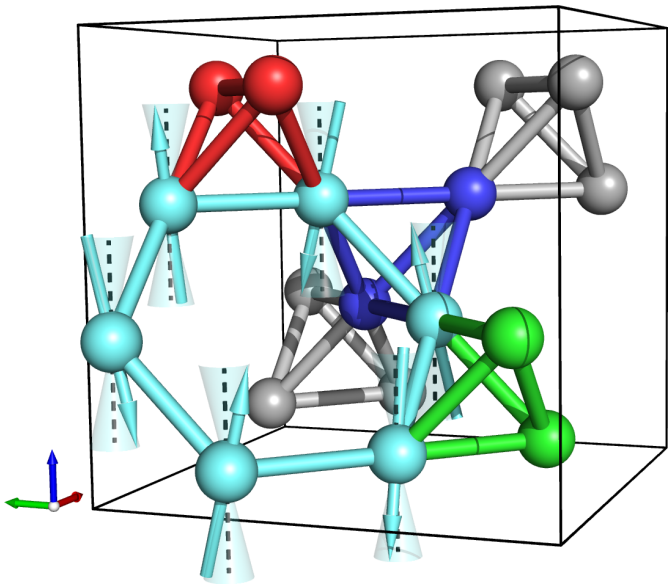

Figure 4.30: Hexagonal loop (cyan bonds) singled out within breathing pyrochlore lattice by local distortions of tetrahedra, marked in the RGB convention (Fig. 4.23). Cyan arrows represent antiferromagnetically coupled moments and their precessive mode around the equilibrium position (black dashed line). Figure adapted from Ref. [159]

antiferromagnetically coupled loops (Fig. 4.28(b)). Such a hexagonal loop can be singled out by local distortions of tetrahedra. In case of a stack of red, blue and green tetrahedra (Fig. 4.30) the distorted shorter bonds with increased exchange interactions form a hexagon. This configuration is consistent with the proposed existence of short-range color order created by majority blue and less represented green and red tetrahedra. As is described in the former paragraph, a collective flip of all moments (i.e. longitudinal excitation) hosted by the loop cannot account for the inelastic feature observed in the data. Other possible excitations within the spin-nematic state compatible with hexagonal clusters are precessive motions of moments around the axis of anisotropy chosen by the nematic state (i.e. transverse excitation). Usually these are referred to as "weathervane modes" and occur at zero-energy cost [166], but presence of biquadratic term or interactions longer range than nearest neighbour exchange may lift them to finite energy.

The results of solving a classical equation of motion for magnetic moments:

$$\frac{\mathrm{d}\boldsymbol{S}_i(t)}{\mathrm{d}t} = -\frac{1}{\hbar}\boldsymbol{S}_i \times \nabla_{\boldsymbol{S}_i(t)} \cdot \mathcal{H}, \tag{4.8}$$

using the biquadratic-bilinear Hamiltonian for $\mathcal{H}$ (Eq. 4.1), gives the value of the energy gap $\Delta E \simeq 8 b_{\mathrm{av}} S^3$, with b_{av} is averaged biquadratic coupling between moments at two types of tetrahedra and small, and for the case of small precessive motions i.e. $S_i^z(t) \simeq S$. Using the estimation from fits to magnetic susceptibility and the energy of the excitation: $J_{\mathrm{av}} = 45$ K one can obtain $b_{\mathrm{av}} \sim 0.05 J_{\mathrm{av}}$ similar to the $b = 0.02$ found in $ZnCr_2O_4$ [167]. Also employing $T_f \simeq bS^4$ [126] gives transition temperature $T_f = 12$ K very close to the value observed in specific heat and NMR experiments.

The inelastic feature in neutron scattering spectrum is far from being resonant. Its Gaussian full-width-half-maximum (FWHM) is close to 2 meV. Using the linear relation-

ship between the J exchange interaction strength and the Cr-Cr distances in ACr_2O_4 [142] it translates into Gaussian distribution of Cr-Cr distances within the hexagonal ring characterized by a standard deviation of ~ 0.1 Å. Indeed, the Rietveld refinement of diffraction data have found a Gaussian distribution of interplanar distances within the nematic phase, but of a magnitude around 4 times smaller than that (Fig. 4.14(a)). On the other hand, this average structure analysis cannot access the structural distortions of a more local character.

Apart from elastic intensity and inelastic feature, even at $T = 5.2$ K still some amount of quasielastic/inelastic intensity can be observed both below and above 5.8 meV peak. The scattering at higher energies might be attributed either to similar precessive excitations of differently sized clusters formed by Cr^{3+} ions (producing similar inelastic features, but placed to close to each other and to weak to resolve properly), or by some spin-wave like excitations of small domains hosting short-ranged magnetic order (contributing to the dynamic structure factor with scattering in form of dispersive branches). Giving an unambiguous answer to this question would require performing neutron scattering experiments on single-crystal samples, giving the access to full $S(\boldsymbol{Q}, E)$.

4.6 Conclusions and outlook

High resolution x-ray and neutron diffraction studies allowed to determine the magnetostructural character for both stages of transition observed in $LiGaCr_4O_8$ ($x = 0$). These stages were found to be reminiscent of thermal crossover in the $T = 18 - 12.5$ K followed by the first-order transition at $T = 13.8$ K. Magnetic intensities corresponding to both reach full saturation at common temperature $T = 12.5$ K. Unfortunately the problem of finding structures of low-temperature phases remains underconstrained with available powder diffraction data. Instead the analysis of magnetic signal was performed.

The first transition associated with single $\boldsymbol{k} = (0, 0, 1)$ (in cubic basis) magnetic propagation vector observed in $LiInCr_4O_8$ ($x = 1$) and the magnetic intensity was successfully refined with the assumption of a $F\bar{4}dm \rightarrow I\bar{4}m2$ cubic-to-tetragonal transition and a magnetic order described by the C_A222_1 magnetic space group.

The second stage results with the onset of a much more complex multi-$\boldsymbol{k}$ structure. The observed magnetic reflections might be indexed with $\boldsymbol{k}_1 = (1/2, 1/2, 0)$ and $\boldsymbol{k}_2 = (1, 0, 1/2)$ (in cubic basis) magnetic propagation vectors, but this combination still cannot be accounted for all of them suggesting the presence of a third component.

Preparation of single-crystal samples and performing x-ray and neutron diffraction experiments on them, would provide an opportunity to identify the structural phases and narrow down the set of possible magnetic orders.

In spite of the detection of a thermodynamical anomaly observed at $T \sim 11$ K in slightly doped $LiGa_{0.95}In_{0.05}Cr_4O_8$, x-ray and neutron diffraction did not find any signs of structural symmetry breaking nor of the onset of magnetic long-range order. This suggests that the suppression of Néel order takes place for much weaker doping levels than it was found out earlier with bulk probes. Reverse Monte Carlo studies on the structure factor of magnetic diffuse scattering and signs of local structural distortions on crossing the temperature of the anomaly lead to the conclusion of the transition being the onset of a classical spin-nematic phase.

Inelastic neutron scattering gave signs of two types of excitations present within the nematic phase one contributing to the resonant feature identified as precessive fluctuations of magnetic moments within hexagonal loops and the second one of quasielastic character being reminiscent of spin flips within those small molecular clusters. Temperature dependence of this dynamics was analyzed with use of neutron spin echo spectroscopy and remaining fluctuations were found down to the lowest temperatures.

Similarly to the case of $x = 0$ acquiring single-crystal samples would allow to expand the picture described in this work, but giving access to the full information concerning the spatial character of the observed excitations. Moreover, application of other resonance techniques (e.g. muon spin resonance) would allow to fill the gaps between time-windows of already employed spectroscopic techniques, thus giving the full description of evolution of dynamics in the nematic phase upon cooling.

Chapter 5

$Tb_3Ga_5O_{12}$ - terbium gallium garnet

Garnets are naturally occurring silicate minerals described by general formula $A_3B_2(SiO_4)_3$, where A=Ca^{2+}, Fe^{2+}, Mg^{2+}, Mn^{2+}, B=Al^{3+}, Cr^{3+}, Fe^{3+}, Mn^{3+}, Si^{3+}, Ti^{3+}, V^{3+}, Zr^{3+} and the Si^{4+} ion forming the SiO_4 group can be partly replaced by Al, Ti or Fe ions [168]. In most instances garnets crystallize in cubic structures with the $Ia\bar{3}d$ (230) space group.

Due to their relatively high hardness (6.5-7.5 on Mohs scale [168]) and lack of cleavage garnets are often utilized as abrasive materials. Moreover, their wide range of colours led to their widespread use as gemstones in jewellery.

In addition to naturally occurring garnets numerous synthetic garnets have been grown and characterized over the years [169, 170, 171, 172]. The family of synthetic garnets consists of pure $A_3B_5O_{12}$ and doped $A_{3-x}A'_xB_5O_{12}$ compounds, where the A/A'-site is populated by magnetic rare-earth (RE) RE^{3+} (apart from La and Lu), or non-magnetic Y^{3+}, La^{3+}, or Lu^{3+} ions. The B-site of synthetic garnets can host either magnetic Fe^{3+}, or non-magnetic Al^{3+}, Ga^{3+} ions. They have found application in various optoelectronic devices e.g. as active media in solid state lasers (RE^{3+} doped $Y_3Al_5O_{12}$ - YAG) [173] or Faraday rotators in optical isolators ($Tb_3Ga_5O_{12}$ - TGG and $Tb_3Al_5O_{12}$ - TAG) [174].

5.1 Rare-earth garnets $RE_3Ga_5O_{12}$ and $RE_3Al_5O_{12}$

The family of rare-earth garnets has drawn attention not only for their magneto-optical properties, but also due to the specific features of the magnetic sublattice [175, 176], which combined with symmetry properties of magnetic ion site gives rise to intriguing magnetic properties. The garnet structure has a high cubic symmetry, with 160 ions per asymmetric unit. The A^{3+} ions occupy exclusively the 24c Wyckoff positions, forming two separated, but interpenetrating half-garnet lattices (Fig. 5.1(a)), which are twisted three-dimensional arrangements of corner sharing triangles. In numerous models describing frustrated systems it is convenient rather to use a medial lattice [177]. The medial lattice is a bipartite lattice which is formed so as to host the sites of the medial lattice (coinciding with the sites of magnetic ions) in the middle of bonds connecting the nearest neighbours of the parent lattice. A good example of this relation is the pyrochlore medial lattice and the diamond lattice with points in the centers of tetrahedra. For a single half-garnet lattice such a medial lattice is the Laves graph [178] with its vertices residing at the center of mass of each triangle. It is an infinite three dimensional graph of cubic symmetry, with the shortest loop formed by 10 vertices (for a diamond lattice it is 6).

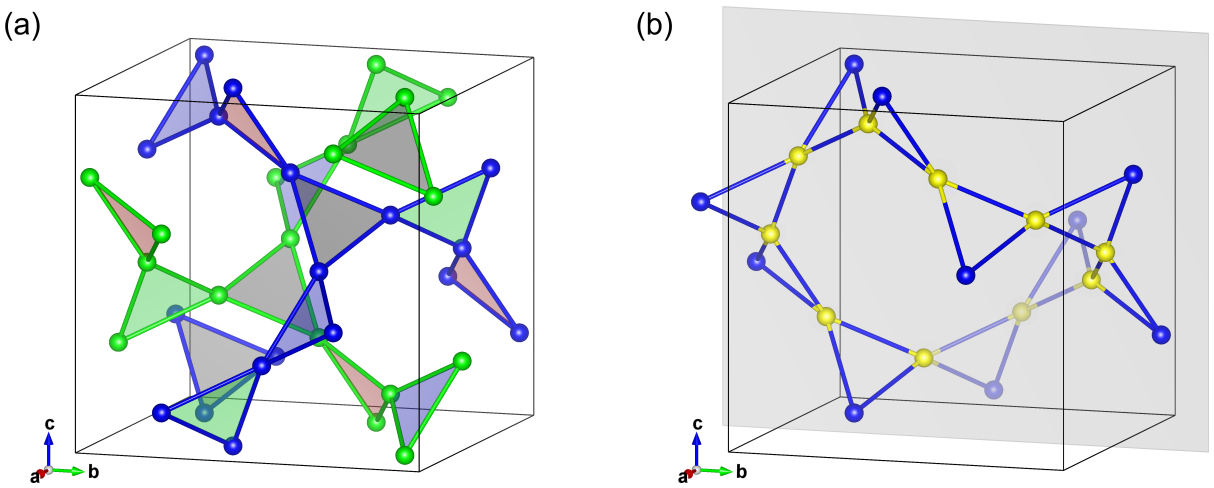

Figure 5.1: (a) Sublattice formed by the 24*c* Wyckoff position. Different colors of vertices and bonds mark two separate inter-penetrating half-garnet lattices. Different fillings of triangles are marking them as being contained within different ⟨111⟩-type planes. (b) Ten-member ring forming the shortest closed loop within the half-garnet lattice (yellow sites), the centers of mass of the drawn triangles form the shortest loop in the Laves graph. The gray plane is the (100) plane shadowing the sites outside of the unit cell with $a < 0$ coordinate. Figure created with `VESTA` software [60].

Each node of the Laves graph is a meeting point of three bonds placed at the 120°. It is worth mentioning that this closed circuit cannot be drawn within one crystallographic unit cell of the garnet structure (Fig. 5.1(b)). Such a ten-membered loop was suggested to play a role as a building block in the hidden order governing the correlated paramagnet phase in one member of the family gadolinium gallium garnet (GGG) [157].

The 24*c* site is characterized by low-symmetry D_2 orthorhombic point-group with three mutually perpendicular twofold rotation axes, forming a local coordinate system (Fig. 5.2). In terms of the local crystal field environment the 24*c* sites might be divided into six groups by the orientation of this local coordinate system. One of its axes (x) is pointing along the ±[100], ±[010], or ±[001] cubic unit cell direction, with two others (y and z) pointing along one of the ⟨110⟩-type directions chosen appropriately to form a right handed coordinate system (Fig. 5.2).

5.1.1 Magnetic order in rare-earth garnets

The vast majority of rare-earth garnets (both aluminum and gallium based) were found to order magnetically in multiaxial antiferromagnetic structures, where the easy axis is imposed by the symmetry of the crystal electric field (CEF) defined by the local environment. DyAlG [179], HoGaG [180] ErGaG, TbAlG and HoAlG[181] follow the $Ia\bar{3}d'$ magnetic space group with six sublattices and the magnetic moments on each pointing along one of the six main crystallographic (⟨100⟩-type) directions of the cubic unit cell. Chains lying along [100]-type directions formed by third nearest rare-earth ion neighbours are populated with magnetic moments following an alternating pattern of antiparallel alignment (± direction along the common easy axis). The feasibility of this structure

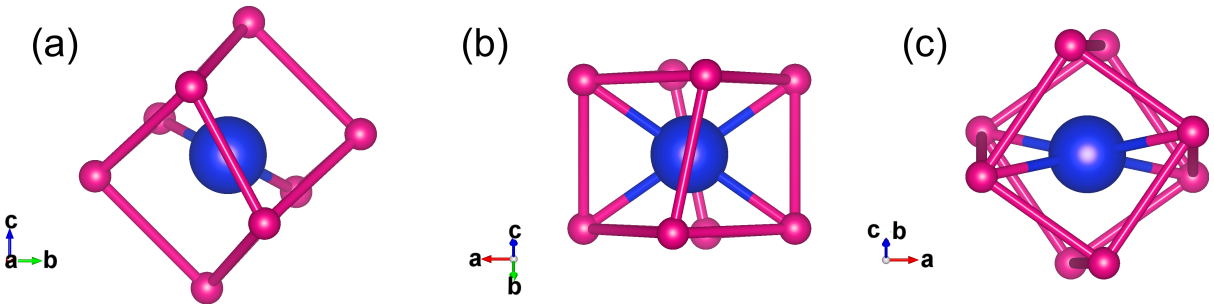

Figure 5.2: Local crystalline environment of the 24*c* Wyckoff position of $RE_3Ga_5O_{12}$ rare-earth garnets at $(0.125, 0, 0.25)$ position (fractional coordinates of the unit cell). Blue and pink spheres mark the positions of rare-earth and oxygen ions respectively. (a), (b) and (c) show projections along the three twofold axes of the D_2 point symmetry: $\pm[100]$, $\pm[011]$ and $\pm[01-1]$ respectively. The bi-color cylinders mark the shorter out of two Tb-O distances. Figure created with `VESTA` software [60].

was also confirmed with calculations using the Luttinger-Tisza method and accounting for dipole-dipole interactions between the rare-earth ions [182]. The magnetic structure of NdGaG was found to be slightly different and correspond to the $Ia'\bar{3}d$ magnetic space group, characterized similarly by six sublattices but arranged such that moments that belong to the same chain point along the same direction, which is the local easy axis.

A more detailed discussion of the magnetic structures associated with rare-earth garnets will be presented in section 5.3 on the example of terbium gallium garnet.

$Dy_3Al_5O_{12}$ - dysprosium aluminum garnet

Dysprosium aluminum (DAG) garnet was one of the first garnet materials to draw researchers' attention with its magnetic behaviour. The onset of Néel long-range order was detected in magnetic susceptibility [183] and specific heat [184]. The second experiment allowed to determine that dipole-dipole interactions contribute $\sim 70\%$ of total interactions between magnetic ions. Neutron scattering studies allowing to access system's staggered magnetic susceptibility and correlation length [185, 186] showed a discrepancy between the critical exponents of the ordering transition observed in DAG and the theoretical values calculated for the three-dimensional Ising model, supporting the presence and significance of long-range dipolar interactions in DAG.

$Gd_3Ga_5O_{12}$ - gadolinium gallium garnet

The only known, fully frustrated garnet is gadolinium gallium garnet [187, 188, 189] (GGG). It does not exhibit long-range order down to $T = 25$ mK. Instead it shows a broad feature in the specific heat at $T \sim 0.8$ K [190, 188], attributed to the development of short-range correlations. On further cooling it undergoes a spin-glass transition at $T_g = 0.14$ K [189]. With $\theta_{CW} \sim 2$ K [191, 192] GGG is a potential host of a correlated but disordered spin-liquid state, detected in powder diffuse neutron scattering [193].

Reverse Monte Carlo (Sec. 4.4.2) analysis of the structure factor of the diffuse neutron scattering at $T = 0.175$ K did not reveal presence of any radial correlations of dipole

magnetic moments which significantly exceed the distance between nearest-neighbours. Further investigations [157] have shown signs of strong antiferromagnetic correlations within the ten-membered loops (Fig. 5.1(b)) marking the shortest closed path within the Laves graph constituting the parent lattice of a single half-garnet structure. These correlations are reflected in the value of a "10-spin director": $\boldsymbol{L}(\boldsymbol{r}) = \frac{1}{10}\sum_n \cos(\pi n)\boldsymbol{S}_n(\boldsymbol{r})$ [157], summed around these loops and assigned as a multipolar order parameter impossible to detect directly with a dipolar probe like neutron scattering. The finite vlaue of this order parameter interpreted as manifestation of multipolar long-range hidden order, the development of which was pointed as a possible source of the aforementioned broad feature in specific heat.

This example demonstrates rare-earth garnets as possible hosts of exotic ground-states lacking an ordinary dipolar order parameter. It is especially important to take into consideration that while GGG is the only synthesized garnet lacking Néel order, it is not the only example where the ordering is suppressed considerably below temperatures suggested by the Curie-Weiss behaviour [194, 195].

$Ho_3Ga_5O_{12}$ - holmium gallium garnet

Ho^{3+} ions are similarly to Tb^{3+} ions, being even-electron non-Kramers systems. This implies that in both cases the degeneracy of crystal field ground-state can be completely lifted resulting in a non-magnetic singlet ground-state. This would require the magnetic order, if observed, to be of induced-moment type (Sec. 5.2.3). Indeed in works by Hammann et. al. [180, 196], the magnetic ordering processes in both holmium gallium garnet (HoGG) and TGG were assigned to the same type of the hyperfine-induced ordering, by means of the mean-field theory. The magnetic transition in HoGG was found to take place at a very low temperature of $T_N = 0.19$ K. The presented theory was based on a low-energy part crystal field level structure consisting of two close-lying singlets, well-separated in the energy from further excited levels (forming so-called quasi-doublet ground-state). However, no details of the structure of these states were included in the model.

5.2 $Tb_3Ga_5O_{12}$ - characteristics and observed phenomena

Terbium gallium garnet (TGG) has been valued for years as an extremely efficient rotator of light polarization for a wide range of wavelengths [197, 198]. It achives this through the Faraday effect [199], which produces a rotation in the plane of polarization of light passing through the material in presence of an external magnetic field. This property has been employed in construction of optical isolators, which are modules preventing the unwanted feedback between elements of fiber optic circuits.

Apart from the interest motivated by its practical applications, TGG has also drawn attention thanks to its peculiarly low ordering temperature ($T_n \approx 0.25$ K) and several effects pointing to strong interplay between spin and lattice degrees of freedom.

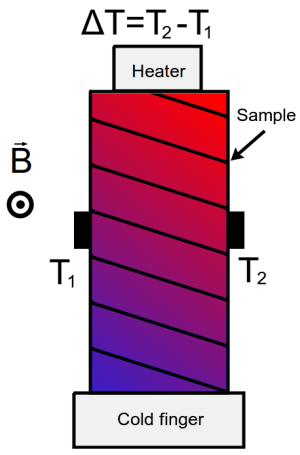

Figure 5.3: Schematic view of a thermal Hall effect measurement setup. The red-blue gradient marks the longitudinal thermal gradient created between the heater and the cold finger, forcing the heat flux. Skew black lines mark the isotherms caused by the transverse gradient ($\Delta T = T_2 - T_1$) of the thermal Hall effect. Black rectangles on the sides of the sample are the thermometers recording the transverse gradient.

5.2.1 Thermal Hall effect

TGG was shown to exhibit a thermal Hall effect [200, 201] (dubbed in some works as the phonon Hall effect), which is a transverse thermal gradient associated with a thermal flux in the presence of perpendicular magnetic field (Fig 5.3). In contrast to metals where a similar heat transport process can be easily assigned to the contribution of charge carriers coupling directly to the magnetic field (Righi-Leduc effect), insulators do not host any candidates for this type of mechanism and TGG is the prototypical material in which such a behaviour was found. Several theoretical models were developed in connection with this observation [202, 203, 204, 205]. They varied from interpretations proposing an intrinsic nature of this effect such as: spin-phonon interactions via coupling to the crystal field [203], to extrinsic-intrinsic involving skew scattering of phonons from CEF levels of superstoichiometric terbium ions [204].

This last model presented in Ref. [204] requires an experimentally detectable inter-site mixing of the ions. It is motivated by the observation of strong suppression of thermal conductivity at $T < 1$ K in crystals grown by the Czochralski method, which is absent in samples grown from solution by the flux method [206]. Superstoichiometric Tb ions are present exclusively in the crystals obtained with the first method[206, 207].

Following this discovery, thermal Hall behaviour was observed in other systems like $Tb_2Ti_2O_7$ [208], a strongly frustrated pyrochlore system; or α-$RuCl_3$ [209] a candidate for an exotic Kitaev spin-liquid state [210, 5]. This has ignited growing interest in the thermal Hall effect as a probe extremely relevant for investigating various exotic topological phases of matter [211, 212, 213, 214], although its occurrence in TGG still lacks a complete microscopic description.

5.2.2 Acoustic Faraday effect

As well as magnetooptical phenomena, TGG was also found to host an acoustic Faraday effect [215] where the plane of polarization of acoustic waves rotates when propagating through a material placed in an external magnetic field [216]. A theory explaining this behaviour by magnetoelastic interactions of $4f$ quadrupole moments with both acoustic and optical phonons [217] was presented. However, this treatment did not include a rigorous treatment of CEF states and used a simplified higher-symmetry cubic local crystal environment. The model can therefore be refined with a more precise description of the CEF scheme in TGG.

5.2.3 Induced-moment type order

The Tb^{3+} ion has [Xe]$4f^8$ electronic configuration, which within the LS-coupling scheme has a $^7F_6$ ground-state term (Sec. 2.1.2). Electronic states of odd-electron (Kramers-type) systems have at least double degeneracy, which is protected by time-reversal symmetry [17]. It can be lifted in case of breaking this symmetry, e.g. by applying a magnetic field. Even-electron non-Kramers ions at the $24c$ Wyckoff position with the low-symmetry point-group D_2 (orthorhombic local environment) should experience a complete lifting of the ground-state term degeneracy (13-fold for $^7F_6$). This is the case observed in TGG [218, 194], where the ground-state is a quasi-doublet formed by two singlets split by small $\Delta \sim 2$ K gap. The non-magnetic singlet ground-state alone cannot account for the appearance of dipole magnetic moments. An additional perturbation is required to admix it with higher CEF states. This phenomenon is referred to as induced-moment ordering.

Historically,the most famous examples of induced moments in singlet ground-state systems are praseodymium (Pr) and Pr-based compounds (e.g. $PrCu_2$ [219], PrNi [220]). These motivated significant effort to create accurate theoretical descriptions of these exotic cases. A mean-field theory [221, 222, 223] was developed that implicates the hyperfine interaction between the magnetic moments of the f-electrons and rare-earth nuclei as triggering the magnetic ordering. It was proposed for case of TGG and HoGaG [180, 218], which undergo the ordering in the milliKelvin regime and are characterized by CEF singlet ground state. However, no investigations accounting for the detailed structure of the low-lying singlets were undertaken. Another theory working within the random-phase approximation [224] proposed a bootstrap process of self-amplifying exchange interactions approaching a critical value and driving the system into the ordered phase. This might be observed as an soft-mode transition in the dispersive CEF excitons, which lose their localized single-ion character due to the aforementioned coupling. Several experimental observations of this phenomena have been made [225, 220], although not many reports have been presented for Tb-based compounds [226]. The availability of new generation time-of-flight and triple-axis neutron spectrometers should allow for the acquisition of high quality data and over broader ranges in $(\boldsymbol{Q}, E)$ space than previously possible should therefore provide the basis for a more detailed examination of thermal Hall and acoustic Faraday effects, and possible reinterpretation of their origin in the light of contemporary theories of solid state physics. TGG offers an excellent opportunity for this type of study and we plan to provide clearer picture of its low-energy physics.

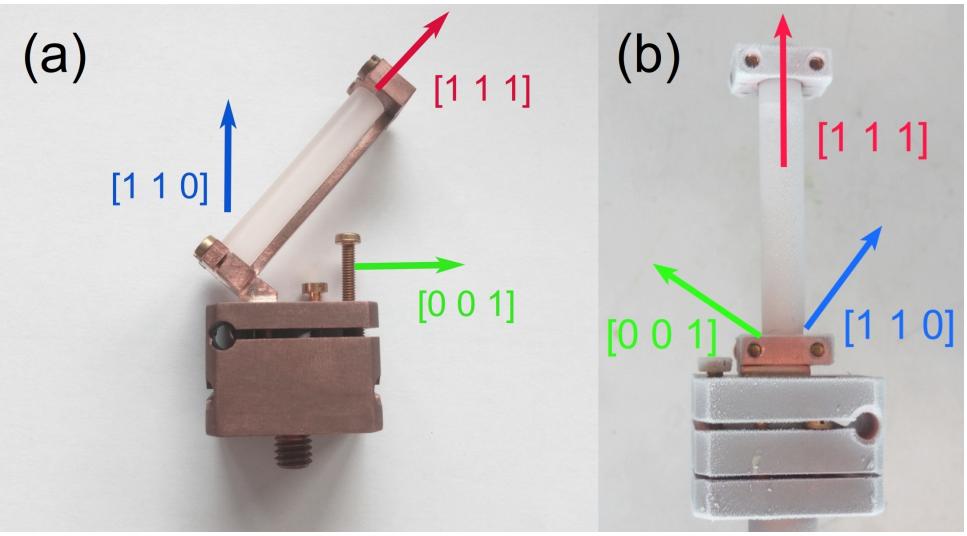

Figure 5.4: Single-crystal samples of TGG attached to copper mounts. Arrows mark the high symmetry crystallographic directions.

5.2.4 Sample characterization and bulk properties of $Tb_3Ga_5O_{12}$

Further details of the experimental procedures behind the results presented in the following sections of this chapter are given in Table A.2 of Appendix A.

Samples

The application of TGG crystals in optical isolators has led to the commercial availability of very high quality crystals. Four single-crystals in the form of a cylindrical rods (Fig. 5.4) with $\varnothing = 6$ mm and $l = 40-50$ mm) were acquired from FEE (Idar-Oberstein, Germany) [227]. The rods were cut out of an ingot grown by the Czochralski method. One of them was crushed to a fine powder in an agate pestle and mortar and used for powder neutron scattering experiments and bulk characterization measurements.

In order to precisely determine the crystalline structure of the samples and check for the presence of superstoichiometric terbium ions a synchrotron x-ray powder diffraction (SXRPD) experiment was performed. Fig. 5.5 shows a Rietveld refinement of SXRPD data and the resulting parameters are shown in Tab. 5.1. The lattice constant of TGG at room temperature was found to be $a = 12.35225(1)$ Å. Superstoichiometric Tb^{3+} ions were found exclusively at the octahedral Ga site 16*a* (with trigonal point-group C_{3i} or $\bar{3}$). They occupy 1.51(2)% of these gallium sites. Attempts to refine site mixing between 24*c* terbium and 24*d* gallium sites led to nonphysical results with negative occupancy for one of the sites. Unfortunately the small difference between the coherent neutron scattering lengths of Tb and Ga (b_c(Tb) = 7.34(2) fm and b_c(Ga) = 7.288(2) fm) did not allow for cross-verification of this result in the following neutron experiments, as strong correlation between the parameters led to the divergence of the fitting. The observation of superstoichiometric Tb^{3+} is in agreement with previous studies on samples grown by the Czochralski method [207] and does not exclude the presence of the thermal Hall mechanism described in Ref. [204].

The initial characterization of the magnetic properties in the paramagnetic phase

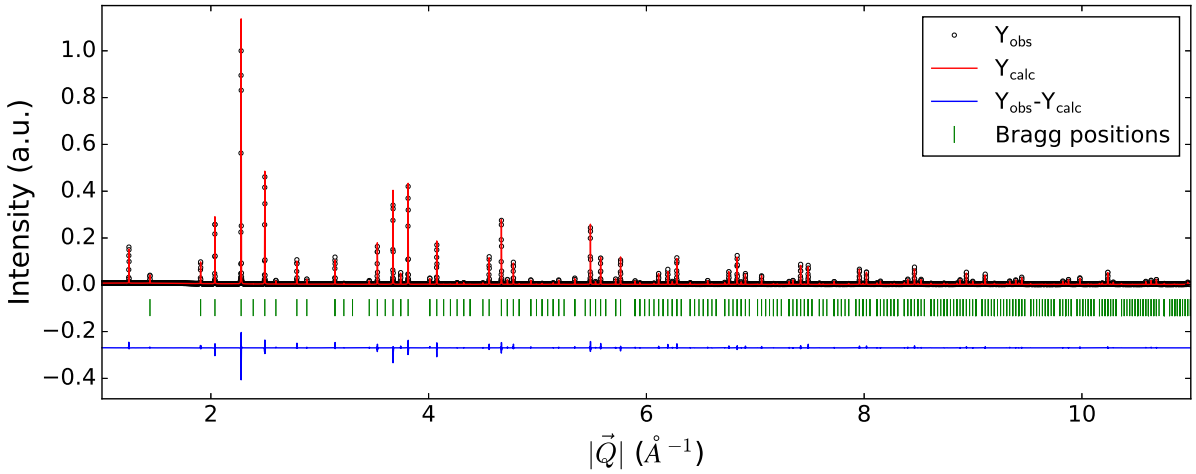

Figure 5.5: Rietveld refinement of synchrotron x-ray powder diffraction data measured on TGG at room temperature ($T = 298$ K). Goodness of fit parameters: $R_{\mathrm{wp}} = 11.6$, $R_{\mathrm{exp}} = 2.87$ and $\chi^2 = 16.4$. Open circles mark the results of measurements, the red and the blue solid lines show the calculated intensities and the difference between refined and measured pattern, respectively. Green markers point the position of Bragg reflections deduced from the refined structural model. The refined structural parameters are shown in Tab. 5.1. The data was measured at the MS - X04SA beamline of the SLS - PSI facility with x-ray wavelength $\lambda = 0.565$ Å.

Table 5.1: Structural parameters obtained by Rietveld refinement of SXRPD pattern measured at room temperature. Tb2 stands for superstoichiometric Tb^{3+} ions at the 16*a* gallium position.

Atom	Wyckoff position	x	y	z	Occupancy	B_{iso} (Å^2)
Ga1	16*a*	0	0	0	1.969(3)	0.217(5)
Tb2*	16*a*	0	0	0	0.031(3)	0.217(5)
Tb	24*c*	1/8	0	1/4	3	0.239(1)
Ga2	24*d*	3/8	0	1/4	3	0.283(3)
O	96*h*	0.286(1)	0.0566(1)	0.6500(1)	12	0.23(2)

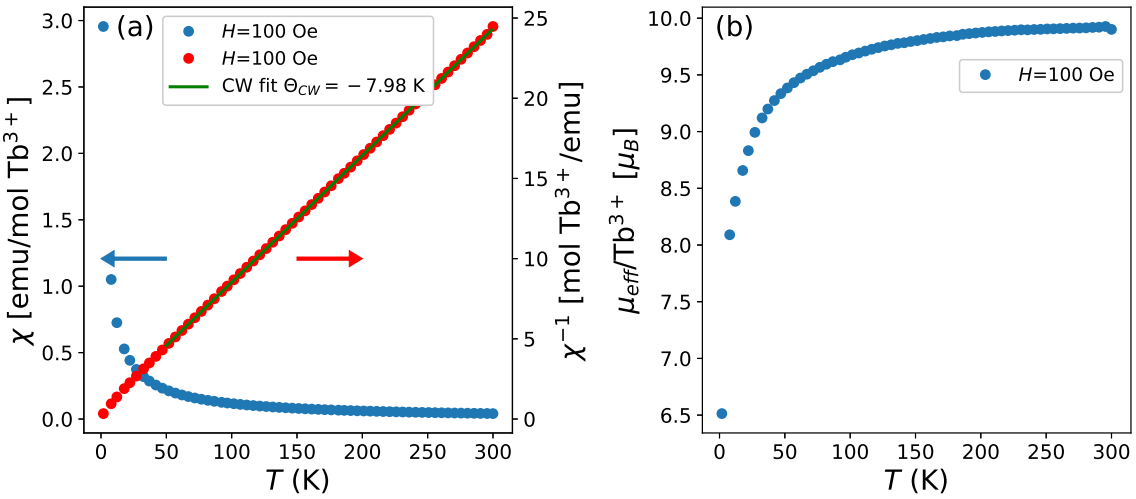

Figure 5.6: The temperature-dependence of (a) static magnetic susceptibility (b) effective paramagnetic moment per Tb^{3+} ion, measured on a powder sample of TGG. The solid green line in (a) shows fit to the Curie-Weiss law with $\Theta_{CW} = -7.98$ K .

was performed on a powder sample using a SQUID magnetometer (Sec. 3.2) (Quantum Design MPMS XL-7 system). Fig. 5.6(a) shows the temperature-dependence of the static magnetic susceptibility and its inverse between 300 and 1.8 K. The inverse susceptibility shows linear behaviour down to $T = 50$ K, which is fitted to the Curie-Weiss law with $\theta_{\mathrm{CW}} = -7.98$ K. In combination with $T_{\mathrm{N}} \sim 0.25$ K, this would give a value of frustration parameter $f \sim 32$ (Sec. 2.5), a much lower value than observed in chromate spinels (Chap. 4), which suggests that the system is moderately frustrated and that a correlated paramagnetic phase is expected for $0.25 < T < 7.98$ K.

The temperature-dependence of the effective paramagnetic moment, $\mu_{\mathrm{eff}} = \sqrt{\frac{3k_{\mathrm{B}}}{N_A\mu_{\mathrm{B}}^2}\chi T}$, is plotted in Fig. 5.6(b). At high-temperature μ_{eff} saturates: for the range $260 < T < 300$ K the average value $\mu_{\mathrm{eff}} = 9.913(3)\ \mu_{\mathrm{B}}$ differs by only 2% from $\mu_{\mathrm{Tb^{3+}}} = 9.72\ \mu_{\mathrm{B}}$, the theoretical paramagnetic moment $\mu = g_J\sqrt{J(J+1)}\ \mu_{\mathrm{B}}$ per Tb^{3+} ion in the $^7F_6$ ground-state multiplet [17]. This value drops slowly on cooling down to $T = 50$ K, where more rapid decrease is observed. At $T = 1.8$ K $\mu_{\mathrm{eff}} = 6.5\ \mu_{\mathrm{B}}$. This suggests that low-energy CEF states are dominated by $J < 6$ states of the $^7F_6$ multiplet and points to the magnitude of the ordered magnetic moment being reduced with respect to the magnitude of the paramagnetic moment.

5.3 Low-temperature ordered magnetic structure of $Tb_3Ga_5O_{12}$

TGG has been reported to undergo magnetic ordering at $T_{\mathrm{N}} = 0.25$ K [180] and $T_{\mathrm{N}} = 0.24$ K [218]. The low-temperature ordered structure was found to be identical with the one of DAG, described by the $Ia\bar{3}d'$ magnetic space group. However, Fig. 2 in Ref. [218] (Fig. 5.8(a)) shows that the magnitude of the spontaneous magnetic moment retrieved from powder neutron diffraction data does not saturate down to $0.2T_{\mathrm{N}} = 0.048$ K

and stays much below $\mu_s = 6.68\ \mu_B$, the ordered magnetic moment obtained with self-consistent mean field calculations in Ref. [180]. Furthermore, the temperature-evolution of the ordered moment presented in this study does not resemble the steep growth of the ordered moment on cooling, expected for ordinary antiferromagnetic ordering in $3d$ Ising antiferromagnets on the simple BCC lattice and observed in DAG [185, 186, 158].

In order to analyze this discrepancy in detail, a time-of-flight neutron powder diffraction experiment was performed. In light of the suppression of thermal conductivity at $T < 1$ K in Czochralski grown TGG samples, the powder used for this experiment sample was compacted inside the can to provide good contact between the grains of powder, as well as between the outer layer of powder and the copper can. The can was indium sealed and equipped with a capillary allowing for injection of ^{4}He exchange gas, which was intended to further facilitate the sample's thermalization. Moreover, prior to the start of the measurement, the sample was precooled for 12 hours, with the mixing chamber of the dilution refrigerator being kept at its base temperature of $T_{base} = 0.03$ K. For the first diffraction patterns, collected immediately after opening the beam shutter the presence of magnetic Bragg peaks was observed in the low-$|\boldsymbol{Q}|$ region. However, it was noted that their intensity decreased with the time of sample's exposure to the neutron beam. The intensity of magnetic reflections was almost completely suppressed after 90 min of counting time and could not be recovered by closing the shutter and stopping the sample's exposure for times as long as two hours while maintaining the refrigeration.

All these observations seem to be consistent with beam-heating effects resulting from the energy deposition due to the absorption of neutrons and emission of photons by the nuclei constituting the sample. The size of the effect is surprising taking into account the values of the absorption cross-section coefficients: $\sigma_{abs\,Tb} = 23.4(4)$, $\sigma_{abs\,Ga} = 2.75(3)$) and $\sigma_{abs\,O} = 1.9(2) \times 10^{-4}$ [228]. On the other hand, suppression of thermal conductivity in TGG and small contact surfaces between the grains of the powder could prevent the thermalization of the heated sample volume with the mixing chamber of dilution refrigerator. Additionally, similar behaviour was observed during a single-crystal measurement on a three-axis neutron spectrometer where no magnetic ordering was observed with the mixing chamber of dilution fridge kept at $T \approx 0.045$ K, until the velocity selector attenuating the beam intensity was introduced.

The magnetic intensity (Fig. 5.7(a)) was retrieved from the data measured between $15 - 55$ min of opening the shutter, which corresponds to the data collected over the time, when partial suppression of the magnetic reflections took place, and hence reflects an average over some range of temperatures below T_N. It was separated by subtracting the data measured at $T = 15$ K in the paramagnetic regime. A flat background was added to avoid negative intensities, which result from paramagnetic diffuse scattering. The observed magnetic reflections were indexed with the $\boldsymbol{k} = (1, 1, 0)$ magnetic propagation vector, which in the case of BCC-type lattice is equivalent to $\boldsymbol{\Gamma} = (0, 0, 0)$ special $\boldsymbol{k}$-vector.

Representational analysis was employed to determine the ordered magnetic structure (Sec. 2.3.4). With the help of the the `ISOTROPY` package [229], eight irreducible representations of the space-group and the propagation vector $\boldsymbol{\Gamma}$ were found ($2 \times$ 1-dimensional: $m\Gamma_2^+$, $m\Gamma_2^-$; $2 \times$ 2-dimensional: $m\Gamma_3^+$, $m\Gamma_3^-$; $4 \times$ 3-dimensional: $m\Gamma_4^+$, $m\Gamma_4^-$, $m\Gamma_5^+$ and $m\Gamma_5^-$; in Miller-Love notation [151]). Their magnetic moment basis functions were projected out and combined with corresponding order parameter directions. These generated fourteen possible sets of basis vector directions. Eleven sets were excluded in preliminary

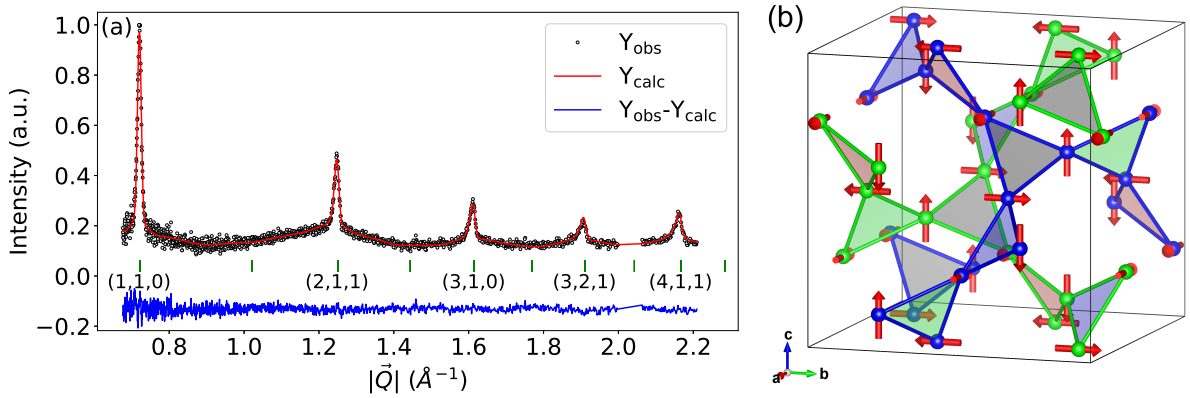

Figure 5.7: (a) Rietveld refinement of magnetic reflections in low-temperature neutron powder diffraction data measured on TGG. Green bars mark the position of magnetic reflections consistent with the $\boldsymbol{k} = (1, 1, 0)$ magnetic propagation vector. Indices of the reflections present in the pattern are given below the green markers. The data was measured on the WISH TOF neutron diffractometer at the ISIS neutron source. (b) resulting magnetic structure described by $Ia\bar{3}d'$ magnetic space group. Figure created with `VESTA` software [60].

analysis as they were incompatible with observed presence or absence of certain magnetic Bragg reflections in the experimental diffraction pattern, i.e. the diffraction data show the presence of $(1, 1, 0)$ antiferromagnetic and absence of $(2, 0, 0)$ ferromagnetic reflections (Fig. 5.7(a)). Rietveld refinement of the remaining possibilities, and examination of the relative intensities of the observed reflections, allowed for unambiguous assignment of the 1-dimensional irreducible representation $m\Gamma_2^+$ to the observed pattern (Fig. 5.7(a)). The determined structure corresponds to the magnetic space-group $Ia\bar{3}d'$. A graphical representation of the determined magnetic structure is shown in Fig. 5.7(b)).

The scale factor of the Rietveld refinement was set by refining the room temperature structural model obtained from the x-ray experiment against the neutron data measured at 15 K. In the course of the magnetic intensity refinement, the wavelength-dependent absorption correction parameters were re-refined to provide a better match in the low-$|\boldsymbol{Q}|$ region, as the previous parameters came from refinements of patterns that were dominated by intensities in the high-$|\boldsymbol{Q}|$ region, which are less sensitive to these parameters. These adjustments permitted an excellent correspondence of the observed and calculated magnetic intensities in this limited $|\boldsymbol{Q}|$-range (Fig. 5.7(a)). The strength of the ordered magnetic moment was determined to be $|\mathbf{m}| = 2.16(9)\ \mu_B$, given the time averaging. This provides a lower limit for the spontaneous magnetic moment in TGG. It is furthermore significantly smaller than that highest value achieve in previous reports for TGG $|\mathbf{m}| = 4\ \mu_B$ [218], but consistent with the heating of the sample towards T_N. The refinement of data measured during a further single-crystal diffraction study (Fig. 5.9) provided an estimate of $|\boldsymbol{m}| = 3.56(3)$. No temperature-dependence of the magnetic moment was collected during that measurement, but there are strong arguments in favour of full thermalization of the sample in this experiment (as in the subsequent three-axis neutron experiment - Fig. 5.8(b)). Firstly, while using cryogenic devices of the same power for

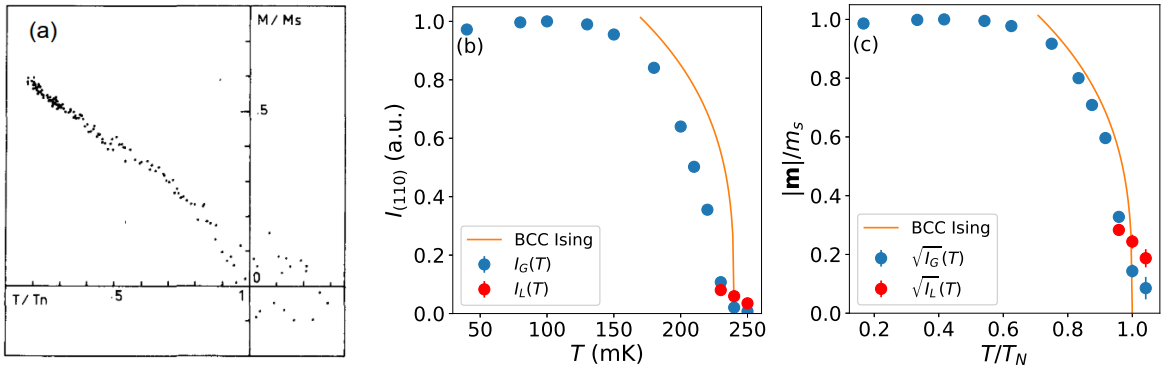

Figure 5.8: (a) the temperature-dependence of the order parameter for the antiferromagnetic transition in TGG presented in Ref. [218], data measured with neutron powder diffraction (adapted from Ref. [218]). (b) the temperature-dependence of the intensity of $(1, 1, 0)$ magnetic Bragg reflection and associated spontaneous magnetisation. Blue and red dots mark the separated Gaussian Bragg and Lorentzian critical scattering respectively. The solid orange line shows the results of calculations described in the text. Data measured on a single-crystal sample (Fig. 5.4(a)) with $k_\mathrm{i} = k_\mathrm{f} = 1.2$ Å^{-1} using Si(111) monochromator and analyzer setup on THALES three-axis neutron spectrometer.

both experiments, the sample used for a single-crystal diffraction was in the form of a small square plaquette ($4 \times 4 \times 1$ mm^3) of mass ~ 50 times smaller than the rod used for three-axis measurement (Fig. 5.4(a)). Secondly, the neutron flux in neutrons/(cm^{2}s) of these instruments in their respective operating modes differs by approximately two orders of magnitude, with a higher flux at the three-axis instrument. This suggests that the magnetic moments observed in the diffraction data (Fig. 5.9) are fully saturated at the nominal temperature.

As the powder diffraction experiment allowed only a partial insight into the development of magnetic order of TGG, this issue was further investigated, along with other aspects in TGG discussed in the following sections of this chapter, in subsequent single-crystal studies. Fig. 5.8(a) shows the temperature-dependence of the magnetic order parameter, of TGG presented in Ref. [218]. Figs. 5.8(b) and 5.8(c) show the temperature dependent intensity of the strongest $(1, 1, 0)$ magnetic Bragg reflection measured on a single-crystal sample and the resulting order parameter curve. The intensities were obtained from Gaussian fits to the Bragg peaks and Lorentzian fits to the magnetic critical scattering [158], which gives a substantial contribution while approaching T_N, similarly to the case of DAG [185, 186]. Contrary to the results from Ref. [218] the order parameter curve presented in Fig. 5.8(c) reaches its saturation value at $T \sim 0.5T_\mathrm{N}$.

The solid lines in Figs 5.8(b) and 5.8(c) represent calculations using the following relation [185]:

$$\sqrt{\frac{I(T)}{I(T=0)}} = \frac{|\boldsymbol{m}|(T)}{|\boldsymbol{m}|(T=0)} = D\left(\frac{T_\mathrm{N} - T}{T_\mathrm{N}}\right)^{\beta}, \tag{5.1}$$

where β is the appropriate critical exponent corresponding to the order parameter of

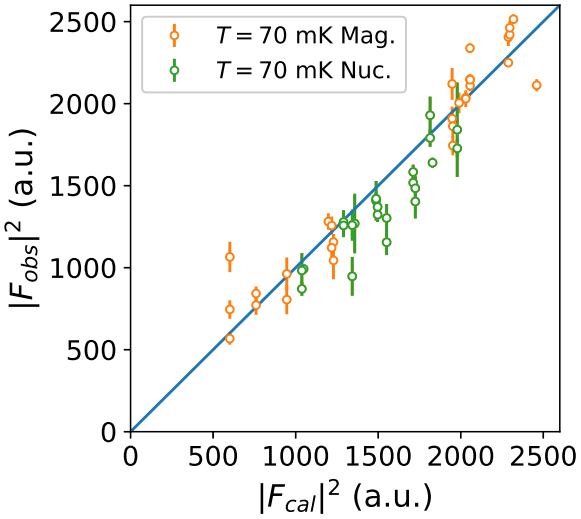

Figure 5.9: Refinement of single-crystal diffraction data consisting of 85 nuclear and magnetic reflections. The orange points mark the purely magnetic reflections while the green represent nuclear reflections and these of mixed character. The magnetic space group of the refined structure is $Ia\bar{3}d'$ and its details are given in the text. The weighted goodness of fit parameter for the refinement is $\chi^2 = 2.51$. Data measured with $\lambda = 2.362$ Å and at $T = 70$ mK on the D23 single-crystal diffractometer at the ILL facility.

the transition and D is a prefactor defined in Ref. [230]. The values of $\beta = 0.312(5)$ [231] and $D = 1.491(1)$ [230] were adapted from a Padé-approximation of the low temperature expansion for the three dimensional Ising antiferromagnet with nearest neighbour interactions. Similarly to the case of DAG, TGG shows a departure from the results obtained with this simplified model, which most probably result from the long-ranged character of dipole-dipole interactions [185]. However the observed deviation is less pronounced than that reported in Ref. [218]. The neutron beam heating effects encountered during our neutron scattering experiments on TGG, are likely the cause of this anomalous result.

5.4 Diffuse scattering in $Tb_3Ga_5O_{12}$

The development of magnetic correlations, in spin-liquid phases of strongly correlated magnets, on cooling towards T_N can be investigated in the structure factor of the diffuse magnetic scattering. A polarized (Sec. 3.1.3) single-crystal diffraction experiment was performed on TGG at the D7 diffuse scattering spectrometer (Fig. 3.10). The sample was aligned with its scattering plane perpendicular to the [111] crystallographic direction ([111] $\parallel z$). (Fig. 5.4(a)). The temperature-dependence of the total structure factor measured for the spin-flip and non spin-flop channels was investigated. These are $\left(\frac{d\sigma}{d\Omega}\right)_z^{SF}$ and $\left(\frac{d\sigma}{d\Omega}\right)_z^{NSF}$ (Eq. 3.26). A full XYZ-difference analysis at two reference temperatures 50 and 1.5 K allowed for separation of the nuclear and nuclear spin-incoherent contributions to the scattering, which were subsequently used to separate the purely magnetic scattering in the SF and NSF data, $M_{z'}$ and M_z, respectively. These channels give access to magnetisation parallel to z ([111]) in case of the former, and perpendicular to z for the

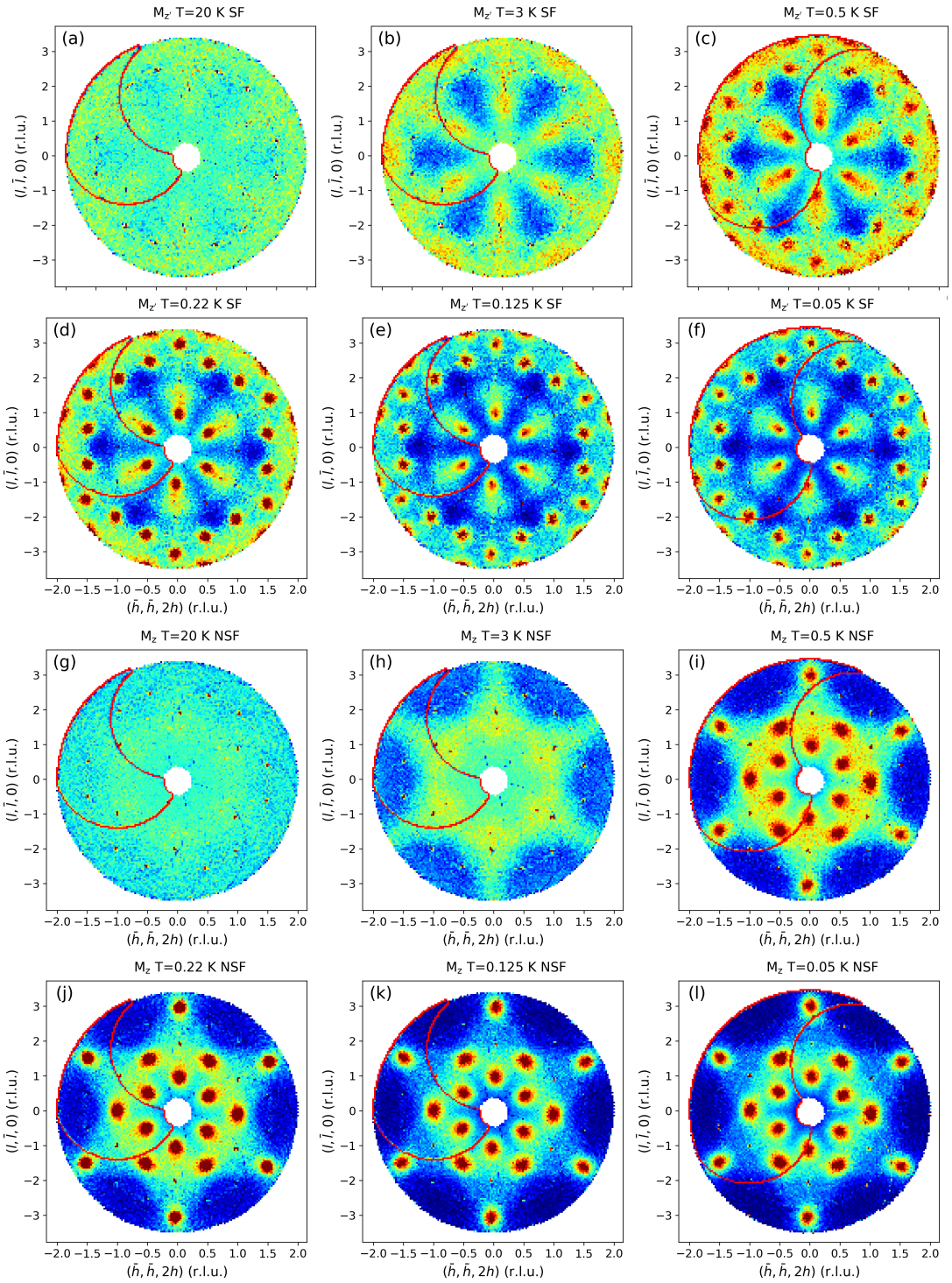

Figure 5.10: The temperature evolution of the structure factor of diffuse neutron scattering measured on a single-crystal sample of TGG. The $M_{z'}$ (SF) and M_z (NSF) intensities refer to spin-flip and non-spin-flip scattering with respect to $z|||[111]$ direction of neutron beam polarization, which reflect the magnetisation component within and out of scattering plane respectively (Sec. 3.1.3). Data measured with $\lambda = 4.855$ Å at the D7 spectrometer at the ILL facility. Datasets were symmetrised accordingly to the rotational symmetry of the scattering plane. Red outlines mark the unsymmetrised data.

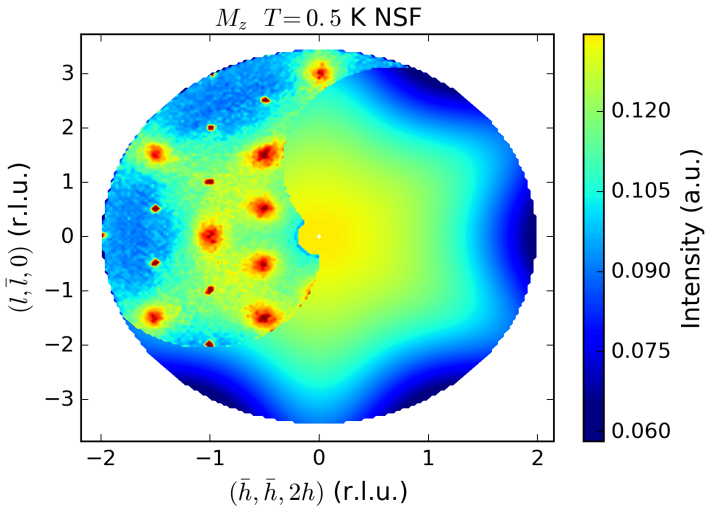

Figure 5.11: Comparison of the magnetic structure factor measured in diffuse non-spin-flip scattering from TGG at $T = 0.5$ K and that calculated for a single triangle in the half-garnet lattice lying in the scattering plane, populated with magnetic moments oriented according to the ordered structure.

latter. Fig. 5.10 shows their temperature-dependence in TGG. Weak signatures of the shapes that dominate the structure factor at lower temperatures can already be noted at temperatures as high as $T = 20$ K. At $T = 3$ K one can easily notice a flower-shaped pattern in the SF scattering (Figs. 5.10(a)-(f)) and a star-shaped one in the NSF scattering (Figs. 5.10(g)-(l)) . The latter resembles the unpolarized magnetic structure factor of a single triangle forming the half-garnet lattice, populated with magnetic moments according to the long-range order in TGG. Fig. 5.11 show the diffuse scattering calculated for a triangle lying in the scattering plane and populated by three mutually perpendicular moments, pointing along main crystallographic directions of the unit cell, similarly to the ordered structure. A good qualitative agreement suggests that a single triangle might be a relevant structural unit for short-range correlations in the cooperative paramagnetic phase present in TGG. However, such a short length of the correlations in the vicinity of T_N would be rather surprising.

The second observation that can be made on the basis of these resutls is that although the magnitude diffuse intensity in the scattering data decreases on cooling down below the ordering temperature, some of it remains present. This is consistent with the reduced value of the ordered moment observed in neutron scattering experiments with respect to the saturated moment from single-crystal magnetisation data (Ref. [180]).

5.4.1 Spin structure annealing.

In an attempt to determine the correlations giving rise to the appearance of the diffuse scattering, a custom procedure for retrieval of spin structures from diffuse scattering was developed. It was based on minimization of the following goodness of fit parameter:

Table 5.2: Goodness of fit parameter for annealed spin configurations and their standard deviation between the 10 refined boxes.

T (K)		0.5	0.05		0.5	0.05
SF	$\langle\chi^2\rangle$	83308	116782	$\sigma(\chi^2)/\langle\chi^2\rangle$	0.016	0.14
NSF	$\langle\chi^2\rangle$	8039	10788	$\sigma(\chi^2)/\langle\chi^2\rangle$	0.012	0.0095

$$\chi^2 = \sum_{\boldsymbol{Q}} \left(\frac{I_{\text{obs}}(\boldsymbol{Q}) - I_{\text{calc}}(\boldsymbol{Q})}{\sigma(\boldsymbol{Q})} \right)^2, \tag{5.2}$$

with $I(\boldsymbol{Q})$ representing the measured and calculated intensities proportional to the magnetic double differential cross-section (Eq. 3.9), and $\sigma(\boldsymbol{Q})$ being the experimental uncertainty. The refinement consisted of a step-wise annealing routine applied to a $5 \times 5 \times 5$ unit cell box, containing 3000 magnetic moments of unit length placed on the crystallographic sites of Tb ions in TGG. The procedure was initialized by generating a random configuration of moments. Their directions were constrained by the sensitivity of given channel for probing specific orientations of the magnetisation within the sample (SF in single plane, $M_{z'} \perp [111]$ and NSF along single direction, $M_z \parallel [111]$). The $I_{\text{calc}}(\boldsymbol{Q})$ was calculated with `SPINDIFF`, a very efficient program for calculating the single-crystal magnetic structure factor of spin structures, distributed alongside the `SPINVERT` RMC software [155]. It speeds up this otherwise computationally expensive procedure by performing calculations for all possible $n \times n \times n$ sub-boxes (in this case $n = 2$ appeared to have optimal efficiency versus fidelity of reproducing details), employing periodic boundary conditions and then averaging over those sub-boxes and applying a fast blurring algorithm [155]. Each annealing step consisted of i random rotations of j magnetic moments (rotations preserved the constraints imposed by scattering channel), where $i = 10^4/j$ and j takes 18 gradually decreasing values between 300 (10% of all magnetic moments in calculation box) and 1, with only the rotations improving χ^2 being accepted. The last step of 10^4 rotations of a single moment was repeated to improve the agreement of fine details between the observed and calculated diffuse scattering. Further attempts at refinement did not result in any significant changes. The refinement process was performed in parallel on ten spin-boxes with different random initial configurations.

In order to test the method, a refinement of the $T = 0.5$ K and $T = 0.05$ K data was performed. The resulting goodness of fit parameters and their standard deviation between the set of ten boxes are presented in Table 5.2. The fitted scattering intensity averaged over all ten boxes for the SF channel at both temperatures is presented in Fig. 5.12. For both datasets excellent agreement with the experimental intensity was achieved, even with the constraint of magnetic moments fixed in the scattering plane, as a result of scattering channel's sensitivity to this in-plane component of the magnetic moments.

Radial spin-spin correlation functions for both refined spin-boxes were retrieved with the use of the `SPINCORREL` code provided with `SPINVERT` [155]. These are plotted in Fig. 5.13. Surprisingly despite the observation of distinct magnetic structure factors, no significant dipolar correlations were found within the refined structures. Moreover, the significant differences between the shape of diffuse features at higher temperatures and

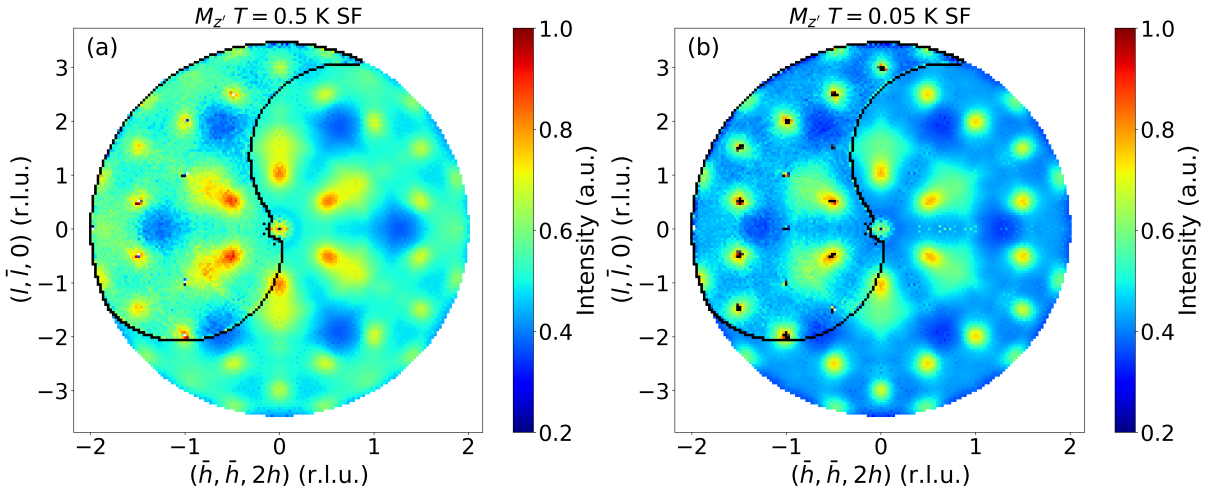

Figure 5.12: Measured data compared with the results of spin structure annealing, for spin-flip diffuse scattering from TGG at $T = 0.5$ and $T = 0.05$ K. The black outline marks the experimental data. The black dots within the outline mark pixels removed as being the magnetic Bragg reflections due to containing high intensity.

below the ordering transitions is not reflected in the radial correlation functions. One can observe a slight decay in $\langle \boldsymbol{S}_0 \cdot \boldsymbol{S}(r) \rangle$ at large distances r, however it does not show a consistent trend and the absolute values are comparable with uncertainties.

Refinements of the data measured in non spin-flip channel (Fig. 5.14) gave similarly good agreement, although the standard deviation of the goodness of the fit is smaller with respect to the average χ^2 for $T = 0.05$ K, in contradiction with the case of refinements on spin-flip data. The radial spin-spin correlations retrieved from these refinements presented in Figure 5.15 reach values three times larger than observed in the psin-flip refinement. Instead of being a signature of dipolar order parameter governing the observed spin-liquid behaviour it should rather be assigned to the much harsher constraints imposed on refined moments, which are fixed to point along the [111] crystallographic direction. Thus relative orientations of the magnetic moments in these structures must be either parallel or antiparallel giving a much higher probability of contributing an average non-zero $\boldsymbol{S}_i \cdot \boldsymbol{S}_j$.

The above results point to the presence of a correlated paramagnetic phase in TGG. The first signatures of the appearance of the correlations in diffuse neutron scattering appear at $T > 3$ K, which is a relatively high value with respect to the temperature of magnetic ordering $T_N = 0.24$ K. However this temperature is low when comparing to the Curie-Weiss constant. The onset of magnetic long-range order does not fully suppress the diffuse intensity suggesting either incomplete ordering with some static component deviating from the long-range order, or presence of the persistent slow dynamics in the form of correlated fluctuations out of the equilibrium of the ordered state. In the former scenario one has to look for more complex non-dipolar order parameters governing this hidden order similarly to the case observed in GGG [157]. The crucial difference between these systems, and the possible of origin of their different correlated states, is the strong anisotropy provided by the Tb^{3+} single-ion physics. The latter option might be examined in detail, for example with use of neutron spectroscopy, or other resonance probe with

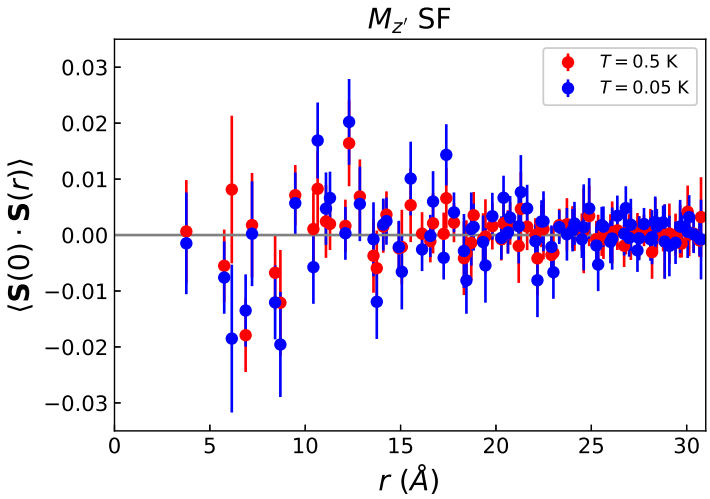

Figure 5.13: Radial spin-spin correlation functions retrieved from spin structures annealed during refinement of spin-flip diffuse scattering intensity in TGG, probing the component of magnetisation perpendicular to z ([111]).

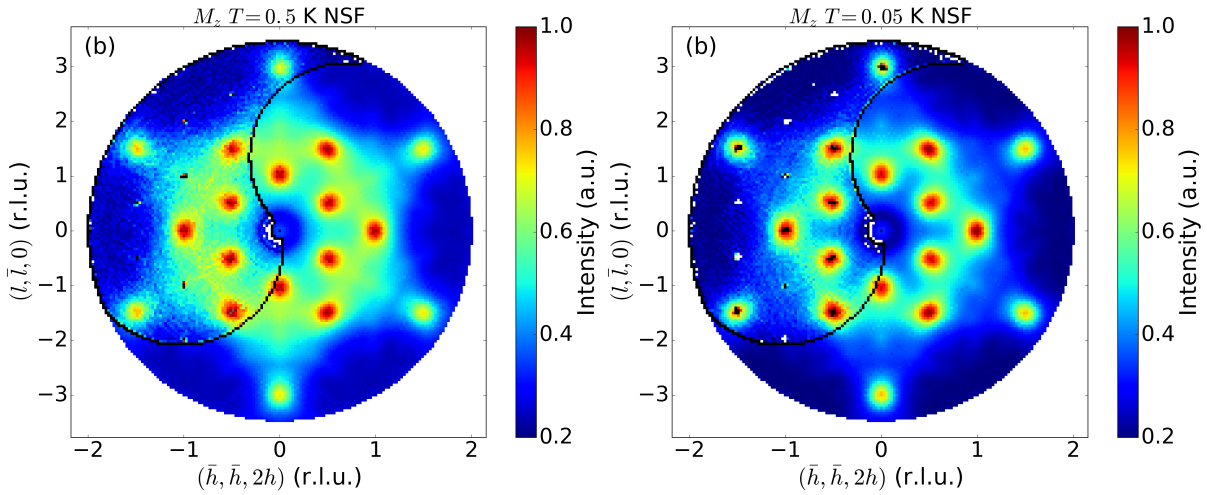

Figure 5.14: Measured data compared with the results of spin structure annealing for non spin-flip diffuse scattering from TGG at $T = 0.5$ and $T = 0.05$ K. The black outline marks the experimental data. Black dots within the outline mark pixels removed for containing nuclear and magnetic Bragg reflections and outliers caused by background and spin-incoherent subtractions.

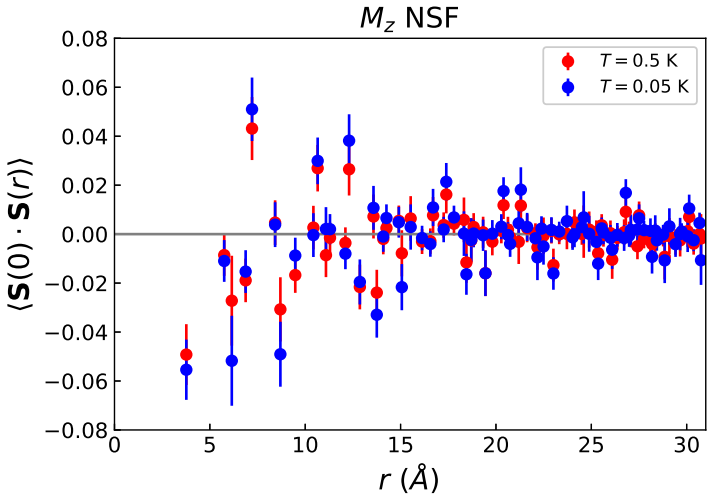

Figure 5.15: Radial spin-spin correlation functions retrieved from spin structures annealed during refinement of non spin-flip diffuse scattering intensity in TGG, probing the component of magnetisation parallel to z ([111]).

appropriate time-window of for the dynamics.

5.5 Crystal field effects in $Tb_3Ga_5O_{12}$

The highly anisotropic magnetically ordered structure observed in TGG and a vast majority of other rare-earth garnets points to the dominant effect of the crystal electric field (CEF) on the low-energy physics. This is generally expected in the case of rare-earth magnets and makes the knowledge of CEF Hamiltonian eigenstates a vital starting point for the further understanding of complex phenomena in TGG.

As was described in Sec. 2.1.3 the Tb^{3+} ion exhibits a 13-fold degenerate $^7F_6$ ground-state manifold. In a low-symmetry orthorhombic local environment this degeneracy should be fully lifted, resulting in a rich spectrum of possible CEF excitations. For orthorhombic site-symmetry and $J = 6$, the following symmetry decomposition of CEF eigenstates is expected [232]: $4\Gamma_1 + 3\Gamma_2 + 3\Gamma_3 + 3\Gamma_4$ (Γ_α, with $\alpha = 1, 2, 3, 4$, are the irreducible representations of the D_2 point-group), where Γ_α states are of the following form: $|\psi_i\rangle = \sum c_{i,M_J} |J, M_J\rangle$, with $i = 0 - 12$. The $|J, M_J\rangle$ states are $^7F_6$ states with $1 \leq J \leq 6$ and $-6 \leq M_J \leq 6$. Earlier attempts to provide a detailed description of CEF effects in TGG were based on the analysis of four energies of transitions from CEF ground-states to excited states, which correspond to differences between the eigenvalues. These were combined with the fits to single-crystal magnetisation data, which shows a step-like feature reflecting the crossing of CEF energy levels in external magnetic field [233]. The Stevens CEF Hamiltonian describing the LS coupling (Sec. 2.1.3) for the D_2 point-group of rare-earth ion site within the ground-state term requires evaluation of 9 parameters:

$$\begin{aligned}\hat{\mathcal{H}}_{\text{CEF D2}} = &\widetilde{B}_0^2\hat{O}_0^2 + \widetilde{B}_2^2\hat{O}_2^2 + \widetilde{B}_0^4\hat{O}_0^4 + \widetilde{B}_2^4\hat{O}_2^4 + \widetilde{B}_4^4\hat{O}_4^4 \\ &+ \widetilde{B}_0^6\hat{O}_0^6 + \widetilde{B}_2^6\hat{O}_2^6 + \widetilde{B}_4^6\hat{O}_4^6 + \widetilde{B}_6^6\hat{O}_6^6.\end{aligned} \tag{5.3}$$

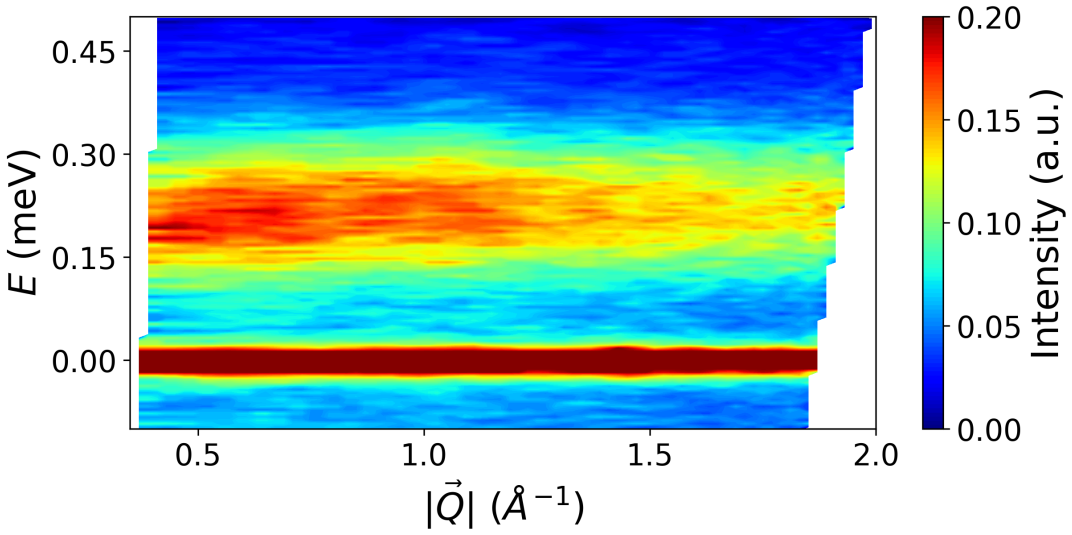

Figure 5.16: Splitting of the quasi-doublet CEF ground-state in the inelastic neutron scattering data measured on a powder sample of TGG at $T = 5$ K, using the PG(002) analyzer setup on the IRIS neutron spectrometer at the ISIS neutron source.

This suggests that the approach adapted in Ref. [233] makes this problem under-constrained.

Inelastic neutron scattering makes an ideal probe for investigating CEF excitation spectra in rare-earth systems, as it can probe energy transfers varying from tens of μeV to above 100 meV, covering the range of usual splittings of the manifold of the ground-state term. The opposite $\boldsymbol{Q}$-dependence for CEF excitations (following the magnetic form factor [234] decreasing scattering intensity with increasing $\boldsymbol{Q}$) and lattice excitations (scattering intensity follows $S \sim \boldsymbol{Q}^2$ dependence) helps to separate the different contributions to the scattering function. Due to the fact that CEF effects, in principle, are strongly localized single-ion effects they should not show any $\boldsymbol{Q}$-dependence and measurement on a powder sample should provide adequate information.

Fig. 5.16 shows the low-energy part of the CEF spectrum, where a transition between the lowest-lying quasi-doublet is observed, confirming the conclusions of previous works [233, 194]. The observed gap $\Delta = 0.22$ meV does not show any anomalous wavevector dependence at this temperature, but the linewidth of the excitation greatly exceeds the instrumental resolution of the IRIS spectrometer with the PG(002) analyzer setup ($\Delta E \approx 17.5$ μeV).

Higher-energy parts of the neutron spectra are shown in Fig. 5.17. In panel (a) one can easily identify a strong feature centered around $E \sim 5$ meV. It is consistent with the only previous report on observation of crystal field levels in TGG [235], where by means of electronic Raman scattering four CEF levels were found in the range $E = 4.2 - 6.6$ meV (Tab. 5.4). At higher energies two more groups of excitations that are flat in $|\boldsymbol{Q}|$ are found. Namely, one centered around $E = 27$ meV, consisting of two distinct lines, and one of more complex shape at $E = 33 - 37$ meV. No clear signs of any other features of magnetic character were found above this energy up to energy transfer $E = 150$ meV.

In order to confirm the magnetic character of the observed spectral features their $|\boldsymbol{Q}|$-

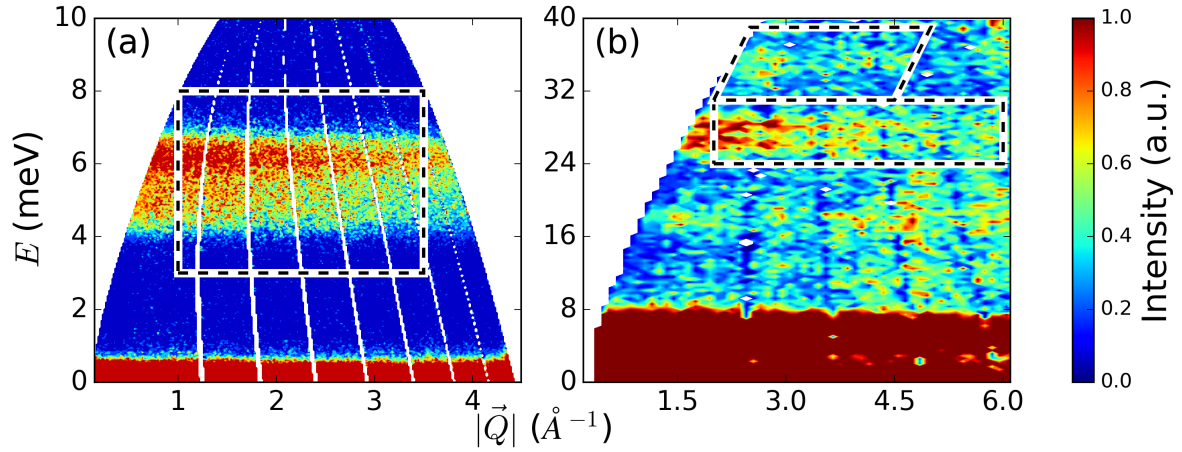

Figure 5.17: CEF excitations in the inelastic neutron scattering data measured on a powder sample of TGG at $T = 5$ K. Data collected on the MARI neutron TOF spectrometer at the ISIS neutron source with (a) $E_i = 12$ meV and (b) $E_i = 50$ meV. Polygons drawn with the black dashed line show the integration ranges for the cuts plotted in Fig. 5.20.

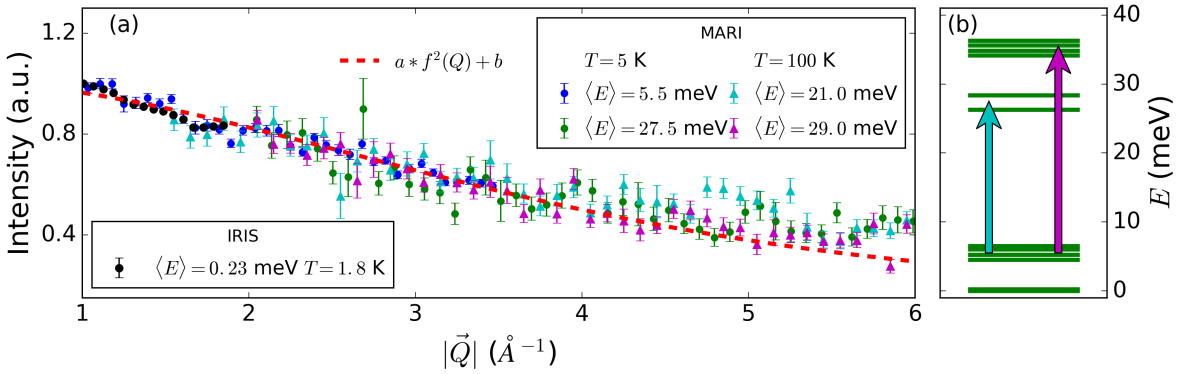

Figure 5.18: (a) $|\boldsymbol{Q}|$-dependence of neutron scattering structure factor of features identified as crystal field excitations at $T = 5$ (Figs. 5.17 and 5.16) and $T = 100$ K . All curves are scaled onto the dipole magnetic form factor of the Tb^{3+} ion [234] plotted with the red dashed line. (b) positions of CEF levels. Colored arrows represent the transitions from thermally populated levels observed at $T = 100$ K (cyan and purple datasets).

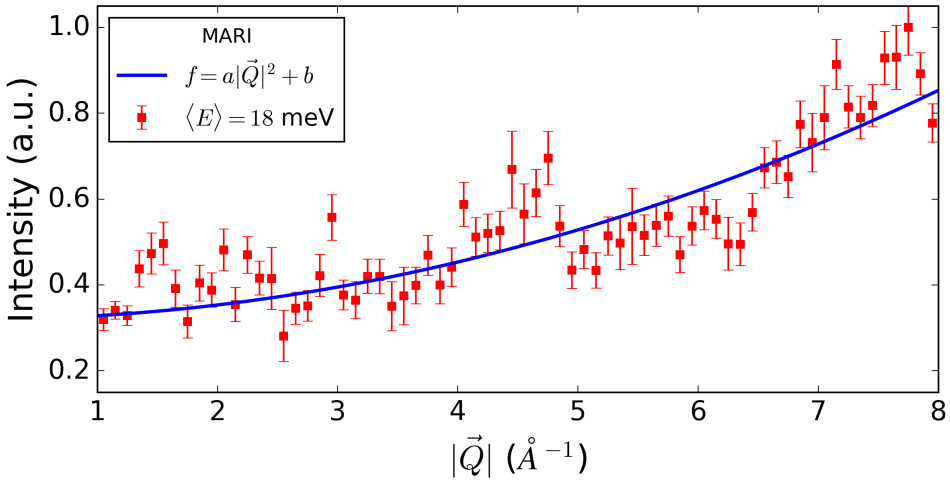

Figure 5.19: $|\boldsymbol{Q}|$-dependence of the neutron scattering structure factor of the feature measured at $E = 18$ meV in TGG with powder neutron spectroscopy. The blue solid line presents the quadratic character expected for the structure factor of phonon branches.

dependence was analyzed. Fig. 5.18 shows constant energy cuts through the $S(|\boldsymbol{Q}|, E)$ map centered around the described excitations. The lines placed close to $E = 5$ and $E = 27$ meV can be well scaled onto the dipole magnetic form factor of the Tb^{3+} ion [234]. For the group of lines lying at $E = 33 - 37$ meV such a dependence cannot be extracted as their high-$|\boldsymbol{Q}|$ part is contaminated with some scattering from phonons. In the data measured at $T = 100$ K two excitations with new characteristic energies ($E = 21$ and $E = 29$ meV) were observed (Fig. 5.21). They appear at the energies corresponding to the transitions between thermally populated levels marked in Fig. 5.18(b) and those with $E = 33 - 37$ meV as the final states, which suggests their crystal field character. These features show a similar magnetic form factor-like dependence as the ones appearing at $T = 5$ K (Fig. 5.18(a)).

Apart from these already listed features, one can also notice another excitation visible in $S(|\boldsymbol{Q}|, E)$-map (Fig. 5.16(b)) around $E = 18$ meV. Inspection suggests that it does not follow the $|\boldsymbol{Q}|$-dependence expected of the magnetic excitaitons. Indeed the energy integrated intensity from that region shows a quadratic $|\boldsymbol{Q}|$-dependence characteristic for lattice excitations [236], so irrelevant to the CEF scheme determination.

With the aim to determine the positions of all observed CEF transitions and thus the eigenvalues of the CEF Hamiltonian, least-squares fits were performed on the $|\boldsymbol{Q}|$-integrated scattering intensities shown in Fig. 5.20. The feature centered around $E = 5$ meV was measured with both MARI and IRIS (in PG(004) mode) spectrometers, where the latter provides an excellent energy resolution of 54 μeV at the elastic line (Fig. 5.20(a)). Intrestingly, the group of transitions still could not be resolved into single levels. One of the causes of this might be rooted in the small but finite splitting between the singlets forming the quasi-doublet. The energy difference of $\Delta = 0.22$ meV between these states means both levels are similarly populated at $T = 5$ K ($F_1/F_0 = e^{\frac{\Delta_{0\to1}}{kT}} = 0.57$), and contributions to the observed spectra by excitations from both of the quasi-doublet levels could be comparable.

Regarding the fitting procedure, the lineshape of the excitations was approximated

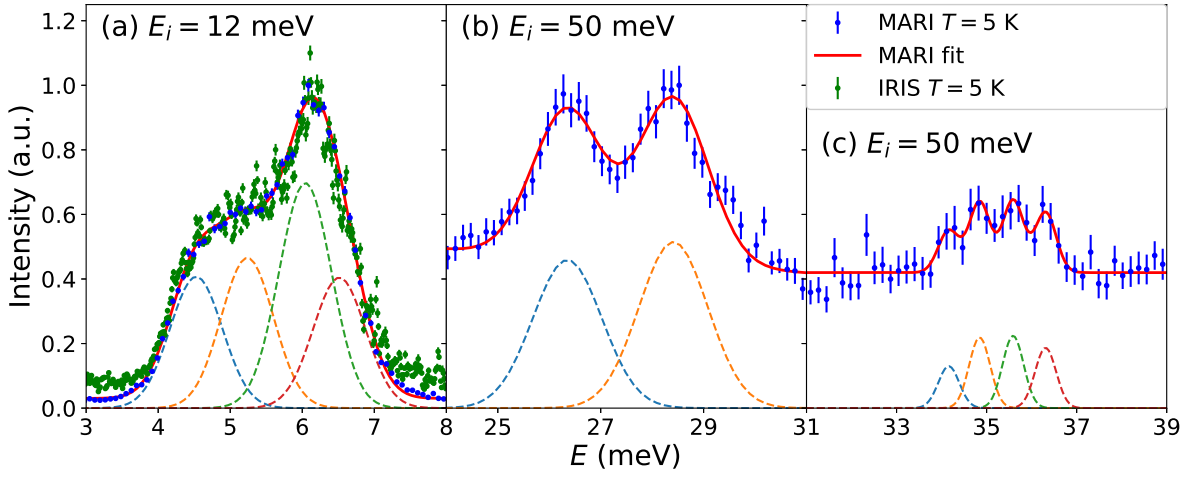

Figure 5.20: Crystal field transitions observed by inelastic neutron scattering in TGG, with excitations fitted with Gaussian peaks. Data presented in figures is integrated around following average $|\boldsymbol{Q}|$-values: (a) $\langle|\boldsymbol{Q}|\rangle = 2.25$ Å^{-1}, (b) $\langle|\boldsymbol{Q}|\rangle = 4$ Å^{-1} and (c) $\langle|\boldsymbol{Q}|\rangle = 3.5$ Å^{-1}

with a Gaussian function and linewidths were fixed for each group of excitations. The fitted positions are presented in Tab. 5.4. The the values obtained for the four levels lying around $E = 5$ meV are in good agreement with previously published results [235]. The fitted full-width half-maxima of peaks plotted in Figs. 5.20(a), 5.20(b) and 5.20(c) are 0.85(3), 1.93(7) and 0.55(5) meV, respectively. The instrumental resolutions calculated with the `PyChop` tool included in the `Mantid` software [237], for these energy transfers, are $dE \sim 0.18$, $dE \sim 0.8$ and $dE \sim 0.8$ meV, respectively. This shows that in the two first cases the width of the fitted lines exceeds the predicted instrumental resolution, while for the last group of excitations is slightly below that value.

Eleven out of twelve transition energies from the ground-state were retrieved, which shows that the low symmetry of crystal field indeed completely lift the degeneracy of the $^7F_6$ ground-state multiplet. This brings with it the requirement of working with the full CEF Hamiltonian required by local crystalline symmetry, allowing nine B_l^m parameters (Eq. 2.15).

The simplest approach to model CEF schemes is the point charge method [18]. It accounts for the ions lying within some distance (usually it does not go much beyond nearest-neighbours), assumes their point-like nature, and represents the electrostatic potential produced by them in the form of spherical (tesseral) harmonics (Sec. 2.1.3), so retrieving the values of the CEF Hamiltonian parameters. The eigenvalues of the CEF Hamiltonian calculated with the point charge method taking into account the eight nearest O^{2-} ions forming a cage in form of slightly distorted cube around the Tb^{3+} (Fig. 5.2) are presented in Tab. 5.4. These were obtained using the `Pointc` program, a part of the `McPhase` suite [238]. No agreement is found between resulting values and the ones retrieved from the neutron spectroscopy data. Extending the calculations by adding further lying ions does not improve the results, leading to even higher energies for the highest levels.

Another way to access the eigenstates of the CEF Hamiltonian is to fit the observed spectrum to eigenvalues produced by calculating the CEF level scheme for a set of Stevens or Wybourne parameters [239]. An attempt to perform this was made with the `SPECTRE` software [240]. It performs a least-squares refinement comparing experimental eigenvalues (and otpionally intensities) and those calculated form the refined parameters. `SPECTRE` by default uses a set of basis functions which is expanded beyond the ground-state manifold of LS-coupling in a scheme referred as intermediate coupling (Sec. 2.1.3). Several sets of starting parameters for closely related rare-earth garnets were tried: NdGG [241], EuGG [242], DyGG [243], ErGG [244] and TbAlG [242], where the parameters were properly rescaled for case of Tb^{3+} ions to correct for different radial electronic distributions (Eq. 2.13). In addition, starting parameters from point charge calculations were also refined.

The best results were obtained with the parameters determined for EuGG [242], although no convergence of the fit was achieved. This solution is characterized by a $\chi^2 = 3.8$ goodness of fit parameter (based on discrepancies between observed and calculated transition energies). The second best result gave $\chi^2 = 12$. In an attempt to improve the fit, a script was prepared combining the modern robust least-squares optimization algorithms offered by the `SciPy` scientific Python library [245] and the module `So1ion` from the `McPhase` software suite [238], which calculates the rystal field scheme in the Stevens formalism, limited to the gorund-state term. At this stage five sets of initial parameters were fed to the fitting algorithm; namely, the TGG parameters from Ref. [233], the best result of refinements with `SPECTRE`, values obtained for TbAlG and EuGG [242], and results of point charge calculations. The set of values minimized by this code consisted of:

$$\chi_n^2 = \frac{(E_n^{obs} - E_n^{calc})^2}{E_n^{calc}}, \tag{5.4}$$

for n, marking the energies of transitions from ground-state to the n^{th} of eleven excited states. The best agreement was achieved with the third set of initial values produced by `SPECTRE` refinements, giving an excellent $\sum_n \chi_n^2 = 2.143 \times 10^{-03}$. Inspection of the calculated neutron intensities showed significant discrepancies between the experimental data and other fitted sets of parameters, further supporting this result.

The final set of CEF parameters is presented in in Tab. 5.3 and the calculated eigenvalues can be found in Tab. 5.4. The calculated neutron spectra compared with the experimental data show rough agreement, but also bring back the issue of line broadening in the experimentally observed excitations. With use of these parameters the $|\psi_i\rangle = \sum c_{i,M_J} |J, M_J\rangle$ decomposition of CEF eigenstates was calculated and their detailed structure is presented in Tab. 5.5.

Table 5.3: Sets of the refined crystal field parameters giving the best value of standard goodness of fit parameter, $\chi^2 = 2.1 \times 10^{-3}$. Parameters are given in Stevens notation.

Parameter	Ref. [233] (meV)	This work (meV)
$\widetilde{B}_2^0$	5.05×10^{-2}	2.66×10^{-2}
$\widetilde{B}_2^2$	-2.60×10^{-1}	-3.24×10^{-1}
$\widetilde{B}_4^0$	-4.10×10^{-3}	-2.47×10^{-3}
$\widetilde{B}_4^2$	3.00×10^{-3}	3.70×10^{-3}
$\widetilde{B}_4^4$	1.50×10^{-2}	8.51×10^{-3}
$\widetilde{B}_6^0$	-5.89×10^{-6}	-1.12×10^{-5}
$\widetilde{B}_6^2$	1.36×10^{-5}	-1.21×10^{-5}
$\widetilde{B}_6^4$	-1.02×10^{-4}	-4.73×10^{-5}
$\widetilde{B}_6^6$	5.32×10^{-7}	8.96×10^{-5}

Table 5.4: CEF transition energies observed by Raman spectroscopy [235], calculated with the parameters given in Ref. [233], calculated with the point charge method as described in the text, determined by the fits to INS data (Figs. 5.16 and 5.20) and calculated with the refined parameters (Tab. 5.3). All values are given in meV.

$E_{obs\,Raman}$[235]	E_{calc}[233]	E_{point}	$E_{obs\,INS}$	E_{calc}
-	0.4	0.108	0.219(1)	0.22
4.2	4.8	11.7	4.52(2)	4.50
5.3	5.0	12.9	5.23(3)	5.25
6.2	5.3	14.3	6.04(4)	6.01
6.6	6.1	16.8	6.51(3)	6.54
-	36.6	27.9	26.30(4)	26.40
-	38.6	35.0	28.38(5)	28.27
-	44.6	37.9	34.16(8)	34.26
-	46.7	54.2	34.85(5)	34.73
-	49.9	54.5	35.59(5)	35.63
-	50.7	72.5	36.31(5)	36.38
-	55.4	72.6	-	38.20

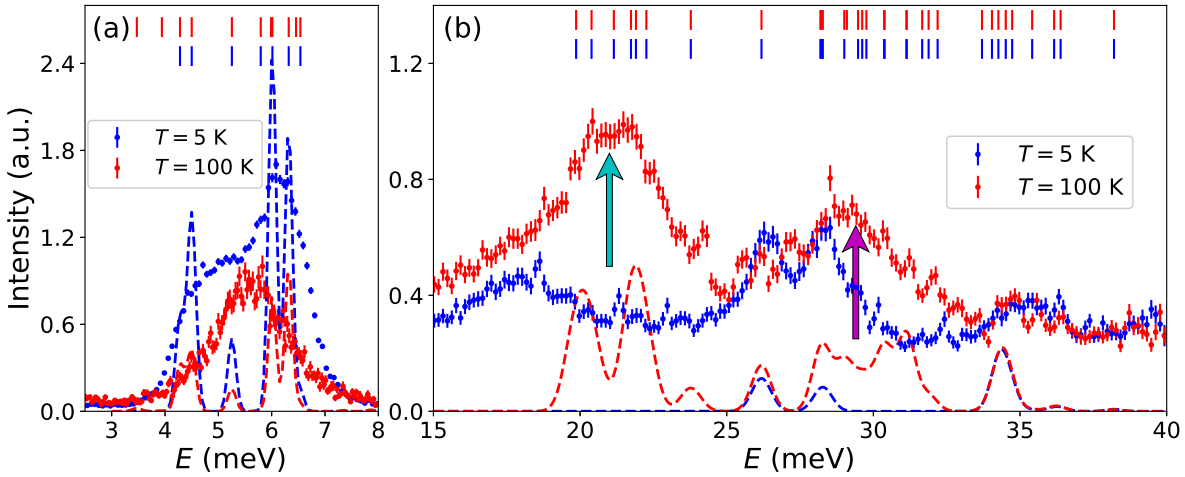

Figure 5.21: The temperature-dependence of crystal field excitation intensities measured with neutron spectroscopy (Fig. 5.17) and spectrum calculated using the fitted crystal field parameters (Tab. 5.3). In (a) $|\boldsymbol{Q}| = 2.25 \pm 1.25$ Å^{-1} and in (b) $|\boldsymbol{Q}| = 4 \pm 2$ Å^{-1} integration ranges were used. Transition intensities were calculated with the `Singleion` module, a part of the `McPhase` software suite [238] and convoluted with instrumental resolution calculated with the `PyChop` tool included in the `Mantid` software [237]. The colored arrows mark the transitions from thermally populated states marked with corresponding colours in Fig. 5.18(b).

Table 5.5: The crystal field eigenstates, $|\psi_i\rangle = \sum c_{i,M_J} |J, M_J\rangle$, expressed as expansions of the $|M_J\rangle \equiv |6, M_J\rangle$ eigenstates of $\hat{J}_z$, in the Russell-Saunders coupling scheme ($J = 6, L = 3, S = 3$) for the $^7F_6$ ground multiplet of Tb^{3+} ion. A blank entry means a zero coefficient. Energy levels given in meV.

		E	$\|-6\rangle$	$\|-5\rangle$	$\|-4\rangle$	$\|-3\rangle$	$\|-2\rangle$	$\|-1\rangle$	$\|0\rangle$	$\|1\rangle$	$\|2\rangle$	$\|3\rangle$	$\|4\rangle$	$\|5\rangle$	$\|6\rangle$
$\|\psi_0\rangle$	Γ_3	0.0		-0.091		-0.026		0.701		0.701		-0.026		-0.091	
$\|\psi_1\rangle$	Γ_1	0.22	0.182		0.122		-0.325		-0.832		-0.325		0.122		0.182
$\|\psi_2\rangle$	Γ_4	4.50	-0.594		0.096		0.371				-0.371		-0.096		0.594
$\|\psi_3\rangle$	Γ_1	5.25	0.683		0.061		-0.085		-0.215		-0.085		0.061		-0.683
$\|\psi_4\rangle$	Γ_4	6.01	0.383		0.115		0.583				-0.583		-0.115		-0.383
$\|\psi_5\rangle$	Γ_2	6.54		-0.005		0.502		0.498		-0.498		-0.502		0.005	
$\|\psi_6\rangle$	Γ_3	26.40		0.032		0.706		0.030		0.030		0.706		0.032	
$\|\psi_7\rangle$	Γ_1	28.27	0.016		0.415		0.535		-0.290		0.535		0.415		0.016
$\|\psi_8\rangle$	Γ_2	34.26		0.566		0.302		-0.298		0.298		-0.302		-0.566	
$\|\psi_9\rangle$	Γ_3	34.73	-0.019		-0.691		0.148				-0.148		0.691		0.019
$\|\psi_{10}\rangle$	Γ_4	35.63		-0.701		0.035		-0.090		-0.090		0.035		-0.701	
$\|\psi_{11}\rangle$	Γ_2	36.38		0.424		-0.397		0.403		-0.403		0.397		-0.424	
$\|\psi_{12}\rangle$	Γ_1	38.20	0.023		0.556		-0.318		0.422		-0.318		0.556		0.023

5.5.1 Beyond the single-ion physics

The measured and calculated magnetic field-dependence of the isothermal magnetisation is presented in Fig. 5.22(a). The calculated values overlap with the results of the measurements for $T > 20$ K, but below that point are no longer in good agreement. The most striking discrepancy is the different magnetisation of the plateau present in the range $H = 15 - 60$ kOe. It is also visible that while for $T > 50$ K the magnetisation might be modeled fairly well with a Brillouin function (dashed line in Fig. 5.22(a)), at the lowest temperature a strong suppression of the magnetic moment consistent with the crystal field quasi-doublet dominated by $J = \pm 1$ and $J = \pm 2$ sates (Tab. 5.5) is observed.

In order to check if this discrepancy comes from an incorrect CEF model based on the eigenvalues retrieved from spectroscopic data, a refinement of the CEF parameters to the experimental magnetisation curves was done. Using the crystal field toolbox of the `Mantid` software. None of the fits to all of the datasets, regardless of the starting parameters, converged, and they usually reproduce only either a few of the highest or the lowest temperature datasets. Separate refinements taking two or three of the highest/lowest temperatures did converge, and in the second case moderate agreement among all the measured temperatures was found. However, none of these solutions gave a set of transition energies remotely close to the ones obtained from the neutron data. This inconsistency might be due to physics not captured in a simple single-ion CEF model.

Nevertheless, the temperature at which the observed disagreement between calculations based on the established CEF model and experiments appears is consistent with the development of short-range correlations observed in diffuse neutron scattering. In order to check for signs of these the magnetisation data was plotted with respect to $\mu_0 H/T$. For an uncorrelated paramagnet datasets measured at all temperatures should fall on a single master curve. This is true for $T > 20$ K, and the deviation from this behaviour gets larger on cooling down, with the appearance of an inflection point for data at $T < 20$ K.

Moreover, the observed inflection manifests as a small spike in dM/dH as a function of magnetic field (Fig. 5.23). This suggests a possibility of a field-induced phase transition into fully or partially ordered phase. One can exclude the option of a metamagnetic transition due to the crossing of a CEF level with significant difference in M_J decomposition (seen in Ref. [233]), as it should be reproduced in the performed calculations.

Broadening of the linewidths was not the only anomaly found in the spectroscopic study of the CEF in TGG. At the lowest measured temperature $T = 1.8$ K the first excited state of the CEF scheme exhibits a signature of internal structure, showing the possibility of containing at least two slightly dispersive branches. This observation cannot be accounted for by single-ion effects described in the CEF theory (Sec. 2.1.3) and reveals the presence of collective excitations resulting from the perturbative action of interactions between the ions on the single-ion states. This is consistent with requirement of the presence of additional perturbations allowing for magnetic ordering in induced-moment type systems with non-magnetic singlet ground-states (Sec. 5.2.3).

The temperature-dependence of $|\boldsymbol{Q}|$-integrated neutron spectra of the quasi-doublet is plotted in Fig. 5.25. It indeed shows that at low temperatures one can distinguish contributions from at least two peaks to the main feature centered around $E = 0.2$ meV. These seem to merge into a single peak at $T = 5$ K, where the growth of quasielastic intensity begins. An additional distinct small feature can be observed at $E \sim 0.45$ meV

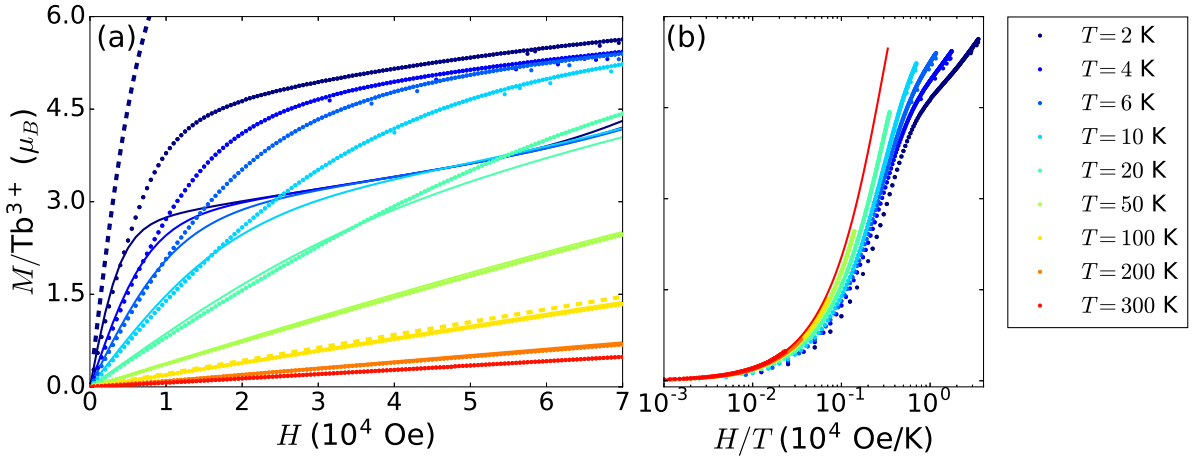

Figure 5.22: Isothermal powder magnetisation of TGG as a function of (a) field H (b) and H/T ratio. Low-T curves in (b) show the departure from scaling expected for the system of uncorrelated spins. Solid and dashed lines in (a) are: the results of calculations performed with the refined CEF parameters and Brillouin functions calculated for the isotropic free Tb^{3+} ion, respectively. The solid red line in (b) marks the expected master curve extrapolated from results calculated with CEF scheme for $T = 300$ K.

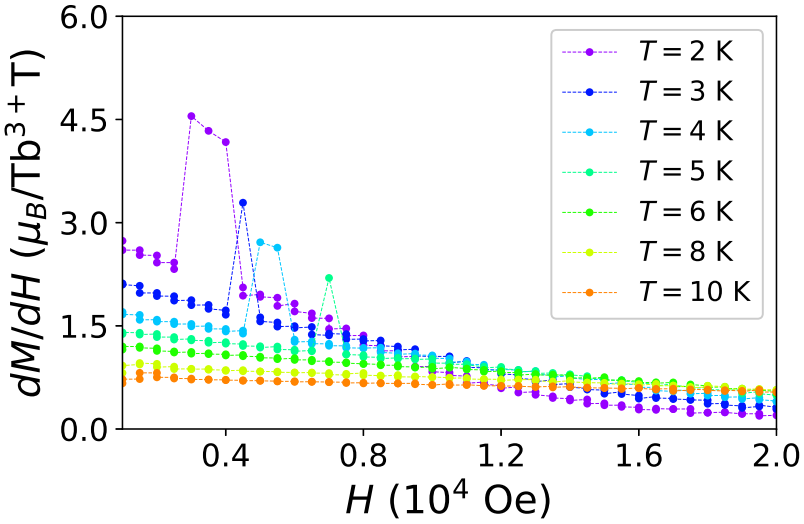

Figure 5.23: Derivative of isothermal powder magnetisation of TGG with respect to the magnetic field as a function of field H. The dashed lines are guides to the eye.

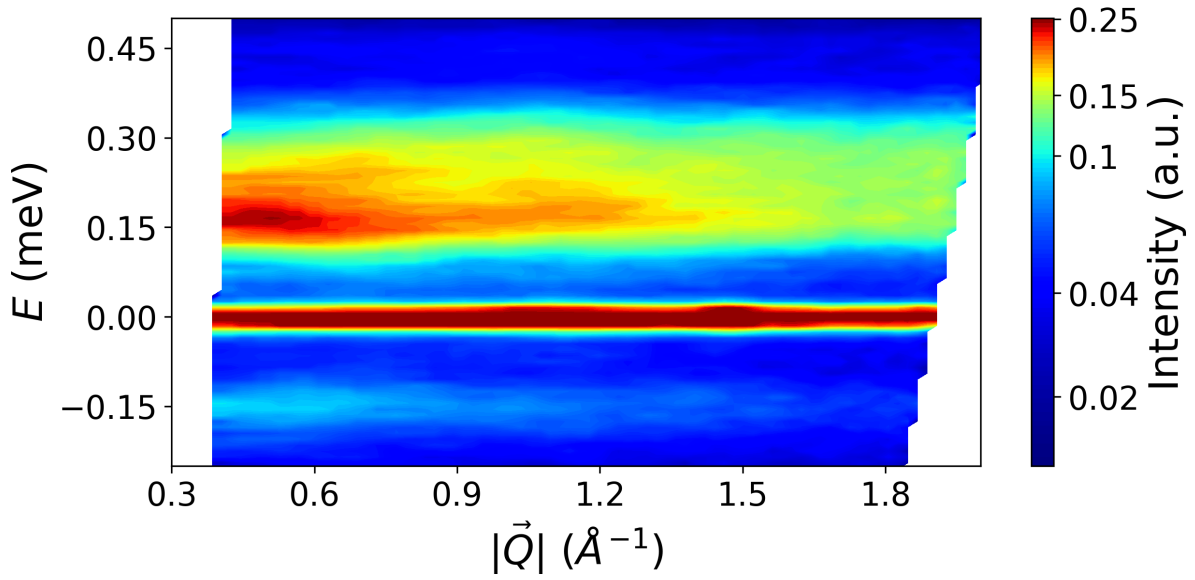

Figure 5.24: Splitting of the quasi-doublet CEF ground-state in inelastic neutron scattering measured on a powder sample of TGG at $T = 1.8$ K, using a PG(002) analyzer setup on the IRIS spectrometer, at the ISIS neutron source. The colormap is on a logarithmic scale in order to show the internal structure of the first excited states.

at the lowest temperatures. This is completely suppressed at $T = 10$ K. These changes coincide with the development of diffuse elastic scattering investigated in Sec. 5.4 and departure of the calculated single-ion magnetisation from the measured values.

5.6 Collective effects and ordering in $Tb_3Ga_5O_{12}$

Inelastic neutron scattering on a powder sample of TGG showed signs of internal structure in the first excited CEF state. In order to investigate its $\boldsymbol{Q}$-dependence a single-crystal experiment on the IN5 time-of-flight spectrometer was performed. The sample was aligned with the $[1\bar{1}0]$ crystallographic direction perpendicular to the scattering plane (Fig. 5.4(a)). The one and two-dimensional cuts through $S(\boldsymbol{Q}, E)$ datasets were prepared with Q_x and Q_y describing the scattering plane of $S(\boldsymbol{Q}, E)$ dataset. For this particular experimental geometry $Q_x = (1, 1, 0)$ and $Q_y = (0, 0, 1)$. The generation of the $S(\boldsymbol{Q}, E)$ and extraction of the cuts was performed with the `Horace` software [246].

Indeed, the experiment showed a band of multiple dispersive branches instead of a single non-dispersive CEF excitation (Fig. 5.26. As was suggested by the powder data, the dispersion persists in the paramagnetic phase and no large qualitative change is observed across the ordering transition. The observed intensity can be assigned to six separate branches, as could be identified in constant-$\boldsymbol{Q}$ cuts made at various points of the covered range of reciprocal space (i.e. Figures 5.27 and 5.28). This is consistent with the presence of six Tb^{3+} sublattices in the garnet structure.

The dispersive excitation spectrum suggests, that interactions between the terbium ions give rise to CEF excitons with a collective character. The complex $\boldsymbol{Q}$-dependence of the dispersion curves might point to a highly anisotropic coupling between the magnetic

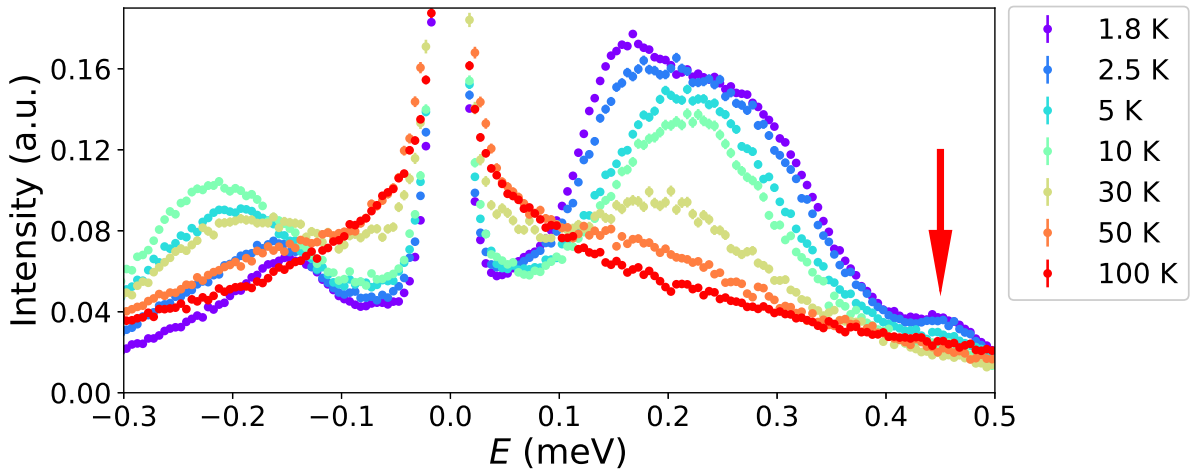

Figure 5.25: The temperature evolution of $|\boldsymbol{Q}|$-integrated ($|\boldsymbol{Q}|$=0.4-1.8 Å^{-1}) neutron spectra of the first excited CEF state measured on a powder sample of TGG, using the IRIS spectrometer at the ISIS neutron source. The red arrow marks the small feature above the main bands.

ions. This would be consistent with dipole-dipole interactions which are sensitive to the relative position between the ions and the direction of the local magnetic moment, which in the case of TGG would reflect the six distinct orientations of local environments determining the magnetic easy axis.

A striking feature was observed in the exciton dispersion relation at the magnetic ordering wavevector. At this point, the low-lying strong mode exhibits a dip in the dispersion at (high) $T = 1$ K, which splits on cooling, revealing its degeneracy. One of the split branches softens towards the magnetic zone center (Fig. 5.26). From these four temperature points it is not clear if the gap of the mode closes, but on cooling down beyond the T_N it moves back to higher energies and the gap increases even beyond the value at $T = 0.5$ K (Fig. 5.27).

It is worth noting that after close examination two weaker non-dispersive branches were found (Fig. 5.28). One of them was already detected in neutron spectra measured on a powder sample. The second one is centered slightly below $E = 0.1$ meV. As the first one is placed above the band of the stronger excitons its featureless flat character can be easily determined. However, the second one is always visible whenever the remaining excitons are pulled towards higher energies. The disappearance of the highest flat band coinciding with the apparent suppression of internal structure of the excitons at $T > 5$ K in powder data points to the crystal field character of those features, despite their peculiar behaviour in presence of magnetic interactions.

Fig. 5.29 shows a constant energy cut in the (h, h, l) plane around the $\boldsymbol{Q} = (1, 1, 0)$ magnetic ordering wavevector. It shows a fairly localized dip in the curvature of the exciton band, and its disappearance in the ordered phase, due to both the slight reduction of the exciton intensity at $T < T_N$ and the opening of the gap, moving the band up from the plane of the cut.

In order to better determine the temperature-dependence of the mode softening across the antiferromagnetic transition and determine if the observed gap closes at T_N, the size of

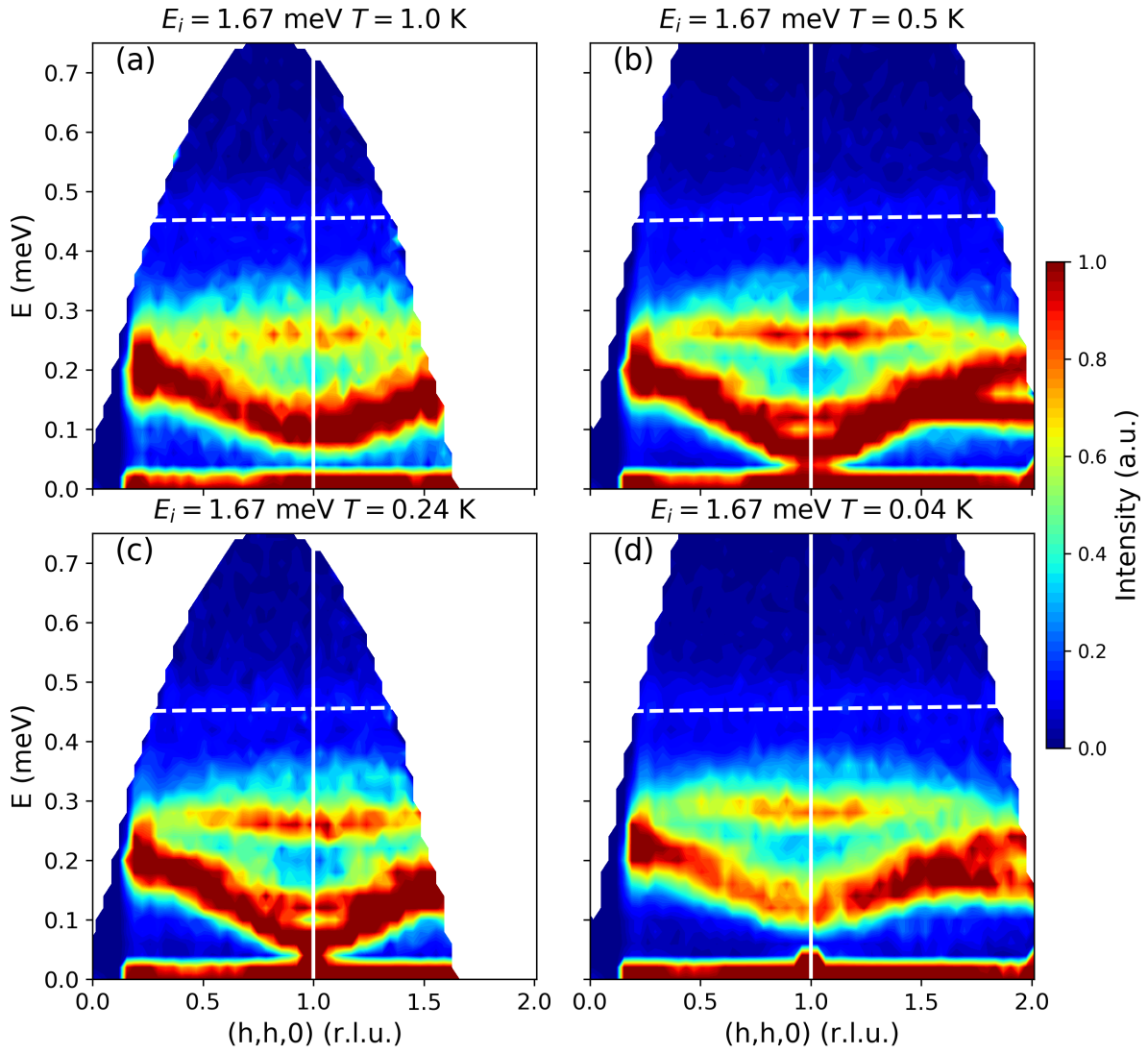

Figure 5.26: The temperature-dependence of the dispersive magnetic excitons in TGG from the first excited CEF state, measured with inelastic neutron scattering. The solid white line marks the antiferromagnetic propagation vector, and also the position of the dip in the dispersion of the lowest energy exciton mode. The dashed white line marks the center of small feature observed in the IRIS data at $E \sim 0.45$ meV $T < 10$ K (inset of Fig. 5.27). Data collected using incident energy $E_\mathrm{i} = 1.67$ meV, with IN5 neutron spectrometer at the ILL neutron facility. The data was integrated in the range: $l = -0.035 - 0.35$ r.l.u.

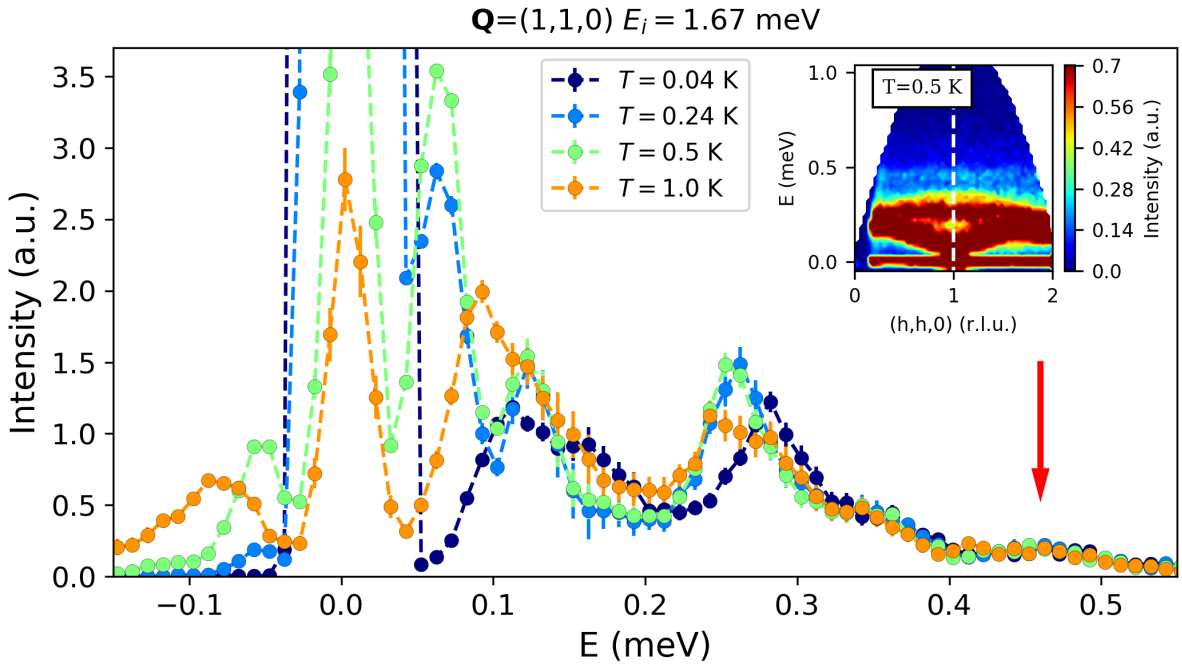

Figure 5.27: The temperature-dependence of the exciton gap measured with inelastic neutron scattering on a single-crystal sample of TGG across the ordering transition at $\boldsymbol{Q} = (1, 1, 0)$ magnetic propagation vector. The data was integrated over the range $h = 0.95 - 1.05$ and $l = -0.05 - 0,05$ Å^{-1}. The dashed lines are guides to the eye. The inset show the color map with the white dashed line showing the position of the cut.

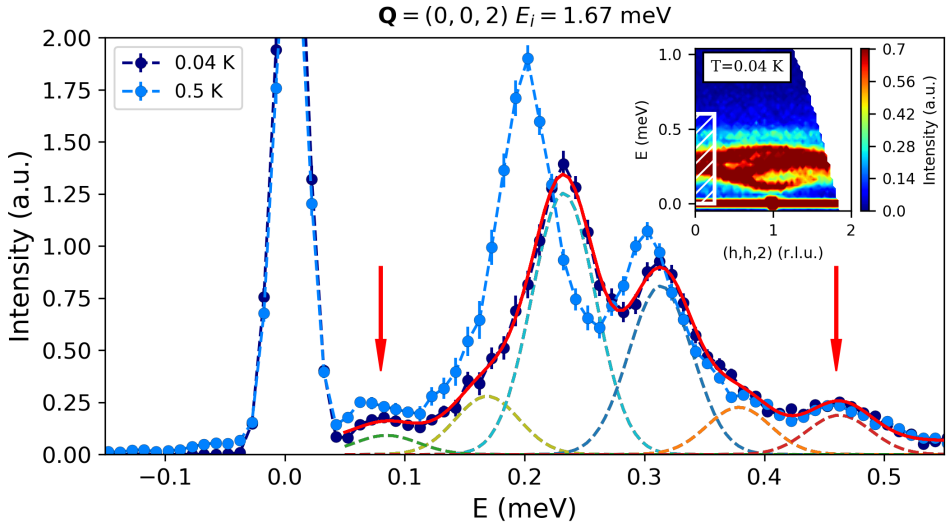

Figure 5.28: Constant-$\boldsymbol{Q}$ cut through the exciton band at $\boldsymbol{Q} = (h, h, 2)$ with $h = -0.25 - 0.25$, measured in TGG at $T = 0.04$ and $T = 0.5$ K. Red arrows point to the positions of two weak non-dispersive branches appearing at whole surface of the Brillouin zone above and below the band more pronounced excitations. The dashed lines of colours corresponding to the colour of data points are guides to the eye. Solid and dashed lines are results of the fit described in the text. The white rectangle in the inset shows the range of data integration.

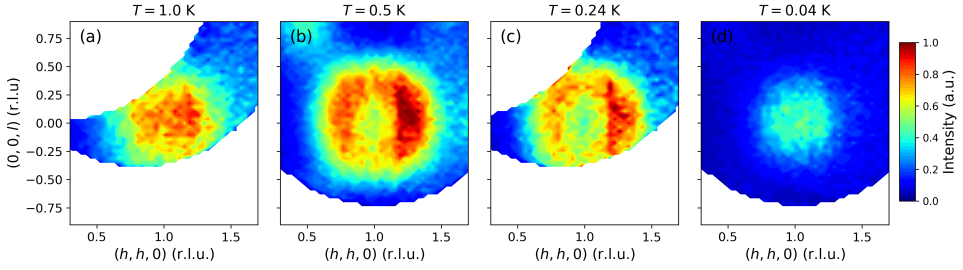

Figure 5.29: The temperature-dependence of constant-E cuts through the dip of the soft mode above the antiferromagnetic ordering wavevector in single-crystal inelastic neutron scattering. Data measured with $E_\mathrm{i} = 1.67$ meV and integrated in range: $E = 0.08 - 0.12$ meV.

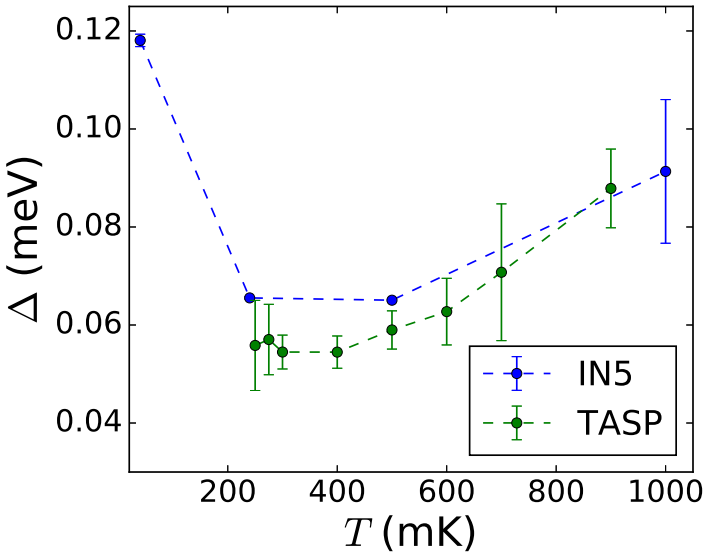

Figure 5.30: The temperature-dependence of the exciton gap at the antiferromagnetic ordering wavevector $\boldsymbol{Q} = (1, 1, 0)$. The IN5 constant-$\boldsymbol{Q}$ cuts, from which the gap opening was obtained are plotted in the Fig. 5.27. The TASP data was measured with PG(002) monochromator/analyzer setup and fixed $k_\mathrm{f} = 1.1$ Å^{-1}. The dashed lines serve as guides to the eye.

the gap was measured on the TASP three-axis neutron spectrometer (Fig. 5.30). Exciton peaks in constant-$\boldsymbol{Q}$ cuts at $\boldsymbol{Q} = (1, 1, 0)$ were fitted with a Gaussian profile with a shared full-width half-maximum (FWHM). The size of the gap was determined by the position of the lowest mode above the elastic line. The data measured at $T > 0.24$ K does not show signs of complete closing of the gap and is thus consistent with the TOF data. The slight shift downwards of the lowest mode position in comparison to the IN5 data is the result of the contribution of the low-E non-dispersive mode which could not be resolved due to its relatively small intensity. On cooling towards T_N resolving the gap became more challenging due to the appearance of critical scattering and the available instrumental resolution. Moreover, below the ordering transition strong magnetic Bragg reflection emerges at $\boldsymbol{Q} = (1, 1, 0)$ that cannot be separated from the intensity measured at very low energy transfers.

The dispersion relations of the exciton branches at base temperature ($T = 0.04$ K) were extracted with a series of fits to the constant-$\boldsymbol{Q}$ cuts through $S(\boldsymbol{Q}, E)$ data. Their lineshape was approximated with Gaussian functions with a single peak-width fitted for every scan. The tiny differences between energy transfers corresponding to every branch suggest that the differences in instrumental resolution between them should be negligible. Every cut was integrated in the range $Q_x \pm 0.05$ and $Q_y \pm 0.05$ Å^{-1}. Taking into account the presence of two non-dispersive branches, the initial fit at $\boldsymbol{Q} = (0, 0, 2)$ was performed to retrieve the energy position of those excitations (Fig. 5.28). Their energies were determined to be 0.085 and 0.46 meV. The final fitting procedure included these two branches at fixed positions and with the linewidth corresponding to the global value determined for a particular constant-$\boldsymbol{Q}$ cut. The remaining four peaks identified in the spectrum were fitted to the data cuts. The results of the described fitting procedure

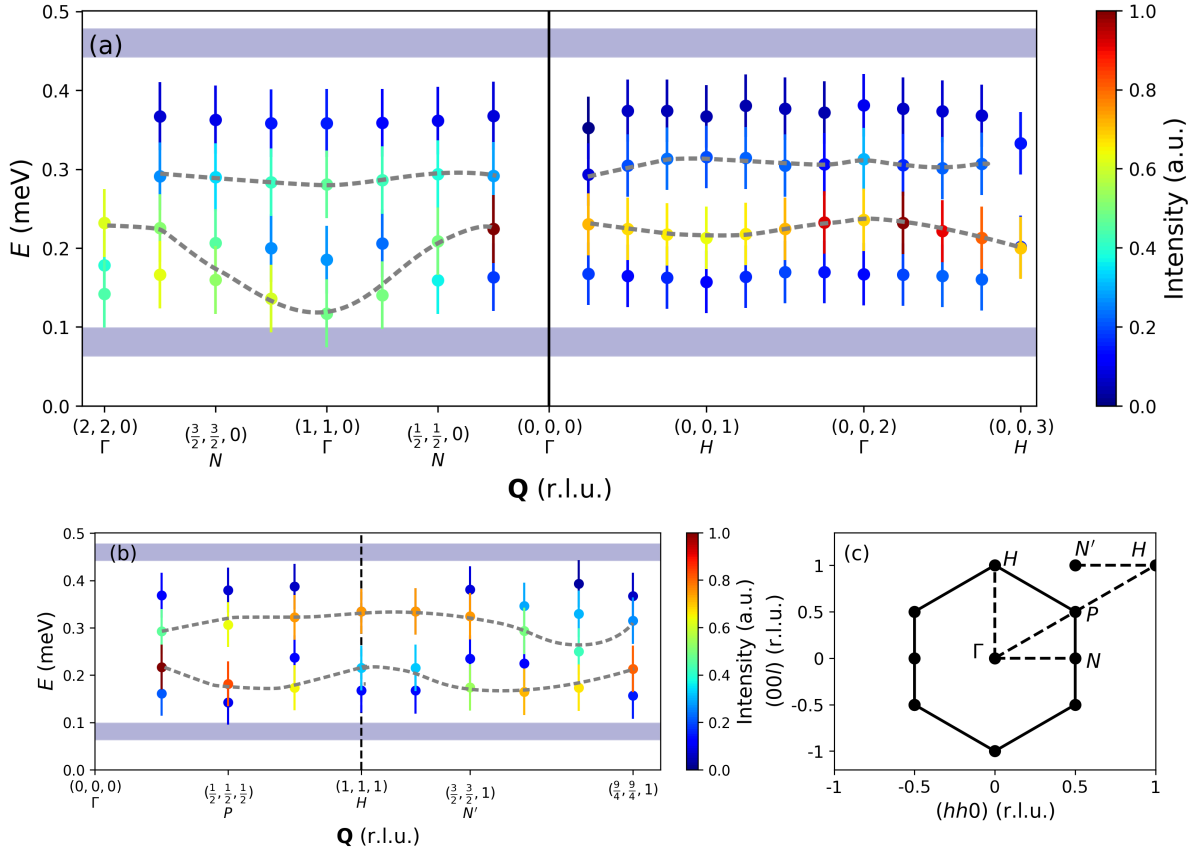

Figure 5.31: Dispersion relations of the exciton branches in TGG at $T = 0.04$ K fitted to the constant-$\boldsymbol{Q}$ cuts through the measured $S(\boldsymbol{Q}, E)$ volume. Points in (a) and (b) represent the peak centres, while their colour matches the intensity. Intensity was normalized within a single panel. The blue stripes mark the position of non-dispersive features. (c) map of the reciprocal space with dashed lines marking the directions equivalent to these along which cuts are presented in (a) and (b). The grey dashed lines are guides to the eye following the two strongest modes in the spectrum.

performed along a few high-symmetry directions in accessible Brillouin zones are plotted in Fig. 5.31.

In the light of the extracted temperature-dependence of the gap size (Fig.5.30) it is safe to assume that the gap persists with finite size while crossing the T_N. Extracting its value at temperatures very close to the ordering transition and below that point using a triple-axis spectrometer is challenging due to strong Bragg contamination of low-energy part of neutron spectra. An additional inquiry with TOF spectrometer focused at $\boldsymbol{Q}$-range close to the ordering wavevector should provide additional details. Basing on that one can exclude the scenario of the soft-mode transition taking place in TGG, in contrast to the conclusions drawn for PrNi [220]. The calculations within the random-phase as those performed for PrNi might shed some light and give basis to establish a comparison between those two induced-moment systems.

Moreover, similar magnetic excitations were observed in HoF_3 [247], whose lowest-

lying crystal field levels are two singlets split by $\Delta \sim 0.7$ meV. It undergoes ordering into a ferrimagnetic phase at $T_C = 0.53$ K. Two branches of singlet-singlet excitaitons were identified in inelastic neutron scattering data [247] above and below the magnetic ordering. The calculations based on mean-field/random-phase approximation including crystal field, dipole-dipole interactions, exchange couplings and hyperfine interactions succeeded to reasonably reproduce the dispersive excitons in the paramagnetic phase, but failed to provide a good agreement with experimental data below T_C. That observation was argued as signature of either magnetoelastic effects influencing the crystal fields, or higher-order correlations effects. These resemblances imply that similar analysis applied to TGG might give an opportunity for explaining the observations described in this section.

In addition to the multi-branch structure of the higher level in the quasi-doublet ground-state, the single-crystal experiment has shown anomalies affecting the CEF levels forming the band at $E \sim 5$ meV. Fig. 5.32(a) and 5.32(b) shows the difference in this CEF band above and below the magnetic ordering temperature. In the ordered phase one can recognize an internal structure with some dispersive branches that the dip at the bottom of the band. This internal structure becomes evident in the constant-E cuts (Figs. 5.32(c) and 5.32(d)). In contrast to the observations made for the lower energy levels, this effect is present exclusively in the ordered phase, which could suggest that it is inherently connected with the magnetic order.

5.7 Lattice dynamics and spin-lattice coupling in $Tb_3Ga_5O_{12}$

In the light of the mentioned effects exhibited by TGG, the possibility of coupling between spin and lattice degrees of freedom comes intuitively into the picture. To establish a model including the description of magnetoelastic coupling one requires good knowledge about lattice dynamics in the investigated system. This can be investigated experimentally by measuring the phonon dispersion relations with neutron spectroscopy and theoretically by calculations using the density functional theorem (DFT) method [249]. In the latter the electronic band structure is obtained by relating the electron density with the energy of the system. Knowing that, one can calculate force constants acting at the displaced ions within the crystal and finally, using this knowledge, calculate the phonon dispersion relations [250].

In Figure 5.33 there are shown examples of constant-E scans along a specific direction in the Brillouin zone, performed on a triple-axis spectrometer. The positions of the phonon branches were extracted by fitting Gaussian peaks with a linearly sloping background. In the case when a single scan covered both the focusing and defocusing [236] side of the dispersion, the position of the branch was fixed to be common for both features.

All of the retrieved dispersion relations of the transverse and longitudinal phonons are presented in Fig. 5.34. They are compared with phonon dispersion relations calculated with the use of the `PhonoPy` code [251] from results of DFT calculations presented in Ref. [248]. The colours in experimental and theoretical results correspond to the polarization of the phonon modes. There is a good agreement between the experimentally determined and calculated positions of the phonon branches and the expected polariza-

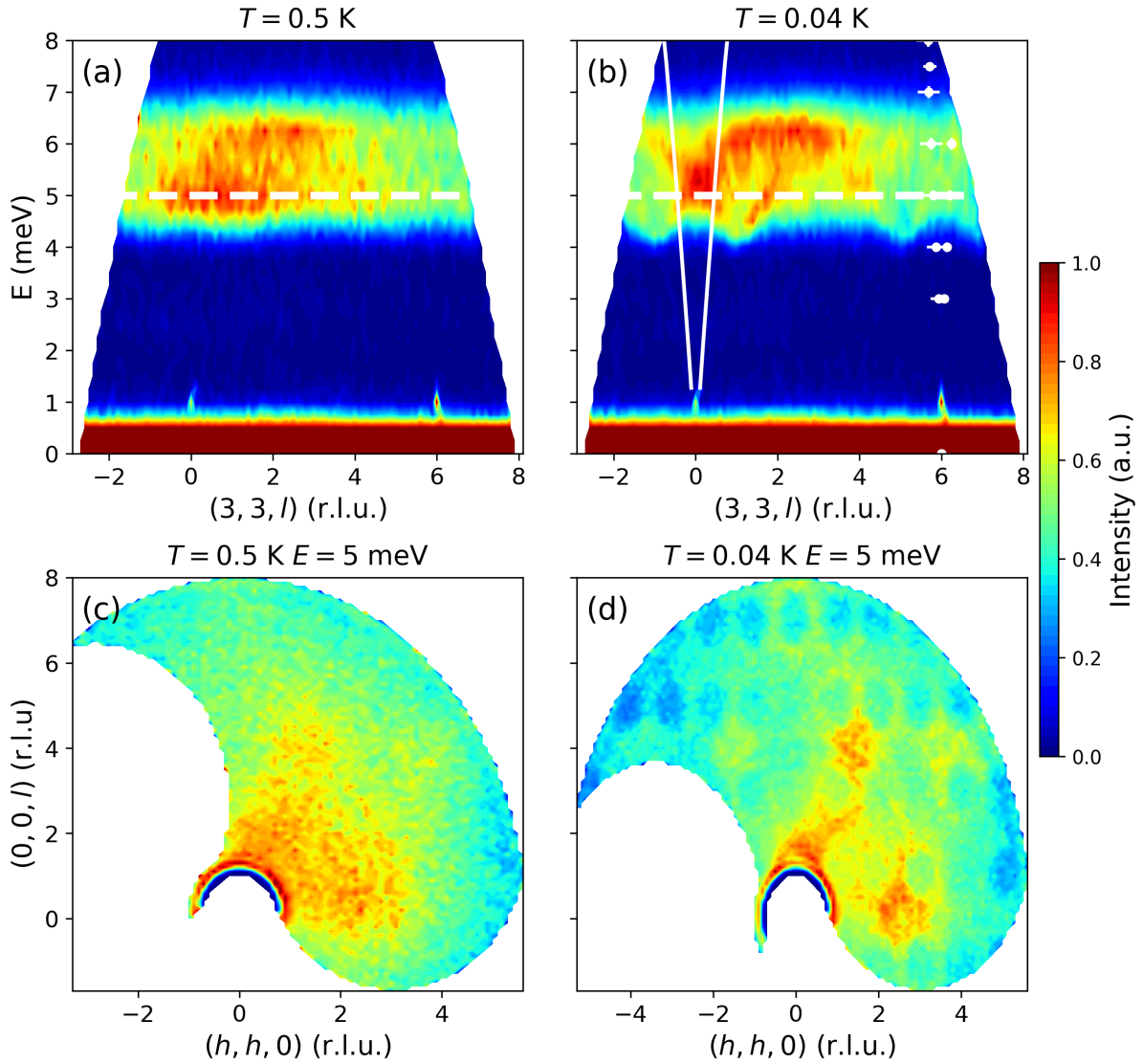

Figure 5.32: The temperature-dependence of the band of CEF levels centered around $E \sim 5$ meV measured on a single-crystal sample of TGG with inelastic neutron scattering. Data collected with $E_i = 12.6$ meV. The white solid line represents the dispersion relation of transverse acoustic phonons extracted from results of calculations with density functional theory presented in Ref. [248]. White dots present the dispersion of longitudinal acoustic phonons measured in single-crystal of TGG, which is discussed in detail in the text.

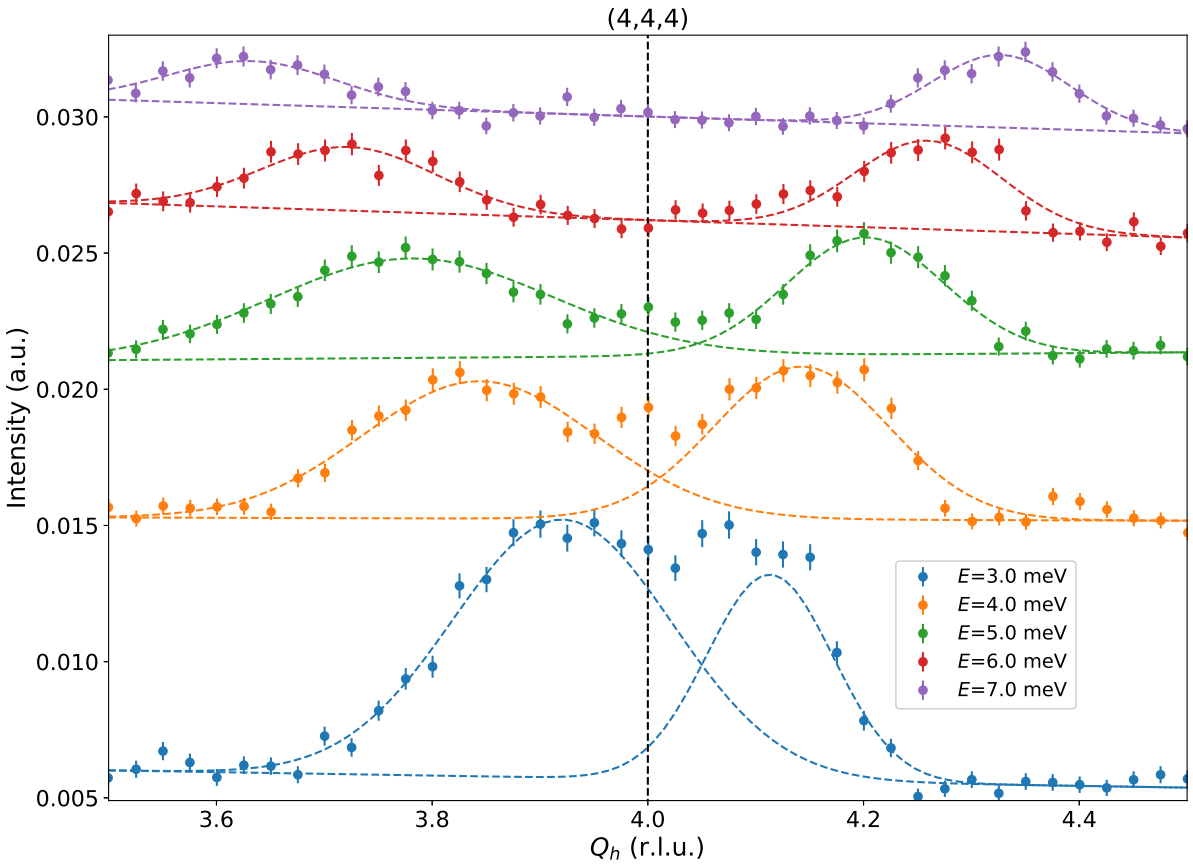

Figure 5.33: An example of constant-E scans in a triple-axis experiment, measured on a single-crystal sample of TGG in order to determine of acoustic phonon dispersion curve. The data show the transverse acoustic phonons along $\Gamma - P$ direction, measured in Brillouin zone with Γ at $\boldsymbol{Q} = (4, 4, 4)$. Focusing and defocusing effects are visible in the widths of measured peaks at opposite sides of Γ point. The black dashed line mark the center of the Brillouin zone. An offset was added for clarity.The measurement was performed with at room temperature on the EIGER triple-axis neutron spectrometer at the SINQ neutron source at the PSI.

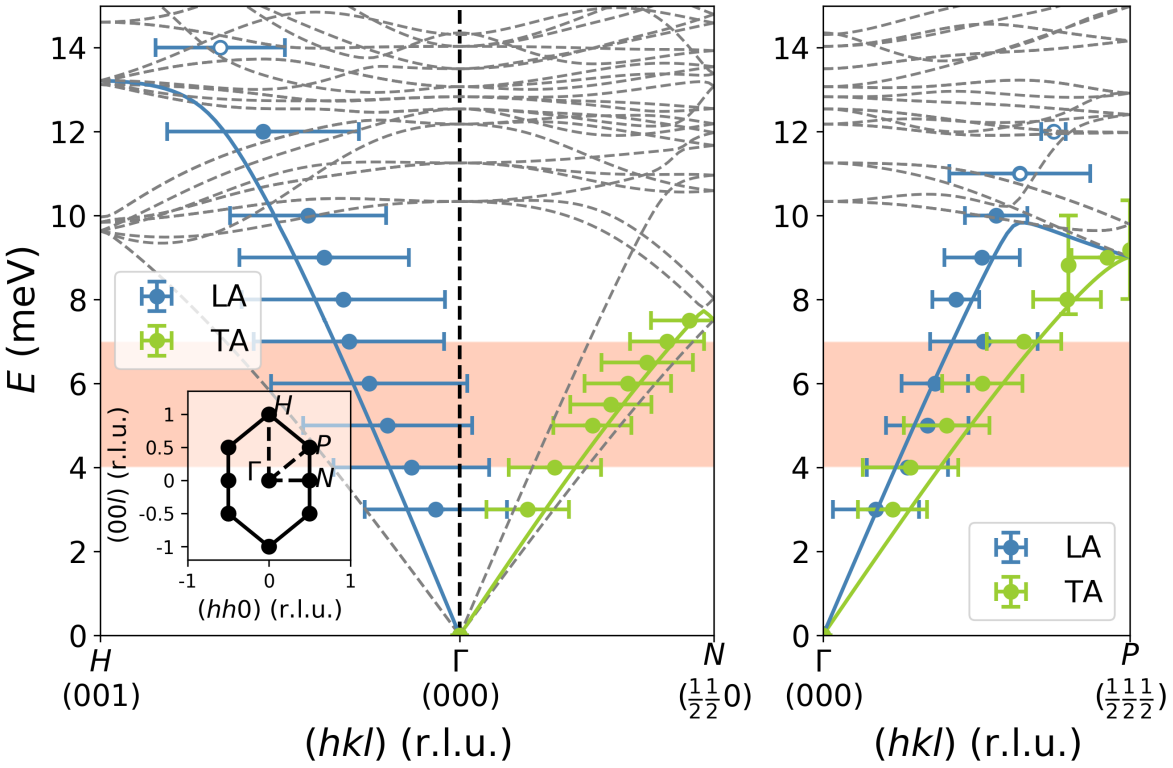

Figure 5.34: Calculated and measured phonon dispersion relations in TGG. Data collected on TASP three-axis neutron spectrometer at room temperature with fixed $k_f = 2.166$ Å^{-1}, at SINQ neutron source at PSI. The instrument was equipped with PG(002) monochromator/analyzer setup. The red stripe shows the position and the extent of the band of CEF levels centered around $E \sim 5$ meV.

tions of the corresponding modes. The empty markers in Fig. 5.34 represent peaks fitted in the constant-E scans that at the time of the measurement were falsely identified as belonging to the lower energy acoustic branches.

Fig. 5.32(b) shows the measured longitudinal and calculated transverse acoustic modes dispersion curves, along appropriate direction within the Brillouin zone, plotted over the anomalous CEF dispersion. In case of magnetoelastic modes resulting form the coupling between lattice and crystal field, in $Tb_2Ti_2O_7$ [252], one would expect the inflections in otherwise flat CEF levels to appear at the wavevector corresponding to crossing of these with phonon branches. In the case of TGG, the coincidence in $S(\boldsymbol{Q}, E)$ of those two features does not unambiguously point to this as the explanation for the observed effects. An inelastic neutron scattering experiment employing polarization analysis could resolve this question.

5.8 Effects of external field on $Tb_3Ga_5O_{12}$

Figure 5.35 shows the field-dependence of the intensity of two purely magnetic Bragg reflections measured in TGG for two directions of the applied magnetic field. These are $(1, 1, 0)$ and $(0, 0, 2)$ (or the equivalents) and they can be used as diagnostic reflections for the magnetic structure in TGG. The $(1, 1, 0)$ reflects the antiferromagnetic arrangements in the magnetic structure. It is present in both magnetic structures found in the rare earth garnets ($Ia\bar{3}d'$ and $Ia'\bar{3}d$) [181]. While the $(0, 0, 2)$ reflects the ferromagnetism in the garnet lattice (non-collinear still respecting the local anisotropy). The situation observed in fields $B > 0.15$ T for both field directions, where the $(1, 1, 0)$ is completely suppressed and the $(0, 0, 2)$ has non-zero intensity means that all of the magnetic moments occupying sublattices sharing the direction of the anisotropy axes are either suppressed, or pointing along the same direction (e.g. only $\boldsymbol{x}$ instead of either $\boldsymbol{x}$ or $-\boldsymbol{x}$). This means that the magnetic order in TGG is extremely sensitive to the external magnetic field, and fields $B \sim 0.1$ T flip or suppress the magnetic moments at half of the terbium sites.

In order to check if this observation is consistent with the dominant role of dipolar interactions in TGG the following calculations were performed. A direct sum of energy of dipolar interactions per one ion was evaluated as a function of the radius of sphere, which contained the ions included into summation (Fig. 5.36(a)). The saturation of the sum was observed below $r = 30$ Å, which was chosen as the cutoff radius providing sufficient precision. The calculation of the field-dependence of energy per single ion in each of the magnetic structures showed the crossing of the energies at $B \sim 0.3$ T. This value is closed to the field where the antiferromagnetic structure is completely suppressed for both directions of the field. This is consistent with the assumption of dipole-dipole coupling dominating the interaction scheme in TGG. The discrepancy might come form the fact that constant value of the magnetic moment $\mu = 3.6\ \mu_B$ was assumed. As TGG is induced moment system and appearance of finite magnetic moment requires additional perturbation introducing mixing of the eigenstates forming the quasi-doublet this might not hold. Interestingly the suppression of AFM order takes place at lower fields in case of the $B \parallel [110]$ in contrast to the results of the calculations.

A general discussion in Ref. [253] concerning the non-Kramers system with two, well-separated from the higher levels, singlets (e.g. quasi-doublet ground-state in TGG)

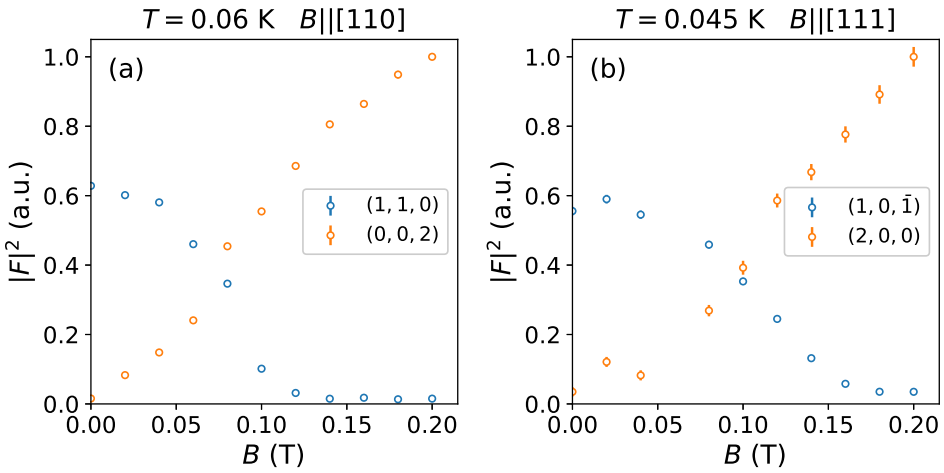

Figure 5.35: Field dependence of the intensity of magnetic Bragg reflections $(1, 1, 0)$ and $(0, 0, 2)$ measured with neutron single-crystal diffraction in the ordered phase of TGG. (a) magnetic field applied along [110] crystallographic direction. Data measured with $\lambda = 2.362$ Å on The D23 diffractometer at the ILL facility. (b) magnetic field applied along [111] crystallographic direction. Data measured with $\lambda = 1.177$ Å on the ZEBRA diffractometer at the SINQ neutron source at the PSI.

showed that these systems exhibit Ising like behaviour with only single non-zero value of the g-tensor. The ordered structure of TGG contains chains of the collinear moments along a, b and c formed by third-nearest-neighbours and the dipole-dipole interactions in the ferromagnetic arrangement between the ions up to that distance are nullified. This raises another concern of TGG hosting akin to the canonical Ising chain in the transverse field [254], which might lead to the suppression of the magnetic moment in the sublattices for which there is non-zero component of the applied filed perpendicular to the anisotropy axis. The refinement of 6 magnetic reflections at $B = 0.14$ T along [110], where no presence of $(1, 1, 0)$ reflection is observed, have confirmed the alignment of the moment along only the a, b and c. The refined moment values for the three sublattices are $2.5(1)$, $-2.1(2)$ and $-1.4(1)$ μ_B respectively. This result is consistent with the described suppression of moments along the c. However, the sources of the difference between the other two sublattices remain unknown. In order to ascertain this observation a survey on larger number of the reflection is necessary.

5.9 Conclusions and outlook

Time-of-flight neutron powder diffraction study allowed to confirm the low-temperature ordered magnetic structure of TGG. It follows the $Ia\bar{3}d'$ magnetic space-group describing the multi-axial antiferromagnet with six sublattices hosting magnetic moments aligned along the principal directions a, b and c of the cubic crystallographic unit cell. A single-crystal neutron scattering experiment revealed $T_N = 0.24$ K and a substantial reduction of the ordered magnetic moment $\mu = 3.56(3)$ μ_B from the free-ion value $\mu_{Tb^{3+}} = 9.72$ was observed. The temperature-evolution of the order parameter was found to deviate form the theoretical prediction for the nearest-neighbour Ising model on a simple BCC

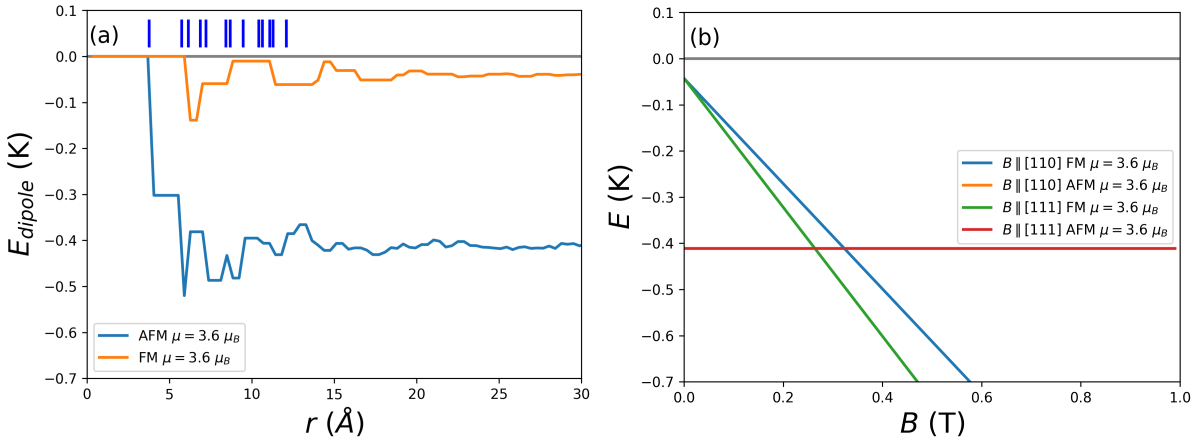

Figure 5.36: Direct sum of the energy of dipolar interactions per single terbium ion in TGG for the magnetic structure described with $Ia\bar{3}d'$ (AFM) and the ferromagnetic arrangement of the magnetic moments described in the text (FM). The value of the magnetic moment was taken form the zero-field ordered magnetic structure. (a) dependence of the energy per ion as a function of the radius of the sphere containing ions taken into account in the summation. The dark-blue marks show few first distances to the n^{nh}-nearest-neighbours. (b) field-dependence of the energy per Tb ion in the two aforementioned magnetic structures. the summation performed within the $r = 30$ Å.

lattice. However, this departure is not as substantial as it was observed in previous studies [218] and could possibly be assigned to the long-ranged character of the dipole-dipole interactions playing the dominant role in the rare-earth garnets.

The development of magnetic correlations was detected, for $T_N < T < 50$ K, in the magnetic structure factor retrieved from the diffuse neutron scattering data. This observation is consistent with the expected appearance of correlated paramagnetic phase. The set of spin structures producing excellent agreement of their calculated structure factor with the experimental results was obtained with the structure annealing algorithm. No signs of the dipolar order parameter were found in the radial spin correlations extracted from the simulation boxes. This suggests presence of non-dipolar type of a hidden order governing the correlated phase. A further analysis of the spin configurations testing more complex possibilities should allow to resolve this issue.

Such significant reduction of the value of spontaneous magnetic moment in the ordered phase points to the importance of the crystal field effects in TGG. The low symmetry local environment of Tb^{3+} site leads to complete lifting of the degeneracy of the crystal field states. Using the inelastic neutron scattering eleven transitions within the multiplet of the ground-state term were detected. The energies of these transitions reflecting the eigenvalues of the crystal field Hamiltonian were used to refine the set of Stevens parameters allowing for a determination of the structure of CEF eigenstates in terms of functions of the $^7F_6$ ground-state term of the Tb^{3+} ion. The resulting detailed crystal field scheme gives an opportunity to reexamine the theories describing the thermal Hall effect and acoustic Faraday effect on a more rigorous basis.

In the following time-of-flight inelastic neutron scattering experiment on a single-

crystal sample six magnetic excitons created from the first excited crystal field state. They manifest strong collective character given by the interactions between the terbium ions. The exciton branches were measured in both the paramagnetic and the ordered regimes without significant changes in their structure between the phases. Softening of one of these branches at the magnetic propagation vector on cooling towards T_N was detected, but closing the gap, and thus the signature of soft-mode character of the ordering transition was not observed. Possibly the mean-field calculations within the random-phase approximation would allow for determination of the interactions responsible for the departure from single-ion behaviour.

In the light of the presence of the magnetoelastic effects in TGG, it is necessary to incorporate the description of lattice excitations into the models describing these effects. a neutron spectroscopy measurement of the acoustic phonon modes in TGG was performed. The fitted dispersion relations show reasonable agreement with the results of DFT calculations published in Ref. [248] and thus prove their feasibility for use in the future calculations including coupling of lattice dynamics to magnetism.

Chapter 6

$RbNiCl_3$ - rubidium nickel chloride

6.1 ABX_3 family

The ABX_3 family (where A =Rb^+, Cs^+, B =Co^{2+}, Cu^{2+}, Fe^{2+}, Mn^{2+}, Ni^{2+}, V^{2+} and X =Cl^-, Br^-, I^-) of triangular antiferromagnets [255] has primarily drawn interest due to two aspects of their structure, which follows the $P6_3/mmc$ (no. 194) hexagonal space group. The sublattice constructed by the B-sites forms chains parallel to the crystallographic c-axis (Fig. 6). These chains are arranged in pattern of equilateral triangles, which results in the formation of a triangular lattice by the B-ions, in the basal ab-plane. In the case where ions carrying a magnetic moment occupy this site, and where these are coupled with nearest-neighbour and next-nearest-neighbour antiferromagnetic interactions, ABX_3 hosts both antiferromagnetic spin-chain and triangular structures. These are of interest due to the exotic physics resulting from lowered dimensionality (Sec. 2.4) and geometrical frustration (Sec. 2.5). Hence, this family is often incorporated into a wider group of stacked triangular antiferromagnets [255]. The ions within a single chain interact via a superexchange interaction through three equivalent X anions along $B-X-B$ path, while there is no direct superexchange path, because of an additional intermediate ion in between the neighbouring chains [255]. The shortest path of interaction is thus $B-X-X-B$. This gives a rise to a difference of two or three orders of magnitude between effective intrachain and interchain interactions. This causes the vast majority of the ABX_3 family to exhibit quasi one-dimensional behavior at low temperatures.

Depending on the choice of magnetic B-ion, the system's behaviour can vary significantly from strong easy-axis anisotropy Ising antiferromagnet (B =Co^{2+}) via isotropic-moment Heisenberg antiferromagnets with weak axial, or easy-plane anisotropies (B =Mn^{2+}, Ni^{2+} and V^{2+}), to a local singlet ground state magnet with suppressed long-range order (B =Fe^{2+}) [255].

In the case of nearly isotropic magnetic moments, ABX_3 might be described by the following Heisenberg antiferromagnetic Hamiltonian:

$$\mathcal{H} = J\sum_{i}^{\text{chain}} \boldsymbol{S}_i \cdot \boldsymbol{S}_{i+1} + J'\sum_{k<l}^{\text{plane}} \boldsymbol{S}_k \cdot \boldsymbol{S}_l + D(S_i^z)^2 - g\mu_{\text{B}}\sum_i \boldsymbol{H}\cdot\boldsymbol{S}_i, \tag{6.1}$$

where J and J' are nearest-neighbour (intrachain) and next nearest-neighbour (interchain) couplings according to the described superexchange paths. D gives the magnitude

Table 6.1: Magnetic transition temperatures, interaction strengths and details of the ordered magnetic structure for Heisenberg triangular antiferromagnets $A\mathrm{NiCl_3}$.

A^+	T_{N1} (K)	T_{N2} (K)	J (meV)	J' (meV)	D (meV)	μ (μ_{B})	θ (°)
$\mathrm{Cs^+}$	4.84 [256]	4.40 [256]	2.28 [257]	0.044 [257]	−0.004 [54]	1.05 [258]	59 [259]
$\mathrm{Rb^+}$	10.9 [260]	-	4.02 [261]	0.116 [261]	−0.0062 [262]	1.3 [263]	57.5 [263]

of the single ion anisotropy and the last term gives the Zeeman coupling to the external magnetic field.

$B =\mathrm{Ni^{2+}}$ compounds are of special interest as $\mathrm{Ni^{2+}}$ with the $3d^8$ valence shell configuration carries $S = 1$ spin angular momentum and shows very small (axial) anisotropy. Due to their negligible anisotropy they are often classified in the literature as triangular Heisenberg antiferromagnets [255] (in contrast to triangular Ising antiferromagnets with strong axial anisotropy), but the investigation presented in this work is focused on the consequences of the chain-like arrangement. As described in Sec. 2.4.1, spin-1 chains, according to the Haldane conjecture [49], are expected to exhibit a singlet ground-state and a gapped triplet excitation spectrum. In contrast to conventional magnets, where the gap is often a sign of single-ion anisotropy, here it is brought on by more fundamental effects of the topology of the magnetic Hamiltonian (Sec. 2.4.1).

The schematic representation of the $H - T$ phase diagram of a classical triangular Heisenberg antiferromagnet with small easy-axis anisotropy is shown in Fig. 6.1. In zero-field it is expected to exhibit two magnetic phase transitions. The first is due to intrachain ordering of components of the magnetic moments aligned along the direction of chains (c-axis). The second transition, occurring at slightly lower temperature, corresponds to the onset of three-dimensional Néel order. The resulting magnetic structure (Fig. 6.2) is characterized by antiparallel arrangements of neighbouring moments belonging to a single chain. However, only in one-third of chains are they aligned along the c-axis. The magnetic moments residing on the remaining two thirds of chains are contained within the ac plane and are canted by an angle $\pm\theta$ from the c-axis. In the absence of single-ion anisotropy $\theta = 60°$ between neighbouring sites along the a and b directions. The easy-axis anisotropy results in $\theta < 60°$, as is observed in $\mathrm{RbNiCl_3}$ (Tab. 6.1).

Table 6.1 shows the ordering temperatures, effective exchanges and features of magnetically ordered phases (size of the ordered moment, canting angles) in $\mathrm{CsNiCl_3}$ and $\mathrm{RbNiCl_3}$ triangular Heisenberg antiferromagnets. The most striking difference between those two compounds is the presence of two ordering transitions in $\mathrm{CsNiCl_3}$ [256], consistent with the expected phase diagram (Fig. 6.1), while only one is observed in $\mathrm{RbNiCl_3}$ [260]. In the former case, both of the transitions should be characterized by critical behaviour of the three-dimensional XY type [264, 255], connected with ordering of the chirality on the triangles formed in the basal plane ($\vec{\kappa} = \frac{2}{3\sqrt{3}}(\boldsymbol{S}_i \times \boldsymbol{S}_j + \boldsymbol{S}_j \times \boldsymbol{S}_k + \boldsymbol{S}_k \times \boldsymbol{S}_i)$ for sites i, j and k occupying a single triangle). This is not the case for $\mathrm{RbNiCl_3}$, where conventional Heisenberg-like behaviour was detected [260]. This discrepancy was attributed to much smaller axial anisotropy in the rubidium compound (Tab. 6.1), which does not suppress the fluctuations of magnetic moments as it does in $\mathrm{CsNiCl_3}$. These fluctuations prevent ordering of the components of magnetic moments parallel to the easy-axis and do not

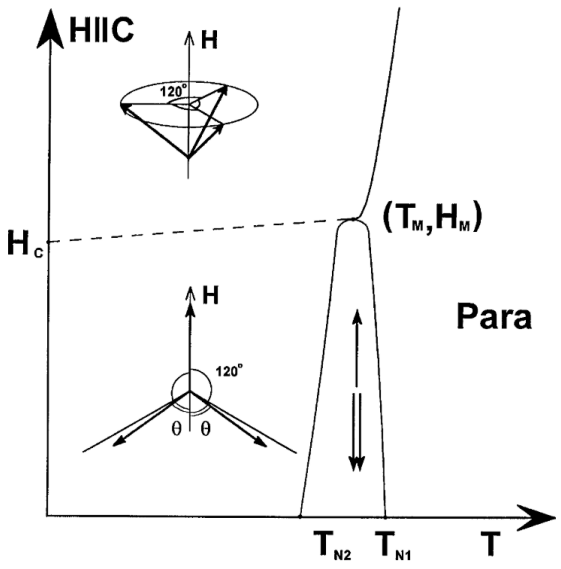

Figure 6.1: Schematic temperature-field phase diagram of Heisenberg triangular antiferromagnet with small easy-axis anisotropy. Figure adapted from Ref. [255].

allow the chiral long-range order to establish.

Signatures of Haldane physics were found in two of the nickel chlorides, namely $CsNiCl_3$ [51, 32] and $RbNiCl_3$ [261, 266]. Both materials exhibit the presence of a well-defined dispersive branches of Haldane modes above T_N, in the quantum-disordered regime of the Haldane spin-liquid. However, observation of the onset of the magnetic order is a sign that the interchain interactions are strong enough to overcome the one-dimensional many body effects generating the Haldane spin-liquid phase [32]. Initial attempts to account for spectra measured in $CsNiCl_3$ [51] were partially successful, but did not result with an unique model describing the system both below and above the onset of the Néel order. For $T > T_N$ a mean-field theory with an additional perturbation from the weak coupling between the chains [267] reproduced the gapped excitation and gave the correct value of the gap. At $T < T_N$ a spin-wave theory was constructed, which has given reasonable agreement between the calculated and observed dispersion relations. Nonetheless, in order to reproduce the gapped modes, present also in the ordered phase, the psin-wave theory required assuming a large single-ion anisotropy inconsistent with measurements of the θ-angle in the ordered phase [259] and the observed value of the spin-flop field [268]. Moreover, the polarization of the mode determined with neutron spectroscopy did not agree with the results obtained with the spin-wave theory. Only when constructing a quantum-field theory taking into account the non-linear effects of quantum fluctuations, present both above and below the ordering transition, allowed to obtain correspondence with the experimental data. However, some discrepancies were still found at higher interchain wave vectors [269].

Additional arguments in favour of the Haldane conjecture being relevant to $CsNiCl_3$ were developed on the basis of a comparison between $CsMnCl_3$ (with Mn^{2+} ions carrying $S = \frac{5}{2}$ [270]) and $CsNiCl_3$. Neutron spectroscopy has shown that while the former system can be described very well within the framework of conventional spin-wave theory, the

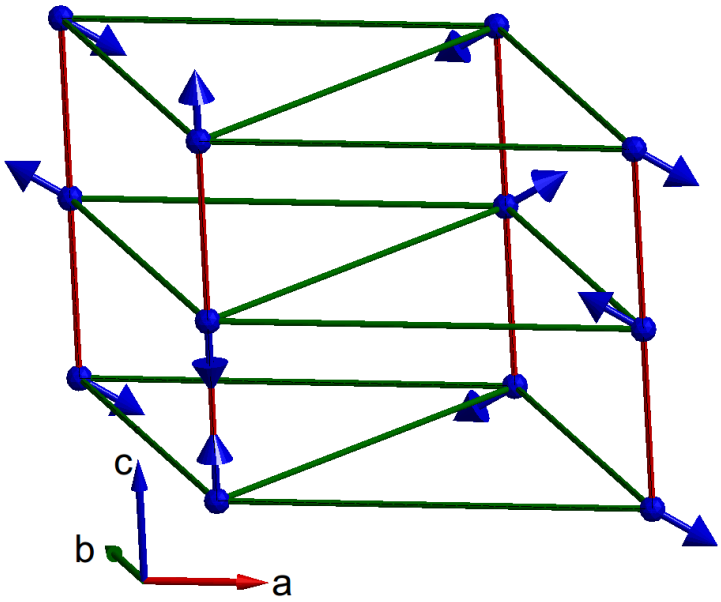

Figure 6.2: Magnetic sublattice and ordered magnetic structure of $RbNiCl_3$. Red bonds mark the strongly coupled chains while the green form the equilateral triangles in the *ab* plane. The moments not aligned along the *c* are canted at the angle given in Tab. 6.2. Figure prepared with use of the `SPINW` software [265].

discrepancies detected in the latter cannot be ascribed to other factors perturbing the basic model, like the presence of geometrical frustration.

Further investigation of $CsNiCl_3$ with high resolution polarized inelastic neutron scattering and unpolarized experiments in magnetic field [271, 272] have pointed to the presence of excitation modes predicted exclusively within the framework of field-theory [32, 273, 274]. These experiments have also found strong longitudinal fluctuations of magnetic moments exhibited even in the three-dimensional ordered phase, proving the triplet character of the observed excitations, and consistent with Haldane conjecture. This scenario also provides an explanation for the reduction of the value of spontaneous magnetic moment in the ordered phase of $CsNiCl_3$ ($RbNiCl_3$ as well), as it is almost 50% lower than the free ion value for Ni^{2+}, $\mu_{\text{free}} = 2\ \mu_{Ni^{2+}}$ (Tab. 6.1).

Apart from the presence of a spectral feature consistent with Haldane's description of integer spin-chains, the appearance of additional spectral weight above the well-defined triplet mode was also observed [54, 55]. A three-particle scattering continuum is expected from theory to appear at antiferromagnetic (AFM) point of the one-dimensional structure factor associated with the direction of the Ni^{2+} chains ($Q_l = 1$), and have an energy gap of $3\Delta_0$, where Δ_0 is the value of the Haldane gap a $T = 0$ K. Moreover, it should exhibit a pronounced maximum at $E \sim 6\Delta_0$ [275, 276]. However, the reported feature in neutron scattering (Fig. 6.3) accounts for 12(2)% of the scattering weight, which is an order of magnitude larger than predictions for three-particle continuum of Haldane modes [49, 54]. Another theoretical work assuming the presence of a biquadratic coupling within the chain [277] suggest that excitations in such a system might be treated within a Majorana fermion framework and predict a multi-particle continuum containig 17% of

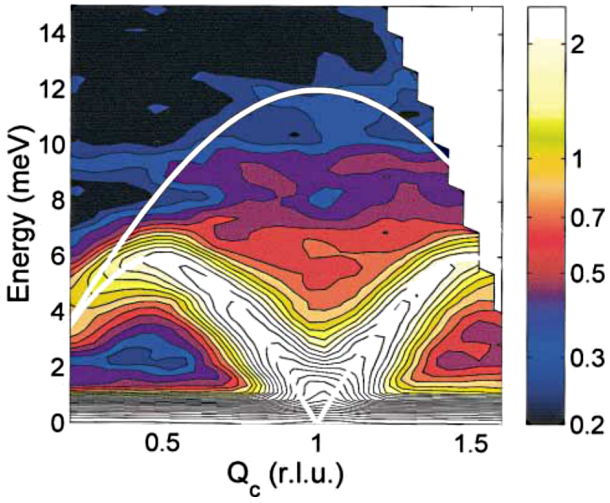

Figure 6.3: Diffuse continuum scattering at $T > T_N$ in $CsNiCl_3$. The white solid lines mark the range of spinon continuum with its lower boundary overlapping with the Haldane mode at $l = 0.5$. Figure adapted from Ref. [54].

the scattering weight at $Q_l = 1$, much closer to the observations on $CsNiCl_3$. Nonetheless, a biquadratic coupling of the strength required for the appearance of the diffuse feature in the dynamical structure factor would also result in an increase of the size of the gap, which is in contrast with experimental observations.

Based on the resemblance between continuum the scattering in $CsNiCl_3$ and the two-spinon continuum found in $S = \frac{1}{2}$ Heisenberg chains [55] it was proposed that it results from the appearance of spin-$\frac{1}{2}$ degrees of freedom brought on by frustrated interactions between the chains. However, the only previous works on the possible existence of fractional-spin objects in the Haldane chains are related to the loose ends of finite-length chains [278, 279].

The lack of a well-established, feasible explanation for the appearance of the multiparticle continuum might suggest the presence of novel physical phenomena contributing to the reported observations. Taking into account the formerly established significance of quantum fluctuations in $CsNiCl_3$, it is reasonable to assume that the crucial role here is played by frustrated interchain interactions [55], which enhance the quantum fluctuations. This would explain some discrepancies found between the theoretical and experimental values of the correlation length and, related to it, the size of the Haldane gap [55]. One can argue that this unexplored feature should be investigated in further detail, especially given that, the interplay of geometrical frustration and Haldane physics, both expected to be present in the nickel chlorides, is still not yet well-understood [280, 281].

6.2 $RbNiCl_3$ - $S = 1$ Heisenberg spin-chain.

$RbNiCl_3$ is characterized by a much stronger interactions than $CsNiCl_3$ (Tab. 6.1). However, inelastic neutron scattering experiments on $RbNiCl_3$ above and below the ordering temperature, showed the presence of Haldane modes and a spin-wave spectrum similar to the one observed in $CsNiCl_3$. The dispersion relations of these modes are also reasonably

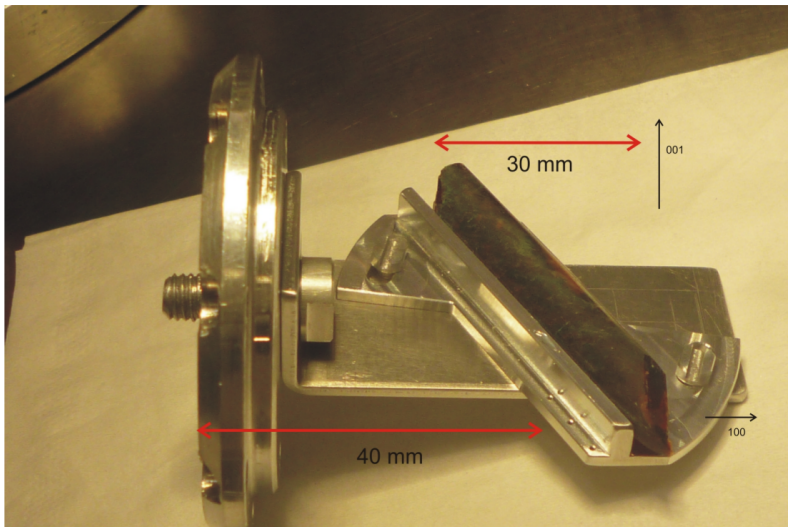

Figure 6.4: Single-crystal of $RbNiCl_3$ on an aluminum sample mount. The black arrows mark the labelled main crystallographic directions.

well described by the field theory [261].

This compound has never been investigated for the presence of continuum scattering as one observed in $CsNiCl_3$. In order to check for of diffuse features in the spectrum, polarized neutron spectroscopy experiment was performed on the state-of-the-art HYSPEC time-of-flight neutron spectrometer which combines the opportunity of employing the a polarization analysis technique (Sec. 3.1.3) with a wide detector array coverage.

6.2.1 $RbNiCl_3$ - excitation spectrum at $T > T_N$

Fig. 6.5 shows the sum of the six scattering channels (both spin-flip and non spin-flip for each beam polarization direction $\boldsymbol{x}$, $\boldsymbol{y}$ and $\boldsymbol{z}$) measured at $T = 13.5$ K, on a single-crystal of $RbNiCl_3$. The sample used during this experiment was a single-crystal rod of length $l \sim 45$ mm and diameter $\phi \sim 5$ mm, aligned with the(hhl) crystallographic plane in the horizontal scattering plane (Fig. 6.4). The polarization analysis was performed with use of a Heusler alloy monochromator and polarizing wide-angle supermirror analyzer (Sec. 3.1.3).

The round feature placed just below $Q_l = 0.5$ Å^{-1} at $E \sim 2$ meV was identified to be a spurious feature caused by scattering of the direct beam transmitted through the sample on aluminum elements of the instrument's construction and should be disregarded.

The dominating feature visible in the dynamic structure factor is a dispersive branch of gapped Haldane excitations. The cuts presented in Fig. 6.5(b) show the energy of this excitation at Q_l corresponding to the antiferromagnetic point and the zone boundary. The gap at $Q_l = 1$ was found to be $\Delta = 2.5$ meV. These cuts are made in a narrow Q_l range to avoid integrating in contribution from modes dispersing away from $Q_l = 1$. The linewidths of the excitations was found to be characterized by the following full-width half-maxima: $FWHM_{\mathrm{AFM}} = 1.97$ and $FWHM_{\mathrm{ZB}} = 1.1$ meV. They are far from the instrumental resolution, expected to vary between 1.1 and 0.32 meV for energy transfers between 0 and 10 meV in the used experimental setup. In the total scattering intensity,

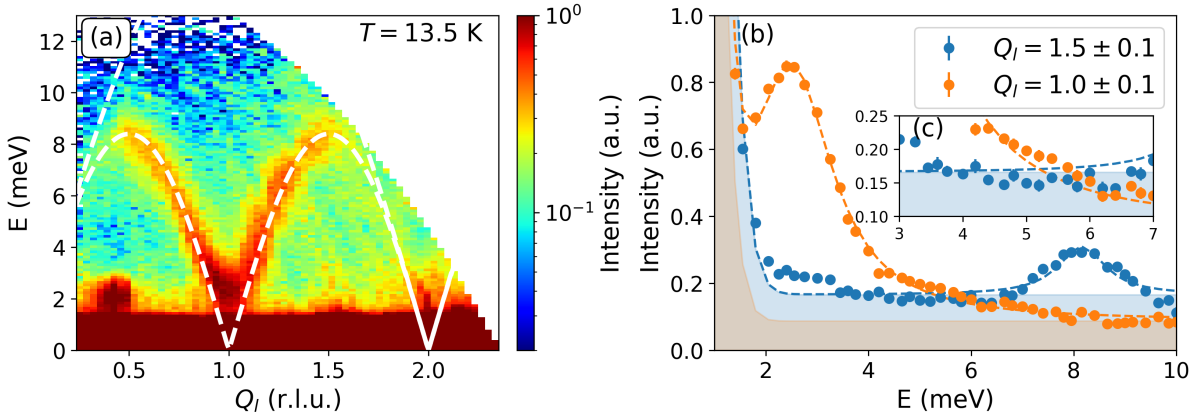

Figure 6.5: Inelastic neutron scattering from a single-crystal of $RbNiCl_3$ at $T = 13.5$ K, above the T_N, showing the presence of the gapped mode of Haldane excitations. (a) dependence of the scattering on the component of wavevector parallel to the chain. The white dashed lines mark the same range as the solid lines in Fig. 6.3. (b) constant-Q_l cuts at the antiferromagnetic point $Q_l = 1$ and at the one-dimensional zone boundary ($Q_l = \frac{1}{2}$). The shaded areas mark the fitted Gaussian peaks of the elastic line with a flat background. Dashed lines show the peak of the Haldane mode fitted with an anti-symmetrized Lorentzian weighted by the Bose factor. Inset (c) shows a small increase of intensity above the excitation where the appearance of continuum scattering is expected. Data measured with $E_i = 15$ meV, on the HYSPEC TOF spectrometer at the SNS at the ORNL facility.

one can observe also weak, but non-zero scattering weight above the fitted tail of Haldane mode (inset of Fig. 6.5(b)), in the same $S(Q_l, E)$ range where continuum scattering was found in $CsNiCl_3$. However, its very weak intensity (much weaker than in $CsNiCl_3$) does not allow for its unambiguous identification.

Two of the scattering channels distinguished with polarization analysis are shown in Fig. 6.6. These are the $\boldsymbol{x}$ spin-flip (XSF) and the $\boldsymbol{x}$ non spin-flip (XNSF). In the experimental configuration used, $\boldsymbol{x}$ and $\boldsymbol{y}$ were contained within the horizontal scattering plane (the (hhl) crystallographic plane of the sample, Fig. 6.4) with $\boldsymbol{x} \parallel \boldsymbol{Q}_{(0,0,1)}$ for zero energy transfer, and k_f pointing to the center of the detector array. In this configuration the best separation of magnetic and nuclear contributions to the measured scattering cross-section is achieved in XSF and XNSF channels. However, the angle between $\boldsymbol{Q}_{(0,0,1)}$ and $\boldsymbol{x}$ changes throughout the spectrum and the separation becomes worse on moving away from the elastic line. This is visible in Fig. 6.6(b), where some remaining intensity from the Haldane modes can be recognized leaking into the XNSF channel.

The different contributions to the scattering cross-section on a single-crystal experiment might be separated using the following relations for XYZ-polarization analysis for multi-detector instrument, as derived in Ref. [116]:

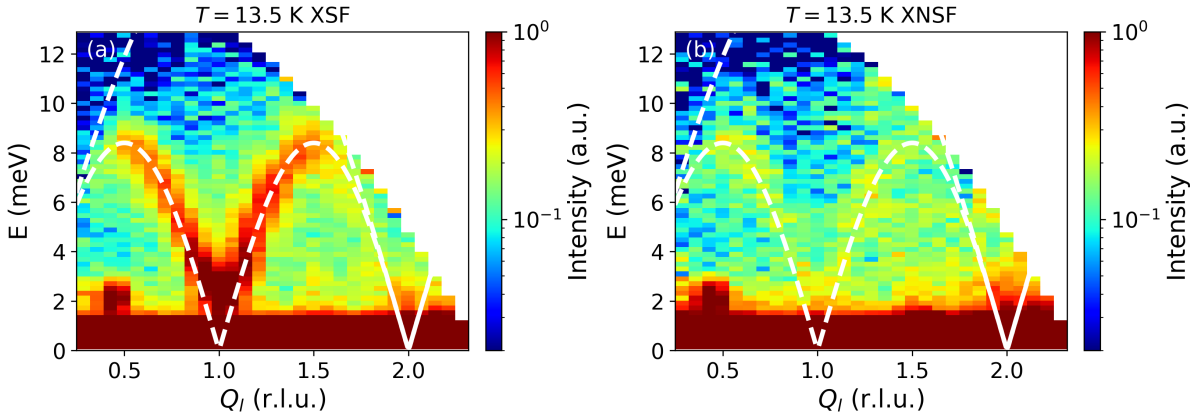

Figure 6.6: Inelastic neutron scattering in the x spin-flip and the x non spin-flip channels separated by the polarization analysis, measured on a single-crystal of $RbNiCl_3$ at $T = 13.5$ K The white dashed lines mark the same range as solid lines in Fig. 6.3. Data measured with $E_i = 15$ meV, on the HYSPEC TOF spectrometer at the SNS at the ORNL facility.

$$N^\dagger N = \frac{1}{2}(\Sigma^{nsf}_{x'} + \Sigma^{nsf}_{y'} - \Sigma^{sf}_{z}), \tag{6.2a}$$

$$I_{si} = \frac{3}{2}\frac{\Sigma^{nsf}_{x'} - \Sigma^{nsf}_{y'}}{\cos^2\alpha - \sin^2\alpha} + \frac{3}{2}\Sigma^{sf}_{z}, \tag{6.2b}$$

$$M^\dagger_{\perp y} M_{\perp y} = \Sigma^{sf}_{z} - \frac{2}{3} I_{si}, \tag{6.2c}$$

$$M^\dagger_{\perp z} M_{\perp z} = \Sigma^{nsf}_{z} - \frac{1}{3} I_{si} - N^\dagger N, \tag{6.2d}$$

where on the left-hand side are the contributions from the nuclear, nuclear-spin incoherent, magnetic from magnetisation along $\boldsymbol{y}$, and magnetic from magnetisation along $\boldsymbol{z}$ scattering, respectively. $\Sigma^{sf/nsf}_{\nu'}$ (with $\nu' = x', y', z$) represent the measured spin-flip or non spin-flip channels. The primed $\boldsymbol{x'}$ and $\boldsymbol{y'}$ coordinates are introduced as every detector tube in the array records different Q_h, which causes the Schärpf angle [112] between the polarization of the beam and the momentum transfer to vary throughout the detector array. Moreover, in the inelastic measurement every tube measure specific trajectory in the $(\boldsymbol{Q}, E)$-space along which the Schärpf angle varies as well.

After a quick inspection of Eq. 6.2 in the presented form, one realizes that separation of the magnetic and the nuclear-spin incoherent intensities fails for $\alpha \approx \frac{\pi}{4}$, where the expression 6.2(b) diverges. In order to overcome this difficulty the following procedure was applied: $I_{si}(Q_l, E)$ was calculated for whole available dataset using the expression 6.2. Region affected by the singularity with α in the range $38° - 52°$ was then removed from the dataset. Narrow E-integrated cuts through obtained $I_{si}(Q_l, E)$ were checked for any signs of Q_l-dependence. None were found, which is consistent with the picture of nuclear spins being localized, uncorrelated scatterers, each of them associated with single nuclei. The resulting dataset was thus Q_l-integrated in the whole non-excluded range and fitted

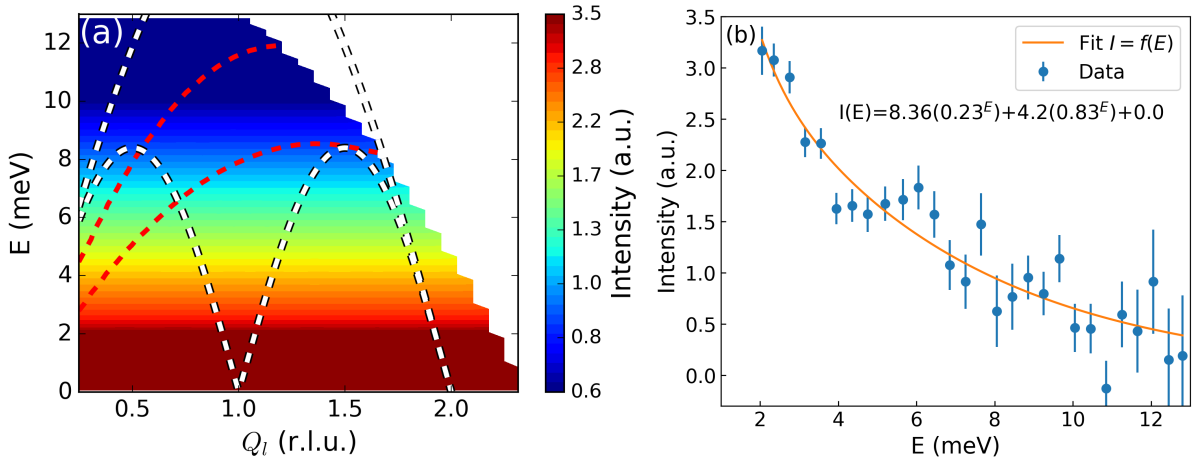

Figure 6.7: Fit to the nuclear-spin incoherent scattering in $RbNiCl_3$ at $T = 13.5$ K. (a) the red dashed lines mark the range $38° < \alpha < 52°$. The white dashed lines in (a) mark the same range as solid lines in Fig. 6.3. (b) $\boldsymbol{Q}$-integrated I_{si}, the $38° < \alpha < 52°$ region was excluded from integration.

with a phenomenological function. The best agreement of the fit was achieved with the sum of two exponential functions 6.7(b). The divergence-free data set prepared with the fitted function (Fig. 6.7(a)) was used as nuclear-spin incoherent component in the separation of magnetic scattering (Eq. 6.2c and 6.2d).

Both of the separated magnetic contributions to the cross-section of $RbNiCl_3$ $M^\dagger_{\perp y}M_{\perp y}$ and $M^\dagger_{\perp z}M_{\perp z}$ at $T = 13.5$ K are shown in Fig. 6.8. They do not reveal any systematic difference in the dynamical structure factor. Moreover, no significant disparity was noted in the constant-Q_l cuts, at $Q_l = 1$ r.l.u. between these contributions. This suggest that magnetization along a-direction of the unit cell and in the plane perpendicular to a have a comparable contribution to the observed spectral features. $M^\dagger_{\perp y}M_{\perp y}$ and $M^\dagger_{\perp z}M_{\perp z}$ were summed into a total magnetic contribution to improve the overall statistics.

Figure 6.9(a) shows the summed $M^\dagger_{\perp y}M_{\perp y}$ and $M^\dagger_{\perp z}M_{\perp z}$ scattering contributions. Upon closer inspection, one can notice an excess of scattering weight, above the branch of Haldane modes. However, this signal is very weak, and the broadness of the excitation peak makes its unambiguous identification in constant-Q_l cuts challenging(Fig. 6.9(b)). In this case there is a possibility of overestimating the width of the Haldane excitation peak in the fitting procedure thus absorbing the present continuum scattering into the tail of the mode.

Another practical difficulty connected with the experiment comes from the fact that measuring all of the polarization channels, as required for the separation of different contributions to the scattering cross-section, is time-consuming. That is why the measurement is usually performed at a limited number of in plane sample orientations. This only allows for covering a limited volume in $S(\boldsymbol{Q}, E)$. This results in the continuum scattering not being covered at exactly the same wavevector $\boldsymbol{Q}$ for all energy transfers. As can be deduced from the inter-chain exchange coupling constants (Tab. 6.1), this interaction is small but still present and should not be completely neglected in case of $RbNiCl_3$.

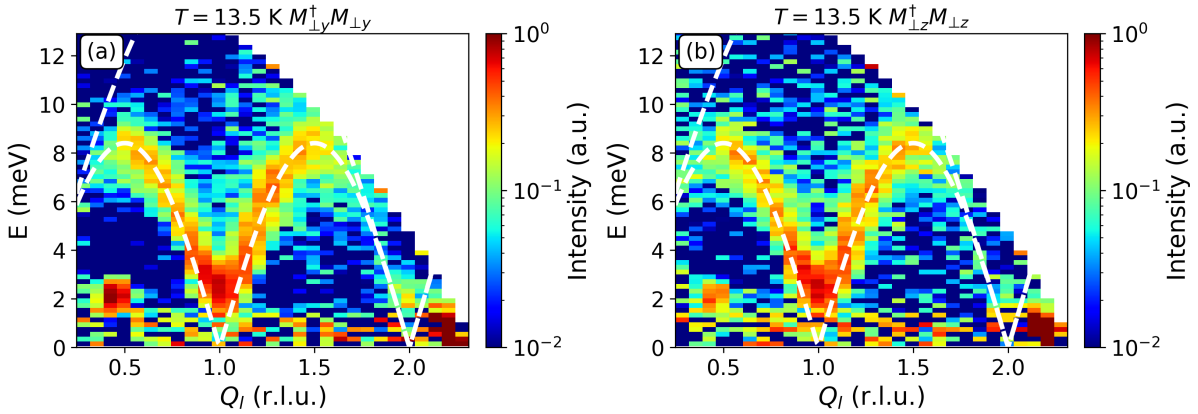

Figure 6.8: Magnetic scattering (a) $M^\dagger_{\perp y}M_{\perp y}$ and (b) $M^\dagger_{\perp z}M_{\perp z}$ from a single-crystal of $RbNiCl_3$ at $T = 13.5$ K separated with use of the XYZ-polarization analysis. The white dashed lines mark the same range as solid lines in Fig. 6.3. Data measured with $E_i = 15$ meV, on the HYSPEC TOF spectrometer at the SNS at the ORNL facility.

This is also visible in the slight modulation of rod-like features presented further in this work (Fig. 6.14(a)). It might result in some Q-dependence of the continuum scattering in the direction perpendicular to the chains and might therefore account for variation of its intensity throughout the experimental E-range.

6.2.2 $RbNiCl_3$ - excitation spectrum at $T < T_N$

Observation of scattering continuum in the ordered phase

In order to check if any signs of the continuum scattering might be found in the three-dimensional ordered phase ($T < T_N$) of $RbNiCl_3$, a measurement of the XSF channel, characterized by the biggest contribution from the magnetic scattering, was performed at $T = 5$ K (Fig. 6.10). The spin-wave branches present in the ordered phase should have much narrower lineshape with smaller tails. This would make the continuum, if present in this phase, easier to distinguish. Indeed, the measured spectrum contains much sharper excitations than the Haldane modes at $T > T_N$. Their linewidths at the same Q_l values were found to be $FWHM_{AFM} = 1.13$ and $FWHM_{ZB} = 0.638$ meV (Fig. 6.10(b)). These are much closer, but still above, the calculated estimates of the resolution, $1.1 - 0.32$ meV for the energy transfers between 0 and 10 meV. Constant-Q_l cuts presented in Fig. 6.10(b) show the presence of a broad, weak feature above the excitation branch suggesting the presence of the continuum below T_N and pointing that its detection might be facilitated by much sharper lines of the well-defined dispersive branches. No quantitative analysis was performed on this data as the magnetic contribution in the scattering measured in this channel varies with the energy and momentum transfer, making any estimates unreliable.

These observations imply the feasibility of further exploration of the multi-particle scattering in both $ANiCl_3$ compounds within the three-dimensional ordered regime. If quantum fluctuations are in any way responsible for appearance of the continuum, its

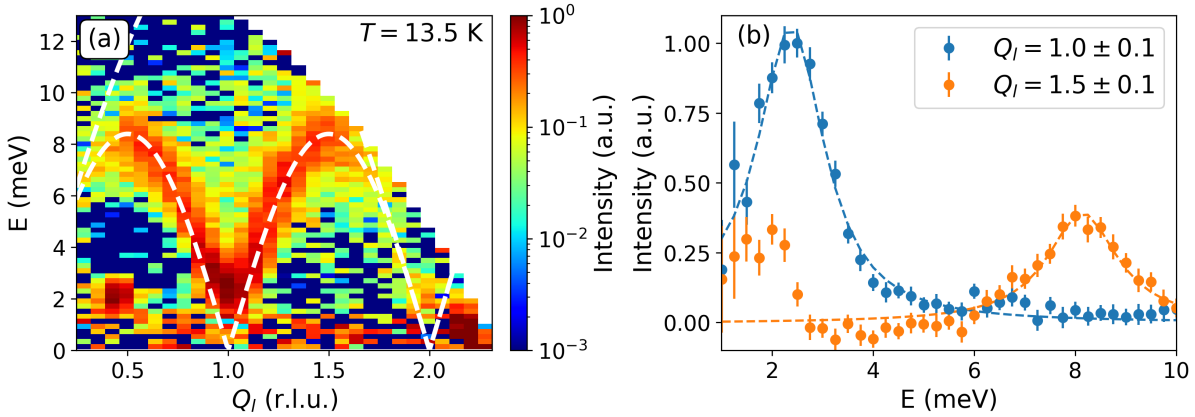

Figure 6.9: Magnetic scattering $M^{\dagger}_{\perp y}M_{\perp y} + M^{\dagger}_{\perp z}M_{\perp z}$ from a single-crystal of $RbNiCl_3$ at $T = 13.5$ K separated with use of the XYZ-polarization analysis. The white dashed lines in (a) mark the same range as solid lines in Fig. 6.3. (b) constant-Q_l cuts at the antiferromagnetic point $Q_l = 1$ and at the zone boundary $Q_l = \frac{3}{2}$. The dashed lines show the peak of the Haldane mode fitted with an antisymmetrized Lorentzian weighted by the Bose factor. Data measured with $E_i = 15$ meV, on the HYSPEC TOF spectrometer at the SNS at the ORNL facility.

presence would be consistent with conclusion of them playing an important role in both $CsNiCl_3$ [272] and $RbNiCl_3$ in the Néel phase.

Figure 6.11 shows the constant-$\boldsymbol{Q}$ scans of the magnetic inelastic neutron scattering at three wavevectors measured on the IN20 three-axis spectrometer. The magnetic scattering was separated from the three (x, y and z) non spin-flip polarization channels. The measured wavevectors are:$\boldsymbol{Q} = (\frac{1}{3}, \frac{1}{3}, 1)$ - the propagation vector of the magnetic structure, $\boldsymbol{Q} = (\frac{2}{3}, \frac{2}{3}, \frac{1}{2})$ at the top of the spin-wave branch and $\boldsymbol{Q} = (\frac{2}{3}, \frac{2}{3}, 0)$. The magnetic modes were fitted with an antisymmetrized Lorentzian weighted by the Bose factor. The averaged intensity of the $\boldsymbol{Q} = (\frac{2}{3}, \frac{2}{3}, 0)$ scan, which not affected by the continuum, was used as a flat background in the fitting procedure. The very low scattering intensity at this $\boldsymbol{Q}$-point is consistent with previous observations of the continuum scattering only at the AFM point. The shaded red area marks the excessive scattering weight above the tail of fitted peak at $\boldsymbol{Q} = (\frac{1}{3}, \frac{1}{3}, 1)$. This area constitutes 5(3)% of the dynamic structure factor at $Q_l = 1$. It is therefore both much weaker than the value of 12(2)% found in $CsNiCl_3$ at $Q_l = 1$ [54] and stronger than three-particle excitaitons predicted by Haldane's theory, which anticipated 1% of the scattering weight in this diffuse feature.

Magnons in $RbNiCl_3$ at $T < T_N$

Apart from the polarized inelastic neutron scattering experiment on the HYSPEC TOF spectrometer a survey over a wide range of $S(\boldsymbol{Q}, E)$ was perofrmed deep in the ordered regime at $T = 2$ K. Series of cuts through the data were used in fits to linear spin-wave theory (LSWT) using the shared interface of the `Horace` [246] and the `SpinW` [265] codes. Thirteen two-dimensional $S(Q_i, E)$ cuts were performed along two types of directions: Q_h or Q_l, within the$[hhl]$ scattering plane. These were$[hh \pm 2]$, $[hh \pm \frac{3}{2}]$, $[hh \pm 1]$, $[hh \pm \frac{1}{2}]$ and

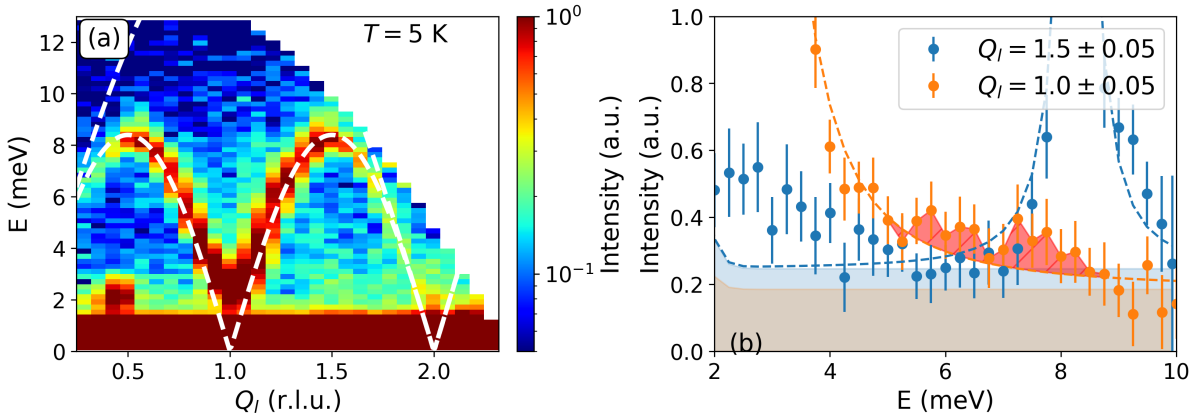

Figure 6.10: Neutron scattering in the x spin-flip channel separated by polarization analysis, measured on a single-crystal of $RbNiCl_3$ at $T = 5$ K. The white dashed lines in (a) mark the same range as solid lines in Fig. 6.3. (b) cuts at the antiferromagnetic point $Q_l = 1$ and at the zone boundary $Q_l = \frac{3}{2}$. Dashed lines show the peak of the Haldane mode fitted with an antisymmetrized Lorentzian weighted by the Bose factor. Data measured with $E_i = 15$ meV, on the HYSPEC TOF spectrometer at the SNS at the ORNL facility.

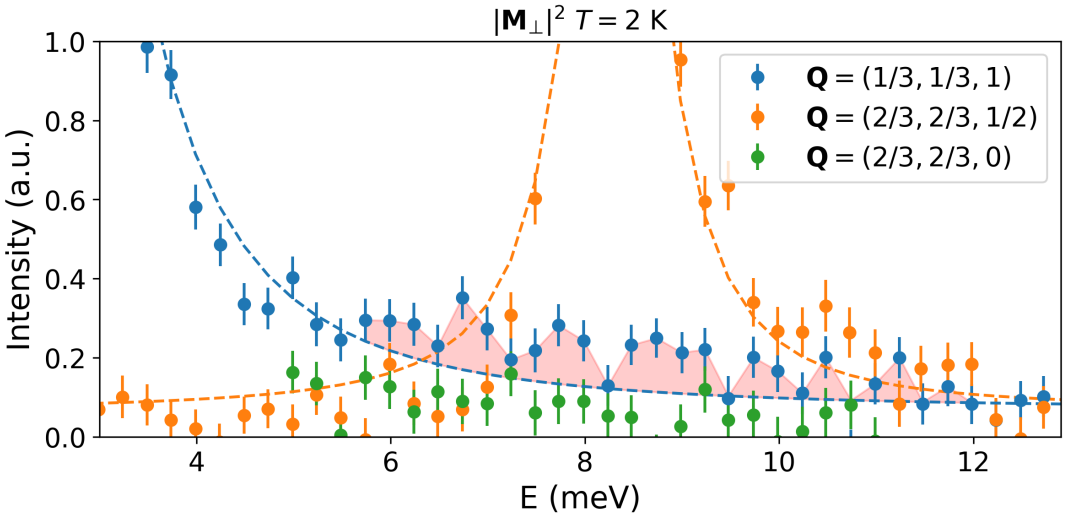

Figure 6.11: Constant-$\boldsymbol{Q}$ scans of the magnetic neutron scattering form a single-crystal of $RbNiCl_3$ measured at $T = 2$ K. Dashed lines show the peak of the Haldane mode fitted with an antisymmetrized Lorentzian weighted by the Bose factor. The red shaded area marks the excess scattering weight assigned to the continuum of multi-particle scattering. Data measured with the longitudinal polarization analysis technique on the IN20 triple-axis spectrometer, equipped with a Heusler alloy monochromator/analyzer setup and fixed $k_f = 2.66$ Å^{-1}.

Table 6.2: Initial and final values of the Hamiltonian parameters for the fitting procedure with the linear spin wave theory to the experimental data measured on a single-crystal of $RbNiCl_3$ at $T = 2$ K.

	J (meV)	J' (meV)	D (μeV)
Initial	4.02	0.116	-6.2
Final	4.012	0.1158	-6.188

$[hh0]$ for the former and $[\pm\frac{1}{2} \pm \frac{1}{2}l]$, $[\pm\frac{1}{3} \pm \frac{1}{3}l]$, $[00l]$ and $[11l]$ for the latter type. The cuts were integrated in perpendicular direction within the range $Q_\perp \pm 0.05$ r.l.u. The fitting procedure used the least-squares method to fit the interaction strength parameters (J, J' and D) of the proposed Hamiltonian (in this case Eq. 6.1). The modelled dispersion curves were convoluted with a Gaussian lineshape, which played a role of the instrumental resolution. This peak profile was used instead of a Lorentzian, a it lead to faster convergence of the fit with much better value of the χ^2 goodness of fit parameter. The FWHM parameter describing the linewidth of the modes was the fourth value allowed to vary during the execution of the code. The amplitudes of the fitted intensities were not scaled differently between the fitted dataset.

The initial parameters used during the fit are presented in Tab. 6.1. Surprisingly the fit converged at the values very close to the starting parameters. These results are presented in Tab. 6.2. The full-with half-maximum ($FWHM$) of the excitation was fitted to $FWHM = 0.9 \pm 0.004$, which is a bit lower than 1.1 meV calculated for the elastic line. Unfortunately the used code does not allow for including any energy dependence of the resolution in the fitted model.

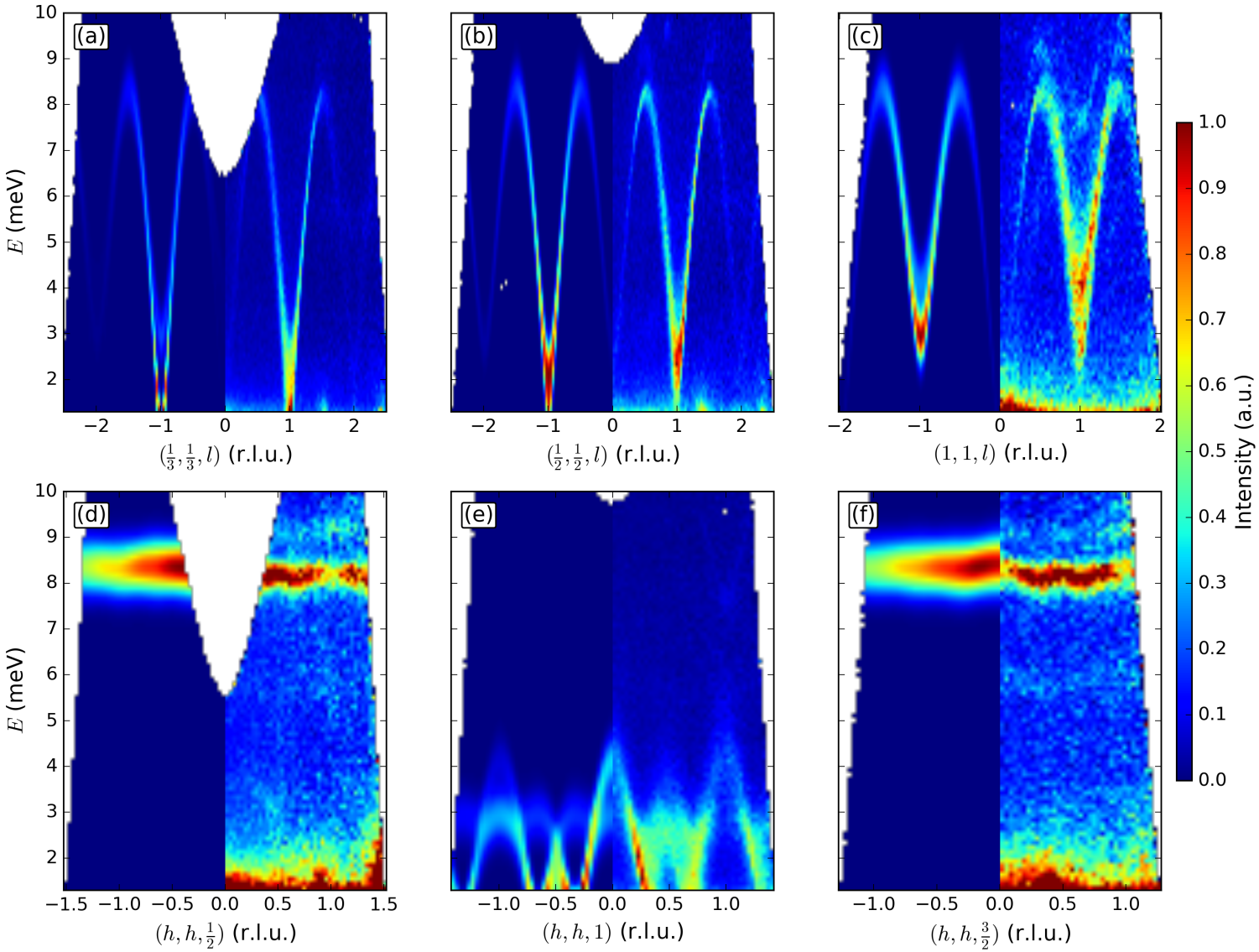

Figure 6.12: Magnon dispersions measured with inelastic neutron scattering in $RbNiCl_3$ at $T = 2$ K and results of the fit to the linear spin-wave theory. The fit was performed using `SpinW/Horace` software. The interaction constants resulting from the fit are given in the text. Data measured with $E_i = 15$ meV, on the HYSPEC TOF spectrometer at the SNS at the ORNL facility.

The simulated dynamical structure factor is presented alongside with the two-dimensional cuts through the experimental $S(\boldsymbol{Q}, E)$ in Fig. 6.12. The first observation is that the fitted parameters provide a good reproduction of the dispersion curves of the spin-wave modes along the chains (Q_l), as can be seen in panels (a)-(c). However, much bigger discrepancies are observed along the directions perpendicular to the chains (Q_h). They are especially pronounced at the low-energies close to the bottoms of dispersion curves, at the antiferromagnetic point $Q_l = 1$ and at the magnetic zone boundaries $Q_l = \frac{1}{2}$ and $Q_l = \frac{3}{2}$. The one-dimensional constant-E cuts made a at a single $\boldsymbol{Q}$ point presented inf Fig. 6.13, show in detail the extent of the mismatch between the LSWT results and the measured neutron spectra. This is particularly visible, that especially at the AFM point, the LSWT fails to reproduce the energy of the modes and the intensity of different components of the spectrum in the neutron scattering data. The conclusion might be drawn here, that indeed the excitaitons observed in the ordered phase of RbNiCl$_3$ cannot be treated as ordinary magnons within the framework of linear spin-wave theory. The data presented here, covering a larger volume of $S(\boldsymbol{Q}, E)$ than it was done in previous studies, could serve as a good reference point for the future calculations employing field-theory developed for Haldane chains. Performed fits did not allow for the variation of the background function as its size is negligible.

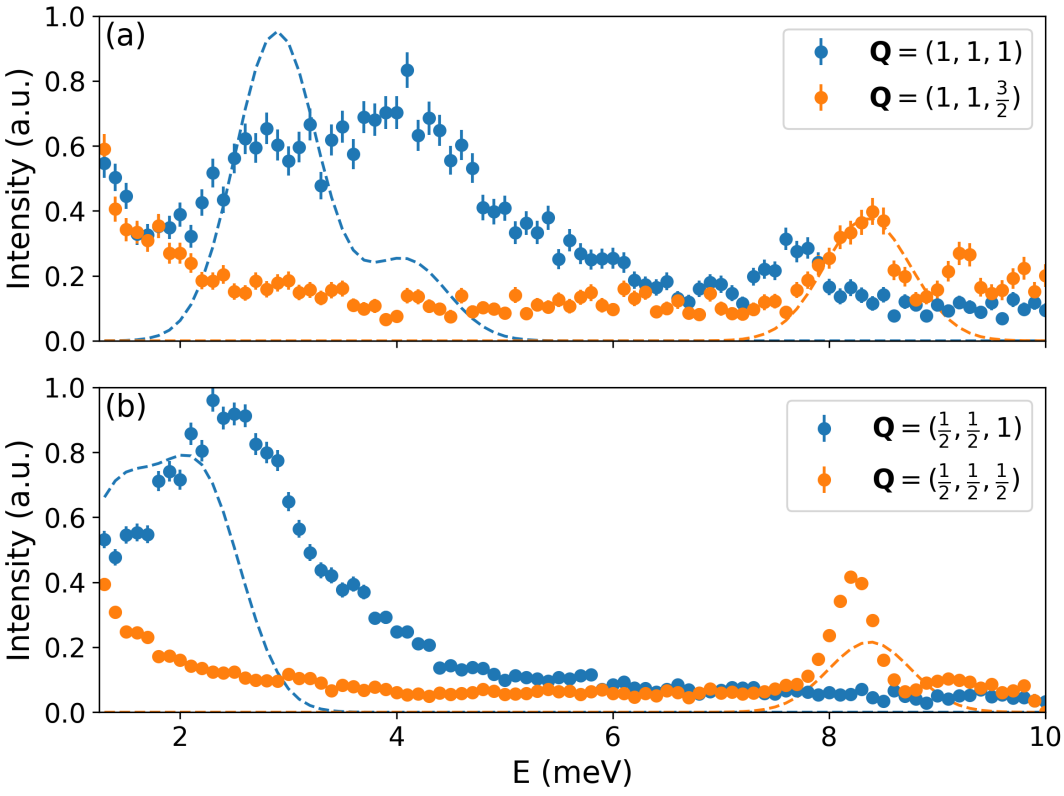

Figure 6.13: Comparison of constant-$\boldsymbol{Q}$ cuts through the inelastic neutron scattering data and the results of the fit to the linear spin-wave theory. Data was measured on a single-crystal of RbNiCl$_3$ at $T = 2$ K, on the HYSPEC TOF spectrometer at the SNS at the ORNL facility.

Departures from LSWT in the ordered phase of $RbNiCl_3$

Two regions with a large discrepancy with respect to LSWT calculations were found, namely the AFM-point ($Q_l = 1$) and the zone-boundaries ($Q_l = \frac{1}{2}$ and $Q_l = \frac{3}{2}$). The effects seen in the former are consistent with the presence of Haldane physics, and associated quantum fluctuations which persist in the ordered phase. These should be more pronounced at lower energies. It worth emphasizing that the differences between the experimental data and predictions of the linear spin-wave theory are visible in both the lineshapes of the excitations and their intensity across $(\boldsymbol{Q}, E)$-space. Moreover, the distribution of the scattering intensities along the $[hh1]$ direction (Fig. 6.12(e)) shows significant quantitative disagreement between the experiment and calculations. These effects are especially pronounced in the one-dimensional cuts through the $S(\boldsymbol{Q}, E)$ shown in Fig. 6.13.

The anomalies in the latter region, around the top of the magnetic excitation branches take place at higher energies, which would suggest them being unrelated to the quantum fluctuations. However, they resemble the observation of anomalous zone-boundary dispersion effects in the two-dimensional $S = \frac{1}{2}$ square-lattice antiferromagnet $Cu(pz)_2(ClO_4)_2$ [282]. These were assigned to quantum fluctuations associated with resonating valence bonds, which are enhanced by frustrated next-nearest-neighbour interactions. The presence of similar phenomena would be consistent with triangular the arrangement of the Ni-chains in $RbNiCl_3$, and the antiferromagnetic coupling between them.

Figure 6.14 shows the results of unpolarized inelastic neutron scattering measurement on $RbNiCl_3$ in the ordered Néel phase, at $T = 2$ K. Well-defined excitation branches are the dominating feature here. Rod-like $\boldsymbol{Q}$-dependence along the $(h, h, 0)$ direction, with only slight dispersion along $(h, h, 1)$, reflects the predominantly one-dimensional character of magnetic interactions in $RbNiCl_3$ (Fig. 6.14(b)).

In this data, it is hard to detect the presence of a diffuse continuum above the magnetic excitation modes. Moreover the lack of polarization analysis does not allow for assigning the magnetic origin of the scattering, which introduces the risk of misinterpreting weak phonon intensity as continuum scattering. This is especially the case given that some phonon branches are expected in this energy range and direction within the Brillouin zone.

That said, two sets of small anomalies were observed in the data. The first are small wing-like branches placed on top of the spin-wave dispersion curves at the zone-boundary. The second one is in the form of well-defined almost parabolic-shaped excitation branches, centered around $\boldsymbol{Q} = (1, 1, 1)$ and $\boldsymbol{Q} = (1, 1, -1)$ points. Dips in these modes appear exactly at the $S(\boldsymbol{Q}, E)$ where the presence of scattering continuum was observed in the $CsNiCl_3$ [54, 55].

The former set of anomalies form of a sharp dispersive excitation over the main mode. Their appearance resemble two scenarios. The first is the lifting of the degeneracy of the main excitation mode at the zone-boundary, possibly related to the aforementioned effects of quantum fluctuations observed in $S = \frac{1}{2}$ square-lattice antiferromagnet. The second is the presence of two-magnon bound states as reported for strong-leg $S = \frac{1}{2}$ spin ladders [283]. In case of the second, the stronger intensity around $Q_l = 1$ and $E = 7.5$ meV could be explained as coming from this mode. Moreover, in case of ladders, there should be a multi-magnon continuum above this bound state mode. However, the

information extracted form the data does not allow to argue for either of the presented options.

Concerning the latter anomalies, constant-E cuts presented in Fig. 6.14(b) have shown a circular feature in the dynamical structure factor at the $\boldsymbol{Q} = (1, 1, 1)$. It would suggest that the observed mode, in contrast to the excitation modes, which have a rod-like shape in this projection, does not have a one-dimensional nature. This observation is not consistent with the predominantly one-dimensional character of the magnetic interactions in $RbNiCl_3$. As the presented data does not allow the determination of the magnetic or nuclear character of this feature, one has to check the possibility of this being an optical phonon mode which should reflect absence of dimensionality lowering in the description of crystalline lattice. The results of DFT calculations for $RbNiCl_3$, analogous to those for TGG used in Sec. 5.7, were also made available in Ref. [284]. Phonon dispersion relations calculated with use of `PHONOPY` code [251] using the results from Ref. [284] are plotted in Fig. 6.16.

The dispersion relation for one of the optical modes obtained from results of DFT calculations agrees well with the observed excitation (Figs. 6.14(a) and 6.15). The main observed discrepancy between them is a slight shift towards lower energies of the strong intensity of the dispersion curve around $\boldsymbol{Q} = (1, 1, 1)$. This might be caused either by insufficient precision of DFT calculations, which is the result of the trade-off between accuracy of the results and computation time. The other reason might be another possibly magnetic excitation appearing at very close in energy to the phonon branch. Due to vicinity in the $(\boldsymbol{Q}, E)$ space of the phonon branch to the suspected magnetic excitations either in form of bound states, or continuum, the possibility of the phonon being coupled to the magnetic degrees of freedom might be present, as it is often observed in frustrated systems.

6.3 Conclusions and outlook

The presence of a multi-particle scattering continuum was investigated in spin-1 Heisenberg antiferromagnet chain $RbNiCl_3$. Neutron scattering spectra at the temperature of the onset of three-dimensional magnetic order ($T_N = 10.9$ K), have shown a broad mode of Haldane triplet excitations. Analysis of the magnetic neutron scattering at $T = 13.5$ K, extracted using XYZ-polarization analysis, did not result in unambiguous identification of the weak intensity above the Haldane modes and in the vicinity of the antiferromagnetic point $Q_l = 1$, as was observed in the case of $CsNiCl_3$. The large linewidth of the Haldane excitaitons affects the region of interest, which together with the uncertainty coming form the separation procedure of the contributions to the neutron scattering cross-section made the identification of the continuum impossible.

However, some scattering weight was observed in the vicinity of $Q_l = 1$ at $T = 5$ K. Suggesting the possibility of multi-particle effects being persistent in the three-dimensional ordered phase Here the lineshape of dispersive excitations should be narrower and affect the region of interest to a smaller extent. Magnetic contribution to the inelastic neutron scattering, extracted using longitudinal polarization analysis from measurement on a three-axis spectrometer at $T = 2$ K have shown a broad signal on top of the tails of well-defined excitations. It constitutes 5(3)% of the total magnetic scattering at $Q_l = 1$,

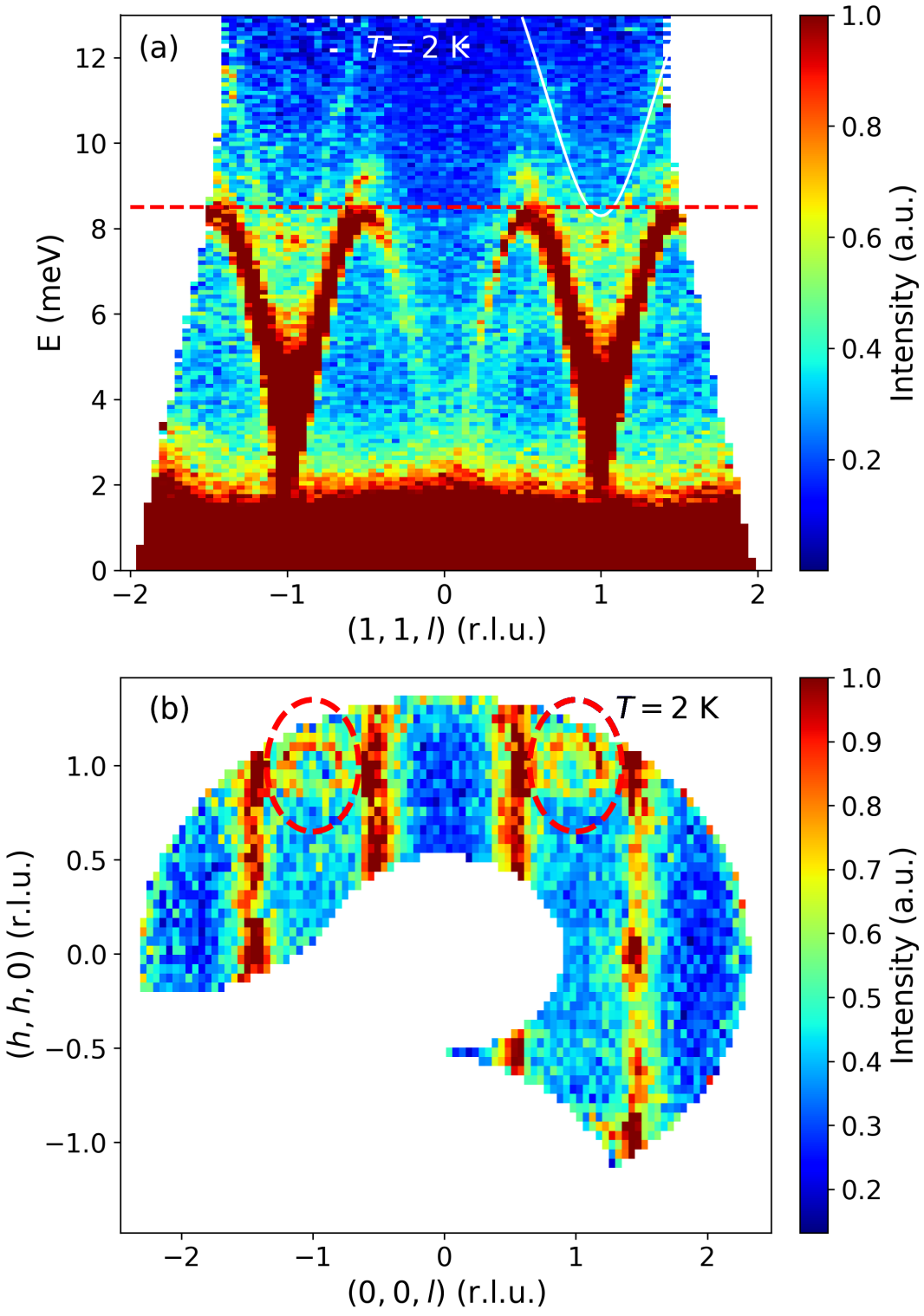

Figure 6.14: Inelastic neutron scattering measured in $RbNiCl_3$ at $T = 2$ K. (a) cut through $S(\boldsymbol{Q}, E)$ along $[11l]$ direction, and integrated in the range $Q_h = 0.9 - 1.1$ Å^{-1}. The red dashed line shows the position of the constant-E cut shown in panel (b). The white solid line marks the calculated dispersion relation [284] of optical phonon assigned to the detected inelastic feature. (b) constant-E cut integrated in the range $E = 8.5 - 9$ meV. The red dashed circles mark the position of the inelastic mode, which is dispersive in three dimensions. Data measured with $E_i = 15$ meV, on the HYSPEC TOF spectrometer at the SNS at the ORNL facility.

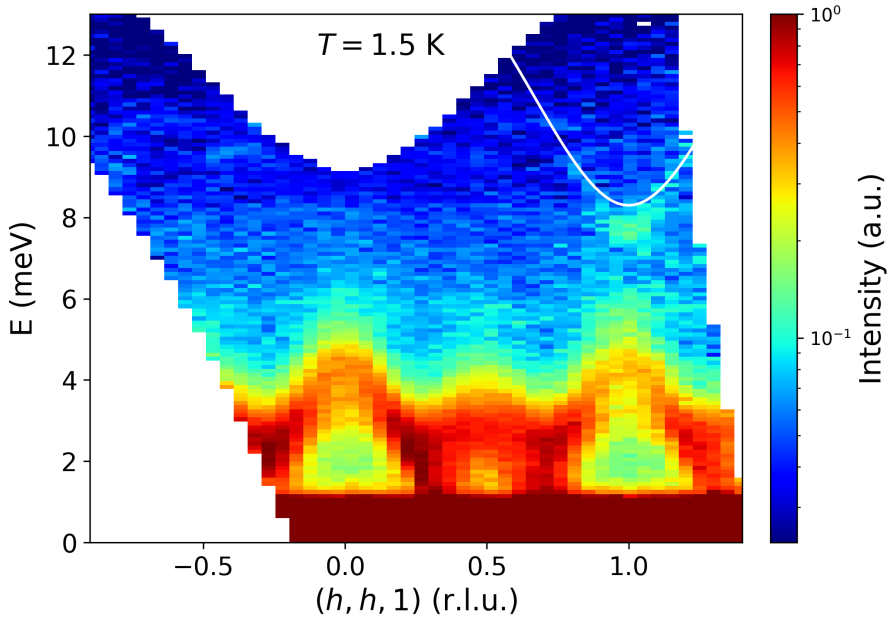

Figure 6.15: Inelastic neutron scattering measured in $RbNiCl_3$ at $T = 2$ K. Cut through $S(\boldsymbol{Q}, E)$ along $[hh1]$ direction, and integrated in the range $Q_l = 0.9 - 1.1$ Å^{-1}. The white solid line marks the calculated dispersion relation [284]. of optical phonon assigned to the detected inelastic feature. Data measured with $E_\mathrm{i} = 15$ meV, on the HYSPEC TOF spectrometer at the SNS at the ORNL facility.

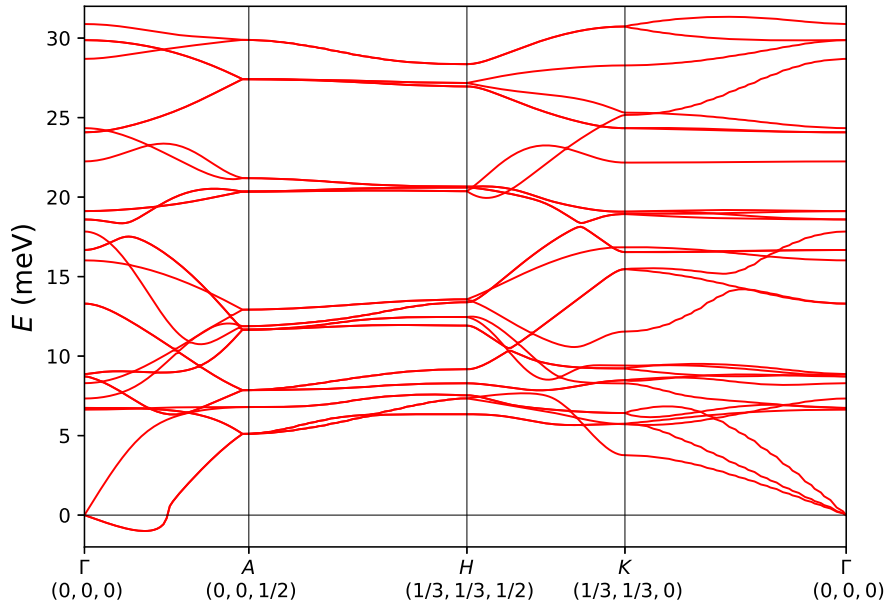

Figure 6.16: Phonon spectra obtained with use of the results of the DFT calculations presented in Ref. [284] plotted along few high-symmetry directions of the Billouin zone of $RbNiCl_3$. Dispersion curves retrieved with use of the `PhonoPy` code [251].

what is less than half of the 12(2)% reported for $CsNiCl_3$ [54], but is still much greater than the 1% predicted by the nonlinear σ model [275, 276].

The linear spin-wave theory fit to the experimental $S(\boldsymbol{Q}, E)$ measured at $T = 2$ K did not result in any further adjustment of the already established parameters of the Heisenberg Hamiltonian including intrachain and interchain interactions with a single-ion anisotropy term. It gives a rough description of the magnetic excitation dispersion. The discrepancies between the calculated and experimental spectra are found in the low-energy part of the spectrum, around the antiferromagnetic point ($Q_l = 1$), and at higher energies at the zone-boundary of the dispersion along the chain ($Q_l = \frac{1}{2}$). The former is consistent with the effect of quantum fluctuations, expected to have stronger influence at lower energies of the spectrum and already reported to be present in the ordered phases of $CsNiCl_3$ and $RbNiCl_3$ [272, 260]. The latter is similar to observations on $S = \frac{1}{2}$ square-lattice antiferromagnet [282], where the frustrated next-nearest-neighbour interactions enhance the quantum fluctuations, which manifest themselves in the anomalous zone-boundary dispersion of the magnetic modes. This is consistent with the triangular arrangement of antiferromagnetically coupled chains in $RbNiCl_3$, providing a configuration for the appearance of geometrical frustration. Performing numerical simulations taking into account the presence of quantum fluctuations could allow to confirm the sources of the observed anomalies. Moreover, an additional mode was found in the inelastic neutron scattering data, at high-energies. Based on the results of DFT calculations [284] it was successfully identified as an optical phonon. Due to its vicinity to the magnetic in the $(\boldsymbol{Q}, E)$ space the possibility of the phonon being coupled to the magnetic degrees of freedom might be present, as it is often observed in frustrated systems.

Chapter 7

Conclusions and perspectives

X-ray and neutron diffraction experiments confirmed the magnetostructural character for both stages of transition observed in $LiGaCr_4O_8$ ($x = 0$). The first transition at $T = 13.8$ K is associated with single $\boldsymbol{k} = (0, 0, 1)$ (in cubic basis) magnetic propagation vector and the magnetic intensity was successfully refined with the assumption of a $F\bar{4}dm \rightarrow I\bar{4}m2$ cubic-to-tetragonal transition and a magnetic order described by the C_A222_1 magnetic space group. The second stage at $T = 12.5$ K, results with the onset of a much more complex multi-$\boldsymbol{k}$ structure. The observed magnetic reflections might be indexed with $\boldsymbol{k}_1 = (1/2, 1/2, 0)$ and $\boldsymbol{k}_2 = (1, 0, 1/2)$ (in cubic basis) magnetic propagation vectors, but this combination still cannot be accounted for all of them suggesting the presence of a third component. These results show the advantages of using the neutron and x-ray studies in solving these type of problems. However, this example also reveals the sheer necessity of availability of single-crystal samples in further studies.

The lack of presence of a long-range order in $LiGa_{0.95}In_{0.05}Cr_4O_8$ proves that the suppression of Néel order takes place for much weaker doping levels than it was found out earlier with bulk probes. Reverse Monte Carlo analysis of the structure factor of magnetic diffuse scattering and results of Rietveld refinement showing the presence of local structural distortions suggest the onset of a classical spin-nematic phase. Inelastic neutron scattering study of excitations present within the nematic phase revealed signs of precessive fluctuations of magnetic moments within hexagonal loops singled out in the breathing pyrochlore lattice by local distortions. Moreover, a quasielastic signal reminiscent of spin flips within small molecular clusters was found in the neutron scattering data. Neutron spin echo spectroscopy have shown the presence of fluctuations persistent down to the lowest temperatures. The application of other resonance techniques (e.g. muon spin resonance) would give an opportunity to obtain the full description of evolution of dynamics in the nematic phase upon cooling.

Low-temperature ordered magnetic structure of TGG was confirmed to follow the $Ia\bar{3}d'$ magnetic space-group. The further single-crystal study has found $T_N = 0.24$ K and a substantial reduction of the ordered magnetic moment $\mu = 3.56(3)$ μ_B from the free-ion value. The temperature-evolution of the order parameter was found to deviate form the theoretical prediction for the nearest-neighbour Ising model what could possibly be assigned to the long-ranged character of the dipole-dipole interactions playing the dominant role in the rare-earth garnets. Diffuse neutron scattering data has shown the development of correlated paramagnetic phase at for $T_N < T < 50$ K was. However, no

signs of the dipolar order parameter were found in the radial spin correlations extracted from the simulation boxes, pointing that further analysis of the spin configurations testing more complex possibilities is necessary to find a complete description of this state.

Observation of the transitions between the levels of the ground-state term multiplet, in neutron spectroscopy data, allowed for refinement the set of Stevens parameters of CEF Hamiltonian and the determination of the structure of CEF eigenstates. The resulting detailed description of the crystal field scheme in TGG provides a foundation for reexamination of the models describing the thermal Hall effect and acoustic Faraday effect on a more rigorous basis. Following single-crystal experiment showed the presence of six dispersive magnetic excitons in place of the first excited CEF state. These are present in both the paramagnetic and ordered regimes, and reflect the collective character crystal field effects in TGG resulting from the couplings between the ions. A softening of one of these modes was observed at the magnetic propagation vector on cooling towards T_{N}. Nonetheless, no closing of the gap was detected. Possibly the mean-field calculations within the random-phase approximation would allow for determination of the interactions responsible for the departure from single-ion behaviour.

Magnetic inelastic neutron scattering in $RbNiCl_3$ in the three-dimensional ordered phase have shown a signs of continuum scattering analogous to the one observed in the quantum-disordered phase of closely related $CsNiCl_3$ [54]. It constitutes 5(3)% of the total magnetic scattering at the antiferromagnetic point of intrachain dispersion, what is less than half of the 12(2)% reported for $CsNiCl_3$ [54], but is still much greater than the 1% predicted by the field-theory for $S = 1$ antiferromagnetic Heisenberg chain. Further study of the continuum scattering at the different points of the Brillouin zone could provide more information, which could be compared with prospective numerical calculations aiming at acocunting for the effects of frustration between the chains.

Moreover, discrepancies were found in between the spectra calculated with linear spin-wave theory and experimental results. These appeared in the low-energy part of the spectrum, around the antiferromagnetic point ($Q_l = 1$), and at higher energies at the zone-boundary of the dispersion along the chain ($Q_l = \frac{1}{2}$). The former is consistent with the effect of quantum fluctuations, expected to have stronger influence at lower energies of the spectrum. The latter is similar to observations on $S = \frac{1}{2}$ square-lattice antiferromagnet [282], where the frustrated next-nearest-neighbour interactions enhance the quantum fluctuations, which manifest themselves in the anomalous zone-boundary dispersion of the magnetic modes. This is consistent with the triangular arrangement of antiferromagnetically coupled chains in $RbNiCl_3$, providing a configuration for the appearance of geometrical frustration. Performing numerical simulations taking into account the presence of quantum fluctuations could allow to confirm the sources of the observed anomalies.

Appendix A

Experimental details

Table A.1: Details of experimental procedures on $LiGa_{1-x}In_xCr_4O_8$, referred in Chapter 4.

Compound	Type of experiment	Instrument/ Beamline (Facility)	Sample details	Instrumental setup
$LiGaCr_4O_8$	SXRPD	MS - X04SA (SLS - PSI)	Powder in boron glass capillary $\varnothing = 0.3$ mm	$\lambda =$ 0.565 Å($E =$ 22 keV)
$LiInCr_4O_8$	SXRPD	MS - X04SA (SLS - PSI)	Powder in boron glass capillary $\varnothing = 0.3$ mm	$\lambda =$ 0.565 Å($E =$ 22 keV)
$LiGa_{0.95}In_{0.05}Cr_4O_8$	SXRPD	MS - X04SA (SLS - PSI)	Powder in boron glass capillary $\varnothing = 0.3$ mm	$\lambda =$ 0.565 Å($E =$ 22 keV)
$LiGaCr_4O_8$	NPD	D20 (ILL)	Powder in V can $\varnothing = 8$ mm $h = 55$ mm	$\lambda = 2.41$ Å
$LiGa_{0.95}In_{0.05}Cr_4O_8$	TOF-NPD	WISH (ISIS - STFC)	Powder in V can $\varnothing = 6$ mm $h = 80$ mm	-
$LiGa_{0.95}In_{0.05}Cr_4O_8$	TOF-INS	MARI (ISIS - STFC)	Powder in Al can $\varnothing = 45$ mm $m \sim 8$ g	$E_i =$ 16 meV
$LiGa_{0.95}In_{0.05}Cr_4O_8$	NSE-INS	IN11 (ILL)	Powder in Al can $m \sim 6$ g	$\lambda = 5.5$ Å

Table A.2: Details of experimental procedures on TGG referred in Chapter 5.

Type of experiment	Instrument/ Beamline (Facility)	Sample details	Instrumental setup
TOF-INS	MARI (ISIS - STFC)	Powder in Al can $\varnothing = 45$ mm $m \sim 7$ g	$E_{\mathrm{i}} = 12, 50, 75, 150$ meV
TOF-NPD	WISH (ISIS - STFC)	Powder in Cu can $\varnothing = 6$ mm m~ 7 g	-
TOF-INS	IRIS (ISIS - STFC)	Powder in Al can $\varnothing = 24$ mm $m \sim 7$ g	PG002 and PG004 analyzer setup
ND	D7 (ILL)	Single-crystal $l \sim 45$ mm $\varnothing \sim 5$ mm	$\lambda = 4.855$ Å
TOF-INS	IN5 (ILL)	Single-crystal $l \sim 45$ mm $\varnothing \sim 5$ mm	$\lambda = 2.55, 7$ Å
TAS-INS	EIGER (SINQ-PSI)	Single-crystal $l \sim 45$ mm $\varnothing \sim 5$ mm	$k_i = 2.662$ Å^{-1}
ND	ZEBRA (SINQ-PSI)	Single-crystal	$\lambda = 1.82$ Å
ND	D23 (ILL)	Single-crystal $4 \times 4 \times 1$ mm	$\lambda = 2.362$ Å
TAS-INS	THALES (ILL)	Single-crystal $l \sim 45$ mm $\varnothing \sim 5$ mm	$k_i = 1.5$ Å^{-1} Coll. M 40' S 40' A

Bibliography

[1] J. C. Maxwell. *A Treatise on Electricity and Magnetism*, volume 1 & 2 of *Cambridge Library Collection - Physical Sciences*. Cambridge University Press, 2010.

[2] A. Einstein. *Annalen der Physik*, 322(10):891–921, 1905.

[3] W. Gerlach and O. Stern. *Zeitschrift für Physik*, 9(1):349–352, Dec 1922.

[4] O. Benton and N. Shannon. *J. Phys. Soc. Jpn.*, 84:104710, 2015.

[5] S.-H. Do, S.-Y. Park, J. Yoshitake, J. Nasu, Y. Motome, Y. Kwon, D. T. Adroja, D. J. Voneshen, K. Kim, T.-H. Jang, J.-H. Park, K.-Y. Choi, and S. Ji. *Nature Physics*, 13:1079 EP –, Sep 2017.

[6] S. A. Wolf, A. Y. Chtchelkanova, and D. M. Treger. *IBM Journal of Research and Development*, 50(1):101–110, Jan 2006.

[7] N. A. Mezaal, K. V. Osintsev, and T. B. Zhirgalova. *IOP Conference Series: Earth and Environmental Science*, 87(3):032024, 2017.

[8] G. E. W. Bauer, E. Saitoh, and B. J. van Wees. *Nature Materials*, 11:391 EP –, Apr 2012. Review Article.

[9] S. N. Andrianov and S. A. Moiseev. *Phys. Rev. A*, 90:042303, Oct 2014.

[10] B. Lian, X.-Q. Sun, A. Vaezi, X.-L. Qi, and S.-C. Zhang. *Proceedings of the National Academy of Sciences*, 115(43):10938–10942, 2018.

[11] K. Yoshida. *Theory of magnetism*. Springer-Verlag, 1996.

[12] P. Fazekas. *Lecture Notes on Electron Correlation and Magnetism*. World Scientific, 1999.

[13] S. Blundell. *Magnetism in Condensed Matter*. Oxford Master Series in Condensed Matter Physics. OUP Oxford, 2001.

[14] J. Sólyom. *Fundamentals of the Physics of Solids: Volume I Structure and Dynamics*. Springer, 01 2007.

[15] A. P. Jenö Sólyom. *Fundamentals of the Physics of Solids - Electronic Properties*, volume Volume II. Springer, 1 edition, 2008.

[16] J. Sólyom. *Fundamentals of the Physics of Solids: Volume I Structure and Dynamics*. Springer, 2010.

[17] J. Jensen and A. Mackintosh. *Rare earth magnetism: structures and excitations*. International series of monographs on physics. Clarendon Press, 1991.

[18] E. Bauer and M. Rotter. *Magnetism of Complex Metallic Alloys: Crystalline Electric Field Effects*, pages 183–248. World Scientific, 2009.

[19] K. W. H. Stevens. *Proceedings of the Physical Society. Section A*, 65(3):209, 1952.

[20] D. J. Newman and B. Ng, editors. *Crystal Field Handbook*. Cambridge University Press, 2000.

[21] J. Kanamori. *Journal of Physics and Chemistry of Solids*, 10(2):87 – 98, 1959.

[22] T. Moriya. *Phys. Rev.*, 120:91–98, Oct 1960.

[23] L. D. Landau and E. M. Lifshitz. *Statistical physics*, volume Volume 5, Part 1. Pergamon, 3 edition, 1969.

[24] A. Zheludev, S. Maslov, G. Shirane, I. Tsukada, T. Masuda, K. Uchinokura, I. Zaliznyak, R. Erwin, and L. P. Regnault. *Phys. Rev. B*, 59:11432–11444, May 1999.

[25] A. Wills. *Le Journal de Physique IV*, 11(PR9):Pr9–133, 2001.

[26] R. Ballou and B. Ouladdiaf. Chapter 3 - representation analysis of magnetic structures. In T. Chatterji, editor, *Neutron Scattering from Magnetic Materials*, pages 93 – 151. Elsevier Science, Amsterdam, 2006.

[27] A. Auerbach. *Interacting electrons and quantum magnetism*. Graduate texts in contemporary physics. Springer-Verlag, 1994.

[28] E. Ising. *Zeitschrift Fur Physik*, 31:253–258, 1925.

[29] L. Onsager. *Phys. Rev.*, 65:117–149, Feb 1944.

[30] H. T. Diep. *Frustrated Spin Systems*. World Scientific, 2004.

[31] H. Bethe. *Zeitschrift für Physik*, 71(3):205–226, Mar 1931.

[32] I. Affleck. *Journal of Physics: Condensed Matter*, 1(19):3047–3072, may 1989.

[33] J. des Cloizeaux and J. J. Pearson. *Phys. Rev.*, 128:2131–2135, Dec 1962.

[34] A. Ovchinnikov. *Zh. Eksp. Teor. Fiz.*, 56:1354, 1969.

[35] L. Faddeev and L. Takhtajan. *Physics Letters A*, 85(6):375 – 377, 1981.

[36] F. D. M. Haldane. *Phys. Rev. Lett.*, 60:635–638, Feb 1988.

[37] B. S. Shastry. *Phys. Rev. Lett.*, 60:639–642, Feb 1988.

[38] F. D. M. Haldane. *Phys. Rev. Lett.*, 67:937–940, Aug 1991.

[39] D. A. Tennant, T. G. Perring, R. A. Cowley, and S. E. Nagler. *Phys. Rev. Lett.*, 70:4003–4006, Jun 1993.

[40] I. A. Zaliznyak, H. Woo, T. G. Perring, C. L. Broholm, C. D. Frost, and H. Takagi. *Phys. Rev. Lett.*, 93:087202, Aug 2004.

[41] M. Enderle, B. Fåk, H.-J. Mikeska, R. K. Kremer, A. Prokofiev, and W. Assmus. *Phys. Rev. Lett.*, 104:237207, Jun 2010.

[42] M. Matsuda, M. Takeda, M. Nakamura, K. Kakurai, A. Oosawa, E. Lelièvre-Berna, J.-H. Chung, H. Ueda, H. Takagi, and S.-H. Lee. *Phys. Rev. B*, 75:104415, Mar 2007.

[43] M. Hase, I. Terasaki, and K. Uchinokura. *Phys. Rev. Lett.*, 70:3651–3654, Jun 1993.

[44] K. Hirota, D. E. Cox, J. E. Lorenzo, G. Shirane, J. M. Tranquada, M. Hase, K. Uchinokura, H. Kojima, Y. Shibuya, and I. Tanaka. *Phys. Rev. Lett.*, 73:736–739, Aug 1994.

[45] T. Sambongi, K. Tsutsumi, Y. Shiozaki, M. Yamamoto, K. Yamaya, and Y. Abe. *Solid State Communications*, 22(12):729 – 731, 1977.

[46] R. E. Peierls. *Quantum theory of solids*. Clarendon Press, 1996.

[47] E. Pytte. *Phys. Rev. B*, 10:4637–4642, Dec 1974.

[48] I. Loa, S. Gronemeyer, C. Thomsen, and R. Kremer. *Solid State Communications*, 99(4):231 – 235, 1996.

[49] F. D. M. Haldane. *Phys. Rev. Lett.*, 50:1153–1156, Apr 1983.

[50] K. Pohlmeyer. *Communications in Mathematical Physics*, 46(3):207–221, Oct 1976.

[51] W. J. L. Buyers, R. M. Morra, R. L. Armstrong, M. J. Hogan, P. Gerlach, and K. Hirakawa. *Phys. Rev. Lett.*, 56:371–374, Jan 1986.

[52] H. Mutka, J. L. Soubeyroux, G. Bourleaux, and P. Colombet. *Phys. Rev. B*, 39:4820–4823, Mar 1989.

[53] A. Zheludev, T. Masuda, I. Tsukada, Y. Uchiyama, K. Uchinokura, P. Böni, and S.-H. Lee. *Phys. Rev. B*, 62:8921–8930, Oct 2000.

[54] M. Kenzelmann, R. A. Cowley, W. J. L. Buyers, R. Coldea, J. S. Gardner, M. Enderle, D. F. McMorrow, and S. M. Bennington. *Phys. Rev. Lett.*, 87:017201, Jun 2001.

[55] M. Kenzelmann, R. A. Cowley, W. J. L. Buyers, Z. Tun, R. Coldea, and M. Enderle. *Phys. Rev. B*, 66:024407, Jun 2002.

[56] F. Haldane. *Physics Letters A*, 93(9):464 – 468, 1983.

[57] L. C. Pauling. *Journal of the American Chemical Society*, 57(12):2680–2684, 1935.

[58] L. C. Pauling. *The Nature of the Chemical Bond*. Cornell University Press, 1960.

[59] J. D. Bernal and R. H. Fowler. *The Journal of Chemical Physics*, 1(8):515–548, 1933.

[60] K. Momma and F. Izumi. *Journal of Applied Crystallography*, 44(6):1272–1276, 2011.

[61] A. P. Ramirez. *Handbook of Magnetic Materials*, 13:423 – 520, 2001.

[62] L. Balents. *Nature*, 464(7286):199–208, Mar 2010.

[63] G. H. Wannier. *Phys. Rev.*, 79:357–364, Jul 1950.

[64] P. Anderson. *Materials Research Bulletin*, 8(2):153 – 160, 1973.

[65] P. W. Anderson. *Science*, 235(4793):1196–1198, 1987.

[66] M. J. Harris, S. T. Bramwell, D. F. McMorrow, T. Zeiske, and K. W. Godfrey. *Phys. Rev. Lett.*, 79:2554–2557, Sep 1997.

[67] A. P. Ramirez, A. Hayashi, R. J. Cava, R. Siddharthan, and B. S. Shastry. *Nature*, 399:333 EP –, May 1999.

[68] S. T. Bramwell and M. J. P. Gingras. *Science*, 294(5546):1495–1501, 2001.

[69] C. Castelnovo, R. Moessner, and S. L. Sondhi. *Nature*, 451:42 EP –, Jan 2008.

[70] T. Fennell, P. P. Deen, A. R. Wildes, K. Schmalzl, D. Prabhakaran, A. T. Boothroyd, R. J. Aldus, D. F. McMorrow, and S. T. Bramwell. *Science*, 326(5951):415–417, 2009.

[71] D. J. P. Morris, D. A. Tennant, S. A. Grigera, B. Klemke, C. Castelnovo, R. Moessner, C. Czternasty, M. Meissner, K. C. Rule, J.-U. Hoffmann, K. Kiefer, S. Gerischer, D. Slobinsky, and R. S. Perry. *Science*, 326(5951):411–414, 2009.

[72] O. Benton, O. Sikora, and N. Shannon. *Phys. Rev. B*, 86:075154, Aug 2012.

[73] M. J. P. Gingras and P. A. McClarty. *Reports on Progress in Physics*, 77(5):056501, may 2014.

[74] K. A. Ross, L. Savary, B. D. Gaulin, and L. Balents. *Phys. Rev. X*, 1:021002, Oct 2011.

[75] R. Sibille, E. Lhotel, M. C. Hatnean, G. Balakrishnan, B. Fåk, N. Gauthier, T. Fennell, and M. Kenzelmann. *Phys. Rev. B*, 94:024436, Jul 2016.

[76] R. Sibille, N. Gauthier, H. Yan, M. Ciomaga Hatnean, J. Ollivier, B. Winn, U. Filges, G. Balakrishnan, M. Kenzelmann, N. Shannon, and T. Fennell. *Nature Physics*, 14(7):711–715, 2018.

[77] P. W. Anderson. *Phys. Rev.*, 102:1008–1013, May 1956.

[78] J. Villain. *Zeitschrift für Physik B Condensed Matter*, 33(1):31–42, Mar 1979.

[79] J. N. Reimers, A. J. Berlinsky, and A.-C. Shi. *Phys. Rev. B*, 43:865–878, Jan 1991.

[80] R. Moessner and J. T. Chalker. *Phys. Rev. Lett.*, 80:2929–2932, Mar 1998.

[81] B. Canals and C. Lacroix. *Phys. Rev. Lett.*, 80:2933–2936, Mar 1998.

[82] B. Canals and D. A. Garanin. *Can. J. Phys.*, 79:1323–1331, 2001.

[83] P. Fulde, K. Penc, and N. Shannon. *Annalen der Physik*, 11(12):892–900, 2002.

[84] L. Savary and L. Balents. *Phys. Rev. Lett.*, 108:037202, Jan 2012.

[85] L. Clark, G. J. Nilsen, E. Kermarrec, G. Ehlers, K. S. Knight, A. Harrison, J. P. Attfield, and B. D. Gaulin. *Phys. Rev. Lett.*, 113:117201, Sep 2014.

[86] R. Sibille, E. Lhotel, V. Pomjakushin, C. Baines, T. Fennell, and M. Kenzelmann. *Phys. Rev. Lett.*, 115:097202, Aug 2015.

[87] O. Tchernyshyov, R. Moessner, and S. L. Sondhi. *Phys. Rev. B*, 66:064403, 2002.

[88] O. Tchernyshyov, R. Moessner, and S. L. Sondhi. *Phys. Rev. Lett.*, 88:067203, Jan 2002.

[89] C. L. Henley. *Phys. Rev. Lett.*, 62:2056–2059, Apr 1989.

[90] S.-H. Lee, H. Takagi, D. Louca, M. Matsuda, S. Ji, H. Ueda, Y. Ueda, T. Katsufuji, J.-H. Chung, S. Park, S.-W. Cheong, and C. Broholm. *Journal of the Physical Society of Japan*, 79(1):011004, 2010.

[91] S. Bordács, D. Varjas, I. Kézsmárki, G. Mihály, L. Baldassarre, A. Abouelsayed, C. A. Kuntscher, K. Ohgushi, and Y. Tokura. *Phys. Rev. Lett.*, 103:077205, 2009.

[92] H. Kawamura and T. Taniguchi. Chapter 1 - spin glasses. In K. Buschow, editor, *Handbook of Magnetic Materials*, volume 24 of *Handbook of Magnetic Materials*, pages 1 – 137. Elsevier, 2015.

[93] D. P. Mitchell and P. N. Powers. *Phys. Rev.*, 50:486–487, Sep 1936.

[94] J. Chadwick. *Proceedings of the Royal Society of London. Series A, Containing Papers of a Mathematical and Physical Character*, 136(830):692–708, 1932.

[95] S. W. Lovesey. *Theory of neutron scattering from condensed matter*. Clarendon Press, 1984.

[96] G. L. Squires. *Introduction to the Theory of Thermal Neutron Scattering*. Cambridge University Press, 3 edition, 2012.

[97] C. J. Carlile and B. T. M. Willis. *Experimental neutron scattering*. Oxford University Press, 2013.

[98] P. J. Brown. Definition of form factors. https://www.ill.eu/sites/ccsl/ffacts/ffactnode2.html. Accessed: 2019-01-28.

[99] E. Kisi and C. Howard. *Applications of Neutron Powder Diffraction*. Oxford University Press, 01 2008.

[100] Institut laue–langevin website. `http://ill.eu`. Accessed: 2019-02-02.

[101] Paul scherrer institut website. `http://psi.ch`. Accessed: 2019-02-02.

[102] L. Liyuan, R. R., and S. H., editors. *Neutron Scattering Instrumentation*, pages 37–104. Springer US, 2009.

[103] R. B. Von Dreele, J. D. Jorgensen, and C. G. Windsor. *Journal of Applied Crystallography*, 15(6):581–589, Dec 1982.

[104] H. M. Rietveld. *Journal of Applied Crystallography*, 2(2):65–71, Jun 1969.

[105] A. L. Bail. *Journal of Solid State Chemistry*, 83(2):267 – 271, 1989.

[106] J. Rodriguez-Carvajal. *Physica B*, 192:55, 1993.

[107] F. Hippert, E. Geissler, J. Louis Hodeau, E. Lelièvre-Berna, and J. René Regnard. *Neutron and X-ray Spectroscopy*. Springer, 12 2005.

[108] M. J. Cooper and R. Nathans. *Acta Crystallographica*, 23(3):357–367, Sep 1967.

[109] M. Popovici. *Acta Crystallographica Section A*, 31(4):507–513, Jul 1975.

[110] J. Saroun and J. Kulda. *Physica B: Condensed Matter*, 234-236:1102 – 1104, 1997. Proceedings of the First European Conference on Neutron Scattering.

[111] J. Ollivier and J.-M. Zanotti. *JDN*, 10:379–423, 2010.

[112] O. Schärpf and H. Capellmann. *Physica Status Solidi (a)*, 135(2):359–379, 1993.

[113] J. R. Stewart, P. P. Deen, K. H. Andersen, H. Schober, J.-F. Barthélémy, J. M. Hillier, A. P. Murani, T. Hayes, and B. Lindenau. *Journal of Applied Crystallography*, 42(1):69–84, Feb 2009.

[114] J. Schweizer. Chapter 4 - polarized neutrons and polarization analysis. In T. Chatterji, editor, *Neutron Scattering from Magnetic Materials*, pages 153 – 213. Elsevier Science, Amsterdam, 2006.

[115] L. Regnault. Chapter 8 - inelastic neutron polarization analysis. In T. Chatterji, editor, *Neutron Scattering from Magnetic Materials*, pages 363 – 395. Elsevier Science, Amsterdam, 2006.

[116] W. Schweika. *Journal of Physics: Conference Series*, 211:012026, feb 2010.

[117] Quantum design website. `https://www.qdusa.com`. Accessed: 27-02-2019.

[118] A. I. B. John Clarke, editor. *The SQUID Handbook: Fundamentals and Technology of SQUIDs and SQUID Systems*. Wiley, 2005.

[119] S. A. W. a. Vladimir Z. Kresin. *Fundamentals of Superconductivity*. Springer US, 1 edition, 1990.

[120] M. Sawicki, W. Stefanowicz, and A. Ney. *Semiconductor Science and Technology*, 26(6):064006, apr 2011.

[121] G. Kalvius, O. Hartmann, D. Noakes, F. Wagner, R. Wäppling, U. Zimmermann, C. Baines, A. Krimmel, V. Tsurkan, and A. Loidl. *Physica B: Condensed Matter*, 378-380:592 – 593, 2006. Proceedings of the International Conference on Strongly Correlated Electron Systems.

[122] T. Rudolf, C. Kant, F. Mayr, J. Hemberger, V. Tsurkan, and A. Loidl. *New Journal of Physics*, 9(3):76, 2007.

[123] A. N. Yaresko. *Phys. Rev. B*, 77:115106, Mar 2008.

[124] H. Tsunetsugu. *Journal of the Physical Society of Japan*, 70(3):640–643, 2001.

[125] K. Penc, N. Shannon, and H. Shiba. *Phys. Rev. Lett.*, 93:197203, Nov 2004.

[126] H. Shinaoka, Y. Tomita, and Y. Motome. *Phys. Rev. B*, 90:165119, 2014.

[127] A. B. Sushkov, O. Tchernyshyov, W. R. II, S. W. Cheong, and H. D. Drew. *Phys. Rev. Lett.*, 94:137202, Apr 2005.

[128] R. Valdés Aguilar, A. B. Sushkov, Y. J. Choi, S.-W. Cheong, and H. D. Drew. *Phys. Rev. B*, 77:092412, Mar 2008.

[129] Y. Motome, K. Penc, and N. Shannon. *Journal of Magnetism and Magnetic Materials*, 300(1):57 – 61, 2006. The third Moscow International Symposium on Magnetism 2005.

[130] N. Shannon, K. Penc, and Y. Motome. *Phys. Rev. B*, 81:184409, 2010.

[131] S. Ji, S.-H. Lee, C. Broholm, T. Y. Koo, W. Ratcliff, S.-W. Cheong, and P. Zschack. *Phys. Rev. Lett.*, 103:037201, 2009.

[132] M. C. Kemei, P. T. Barton, S. L. Moffitt, M. W. Gaultois, J. A. Kurzman, R. Seshadri, M. R. Suchomel, and Y.-I. Kim. *Journal of Physics: Condensed Matter*, 25(32):326001, jul 2013.

[133] S. Gao, K. Guratinder, U. Stuhr, J. S. White, M. Mansson, B. Roessli, T. Fennell, V. Tsurkan, A. Loidl, M. Ciomaga Hatnean, G. Balakrishnan, S. Raymond, L. Chapon, V. O. Garlea, A. T. Savici, A. Cervellino, A. Bombardi, D. Chernyshov, C. Rüegg, J. T. Haraldsen, and O. Zaharko. *Phys. Rev. B*, 97:134430, Apr 2018.

[134] J.-H. Chung, M. Matsuda, S.-H. Lee, K. Kakurai, H. Ueda, T. J. Sato, H. Takagi, K.-P. Hong, and S. Park. *Phys. Rev. Lett.*, 95:247204, Dec 2005.

[135] S.-H. Lee, C. Broholm, W. Ratcliff, G. Gasparovic, Q. Huang, T. H. Kim, and S.-W. Cheong. *Nature*, 418:856 EP –, Aug 2002.

[136] S.-H. Lee, C. Broholm, T. H. Kim, W. Ratcliff, and S.-W. Cheong. *Phys. Rev. Lett.*, 84:3718–3721, Apr 2000.

[137] W. Ratcliff, S.-H. Lee, C. Broholm, S.-W. Cheong, and Q. Huang. *Phys. Rev. B*, 65:220406, Jun 2002.

[138] K. Tomiyasu, H. Suzuki, M. Toki, S. Itoh, M. Matsuura, N. Aso, and K. Yamada. *Phys. Rev. Lett.*, 101:177401, Oct 2008.

[139] L. Ortega-San-Martín, A. J. Williams, C. D. Gordon, S. Klemme, and J. P. Attfield. *Journal of Physics: Condensed Matter*, 20(10):104238, 2008.

[140] H. Ueda, H. Mitamura, T. Goto, and Y. Ueda. *Phys. Rev. B*, 73:094415, Mar 2006.

[141] J.-C. Joubert and A. Durif-Varambon. *Bulletin de Minéralogie*, 89(1):26–28, 1966.

[142] Y. Okamoto, G. J. Nilsen, J. P. Attfield, and Z. Hiroi. *Phys. Rev. Lett.*, 110:097203, Feb 2013.

[143] Y. Okamoto, G. J. Nilsen, T. Nakazano, and Z. Hiroi. *J. Phys. Soc. Jpn.*, 84:043707, 2015.

[144] V. F. Sears. *Neutron News*, 3(3):26–37, 1992.

[145] Y. Tanaka, M. Yoshida, M. Takigawa, Y. Okamoto, and Z. Hiroi. *Phys. Rev. Lett.*, 113:227204, 2014.

[146] G. J. Nilsen, Y. Okamoto, T. Masuda, J. Rodriguez-Carvajal, H. Mutka, T. Hansen, and Z. Hiroi. *Phys. Rev. B*, 91:174435, 2015.

[147] R. Saha, F. Fauth, M. Avdeev, P. Kayser, B. J. Kennedy, and A. Sundaresan. *Phys. Rev. B*, 94:064420, Aug 2016.

[148] S. Lee, S.-H. Do, W.-J. Lee, Y. S. Choi, M. Lee, E. S. Choi, A. P. Reyes, P. L. Kuhns, A. Ozarowski, and K.-Y. Choi. *Phys. Rev. B*, 93:174402, 2016.

[149] S.-H. Lee, G. Gasparovic, C. Broholm, M. Matsuda, J.-H. Chung, Y. J. Kim, H. Ueda, G. Xu, P. Zschack, K. Kakurai, H. Takagi, W. Ratcliff, T. H. Kim, and S.-W. Cheong. *Journal of Physics: Condensed Matter*, 19(14):145259, mar 2007.

[150] S. E. Dutton, Q. Huang, O. Tchernyshyov, C. L. Broholm, and R. J. Cava. *Phys. Rev. B*, 83:064407, Feb 2011.

[151] S. C. Miller and W. F. Love. *Tables of irreducible representations of space groups and co-representations of magnetic space groups.* Pruett Press, Boulder, Colo., 1967.

[152] R. Wawrzyńczak, Y. Tanaka, M. Yoshida, Y. Okamoto, P. Manuel, N. Casati, Z. Hiroi, M. Takigawa, and G. J. Nilsen. *Phys. Rev. Lett.*, 119:087201, Aug 2017.

[153] P. W. Stephens. *J. Appl. Cryst.*, 32:281, 1999.

[154] S. V. Isakov, K. Gregor, R. Moessner, and S. L. Sondhi. *Phys. Rev. Lett.*, 93:167204, 2004.

[155] J. A. M. Paddison, J. R. Stewart, and A. L. Goodwin. *J. Phys.: Condens. Matter*, 25:454220, 2013.

[156] N. Metropolis and S. Ulam. *Journal of the American Statistical Association*, 44(247):335–341, 1949. PMID: 18139350.

[157] J. A. M. Paddison, H. Jacobsen, O. A. Petrenko, M. T. Fernández-Díaz, P. P. Deen, and A. L. Goodwin. *Science*, 350(6257):179–181, 2015.

[158] M. F. Collins. *Magnetic critical scattering*. New York : Oxford University Press, 1989.

[159] Y. Tanaka, R. Wawrzyńczak, M. D. Le, T. Guidi, Y. Okamoto, T. Yajima, Z. Hiroi, M. Takigawa, and G. J. Nilsen. *Journal of the Physical Society of Japan*, 87(7):073710, 2018.

[160] G. J. Nilsen, Y. Okamoto, C. Tassel, T. Masuda, H. Mutka, and Z. Hiroi, *ILL Experimental Report 5-31-2275*, Available at: https://userclub.ill.eu.

[161] P. H. Conlon and J. T. Chalker. *Phys. Rev. Lett.*, 102:237206, Jun 2009.

[162] J. N. Reimers, J. E. Greedan, and M. Björgvinsson. *Phys. Rev. B*, 45:7295–7306, Apr 1992.

[163] Supplemental material of ref. [152]. `https://journals.aps.org/prl/supplemental/10.1103/PhysRevLett.119.087201`. Accessed: 2019-03-30.

[164] J. von Delft and C. L. Henley. *Phys. Rev. B*, 48:965–984, Jul 1993.

[165] M. Taillefumier, J. Robert, C. L. Henley, R. Moessner, and B. Canals. *Phys. Rev. B*, 90:064419, Aug 2014.

[166] Y. Wan and M. J. P. Gingras. *Phys. Rev. B*, 94:174417, Nov 2016.

[167] A. Miyata, H. Ueda, Y. Ueda, Y. Motome, N. Shannon, K. Penc, and S. Takeyama. *Journal of the Physical Society of Japan*, 80(7):074709, 2011.

[168] R. V. Dietrich. *"Garnet", Encyclopædia Britannica Online*. Encyclopedia Britannica Inc., 1999.

[169] R. Pauthenet. *Ann. Phys.*, 13(3):424–462, 1958.

[170] J. F. Dillon and J. W. Nielsen. *Phys. Rev.*, 120:105–113, Oct 1960.

[171] A. H. Cooke, T. L. Thorp, and M. R. Wells. *Proceedings of the Physical Society*, 92(2):400–407, oct 1967.

[172] V. F. Kitaeva, E. V. Zharikov, and I. L. Chistyi. *physica status solidi (a)*, 92(2):475–488, 1985.

[173] J. E. Geusic, H. M. Marcos, and L. G. Van Uitert. *Applied Physics Letters*, 4(10):182–184, 1964.

[174] N. P. Barnes and L. B. Petway. *J. Opt. Soc. Am. B*, 9(10):1912–1915, Oct 1992.

[175] H. Capel. *Physica*, 31(7):1152 – 1176, 1965.

[176] K. P. Belov and V. I. Sokolov. *Soviet Physics Uspekhi*, 20(2):149–166, feb 1977.

[177] C. L. Henley. *Annual Review of Condensed Matter Physics*, 1(1):179–210, 2010.

[178] H. S. M. Coxeter. *Canadian Journal of Mathematics*, 7:18–23, 1955.

[179] J. M. Hastings, L. M. Corliss, and C. G. Windsor. *Phys. Rev.*, 138:A176–A177, Apr 1965.

[180] J. Hamman and P. Manneville. *J. Phys. France*, 34(7):615–622, 1973.

[181] J. Hammann. *Étude par diffraction des neutrons a 0,3° K des propriétés magnétiques de grenats de terre rare et d'aluminium ou e gallium.* PhD thesis, Centre d'Études Nucléaires de Saclay, 1969.

[182] J. Felsteiner and S. K. Misra. *Phys. Rev. B*, 24:2627–2633, Sep 1981.

[183] M. Ball, G. Garton, M. J. M. Leask, D. Ryan, and W. P. Wolf. *Journal of Applied Physics*, 32(3):S267–S269, 1961.

[184] M. Ball, M. J. M. Leask, W. P. Wolf, and A. F. G. Wyatt. *Journal of Applied Physics*, 34(4):1104–1105, 1963.

[185] J. C. Norvell, W. P. Wolf, L. M. Corliss, J. M. Hastings, and R. Nathans. *Phys. Rev.*, 186:557–566, Oct 1969.

[186] J. C. Norvell, W. P. Wolf, L. M. Corliss, J. M. Hastings, and R. Nathans. *Phys. Rev.*, 186:567–576, Oct 1969.

[187] S. Hov, H. Bratsberg, and A. Skjeltorp. *Journal of Magnetism and Magnetic Materials*, 15-18:455 – 456, 1980.

[188] A. P. Ramirez and R. N. Kleiman. *Journal of Applied Physics*, 69(8):5252–5254, 1991.

[189] P. Schiffer, A. P. Ramirez, D. A. Huse, P. L. Gammel, U. Yaron, D. J. Bishop, and A. J. Valentino. *Phys. Rev. Lett.*, 74:2379–2382, Mar 1995.

[190] D. G. Onn, H. Meyer, and J. P. Remeika. *Phys. Rev.*, 156:663–670, Apr 1967.

[191] W. I. Kinney and W. P. Wolf. *Journal of Applied Physics*, 50(B3):2115–2117, 1979.

[192] N. d'Ambrumenil, O. A. Petrenko, H. Mutka, and P. P. Deen. *Phys. Rev. Lett.*, 114:227203, Jun 2015.

[193] O. A. Petrenko, C. Ritter, M. Yethiraj, and D. McK Paul. *Phys. Rev. Lett.*, 80:4570–4573, May 1998.

[194] K. Kamazawa, D. Louca, R. Morinaga, T. J. Sato, Q. Huang, J. R. D. Copley, and Y. Qiu. *Phys. Rev. B*, 78:064412, Aug 2008.

[195] S. Nagata, H. Sasaki, K. Suzuki, J. Kiuchi, and N. Wada. *Journal of Physics and Chemistry of Solids*, 62(6):1123 – 1130, 2001.

[196] J. Hammann and M. Ocio. *Physica B+C*, 86:1153 – 1155, 1977.

[197] D. J. Dentz, R. C. Puttbach, and R. F. Belt. *AIP Conference Proceedings*, 18(1):954–958, 1974.

[198] A. B. Villaverde, D. A. Donatti, and D. G. Bozinis. *Journal of Physics C: Solid State Physics*, 11(12):L495, 1978.

[199] P. N. Schatz and A. J. McCaffery. *Q. Rev. Chem. Soc.*, 23:552–584, 1969.

[200] C. Strohm, G. L. J. A. Rikken, and P. Wyder. *Phys. Rev. Lett.*, 95:155901, Oct 2005.

[201] A. V. Inyushkin and A. N. Taldenkov. *JETP Letters*, 86(6):379–382, Nov 2007.

[202] L. Sheng, D. N. Sheng, and C. S. Ting. *Phys. Rev. Lett.*, 96:155901, Apr 2006.

[203] Y. Kagan and L. A. Maksimov. *Phys. Rev. Lett.*, 100:145902, Apr 2008.

[204] M. Mori, A. Spencer-Smith, O. P. Sushkov, and S. Maekawa. *Phys. Rev. Lett.*, 113:265901, Dec 2014.

[205] H. Lee, J. H. Han, and P. A. Lee. *Phys. Rev. B*, 91:125413, Mar 2015.

[206] A. V. Inyushkin and A. N. Taldenkov. *Journal of Experimental and Theoretical Physics*, 111(5):760–769, Nov 2010.

[207] G. A. Slack and D. W. Oliver. *Phys. Rev. B*, 4:592–609, Jul 1971.

[208] M. Hirschberger, J. W. Krizan, R. J. Cava, and N. P. Ong. *Science*, 348(6230):106–109, 2015.

[209] Y. Kasahara, K. Sugii, T. Ohnishi, M. Shimozawa, M. Yamashita, N. Kurita, H. Tanaka, J. Nasu, Y. Motome, T. Shibauchi, and Y. Matsuda. *Phys. Rev. Lett.*, 120:217205, May 2018.

[210] H.-S. Kim, V. S. V., A. Catuneanu, and H.-Y. Kee. *Phys. Rev. B*, 91:241110, Jun 2015.

[211] A. Vishwanath. *Phys. Rev. Lett.*, 87:217004, Nov 2001.

[212] H. Katsura, N. Nagaosa, and P. A. Lee. *Phys. Rev. Lett.*, 104:066403, Feb 2010.

[213] M. Stone. *Phys. Rev. B*, 85:184503, May 2012.

[214] S. A. Owerre. *Journal of Applied Physics*, 120(4):043903, 2016.

[215] A. Sytcheva, U. Löw, S. Yasin, J. Wosnitza, S. Zherlitsyn, P. Thalmeier, T. Goto, P. Wyder, and B. Lüthi. *Phys. Rev. B*, 81:214415, Jun 2010.

[216] B. Lüthi. *Physical Acoustics in the Solid State*. Springer Series in Solid-State Sciences. Springer Berlin Heidelberg, 2007.

[217] P. Thalmeier. *Phys. Rev. B*, 80:214421, Dec 2009.

[218] J. Hammann and M. Ocio. *Physics Letters A*, 55(3):195 – 196, 1975.

[219] K. Andres, E. Bucher, J. P. Maita, and A. S. Cooper. *Phys. Rev. Lett.*, 28:1652–1655, Jun 1972.

[220] E. Clementyev, P. Alekseev, P. Allenspach, and V. Lazukov. *Applied Physics A*, 74(1):s589–s591, Dec 2002.

[221] T. Murao. *Journal of the Physical Society of Japan*, 31(3):683–690, 1971.

[222] K. Andres. *Phys. Rev. B*, 7:4295–4300, May 1973.

[223] T. Murao. *Journal of the Physical Society of Japan*, 39(1):50–57, 1975.

[224] Y.-L. Wang and B. R. Cooper. *Phys. Rev.*, 172:539–551, Aug 1968.

[225] A. Zheludev, J. M. Tranquada, T. Vogt, and D. J. Buttrey. *Phys. Rev. B*, 54:6437–6447, Sep 1996.

[226] T. M. Holden, E. C. Svensson, W. J. L. Buyers, and O. Vogt. *Phys. Rev. B*, 10:3864–3876, Nov 1974.

[227] Fee website. `https://www.fee-io.de/`. Accessed: 27-05-2019.

[228] A. Dianoux, G. Lander, and I. Laue-Langevin. *Neutron Data Booklet*. Institut Laue-Langevin, 2002.

[229] H. T. Stokes, D. M. Hatch, and B. J. Campbell. Isotropy software suite.

[230] J. W. Essam and M. E. Fisher. *The Journal of Chemical Physics*, 38(4):802–812, 1963.

[231] G. A. Baker and D. S. Gaunt. *Phys. Rev.*, 155:545–552, Mar 1967.

[232] H. Bethe. *Annalen der Physik*, 3(2):133–208, 1929.

[233] M. Guillot and A. Marchand. *Journal of Physics C: Solid State Physics*, 18(18):3547, 1985.

[234] P. J. Brown. Magnetic form factors. In E. Prince, editor, *International Tables for Crystallography, Volume C: Mathematical, Physical and Chemical Tables*, chapter 4.4, pages 454–461. International Union of Crystallography, 2006.

[235] J. A. Koningstein and C. J. Kane-Maguire. *Canadian Journal of Chemistry*, 52(20):3445–3450, 1974.

[236] G. Shirane, S. M. Shapiro, and J. M. Tranquada. *Neutron Scattering with a Triple-Axis Spectrometer: Basic Techniques*. Cambridge University Press, 2002.

[237] O. Arnold, J. Bilheux, J. Borreguero, A. Buts, S. Campbell, L. Chapon, M. Doucet, N. Draper, R. F. Leal, M. Gigg, V. Lynch, A. Markvardsen, D. Mikkelson, R. Mikkelson, R. Miller, K. Palmen, P. Parker, G. Passos, T. Perring, P. Peterson, S. Ren, M. Reuter, A. Savici, J. Taylor, R. Taylor, R. Tolchenov, W. Zhou, and J. Zikovsky. *Nuclear Instruments and Methods in Physics Research Section A: Accelerators, Spectrometers, Detectors and Associated Equipment*, 764:156 – 166, 2014.

[238] M. Rotter. *Journal of Magnetism and Magnetic Materials*, 272-276:E481 – E482, 2004. Proceedings of the International Conference on Magnetism (ICM 2003).

[239] A. Abragam and B. Bleaney. *Electron Paramagnetic Resonance of Transition Ions*. Clarendon Oxford, 1970.

[240] A. T. Boothroyd. Spectre, a program for calculating spectroscopic properties of rare earth ions in crystals, 1990.

[241] E. Antic-Fidancev, C. K. Jayasankar, M. Lemaitre-Blaise, and P. Porcher. *Journal of Physics C: Solid State Physics*, 19(32):6451, 1986.

[242] D. Boal, P. Grunberg, and J. A. Koningstein. *Phys. Rev. B*, 7:4757–4763, Jun 1973.

[243] H. M. Crosswhite and H. W. Moos, editors. *Conference on Optical Properties of Ions in Crystals*, New York, 1967. Interscience Publishers, Inc.

[244] E. Orlich and S. Hfner. *Journal of Applied Physics*, 40(3):1503–1504, 1969.

[245] Scipy. `https://www.scipy.org/`. Accessed: 2019-05-10.

[246] R. Ewings, A. Buts, M. Le, J. van Duijn, I. Bustinduy, and T. Perring. *Nuclear Instruments and Methods in Physics Research Section A: Accelerators, Spectrometers, Detectors and Associated Equipment*, 834:132 – 142, 2016.

[247] M. Leask, M. Wells, R. Ward, S. Hayden, and J. Jensen. *Journal of Physics: Condensed Matter*, 6(2):505, 1994.

[248] $Tb_3ga_5o_{12}$ entry - phonon database at kyoto university. `http://phonondb.mtl.kyoto-u.ac.jp/ph20180417/d005/mp-5965.html?highlight=tb3ga5o12`. Accessed: 2019-04-10.

[249] F. Giustino. *Materials Modelling using Density Functional Theory: Properties and Predictions*. OUP Oxford, 2014.

[250] Zbiri, M., Johnson, M., Schober, H., Rols, S., Qureshi, N., Clarke, S., and Mittal, R. *JDN*, 12:77–104, 2011.

[251] A. Togo and I. Tanaka. *Scr. Mater.*, 108:1–5, Nov 2015.

[252] T. Fennell, M. Kenzelmann, B. Roessli, H. Mutka, J. Ollivier, M. Ruminy, U. Stuhr, O. Zaharko, L. Bovo, A. Cervellino, M. K. Haas, and R. J. Cava. *Phys. Rev. Lett.*, 112:017203, Jan 2014.

[253] R. Bidaux, A. Gavignet-Tillard, and J. Hammann. *Journal de Physique*, 34(1):19–26, 1973.

[254] P. Pfeuty. *Annals of Physics*, 57(1):79 – 90, 1970.

[255] M. Collins and O. Petrenko. *Canadian journal of physics*, 75(9):605–655, 1997.

[256] R. H. Clark and W. G. Moulton. *Phys. Rev. B*, 5:788–795, Feb 1972.

[257] H. A. katori, Y. Ajiro, T. Asano, and T. Goto. *Journal of the Physical Society of Japan*, 64(8):3038–3042, 1995.

[258] W. B. Yelon and D. E. Cox. *Phys. Rev. B*, 7:2024–2027, Mar 1973.

[259] D. E. Cox and V. J. Minkiewicz. *Phys. Rev. B*, 4:2209–2212, Oct 1971.

[260] M. C. Rheinstädter, M. Enderle, and G. J. McIntyre. *Phys. Rev. B*, 70:224420, Dec 2004.

[261] Z. Tun, W. J. L. Buyers, A. Harrison, and J. A. Rayne. *Phys. Rev. B*, 43:13331–13334, 1991.

[262] E. Cohen and M. Sturge. *Solid State Communications*, 24(1):51 – 53, 1977.

[263] W. B. Yelon and D. E. Cox. *Phys. Rev. B*, 7:2024–2027, Mar 1973.

[264] H. Kawamura. *Journal of Applied Physics*, 61(8):3590–3594, 1987.

[265] S. Toth and B. Lake. *Journal of Physics: Condensed Matter*, 27(16):166002, mar 2015.

[266] W. Buyers, Z. Tun, A. Harrison, J. Rayne, and R. Nicklow. *Physica B: Condensed Matter*, 180-181:222 – 224, 1992.

[267] D. J. Scalapino, Y. Imry, and P. Pincus. *Phys. Rev. B*, 11:2042–2048, Mar 1975.

[268] M. L. Plumer, K. Hood, and A. Caillé. *Phys. Rev. Lett.*, 60:45–48, Jan 1988.

[269] Z. Tun, W. J. L. Buyers, R. L. Armstrong, K. Hirakawa, and B. Briat. *Phys. Rev. B*, 42:4677–4681, Sep 1990.

[270] M. Enderle, K. Kakurai, K. N. Clausen, T. Inami, H. Tanaka, and M. Steiner. *Europhysics Letters (EPL)*, 25(9):717–722, mar 1994.

[271] M. Enderle, K. Kakurai, M. Steiner, and H. Weinfurter. *Journal of Magnetism and Magnetic Materials*, 104-107:809 – 810, 1992. Proceedings of the International Conference on Magnetism, Part II.

[272] M. Enderle, Z. Tun, W. J. L. Buyers, and M. Steiner. *Phys. Rev. B*, 59:4235–4243, Feb 1999.

[273] I. Affleck. *Phys. Rev. B*, 41:6697–6702, Apr 1990.

[274] I. Affleck and G. F. Wellman. *Phys. Rev. B*, 46:8934–8953, Oct 1992.

[275] M. D. P. Horton and I. Affleck. *Phys. Rev. B*, 60:11891–11893, Nov 1999.

[276] F. H. L. Essler. *Phys. Rev. B*, 62:3264–3270, Aug 2000.

[277] A. M. Tsvelik. *Phys. Rev. B*, 42:10499–10504, Dec 1990.

[278] S. H. Glarum, S. Geschwind, K. M. Lee, M. L. Kaplan, and J. Michel. *Phys. Rev. Lett.*, 67:1614–1617, Sep 1991.

[279] M. Kenzelmann, G. Xu, I. A. Zaliznyak, C. Broholm, J. F. DiTusa, G. Aeppli, T. Ito, K. Oka, and H. Takagi. *Phys. Rev. Lett.*, 90:087202, Feb 2003.

[280] M. L. Plumer and A. Caillé. *Phys. Rev. Lett.*, 68:1042–1045, Feb 1992.

[281] A. K. Kolezhuk and U. Schollwöck. *Phys. Rev. B*, 65:100401, Feb 2002.

[282] N. Tsyrulin, T. Pardini, R. R. P. Singh, F. Xiao, P. Link, A. Schneidewind, A. Hiess, C. P. Landee, M. M. Turnbull, and M. Kenzelmann. *Phys. Rev. Lett.*, 102:197201, May 2009.

[283] D. Schmidiger, P. Bouillot, T. Guidi, R. Bewley, C. Kollath, T. Giamarchi, and A. Zheludev. *Phys. Rev. Lett.*, 111:107202, Sep 2013.

[284] $Rbnicl_3$ entry - phonon database at kyoto university. `http://phonondb.mtl.kyoto-u.ac.jp/ph20180417/d023/mp-23486.html?highlight=rbnicl3`. Accessed: 2019-04-10.

Acknowledgements

I would like to thank my supervisors Dr Martin Boehm, Dr Tom Fennell, Prof. Dr Michel Kenzelmann, Dr Gøran Nilsen. Firstly, I would like to express my gratitude for giving me opportunity to join the PhD project under their supervision. Secondly I am very grateful for valuable advice, support and guidance offered to me over these four years. I was extremely fortunate to have a chance to benefit from vast knowledge and experience of so many brilliant scientists.

I am very grateful to my close collaborators Dr Nicolas Gauthier, Dr Yu Tanaka and Dr Bruno Tomasello for contribution to the work described in this manuscript and countless hours of discussions. Without their input a lot of work presented here would be incomplete or lack important context. Moreover I would like to thank for useful discussions with Dr Tim Ziman and Dr Olivier Cépas.

Acquiring the data presented in this work would not be possible without involvement of numerous people running the large scales facilities which I have stayed at or briefly visited on the course of my project: Institut Laue-Langevin (ILL), SINQ and SLS at Paul Scherrer Institut (PSI), ISIS-STFC and Spallation Neutron Source (SNS) at ORNL. I am grateful to all the people who showed their hospitality making these visits a fruitful, but also pleasant experience. I would like to thank especially the instrument scientists building, maintaining and developing the instrumentation serving the scientific community. Here I would like to mention my local contacts offering me help during my measurements Dr Thomas Hansen, Dr Hannu Mutka, Dr Andrew Wildes, Dr Lucille Mangin-Thro, Dr Jacques Ollivier, Dr Peter Fouquet, Dr Denis Cheptiakov, Dr Vladimir Pomjakushin, Dr Bertrand Roessli, Dr Oksana Zaharko, Dr Uwe Stuhr, Dr Romain Sibille and Dr Nicola Casati, Dr Tatiana Guidi, Dr Duc Le, Dr Victoria Garcia Sakai, Dr Pascal Manuel, Dr Helen Walker, Dr Dmitry Khalyavin, Dr. Fabio Orlandi, Dr Barry Winn and Dr Ovi Garlea.

Some of the preformed experimental procedures would not be possible without support from sample environment specialists from all of the mentioned facilities. Here, I would like to especially thank Dr Marek Bartkowiak and Dr Markus Zolliker from PSI.

My stay at ILL would not be the same without all members of the PhD graduate school, whom I would like to thank for all the scientific and non-scientific activities I had a chance to join. I would like to give special thanks to my PhD fellows Javier, Diane, Ana, Radu, Tim, Marta, Maria, Stas, Dominik, Palmerina, Adrian, Marco, Simon, Lidia, Kristijan and Tetiana. During my stays at PSI I have enjoyed the company of Alexandra, Daniel and Guratinder.

I would also like to thank all my friends back in Poland and especially Katarzyna, Janek, Offca, Stefan and Witek, who made the holiday visits back at home and occasional meetings in various places around the world awaited points of my schedule.

Finally, this would not be possible without continuous support and encouragement form my wife Karolina and my parents Bernadeta and Stanisław, to whom I would like to give the biggest thanks for always being there for me.

Curriculum vitæ

PERSONAL INFORMATION

Last name:	Wawrzyńczak
First name:	Rafał
Date of birth:	12/06/1991
Place of birth:	Łódź, Poland

EDUCATION

PhD in Experimental physics 07/2015-07/2019
Faculty of Science, University of Basel, Institut Laue-Langevin and Paul Scherrer Institut

MSc in Applied physics 02/2014-07/2015
Faculty of Physics, Warsaw University of Technology

BSc in Technical Physics 10/2010-02/2014
Faculty of Technical Physics, Information Technology and Applied Mathematics, Lodz University of Technology

High school diploma 09/2007-06/2010
Public High School of Lodz University of Technology

Publications

Magnetic order and single-ion anisotropy in $Tb_3Ga_5O_{12}$

R. Wawrzyńczak, B. Tomasello, P. Manuel, D. Khalyavin, M. D. Le, T. Guidi, A. Cervellino, T. Ziman, M. Boehm, G. J. Nilsen, and T. Fennell,
Phys. Rev. B **100**, 094442 **(2019)**.

Inelastic Neutron Scattering Study of the Spin Dynamics in the Breathing Pyrochlore System $LiGa_{0.95}In_{0.05}Cr_4O_8$

Y. Tanaka, **R. Wawrzyńczak**, M.D. Le, T. Guidi, Y. Okamoto4, T. Yajima, Z. Hiroi, M. Takigawa, and G.J. Nilsen,
J. Phys. Soc. Jpn. **87**, 073710 **(2018)**.

Classical Spin Nematic Transition in $LiGa_{0.95}In_{0.05}Cr_4O_8$

R. Wawrzyńczak, Y. Tanaka, M. Yoshida, Y. Okamoto, P. Manuel, N. Casati, Z. Hiroi, M. Takigawa, and G.J. Nilsen,
Phys. Rev. Lett. **119**, 087201 **(2017)**.